Electrochemical studies on functionalized Indium Tin Oxide (ITO) and Graphite Oxide (GrO) surfaces

by

Venkata Jagadeesh Rachuri

Raman Research Institute
Bangalore

Thesis submitted to the Jawaharlal Nehru University

for the degree of

Doctor of Philosophy

April 2018

Dedicated to my Parents and Uncle

Certificate

This is to certify that the thesis entitled "**Electrochemical studies on functionalized Indium Tin Oxide (ITO) and Graphite Oxide (GrO) surfaces**" submitted by VENKATA JAGADEESH RACHURI for the degree of DOCTOR OF PHILOSOPHY of the Jawaharlal Nehru University is his original work. This has not been published or submitted to any other University for any other degree or diploma.

Prof. V. Lakshminarayanan
(Thesis Supervisor)

Dr. Arun Roy
(Thesis Co-Supervisor)

Director
Raman Research Institute
Bangalore 560 080-INDIA

Declaration

I, hereby, declare that this thesis is composed independently by me, at Raman Research Institute, Bangalore, India, under the supervision of Prof. V. Lakshminarayanan. The subject matter presented in this thesis has not previously formed the basis for the award of any degree, diploma, membership, associateship, fellowship or any other similar title of any university or institution. I also declare that I have run it through the **Turnitin** plagiarism software.

(Prof. V. Lakshminarayanan)
(Thesis Supervisor)
Raman Research Institute

(Dr. Arun Roy)
(Thesis Co-Supervisor)
Raman Research Institute

(Venkata Jagadeesh Rachuri)

Acknowledgements

It was a pleasure working with Prof. V. Lakshminarayanan. It was a great learning experience and the interactions with him made me feel confident in pursuing research in chemistry. He is an enthusiastic scientist, whose intuition towards the research motivates students to pursue research as career.

Thanks to Dr. Arun Roy, for being my co-supervisor for my PhD work and the constant support and suggestions during crucial times of my research. I would like to thank my thesis advisory committee members Prof. Pratibha and Prof. Sandeep Kumar for their valuable suggestions to keep my thesis work on track. I have learnt a lot from my intermittent interactions with Prof. Raghunathan and Prof. Yashodhan. I am thankful to Prof. A. K. Shukla, SSCU, IISc Bangalore for his motivation and help in my research work. I would also like to thank Dr. Ganesh for discussions regarding my work and doing contact angle studies. Thanks to Mr. Krishna, for helping me through administration in tough times of PhD.

I also thank N. Ravisankar for his invaluable help in the lab. My sincere thanks to Dhason and Yatheendran for their help in SEM, AFM and STM imaging, Mani for his help in fabricating ITO plates electrodes for various experiments and H.T. Sreenivasa for technical help. I thank Mrs. Vasudha for her help in spectroscopic measurements. I would like to thank Mr. K. Radhakrishna for his help throughout my PhD in RRI. Thanks to Murali and Raja for their valuable and timely help throughout my research work.

I would like to thank my colleague, Anu for her constant involvement and encouragement in my research progress. I drew a lot of inspiration from her especially time management skills. My sincere gratitude to Swamy, for helping me in giving valuable inputs to my research work through discussions and also for providing me all possible help while writing thesis. Thanks to Siva Irla for all the help and suggestions in increasing the pace of my work. Madhukar and JK, two rare personalities from whom I learnt to see things from different perspectives and keeping things simple. Mari, Surendar, Surya, Anindya, Asha, Chandan, Anjan, Prakyath,

Satyanarayana, Sreeja, Sreyas, Subodh, Venu, GB, Avinash and RK, without you guys PhD would have been a difficult ride, thanks for criticizing when I made wrong decisions.

It was always fun to be with Saichand, Pruthvi, Nishant, Meera, Adwaith, Rashmi, Srinu and Shiva and I thank them for all the wonderful time spent. I am thankful to Sanathana for writing a LabVIEW program, which I have extensively used for carrying out the adsorption kinetics work in my thesis. I would like to thank all the present and past students of RRI, for providing me good memories.

Sports has been always my stress buster during my stay in RRI, and RRI has a supportive environment where one can better their skills.

I thank RRI staff members in some of its facilities who helped me at various stages of my RRI years.

Last but not least thanks to my parents, uncle, and family for the persistent support.

Contents

Abbreviations

CV Cyclic Voltammetry

EIS Electrochemical Impedance Spectroscopy

CE Chronopotentiometry

CA Chronoamperometry

XRD X-ray diffraction

STM Scanning Tunneling Microscopy

AFM Atomic Force Microscopy

SEM Scanning Electron Microscopy

EDAX Energy Dispersive X-ray Analysis

SAM/SAMs Self-Assembled Monolayer(s)

ITO Indium Tin Oxide

GS Flexible Graphite Sheet

(-)IGS Negative potential intercalated graphite sheet

(+)IGS Positive potential intercalated graphite sheet

Pd GS Pd on graphite sheet

ν Scan rate

I_p Peak current

I_p^a Anodic Peak Current

I_p^c Cathodic Peak Current

ΔE_p Peak Separation

$E_{1/2}$ Half peak potential

ε Dielectric constant of the monolayer

ε_0 Permittivity of free space or vacuum

D Diffusion coefficient

Z Total impedance

Z' Real part of impedance

Z'' Imaginary part of impedance

Z_f' Real part of faradaic impedance

$Z_f^{''}$ Imaginary part of faradaic impedance

Z_f Faradaic Impedance

R_a Average roughness

PPA 3-Phosphonopropionic acid

ABPA 4-Aminobenzylphosphonic acid

BPA Benzylphosphonic acid

BuPA Butylphosphonic acid

DecPA Decylphosphonic acid

HDPA Hexadecylphoshphonic acid

ODPA Octadecylphosphonic acid

HDTMS Hexadecyltrimethoxysilane

ODTMS Octadecyltrimethoxysilane

PTA Palmitic acid

STA Stearic acid

APTMS 3-Aminopropyltrimethoxysilane

DPPC 1,2-Dipalmitoyl-*sn*-glycero-3-phosphocholine

TPP^+ Tetraphenylphosphonium iodide

$TPhB^-$ Tetraphenylborate

$[Fe(CN)6]^{3-|4-}$ Potassium ferrocyanide/ferricyanide complex

$[Ru(NH3)6]^{2+|3+}$ Hexaammineruthenium(III/II) chloride

FcOH Ferrocenemethanol

Fc Ferrocene

Fcdc 1, 1'-Ferrocenedicarboxylic acid

FcAc Ferroceneacetic acid

NaF Sodium Flouride

Cyt c Cytochrome *c*

R_s Solution resistance

R_{ct} Charge transfer resistance

W Warburg impedance

Q/CPE Constant phase element

C_{dl} Double layer capacitance

η Overpotential

ω Angular frequency

λ Wavelength

SCE Saturated calomel electrode

PANI Polyaniline

Pd-PANI Palladium and polyaniline nanocomposite

Synopsis

Electrochemical studies on functionalized Indium Tin Oxide (ITO) and graphite oxide (GrO) surfaces

This thesis describes the electrochemical studies on functionalized indium tin oxide (ITO) and electrochemically intercalated graphite substrates (+/-IGS). Modification of ITO surfaces with organic thin films open up various applications in using them as electrodes since they have the potential to tune the surface characteristics. By tailoring the terminal functional groups of monolayer it is possible to explore the modified surfaces for applications in bio sensors, micro-arrays, molecular electronics, and nanostructures.

A comparative adsorption kinetics and electrochemical studies of phosphonic acid (PA), silane, and carboxylic acid (CA) modified ITO surfaces have been the focus of early chapters. The highlights of this part are the studies on adsorption and electron transfer kinetics of phosphonic acids by varying their terminal functional groups. This is to understand the interaction between the functionalized redox molecules and the modified surfaces and its influence on the adsorption and electron transfer kinetics. The PA modified surfaces have been demonstrated to adsorb proteins which in turn have been studied for their bio sensing property. In addition, the 3-aminopropyltrimethoxysilane (APTMS) was studied for several interesting properties with potential application for bio-molecular adsorption.

In the latter part of the work, the results of the studies on graphite substrates which are electrochemically intercalated by the application of DC potential are presented. By controlled intercalation these are used as integral graphite substrate electrodes. Since the layers in between graphite are held together by Van der Waals forces, they have been separated by the application of an electric field in an electrolytic medium. The intercalated graphite substrate (+/-)IGS has been used as a support for immobilization of bio-molecules and metal nanoparticles.

Chapter 1: Introduction

This chapter gives a brief introduction to the topics covered in the thesis and contains two parts. First part deals with the materials and methods used in the work. This includes a description about the self-assembled monolayers and their characterization. The second part of the chapter deals with the different experimental techniques that have been used in the thesis. Electrochemical techniques like cyclic voltammetry (CV), chronoamperometry (CA), chronopotentiometry (CE) and electrochemical impedance spectroscopy (EIS) have been used for the characterization of different systems. This section also deals with other experimental techniques like Raman spectroscopy, X-ray diffraction (XRD), scanning tunneling microscopy (STM), atomic force microscopy (AFM), and scanning electron microscopy (SEM).

Chapter 2: Adsorption kinetics of phosphonic acids and proteins on functionalized Indium tin oxide (ITO) surfaces using electrochemical impedance spectroscopy

Phosphonic acids (PAs) bind strongly to the ITO and their resistance towards homocondensation polymerization makes them preferable for supports in bio-sensing applications. In this chapter, the adsorption kinetics of phosphonic acids onto ITO using electrochemical impedance spectroscopy are presented. It is shown that the rate of adsorption of PAs occurs in two different steps. EIS has an advantage over other electrochemical techniques since it uses very small amplitude voltage signals without significantly perturbing the electrochemical interface thereby providing reliable measurement of interfacial parameters such as charge transfer resistance (R_{ct}) and double layer capacitance (C_{dl}). Such a small AC voltage perturbation causes measurable variations in the impedance of the interface in a way that is related to the properties of the liquid or solid under investigation. The adsorption kinetics was measured at an identified frequency for various phosphonic acid molecules by following the changes in imaginary component of the impedance with adsorption time (t) by keeping the frequency constant.

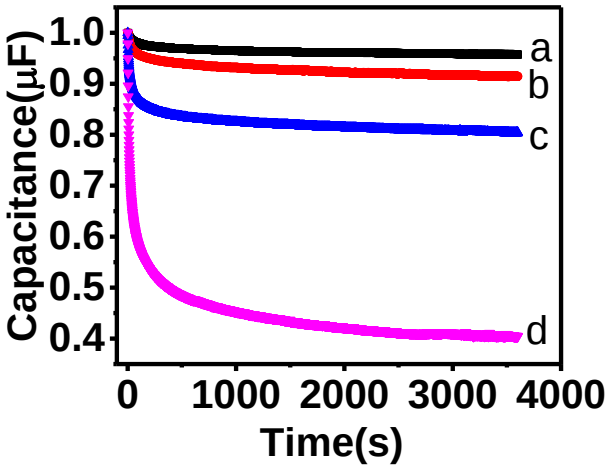

Figure 1. *Normalized capacitance vs. time curves for ITO in 10mM PPA using 0.1M NaF as supporting electrolyte at ocp vs. SCE, (a). 1mM PPA, (b). 5mM PPA, (c). 10mM PPA, (d). 20mM PPA.*

For our studies on PA adsorption, on ITO surface, we have used small chain length PAs such as PPA, BuPA, BPA, and ABPA along with a long chain decylphosphonic acid (DecPA). We have also studied the adsorption of a heme protein c*yt c* and an enzyme, urease on the PA modified surfaces. The adsorption of these bio molecules on PA modified surface was confirmed using atomic force microscopy (AFM) and the retention of their activity studied using chronoamperometry (CA) and electrochemical impedance spectroscopy (EIS) measurements.

Chapter 3: Adsorption kinetics and electron transfer reactions on self-assembled monolayers (SAMs) of long chain alkylphosphonic acids, silanes, and carboxylic acids on Indium Tin Oxide (ITO) surface

This chapter deals with the electron transfer barrier properties of self-assembled monolayers (SAMs) of long chain alkyl phosphonic acids (PAs), alkyl silanes, and carboxylic acids (CAs) on ITO in ethanol, water (only PA), toluene, hexane, and neat solvent (except in the case of PA). It is concluded that long chain PA monolayers can form more impermeable films on ITO than silanes and carboxylic acids. A study of the adsorption kinetics of PAs,

silanes, and CAs in ethanol show that the adsorption follows two distinct kinetic steps for the formation of complete monolayer. Adsorption rate depends on the chain length of monolayer also.

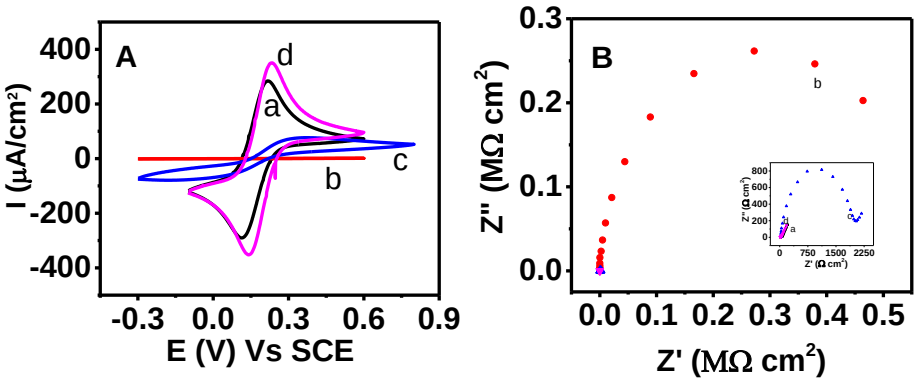

Figure 2. *(A) Cyclic voltammograms and (B) Electrochemical impedance spectroscopy plots of 1mM $[Fe(CN)_6]^{3-/4-}$ in 0.1M NaF supporting electrolyte towards (a) bare ITO, (b) ODPA/ITO, (c) ODTMS/ITO and (d) STA/ITO respectively.*

Chapter 4: Electron transfer studies of ferrocene derivatives on short chain phosphonic acid (PA) modified Indium Tin Oxide (ITO) surfaces

This chapter reports the electrochemical studies of different ferrocene derivatives for the purpose of understanding the effect of substituents on the rate of electron transfer process on the hydroxylated ITO and phosphonate monolayers formed by benzyl phosphonic acid (BPA), 3-phosphonopropionic acid (PPA), butylphosphonic acid (BuPA), and 4-aminobenzylphosphonic acid (ABPA). The behaviors of phosphonate monolayers show that the monolayer functionality influences the electron transfer behavior.

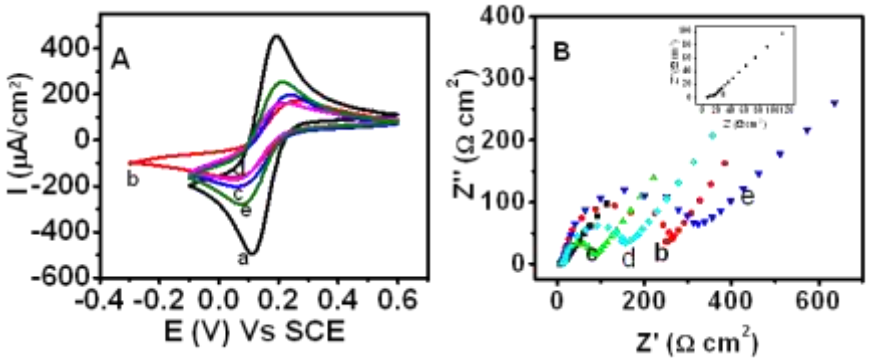

Figure 3. *(A) Cyclic voltammetry and (B) Electrochemical impedance spectroscopy plots of 1mM* $[Fe(CN)_6]^{3-/4-}$ *in 0.1M NaF supporting electrolyte towards (a) bare ITO, (b) Benzylphosphonic acid (BPA), (c) 3-Phosphonopropionic acid (PPA), (d) Butylphosphonic acid (BuPA) and (e) 4-Aminobenzylphosphonic acid (ABPA).*

It is shown here that the blocking behavior of modified ITO electrodes depend upon the terminal groups, nature of the redox moiety, and solvent under study. For ionic redox species, electrostatic interaction stabilizes the redox species within the film which leads to a positive shift in formal potentials of redox moieties. However, in the case of hydrophobic redox species it is observed that the formal potential shifts towards negative side of the potential axis.

The electrochemical behavior of these modified electrodes has been characterized using CV and EIS. Phosphonic and carboxylic acids form better monolayers in ethanol solvent, whereas silanes form compact monolayers in chloroform solvent. The difference in adsorption and electrochemical behavior is explained by the stability of the monolayer binding to the substrate. The distribution of pinholes and defects in the monolayer are characterized using electrochemical impedance spectroscopy.

Chapter 5: Electrochemical and morphological characterization 3-aminopropyltrimethoxysilane (APTMS) on indium tin oxide (ITO) surfaces

In this chapter, the studies on 3-aminopropyltrimethoxysilane (APTMS) modified ITO surface have been presented. Unlike phosphonic acids and carboxylic acids which bind to the

oxide surfaces by losing a proton from the adsorbate, whereas silanes adsorb onto oxide surface by losing its hydroxyl group by reacting with hydrogen of metal hydroxide. The terminal amino group of APTMS has good anchoring ability to bind bio macromolecules. This property was used to anchor biomolecules like lipids, lipophilic compounds, and proteins etc. The morphologies of these substrates were studied through atomic force microscopy (AFM) and scanning electron microscopy (SEM) which show vesicle like features on the surface. The electrochemical studies show that redox active molecules like $[Fe(CN)_6]^{3-/4-}$, $[Ru(NH_3)_6]^{3+/2+}$, and ferrocene methanol (FcOH) adsorb onto the silane films and undergo electron transfer process by diffusing through the film. Due to the presence of amino groups at the terminal, electrochemical behavior of the APTMS/ITO electrode is highly pH dependent.

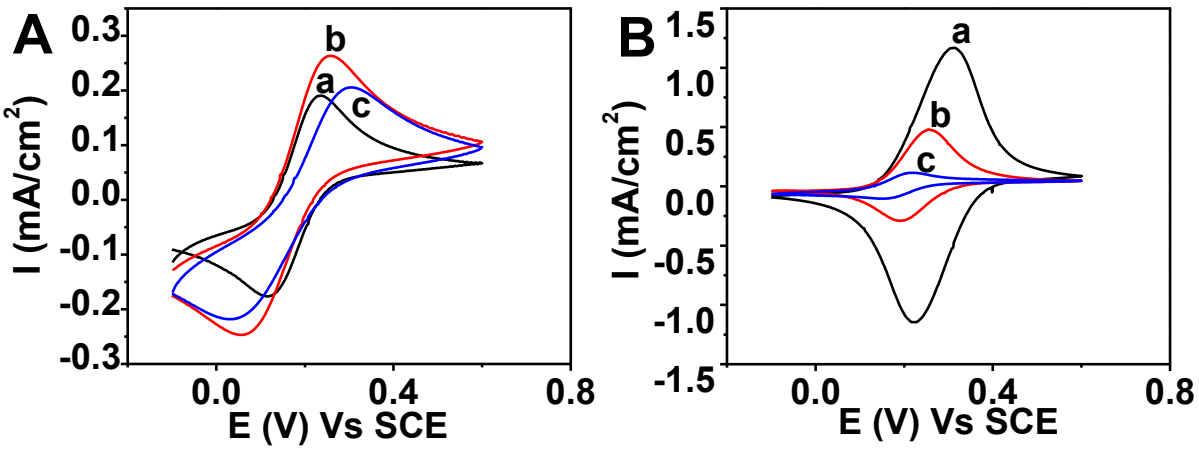

Figure 4. *Cyclic voltammograms of 1mM potassium $[Fe(CN)_6]^{3-/4-}$ redox couple using 0.2M phosphate buffer solution at (A) bare ITO, (B) APTMS/ITO substrate in (a) acidic, (b) neutral, and (c) basic pH conditions.*

Chapter 6: Electrochemically exfoliated graphite substrates for immobilization of metal nanostructures

In this chapter, the studies on electrochemically intercalated graphite oxide surface are presented. A large increase of electroactive surface area takes place due to the intercalation of ions between the layers of graphite. This provides an ideal surface for electrodeposition

of metal nanoparticles. The electrodepositied nanoparticles onto intercalated exfoliated graphite substrates used as an electrocatalyst for ethanol and methanol oxidation studies. The electrocatalytic activity of these substrates were evaluated by cyclic voltammetry, Tafel analysis, and Arrhenius plots.

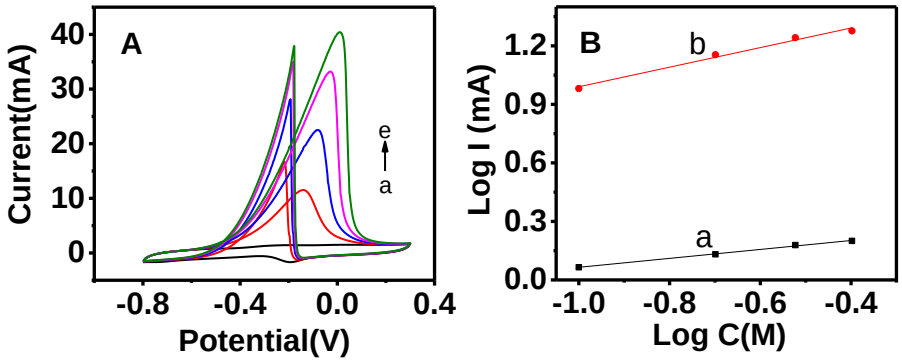

Figure 5*. (A) Cyclic voltammograms and (B) reaction order calculation plots obtained for ethanol oxidation reaction on Pd/GS electrode.*

Chapter 7: Summary and future scope of the work

This chapter summarizes the results and conclusions and future of the work.

List of Publications

[1] R.V. Jagadeesh, V. Lakshminarayanan, Adsorption kinetics of phosphonic acids and proteins on functionalized Indium Tin Oxide surfaces using electrochemical impedance spectroscopy, Electrochim. Acta. 197 (2016) 1–9. doi:10.1016/j.electacta.2016.03.008.

[2]. R.V. Jagadeesh, V. Lakshminarayan, Self-assembled monolayers (SAMs) of long chain alkylphosphonic acids, silanes, and carboxylic acids on Indium Tin Oxide (ITO)-A study of electron transfer reaction using cyclic voltammetry and electrochemical impedance spectroscopy, manuscript under preparation.

[3]. R.V. Jagadeesh, V. Lakshminarayan, Electron transfer studies of ferrocene derivatives on short chain phosphonic acid (PA) modified Indium Tin Oxide (ITO) surfaces, manuscript under preparation.

Conferences /Workshops Attended

1. Conference on "Soft Matter Chemistry (SMC 2011)" SCM group, Raman Research Institute Bangalore, 9-11 November, 2011.

2. Science Academics Lecture Workshop on "Current Trends in Nanoscience and Technology", Department of Chemistry, National Institute of Technology Warangal, 23-24 December, 2011.

3. National conference on "Interface between Chemical Sciences and Technologies", Department of Chemistry, National Institute of Technology Warangal, 29–30 December, 2011.

4. Workshop on "NOVOCONTROL DIELECTRIC/IMPEDANCE ANALYZER WORKSHOP" (NDAC 2014), SCM Group RRI Bengaluru.

5. Presented a Poster titled "Studies on Silane Modified Thin Films" in "International conference on Electrochemical Science and Technology (ICONEST-2014), IISc Bengaluru, 7-9 August, 2014.

6. Presented a Poster titled "Studies on Silane Modified Thin Films" in Frontiers in Chemical Sciences and Technology (FCST 2016), Department of Chemistry National Institute of Technology Warangal, 2016.

7. Presented a Poster titled "Enhanced Electrocatalytic Activity of Pd dispered on Graphite and Intercalated Graphite Systems towards Ethanol Oxidation Reaction" in International Conference on Nanoscience and Technologies (ICONSAT 2016), IISER Pune, 29-31 March, 2016.

8. Presented a poster titled "Enhanced Electrocatalytic Activity of Pd Dispered on Graphite and Intercalated Graphite Systems towards Ethanol Oxidation Reaction" in 67th Annual Meeting of ISE, The Hague, Netherlands, International Society of Electrochemistry (ISE), 21-26 August, 2016.

9. Attended a "Short Course on Spectroscopic Ellipsometry", SCM Group, Raman 1Research Institute, Bengaluru, 24 -25 January, 2018.0

10. Workshop on "Shape Anisotropic Materials and their Applications in Display Devices", BMS College of Engineering, Bengaluru, 19 February-2 March, 2018.

Chapter 1

Introduction

The recent progress in materials chemistry has provided several new and powerful opportunities for applications in surface electrochemistry ranging from micro to nano-electronics, energy harvesting and energy conversion devices, sensors, biosensors, *etc.* [1–6]. While traditionally, the focus had been on the metal and alloy surfaces, the advent of molecular self–assembly has provided a means of modifying the surfaces and developing applications, taking advantage of some unique functional properties of the modifiers [7–9]. For example, one of the most extensively studied phenomena in electrochemistry for the past three decades is the self-assembled monolayers (SAM) of organic thiols on noble metal surfaces, especially on gold [9–13]. The voluminous studies of the SAMs on gold has enriched electrochemistry, especially in our understanding of the kinetics of the formation of molecular self-assembly on surfaces, electron transfer properties across SAM which eventually lead to the development of biosensors including DNA array biosensor, biological self-assembly, surface wetting, corrosion, passivation, *etc.* [9,14–18]. While such studies provided the wealth of information and have opened up several potential applications, the cost of using noble metal like gold as a substrate is a hindrance for wider applications. The advantage of gold is that, apart from being inert in almost all solvents and electrolytes, it is easy to clean and does not oxidize under ambient conditions, thereby ensuring excellent surface reproducibility. There have been several attempts to explore alternative and less expensive electrode materials such as silver, copper, and nickel, whose surface can be modified or functionalized to suit any specific requirement [9]. However, these surfaces are very much prone to surface oxidation in ambient atmosphere and therefore it is difficult to modify the surfaces and use them for further studies except under strictly controlled conditions.

In this work, two major oxide materials, namely, indium tin oxide (ITO) and graphite oxide (GO) explored as electrode materials for surface modification with organic self-assembly and functionalization. The advantage of the ITO as an electrode material is that it is an optically transparent conducting oxide (TCO) that is relatively inert, inexpensive, and can be surface functionalized with hydroxyl groups on which organic thin films can be formed. The graphite

oxide is another electrode surface, which is conductive, inexpensive, and the surface functionalization can be achieved relatively easily for further modification.

The first part of the thesis deals with the modification of hydroxyl-functionalized ITO surface with organosilanes, organophosphonates, and carboxylates by solution processing method. The major focus of the study on ITO electrodes is the adsorption kinetics of formation of the organic self-assembled film and subsequent electron transfer behavior of the modified surface towards some chosen redox species. The purpose of such a study is to explore the possibility of utilizing the transparent conducting oxide in electrochemical applications especially relating to sensors and biosensors.

The latter part of the thesis deals with electrochemical exfoliation of flexible graphite sheets (GS) to form functionalized graphite oxide and developing them as an electrode support for electrodeposition of Pd nanoparticles and Pd-PANI nanocomposites. The Pd modified surface explored for potential applications as an electrocatalyst for the electro-oxidation of small organic molecules such as methanol and ethanol. This surface makes the current study relevant for direct alcohol alkaline fuel cells (DAAFCs) with some potential advantages over the more extensively studied acid based direct alcohol fuel cells (DAFCs). Cyclic voltammetry, Tafel analysis, and Arrhenius plots were employed to analyze the electrocatalytic behavior of the electrocatalysts. Surface characterization of the catalytic material was done by using x-ray diffraction (XRD), scanning electron microscopy (SEM), Raman spectroscopy, and energy dispersive x-ray spectroscopy (EDAX).

1.1. Self-Assembled Monolayers (SAM):

Self-assembled monolayers (SAMs) are extremely thin organic films of single molecular thickness spontaneously formed on an appropriate solid substrate, by immersion into dilute solutions of organic molecules. A study on SAMs enhances the fundamental understanding of the mechanism of self-organization, structure-property relationships, and interfacial phenomena. The possibility of functionalizing with appropriate head or tail groups of the adsorbing molecules provides a route for attaching bio-molecules and metal nanostructures on the surface. There are several molecules which form self-assembly over solids, *e.g.* thiols (-SH) on gold, silver, and copper, organosilicons ($-SiX_3$), organophosphonates ($-PO_3H_2$), and carboxylic acids (-COOH) on hydroxylated surfaces

(Al, Au, ITO, SiO_2 *etc.*), alcohols, and amines on platinum [10]. A schematic representation of self-assembled monolayer is shown in figure 1.

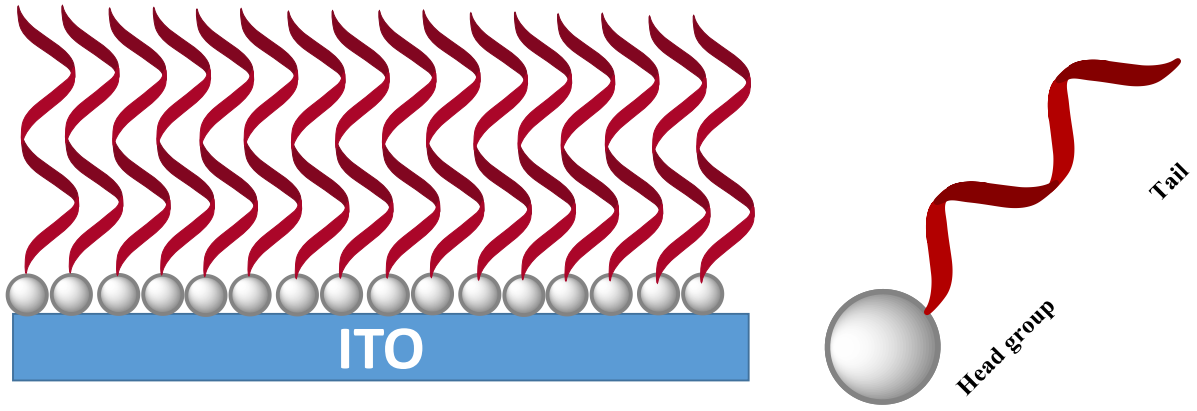

Figure 1. *Schematic diagram of self-assembled monolayer (SAM).*

1.1.1. Organosilicon self-assembly on ITO:

Organosilicon compounds ($-SiX_3$, -X = -Cl, -OR) are organometallic compounds containing covalently bonded carbon–silicon atoms. Formation of organosilicon self-assembly requires surface hydroxyl groups for anchoring. The driving force for this self-assembly is the *in situ* formation of highly reactive silanol (-SiOH) groups, by the reaction between water and the functional groups of silane (equation 1).

$$2RSiX_3 + 6H_2O \longrightarrow 2RSi(OH)_3 + 6HX \quad (1)$$

where X- -Cl, $-OCH_3$, $-OC_2H_5$ *etc.*

Water for the above process derived from the ambient atmosphere, the solvent, and the hydroxylated substrate.

These reactive silanols undergo two reactions:

(1). Homocondensation with silanol groups of nearest molecules and form polysiloxane (Si-O-Si) network.

$$RSi(OH)_3 + RSi(OH)_3 \longrightarrow R(OH)_2Si\text{-}O\text{-}Si(OH)_2R \quad (2)$$

(2). Covalent binding with the hydrogen atom of surface hydroxyls leading to the hetero-condensation reaction.

$$MOH + RSi(OH)_3 \longrightarrow MO\text{-}Si(OH)_2R \quad (3)$$

The above two reactions occur simultaneously in the solution. There is a competition between polysiloxane formation and the reaction of silanols with the surface hydroxyl groups. Since silane oligomers have better tendency to bind hydroxyl surfaces, it is enriched with the polymeric silanes after adsorption. Silanes, however, form disorganized films over the substrate leaving pinholes and voids within the polymer chain. Substrates on which these films have been successfully prepared include silicon oxide [19–24], aluminum oxide [25,26], quartz [22–24], glass [27], mica [28–31], zinc selenide [25,27], germanium oxide [27], and gold [32,33]. Goss *et al.* employed mercaptotrimethoxysilane (MPTMS) as a molecular adhesive to fabricate vapor deposited gold electrodes on glass and mica substrates making the silane an excellent replacement as an underlayer for the deposition of noble metals on insulating materials like glass, mica, and various metal oxides [34]. Markovich *et al.* studied the electrochemical behavior of octadecyltrimethoxysilane (ODTMS) on ITO towards $[Fe(CN)_6]^{3-/4-}$ redox couple and suggested that silanes form disorganized monolayers unlike thiols [35]. These disorganized films contain micron-sized pores through which amphiphilic species like redox active proteins, cyclams, redox species, *etc.* can be immobilized [35–38]. Muthurasu *et al.* studied the electron transfer behavior of various silanes by varying the terminal groups of the adsorbate [39]. Schematic illustration of silane formation on oxide surfaces is shown in figure 2.

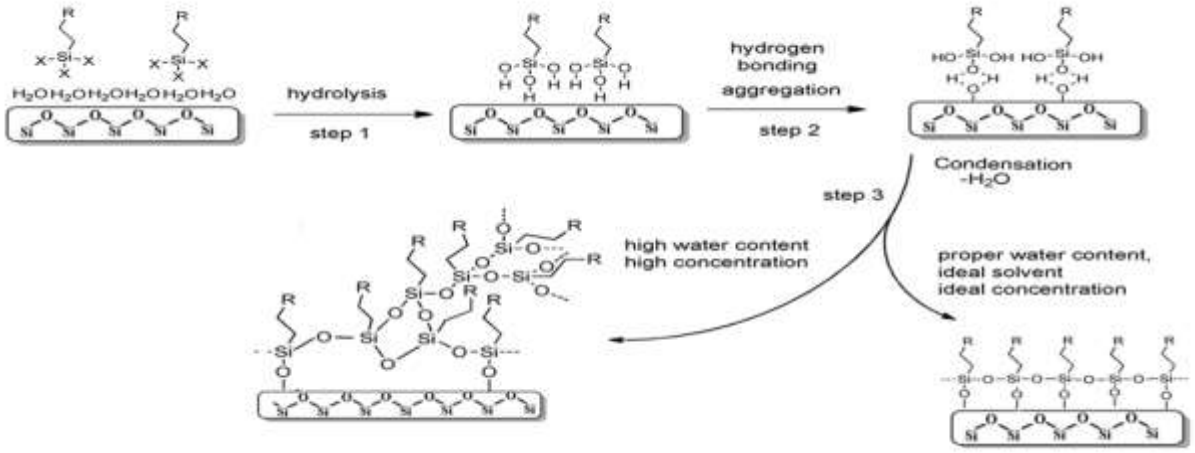

Figure 2. *Schematic illustration of the mechanism of siloxane bond formation with the surface hydroxyl groups and within the solution.*

1.1.2. Phosphonic acid self-assembly on ITO:

Phosphonic acids or organophosphonates (-PO_3H_2) show high affinity to bind hydroxyl terminated solid substrates. Unlike silanes, phosphonic acids do not undergo homo-condensation reactions to form a polymer thereby making it possible to avoid stringent environmental conditions for adsorption [40]. Phosphonic acids form stronger bonds than carboxylic acids and silanes on an extensive range of metal oxides, developing well-packed SAMs with excellent thermal stability [41]. Ramsier *et al.* adsorbed and studied the vibrational spectra of several phosphorous acids adsorbed on alumina and suggested that these acids adsorb through hetero-condensation reaction [42]. Phosphonic acids form a symmetrical tridentate bonding with the substrate using all three oxygen atoms. The strong P-O-M bond enables the fabrication of electronic structures, modifying the work function, and organic field effect transistor (FET) devices [43–45]. Phosphonates bind to oxide substrates with weak hydrogen bonds between (6)-PO_3H_2 head group and the surface hydroxyl group of oxide substrates. An annealing step is required at the end of the adsorption process to get better adhesion for phosphonate molecules to the substrate [46]. To enhance the binding of phosphonates to glass or silica substrates, an ultrathin layer of metal oxide is deposited to overcome the weak physical interactions between the phosphonic acid precursor and SiO_x [47]. Giza *et al.* observed that octadecylphosphonic acid (ODPA) undergoes adsorption at an enhanced rate after application of water plasma prior to modification. Thus they suggested that adsorption behavior of phosphonates depend on the number of surface hydroxyl groups on the surface [48]. Felhosi *et al.* studied the corrosion resistance properties of alkyl diphosphonates on oxides of iron [49].

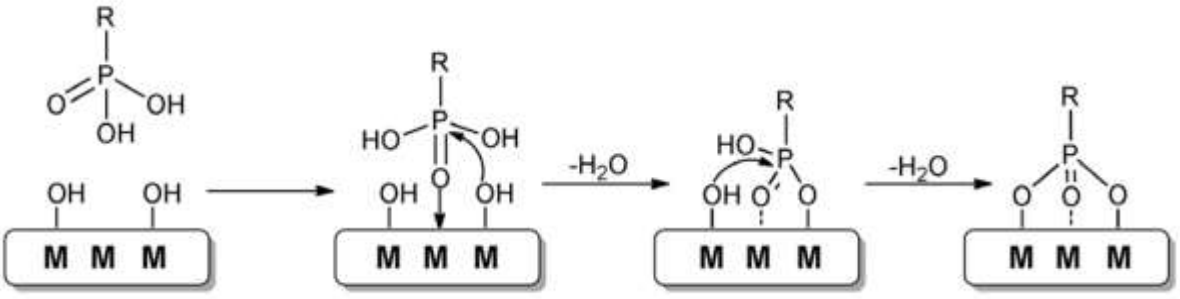

Figure 3. *Mechanism of phosphonate binding to the metal oxides after hydroxyl functionalization.*

1.1.3. Self-assembly of carboxylic acid on ITO:

Carboxylic acid-based monolayers on ITO have been investigated systematically, [10,50–54] with a focus on long chain aliphatic carboxylic acids, as they were expected to form close-packed, highly organized monolayer films [51,52,55]. Carboxylic acid monolayers usually prepared by three methods (1) Langmuir–Blodgett (LB) technique, (2) attachment from a dilute solution, and (3) vapor phase growth [56,57]. Solution based monolayer preparation is a preferred technique since it produces better quality monolayers. Since carboxylic acids chemisorb onto the metal surface, the metal-carboxylic acid moiety in such layers has been labeled as an "inner-sphere adsorption complex" [58]. Adsorption mechanism of alkanoic acids involves dissociation of proton of the carboxylic acid head group to form carboxylate [51]. The binding characteristics of the carboxylate to metal oxides had been analyzed using IR spectroscopy [59]. Compared to phosphonic acids, carboxylic acids form weak bonding to the substrate surface at room temperatures. This behavior is due to the reversible hydrolysis of carboxylates with the chemisorbed water on substrates [60,61]. Heating the modified substrate at higher temperatures above 100ºC results in the formation of stable monolayers, since annealing process releases water from the substrate surface. Allara and Nuzzo have studied the formation, dynamics, and physical properties of long-chain *n*-alkanoic acids adsorbed from solution on an oxidized aluminum surface using IR spectroscopy [52]. They suggested that carboxylic acids form stable monolayers over aluminum oxide surfaces and found that the order of the monolayers increases with the increase in its chain length.

The multi-dentate binding behavior of alkanoic acids had been used for attaching to CNTs and fullerene [62] which finds applications in dye-sensitized solar cells [63], high-temperature superconductors [64], and industrial scale surface coatings typically as lubricants, corrosion-resistant materials, and as linkers to catalysts [65–72].

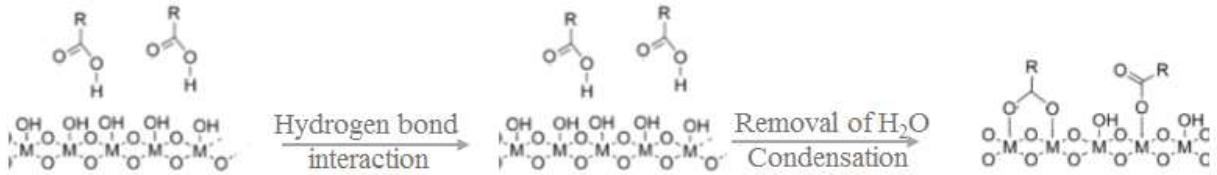

Figure 4. *Mechanism of the carboxylic acid binding to metal oxide surfaces.*

1.2. Flexible graphite sheet (GS):

Graphite is an allotropic form of carbon which possesses electrical conducting behavior and is its most stable form at room temperature. It is made up of sp^2 hybridized carbon atoms arranged in a honeycomb lattice with a C-C bond distance of 0.142nm forming two-dimensional graphene layers connected by weak Van der Waals forces in the perpendicular direction and separated by a distance of 0.335nm. Graphite shows anisotropic properties due to the presence of strong covalent bonds within the graphene layers and weak Van der Waals forces in between graphene layers. The weak Van der Waals bonds between graphite layers make graphite vulnerable for soft chemical reactions to take place without disrupting the covalent bonds thus expanding the gap between graphene layers during the reaction to accommodate the reagent. These soft reactions are called intercalation reactions, and they are reversible in most cases. In these reactions, carbon acts as an amphoteric element, where graphite can provide or accept electrons [73]. Due to the intercalation process, graphite layers increase their interlayer separation and expand. The expanded graphite acts as an efficient substrate due to the increased surface area. These expanded graphite substrates can be used as conductive fillers, high-temperature gaskets, seals, lubricant supports, and packing [74]. Intercalation improves the thermal stability and electrical conductivity [75]. Intercalation of graphite can be carried out by top-down approaches like mechanical, solution processing, chemical, and electrochemical methods as well as bottom-up approaches like chemical synthesis, epitaxial growth, and chemical vapor deposition [76].

1.2.1. Electrochemical exfoliation of graphite:

Electrochemical intercalation of ions and compounds within graphite is carried out by the application of potential for certain interval or by scanning the potential of the graphite electrode within a potential range [77–79]. The intercalation experiments can be carried out in both aqueous and organic solvents. By the application of a positive potential, intercalation of negatively charged ions into the graphite layers can occur and *vice versa*. Alanyalioglu *et al.* electrochemically synthesized graphene flakes with an average size of 500nm and a thickness of 1nm successfully [80]. Application of high positive potentials yield oxidized graphene (graphene oxide), which is rich in oxygen functional groups and structural defects, while the negative potential reduces some of the oxygen functional groups, but this process, however, cannot reconstruct a pristine graphene structure [81]. This method has several advantages over other methods, indeed more environmentally friendly and can be employed under room temperature conditions, while

exfoliation can be carried out precisely by controlling the applied potential or current and is fast and efficient. However, it is hard to produce graphene sheets and a layer with a homogeneous distribution. The functional groups created on graphite due to the intercalation are at the expense of sp^2-hybridized carbon network. The method is irreversible since it is not possible to regenerate the sp^2-hybridized carbon network to the state of defectless graphene after the electrochemical process. Besides, the structural damage and oxygen functionality, intercalation has an enormous impact on the electrochemical properties of the resulting graphene [82,83].

Exfoliation of graphite results in a 3-dimensional structure of the highly rough surface and enhanced electrical conductivity due to the corrugations which makes it an excellent substrate to deposit a large number of metal nanostructures and immobilization of biomolecules [84]. These deposited substrates are useful in electrocatalytic studies like alcohol oxidation, oxygen reduction, and hydrogen evolution. The high surface area allows diffusion of the reactant molecules thus avoiding liquid sealing effect [85].

The exfoliation process also introduces several surface and edge functional groups such as –OH, -COOH, epoxides, *etc.* [86] which are hydrophilic and used as anchoring sites for biomolecules.

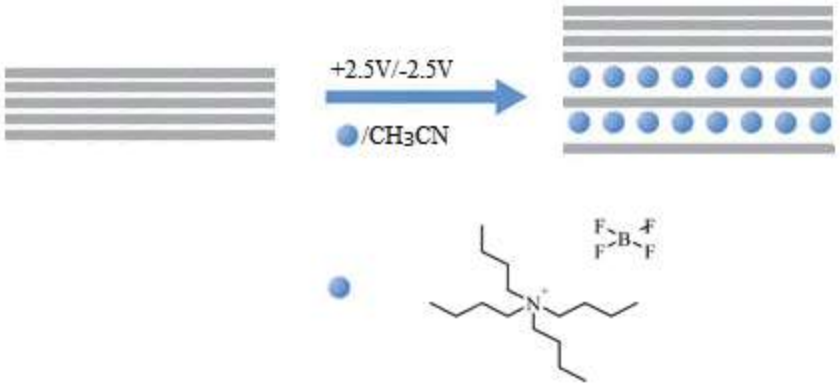

Figure 5. *Schematic representation of electrochemical intercalation of graphite substrates.*

1.2.2. Substrate for electrochemical deposition of nanomaterials:

Flexible graphite sheets are made by compression of graphite particles without using a binder. These are stable and produce high currents due to the presence of a large number of edge planes [87]. Electrochemical exfoliation of flake graphite sheets creates a vast amount of defects within the planes of graphite resulting in increasing the edge sites as well as the electrochemical surface

area. Controlled exfoliation of graphite enables us to use these substrates as electrode supports. Due to the creation of defects after intercalation process which gives rise to an in-plane disorder, the exfoliated substrate provides a large surface area for the dispersion of metal particles. The micrometer-sized highly rough domains in the exfoliated graphite substrates act as structure units to form pores and channels that significantly reduce the liquid sealing effect for electrocatalytic oxidation of alcohol [85,88]. Due to this, the fuel circulates through the pores and evolves CO_2 out of the catalyst layer easily.

1.3. Electrochemical cell and electrodes:

The experiments have been performed by the use of a conventional three-electrode electrochemical cell. The cell prepared by closing one end of the B-55 glass cone with a Teflon lid designed to fit its mouth. Teflon lid consists of three holes through which working, counter, and reference electrodes can fit. All the electrodes were made to fit with a B-14 ground joint glass for use in the arrangement of the cell. A platinum foil sealed to a glass tube used as counter electrode. The Ohmic drop of the electrolyte minimized by the addition of supporting electrolyte to the analyte solution. Gold plated brass rod used as an electrode holder, with a slot at one end to hold the working electrode, is used as an electrical contact. Teflon B-14 cone has fixed to the sample holder which is made to fit the socket of the central ground joint. Schematic illustration of the electrochemical cell is shown in figure 6.

The working electrodes used in our studies were indium tin oxide (ITO) coated glass plate and mechanically compressed flexible graphite sheet (GS). Platinum foil or platinum wire used as counter electrode. Saturated calomel electrode (SCE), Ag/Ag^+ (non-aqueous)/0.1M salt, Ag/AgCl/3MNaCl, and mercury-mercurous oxide (Hg/HgO) were used as reference electrodes, whereas silver wire used as a quasi-reference electrode for particular electrochemical studies.

Indium tin oxide (ITO) glass plate of dimensions 355mm X 406mm X 1.1mm were purchased from XINYAN technology limited, Singapore. These glass plates are fabricated into appropriate sizes for experimental purposes in our laboratory. Prior to the use, ITO strips were cleaned by ultrasonication in acetone, ethanol, and Millipore water for 15 minutes each. These strips were transferred immediately after cleaning into a solution mixture of hydrogen peroxide (H_2O_2, one part): ammonia (NH_3, three parts): water (H_2O, ten parts), for surface pre-treatment (hydroxylation). Pre-treated indium tin oxide (ITO) is used as a substrate for self-assembly of

phosphonic acids, silanes, and carboxylic acids. Modification of ITO with the amphiphiles mentioned above was carried out by immersing the pre-treated ITO substrate in respective SAM solutions. The modified substrates (except carboxylic acids case) were kept in a hot air oven at 100°C for at least an hour and allowed to cool down to room temperatures.

0.3mm thick flexible graphite sheets (GS) (Changyi Dong Feng sealing materials, China) were kindly provided by Prof. A.K. Shukla, SSCU, IISc Bangalore. This sheet is cut into a size of 4mm X 10mm and used as a working electrode for our studies. Since these sheets are very thin, they can be cut into desired sizes by the use of scissors. These fabricated strips were cleaned by ultrasonication for 15 minutes each in ethanol and Millipore water. These strips are electrochemically exfoliated by the application of constant potential for a certain interval of time. The flexible graphite sheet (GS) and exfoliated graphite sheets have been used as substrates for electrochemical deposition of Pd-PANI and its electrocatalytic activity for ethanol and methanol were studied.

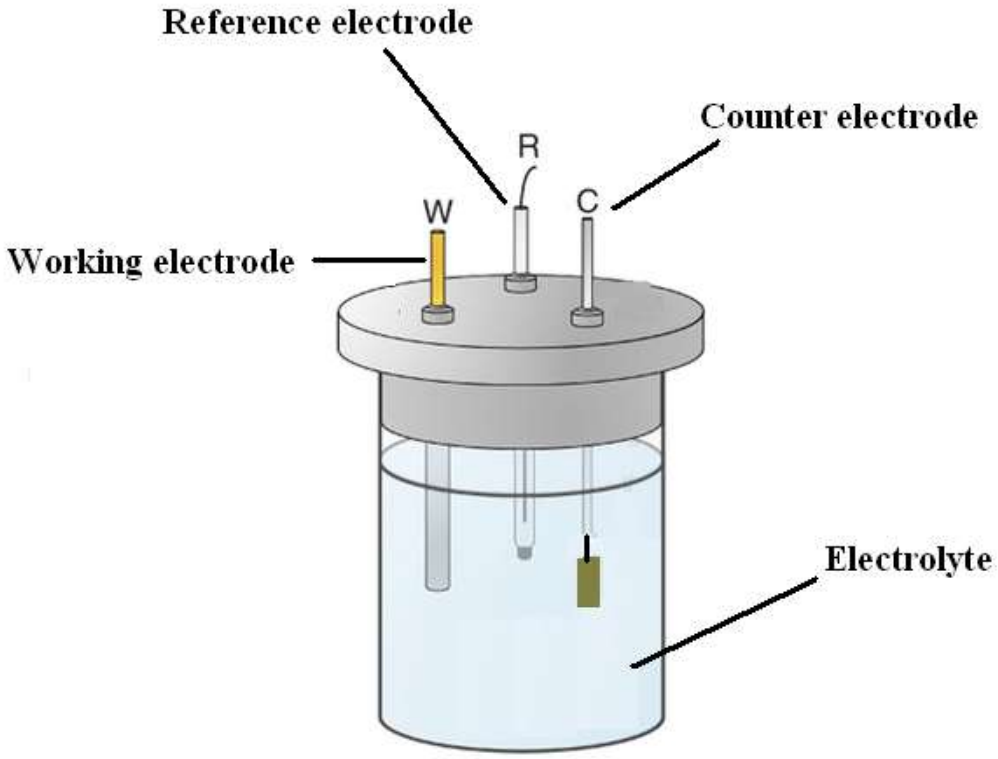

Figure 6. *Schematic diagram of a 3-electrode compartment of an electrochemical cell.*

1.4. Electrochemical studies:

Electrochemical experiments were carried out using cyclic voltammetry (CV), chronopoteniometry (CP), chronoamperometry (CA), and electrochemical impedance spectroscopy (EIS). The electron transfer blocking properties of various self-assemblies have evaluated by using the potassium ferrocyanide/potassium ferricyanide couple [$K_{3/4}(Fe(CN)_6)$], hexammineruthenium (III) chloride/hexammineruthenium (II) chloride [$Ru(NH_3)_6]Cl_{3/2}$, ferrocene methanol (FcOH), ferrocenedicarboxylic acid (Fcdc), and ferrocene acetic acid (FcAc) for aqueous solution while ferrocene (Fc) redox probe used for electrochemical studies in non-aqueous systems.

Cyclic voltammetric studies of the redox probes were performed in appropriate supporting electrolyte solutions. The EIS measurements were carried out in a solution containing equal concentrations of redox couple by the application of 10mV amplitude at the formal potential of the redox couple. All EIS measurements were carried out in the frequency range of 100kHz to 100mHz, whereas adsorption kinetics experiments were carried out at a constant frequency.

1.5. Instrumentation:

Cyclic voltammetry (CV) and chronoamperometry (CA) were carried out using an EG&G potentiostat (model 263A) interfaced to a PC through a GPIB card. Chronopoteniometry (CP) was carried out using EG&G potentiostat in the galvanostatic mode for electrochemical deposition. Electrochemical impedance spectroscopy (EIS) was carried out using EG&G (model 5210) lock-in amplifier along with EG&G potentiostat (Model 263A) interfaced with PC.

AFM and STM studies were carried out at room temperature in air. We have used a Pico plus (Agilent) AFM in the non-contact mode with a silicon tip. STM studies were carried out in constant current mode at a bias voltage of +100mV by using finely scissored platinum wire as a probe. SEM images and EDAX profiles were recorded using Ultra plus field emission scanning electron microscope (FESEM). X-ray diffraction studies (XRD) were performed by using Cu-Kα (λ=1.54Å) radiation from a Rigaku Ultrax18 rotating anode generator (5.4kW) monochromated with a graphite crystal. Raman spectra were obtained with a high-resolution triple Raman spectrometer (T64000, Horiba Jobin Yvon), using a He–Ne Laser (λ=514.0nm) with a 50X objective lens. Laser power maintained at 23mW.

1.5.1. Cyclic Voltammetry (CV):

Cyclic voltammetry is often carried out in an electroanalytical study for understanding the mechanism of electrochemical reactions. This technique gives the necessary information on the thermodynamics and diffusion behaviors of redox processes. In cyclic voltammetry, the potential of the working electrode (*wrt* a reference electrode) swept between the potential limits E_1 and E_2 as a function of time in a triangular waveform, and the current response at the working electrode is measured (figure 7). Mass transport and heterogeneous reaction kinetics of an electrochemical reaction can be determined by the varying the scan rate.

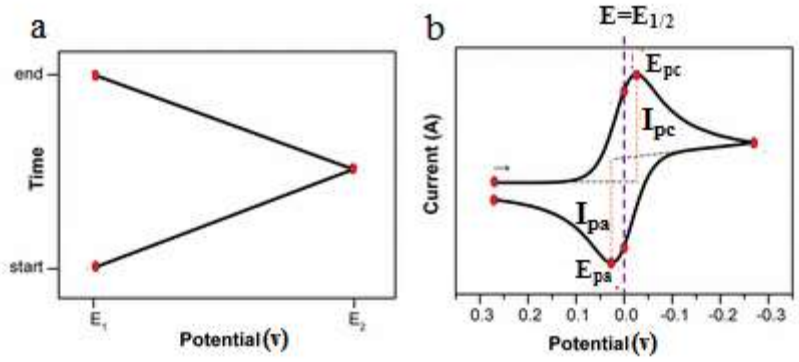

Figure 7. *(a) Potential-time waveform applied (b) current-potential profile in a cyclic voltammetric experiment.*

The currents obtained during the CV scan are due to two reasons: [89,90]

(i). Capacitive currents are owing to double layer charging of the electrode/electrolyte interface. The capacitive currents can be observed typically in a supporting electrolyte solution that contains no electroactive species.

(ii). Faradaic current arises due to the electrochemical processes like redox reactions.

For a usual reversible one-electron redox reaction of the type,

$$O + e^- \leftrightharpoons R$$

Typically, reversible electrochemical reactions follow Nernst equation and ratio of the concentration of oxidized (C_O) and reduced species (C_R) are given by:

$$E = E_0 + \left(\frac{RT}{F}\right) \ln \frac{C_R}{C_0}$$

The region adjacent to the electrode surface called as Nernst diffusion layer, where the concentration gradient of the electroactive species is linear. During the negative potential sweep,

the surface concentration of the oxidant decreases by the reduction reaction. This results in an increase in concentration gradient near the surface of the electrode due to which the currents are increased. The surface concentration of the oxidant reduces further with the continuous increase of negative potential due to which the concentration of oxidant eventually becomes zero. The concentration gradient reaches the maximum at this point, and the maximum current obtained. At the potential beyond this point, the concentration gradient starts to decrease due to the diffusion of oxidant from the convection layer of the solution, causing a decrease in concentration gradient which results in the decrease in current. The peak-shaped current response obtained in cyclic voltammograms is due to the initial increase which is followed by a decrease in the concentration gradient. The scan in reverse, *i.e.*, towards the positive side of the potential axis also gives similar I-V profile but with an opposite sign.

The length of the diffusion layer changes with the scan rate. The diffusion layer grows substantially further from the electrode at slow scan rates. Accordingly, the diffusion of analyte species to or from the electrode surface is considerably smaller at slow scan rates. Consequently, the currents are lower at slow scan rates. Large currents at high scan rates are because of the insufficient time provided for the diffusion layer to relax due to which the concentration gradient, as well as the current resulting from it, also increases [91].

The peak current in cyclic voltammetry determined by using the *Randles-Sevcik* equation,

$$i_p = (2.69\times105)\, n^{3/2} A D^{1/2} \nu^{1/2} C$$

where n-number of electrons in the redox reaction, A-area of the working electrode, D-diffusion coefficient for the analyte, ν-scan rate, and C-concentration of analyte solution. If the concentration of the analyte is known, then cyclic voltammetry can be used to calculate the diffusion coefficient of the analyte.

The cyclic voltammogram of a reversible redox reaction is described by, [89]

1. $\Delta E_p = |E_{pa} - E_{pc}| = 59/n$ mV
2. $|E_p - E_{p/2}| = 59/n$ mV
3. $|I_{pa} / I_{pc}| = 1$
4. $I_p \alpha \nu^{1/2}$
5. E_p is independent of ν

where E_{pa} and E_{pc} are the peak potentials, I_{pa} and I_{pc} are the peak currents of anodic and cathodic reactions respectively.

1.5.2. Electrochemical Impedance Spectroscopy (EIS):

Electrochemical impedance spectroscopy (EIS) is an analytical AC technique that gives accurate, kinetic, and mechanistic information on redox reactions. It is carried out by the application of a very small perturbation voltage of 10mV amplitude sine wave to the test electrode at an appropriate DC potential in a range of frequencies onto a system which is close to the steady-state equilibrium. From the input AC potential and the resulting current response of the test electrode, the corresponding impedance is calculated at any given frequency. A plot of the logarithm of measured impedance against frequency is known as Bode plot, while the plot of real part of the impedance (Z') against imaginary component (Z") at a range of frequencies is the Nyquist plot.

Figure 8 shows the current response (I) to the sinusoidal perturbation (V) on the test electrode of the electrochemical system. The data on charge transfer kinetics, electrode capacitance, and diffusion of the redox species can be obtained through the measurement of phase difference and amplitude of the current response with respect to the applied potential signal over a wide frequency range and plotting them as Bode or Nyquist plots. For this reason, EIS has found wide applications in diverse areas of research in electrochemistry like corrosion, batteries, ionic solids, chemically modified electrodes, membranes, solid electrolytes, and template deposited porous electrodes.

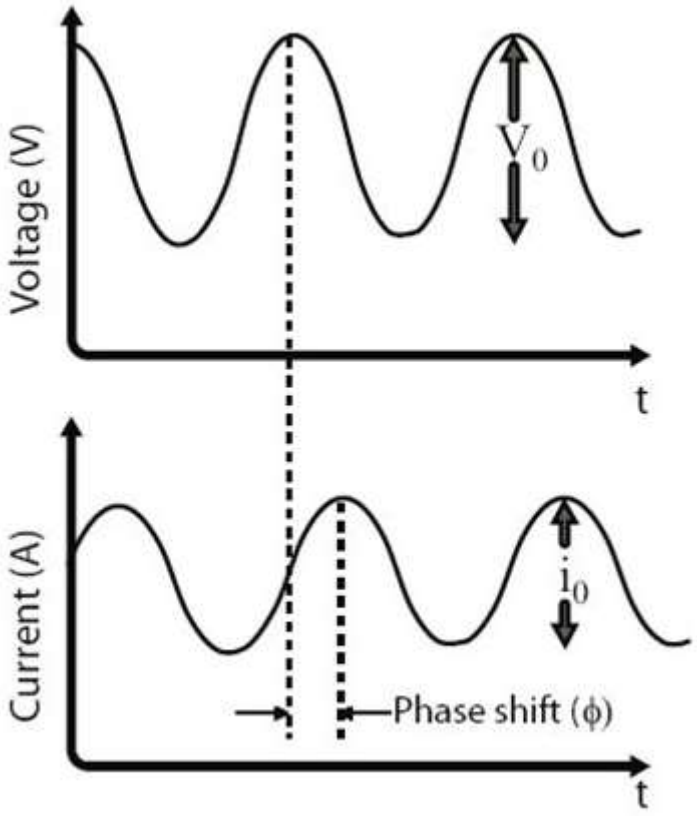

Figure 8. *Schematic representation of a small sinusoidal applied perturbation (E) and the current response (I).*

1.5.2.1. The Principle of AC circuits:

A theoretical understanding of the fundamentals of AC circuits is a pre-requisite to analyze the electrochemical response of a cell to an AC perturbation. By the application of a sinusoidal signal of voltage, $V = V_0 \sin(\omega t)$ to an electrical circuit which is made up of a combination of resistors and capacitors, the resulting current response, is given by $I = I_o \sin(\omega t + \Phi)$. Here, V_0 is the maximum amplitude, I_o is the maximum current, ω is the angular frequency, and Φ is the phase angle between the applied potential and current response. Impedance (Z) is the proportionality factor for the applied potential (V) and current response (I). According to the concept of phasors, the current and potential are considered as rotating vectors and separated by a phase angle in the polar diagram. The phase angle (Φ) is zero in the case of the resistor (R) which means that the applied potential and the response current are in-phase. The relation $I = V_0 \sin(\omega t)/R$ acquired from the Ohm's law, $V = IR$ for the simple resistor. The current (I) is given by, $I = C\,(dV/dt)$ in

case of a pure capacitor (C). Thus, substituting the value of $V = V_0$ Sin (ωt) followed by differentiating, the equation becomes,

$$I = \omega C V_0 \, Sin \, (\omega t + \Phi/2),$$

$$I = V_0 \, Sin \, (\omega t + \Phi/2)/X_C$$

where $X_C = (\omega C)^{-1}$ is known as the capacitive reactance. Thus, from the above equation, it can be seen that the current leads the potential by 90°or $\pi/2$ in case of a pure capacitor. By following the similar calculation, for a pure inductance electrical circuit, the potential leads the current by 90°or $\pi/2$.

1.5.2.2. The equivalent circuit of an electrochemical cell:

The electrochemical reactions taking place at the electrode/electrolyte interface can be modeled to an electronic circuit made up of the specific combination of resistors and capacitors. The values are ascertained by investigating these analogous circuits, regarding the interfacial phenomena occurring at the electrode-solution interface. For an electrochemical reaction,

$$O + ne^- \leftrightharpoons R$$

Figure 9 shows the electrical double layer and a simplified equivalent circuit proposed by Randles. The charge transfer at the electrode interface leads to both faradaic and non-faradaic components, the former arising due to redox processes and the latter due to purely charging of the electrode/electrolyte interface.

An electrode/electrolyte interface can be regarded as impedance which is sensitive to a small sinusoidal excitation. The impedance of the electrochemical interface is a complex function, Z (ω) that can be expressed either by Cartesian or polar coordinates,

$$Z\,(\omega) = Z'(\omega) + j\,Z''(\omega)$$

$$Z(\omega) = |Z|e^j$$

$$|Z|^2 = |Z'|^2 + |Z''|^2$$

where Z' and Z''-the real and imaginary components of the impedance.

The phase angle (Φ) can be expressed as,

$$\Phi = \arctan\,(Z'/Z''),$$

$$Z'(\omega) = |Z|\,Cos\Phi, \text{ and}$$

$$Z''(\omega) = |Z\,|\,Sin\Phi$$

Figure 9(b) shows an equivalent circuit for a diffusion controlled electron transfer reaction (Randles equivalent circuit). The electrical components of the circuit are solution resistance (R_s),

double layer capacitance (C_{dl}), charge transfer resistance (R_{ct}), and the Warburg impedance (W). The net current at the working electrode is attained by the sum of the individual contributions of the Faradaic current (I_f) and the double layer charging current (I_c). The double layer capacitance values measured at the electrode/electrolyte interface are due to the formation of charges at the interface which is analogous to an electrical capacitor and hence it is denoted by C_{dl} in the equivalent circuit. The Faradaic impedance (Z_f) has two components namely, the charge transfer resistance (R_{ct}), and the Warburg impedance (W). While the resistance offered to the electron transfer is given by the charge transfer resistance (R_{ct}), the impedance to the diffusion of the redox probe is given by the term W. The term W is small at high frequencies because the reactants do not have sufficient time to diffuse towards the interface. However, at low frequencies, the diffusing reactants have to move very far towards or away from the electrode/electrolyte interface during each cycle and hence the Warburg impedance (W) is very high at these frequencies. The solution resistance (R_s) occurs between the working electrode and the reference electrode. While depicting the equivalent circuit, the uncompensated solution resistance (R_s) is inserted as a series element since all the current has to pass through this element. For a planar diffusion, the value of R_{ct} is given by,

$$R_{ct} = RT/nFI_0$$

where I_0 is the exchange current density.

The solution resistance (R_s) expressed as,

$$R_s = x/kA$$

where x is the distance of the capillary tip from the electrode, k is the conductivity of the solution, and A is the area of the electrode.

The relative magnitude of R_{ct} and W at any frequency provides the information of the kinetic and diffusion controlled behavior of the electron transfer. If I_o is very large, $R_{ct} \rightarrow 0$ and will be too small to measure and only W will be effective. In other cases, a slow electrochemical reaction exhibits a very high value of R_{ct} that will be dominant over Warburg component (W). The total analysis of the impedance recognized as complex plane impedance analysis. Randles equivalent circuits are used for the depiction of the elements incorporated in the circuits which are in series and a parallel combination of the different elements like capacitors and resistors. There are two limiting cases.

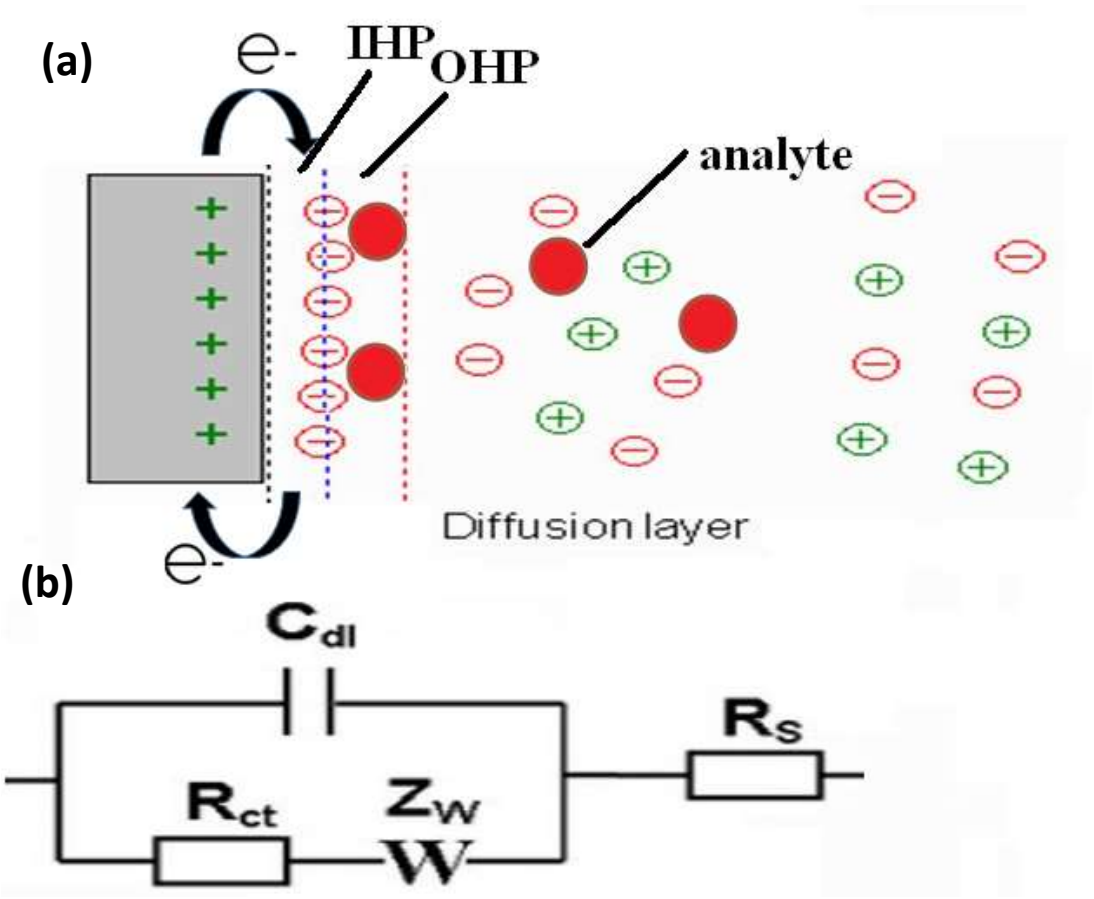

Figure 9*. (a). Electrified interface with a positively charged electrode; counter anions aligned along the electrified surface. (b). The electrical circuit elements corresponding to each interface component.*

At low frequencies, as $\omega \rightarrow 0$, the real and imaginary parts of impedance are presented by,

$$Z' = R_s + R_{ct} + \sigma\omega^{-1/2}$$

$$Z'' = \sigma\omega^{-1/2} + 2\,\sigma^2 C_{dl}$$

where $\sigma = \left(RT/\sqrt{2}n^2F^2AD^{1/2}\right)\left(\frac{1}{C_o^{\infty}} + \frac{1}{C_R^{\infty}}\right)$, D is the diffusion coefficient of the species in solution, A is the area of the electrode, C_O and C_R are the bulk concentrations of the oxidized, and reduced species. By rearranging these equations, we get,

$$Z'' = Z' - [R_s + R_{ct} - 2\,\sigma^2\,C_{dl}]$$

This above equation corresponds to a straight line of a unit slope. The intercept on the real Z' axis is given by $R_s + R_{ct} - 2\sigma^2 C_{dl}$.

At high frequencies, where the Warburg impedance (W) is negligible in comparison to R_{ct}, the two components are represented by,

$$Z' = R_s + R_{ct}/(1+\omega^2 R_{ct}^2 C_{dl}^2) \text{ and}$$

$$Z'' = C_{dl} R_{ct}^2 \omega/(1+ \omega^2 R_{ct}^2 C_{dl}^2).$$

Eliminating ω from these two equations gives,

$$(Z' - R_s - R_{ct}/2)^2 + (Z'')^2 = (R_{ct}/2)^2$$

which is the equation of a circle with center at $Z' = R_s + R_{ct}/2$ and a radius of $R_{ct}/2$.

A plot of the whole expression for Z' vs. Z", which is known as Cole-Cole plot or a Nyquist plot, for a kinetically controlled and a diffusion controlled reactions shown in figure 10. For a charge transfer controlled reaction, the plot of Z' and Z" at different frequencies (Cole-Cole plot) gives a semicircle.

At infinite frequency, the capacitance in the equivalent circuit offers a very little impedance and hence imaginary component (Z") approaches zero. Whereas at low frequencies, the impedance becomes purely resistive, because the reactance of C is very large. The real axis value at the high-frequency intercept corresponds to R_s. In the semi-circular region, at the peak position the maximum value of Z" is obtained where $\omega_p = 1/R_{ct} C_{dl}$ gives the value of C_{dl}. The diameter of the semicircle provides the value of R_{ct}. The Warburg impedance (W) term becomes significant for a diffusion-controlled reaction which varies inversely with frequency.

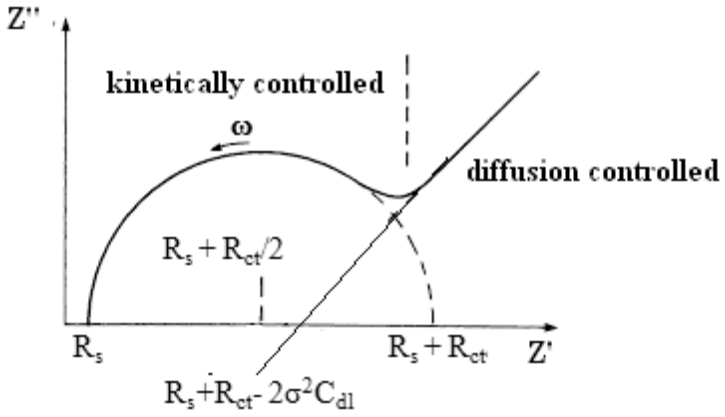

Figure 10. *Nyquist plot depicting kinetically controlled and diffusion controlled regions for an electrochemical reaction.*

The value of W is very high at very low frequencies. At these frequencies, the value of W controls the electron transfer behavior and gives a straight line with a phase angle of 45°. A plot of log |Z| vs. frequency (f) is known as Bode plot. Phase angle (Φ) component also has been used in Bode

plot which provides the information concerning magnitude and phase angle at a frequency. In EIS, the resistor and capacitor are related to a phase angles of 0° and 90°, as mentioned earlier. Thus, the Bode plots for a pure resistor and a capacitor are described by a horizontal line and straight line of unit slope respectively.

The potential of the working electrode is held at a DC potential of interest using a potentiostat. Small amplitude of sinusoidal AC voltage with 10mV peak-to-peak is applied to the cell from a lock-in amplifier. The lock-in amplifier measures the phase difference of the current output with respect to the input voltage and the amplitude of the current response, which can be converted to the real and imaginary part of the impedance.

1.5.3. Chronopotentiometry (CP):

Chronopotentiometry is a galvanostatic technique, in which the current flowing in an electrochemical cell is instantly stepped from zero to a certain finite value, *i.e.*, the overall reaction rate is fixed and the potential of the working electrode is observed continuously as a function of time. The graph obtained for variation of potential (E) as a function of time (t) is called chronopotentiogram.

For a simple one-electron electrochemical reaction, a chronopotentiogram will typically look like the plot in figure 11.

$$O + ne^- \leftrightharpoons R$$

There is a sharp decrease in potential which is observed initially as the current pulse is applied, during the charging of double layer capacitance. This sharp decrease in potential continues, as more and more O is reduced to R. Later, the potential decreases slowly as determined by the Nernst equation, until the surface concentration of O reaches nearly zero. At this point, the flux of O to the electrode surface is no longer sufficient to maintain the applied current; thus another sharp fall in the electrode potential occurs. This continues till electrode process, if any, starts.

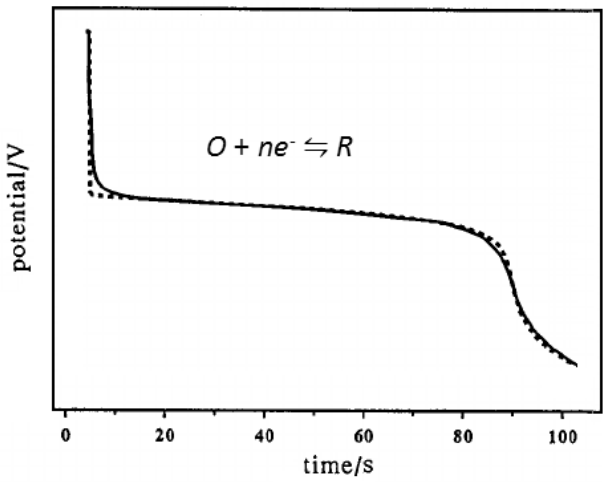

Figure 11. *Schematic diagram of a chronopotentiogram for a reversible system.*

1.5.4. Chronoamperometry (CA):

Chronoamperometry is an electrochemical technique, where the potential of the working electrode is stepped, and the current response at the electrode followed as a function of time. Figure 12 shows the typical potential-time profile applied and the current response measured as a function of time. The Cottrell equation describes the change in electric current response with respect to time for the electrochemical system under study. The sharp increase in current at initial stages is due to the double layer charging at the interface. Nevertheless, this current is substantial only during the initial period.

$$i = nFACD_O^{1/2}/\sqrt{\pi t}$$

where i = current (A),

n = number of electrons,

F = Faraday constant, 96485 C/mol,

A = area of the (planar) electrode (cm^2),

C = initial concentration of the reducible analyte (mol/cm^3),

D = diffusion coefficient for species (cm^2/s),

t = time (s).

As the faradaic reaction starts, the current response shows a decrease as a function of time due to its dependence on concentration gradient. The chronoamperometry technique can be used to measure the currents at different overpotentials applied as steps. This method was utilized to carry out Tafel analysis in this work.

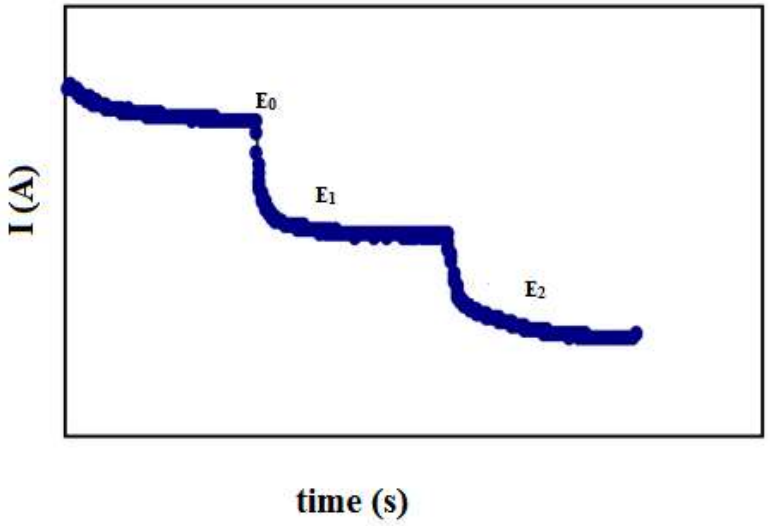

Figure 12. *Schematic representation of potential step applied during chronoamperometry.*

1.5.5. Tafel plot analysis:

Tafel plots are polarization curves, in which the logarithm of current density (I) plotted against overpotential (η) (figure 13). The difference of applied potential from the steady state or equilibrium potential of the electrochemical system under study is known as overpotential (η). The slope of the lines measured from these plots provide information of the reaction mechanism and the rate determining step involved in the process, while the intercept of the straight line at current axis gives the value of the exchange current density (I_0). Tafel plots have extensive applications in corrosion and electrocatalysis studies. In this work, Tafel analysis was carried out for the evaluation of electrocatalytic activity of the nanocomposites. In electrocatalysis, low Tafel slopes indicate better electrocatalytic behavior. The electrocatalytic activity of different materials can be compared with their respective Tafel slope values. The extent of deviation of Tafel slopes from its ideal values provides a measure of the catalytic property and the surface coverage by reaction intermediates or poisoning by any impurities [92–94].

The general form of the Tafel equations given as follows:

For a cathodic reaction,

$$\log |I| = \log I_0 - \alpha CnF\eta/2.303RT$$

while for an anodic reaction,

$$\log |I| = \log I_0 + \alpha AnF\eta/2.303RT$$

where I is the total current density, I_0 is the exchange current density, αC and αA are the respective cathodic and anodic Tafel slopes, and η is the overpotential.

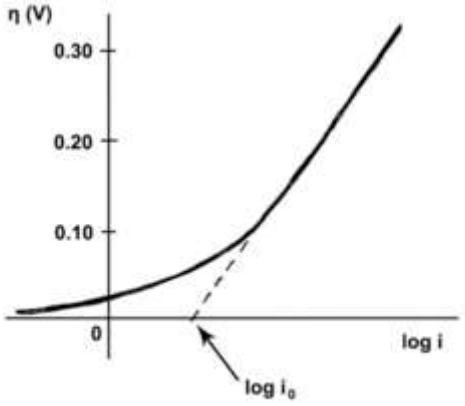

Figure 13. *Tafel plot for an anodic process.*

1.5.6. Scanning electron microscopy (SEM):

Scanning electron microscopy (SEM) is a powerful imaging tool which provides images of a sample surface at very high resolution by focusing a beam of electrons on the sample surface. The electron beam interacts with atoms in the sample surface, producing various signals which consist of the information regarding the sample's surface topography and composition. The incident beam scanned in a raster pattern over the sample and its position is combined with the identified signal to produce an image. These signals are due to the secondary electrons, backscattered electrons (BSE), photons, and heat. Secondary electrons and BSE are useful for imaging of samples. In addition to that, secondary electrons provide necessary information on the morphology and topography of samples, whereas the backscattered electrons show the contrasts of composition in multiphase samples. The detected signals provide the information regarding the sample which comprises the chemical composition and external morphology (texture) orientation of materials forming the sample. A resolution better than one nanometer can be achieved by using SEM. It can also be operated with the variation of pressure and temperature.

In this study, the morphological characterization of the electrodeposited nanoparticles was carried out by FESEM. SEM images and EDAX profile were recorded using Zeiss (Ultra plus) field emission scanning electron microscope (FESEM).
Necessary components of all SEMs comprise the following:

1. Electron source (Gun)
2. Electron lenses
3. Sample stage
4. Detectors for all signals of interest
5. Display/Data output devices
6. Infrastructure requirements:
    - Power supply
    - Vacuum system
    - Cooling system
    - Vibration-free floor
    - Room free of ambient magnetic and electric fields

The electron source at the top signifies the electron gun through which a stream of electrons produced. This electron stream is concentrated when passed through the first condenser lens which is used to form the beam and limit the amount of current in the beam by discarding a few high-angle electrons using an aperture. A coherent beam is formed with the remaining electrons by passing through the second condenser lens. When the beam collides with the sample, the interactions occur inside the sample and the secondary, as well as backscattered electrons (BSEs), are detected. Before the beam moves to the next point, the sample is raster scanned, and further processing constructs the morphological surface image. An essential requirement in SEM studies is that the sample should be conducting. X-rays of fixed wavelength emitted, as the excited electrons return to lower energy states (difference in energy levels of electrons in different shells are the characteristic of a given element).

SEM system can also be employed for energy dispersive X-ray spectroscopy (EDAX) which is an analytical technique used for the elemental analysis or chemical characterization of a sample. It depends on the probing of a sample through interactions between electromagnetic radiation and

matter, analyzing X-rays emitted by the material in response to being struck with electron beams. The characterization based on the principle that each element has a distinct atomic structure which allows X-rays that are specific to an element's atomic structure to be recognized uniquely from one another. In our studies, EDAX was used for obtaining the composition of the nanocomposites.

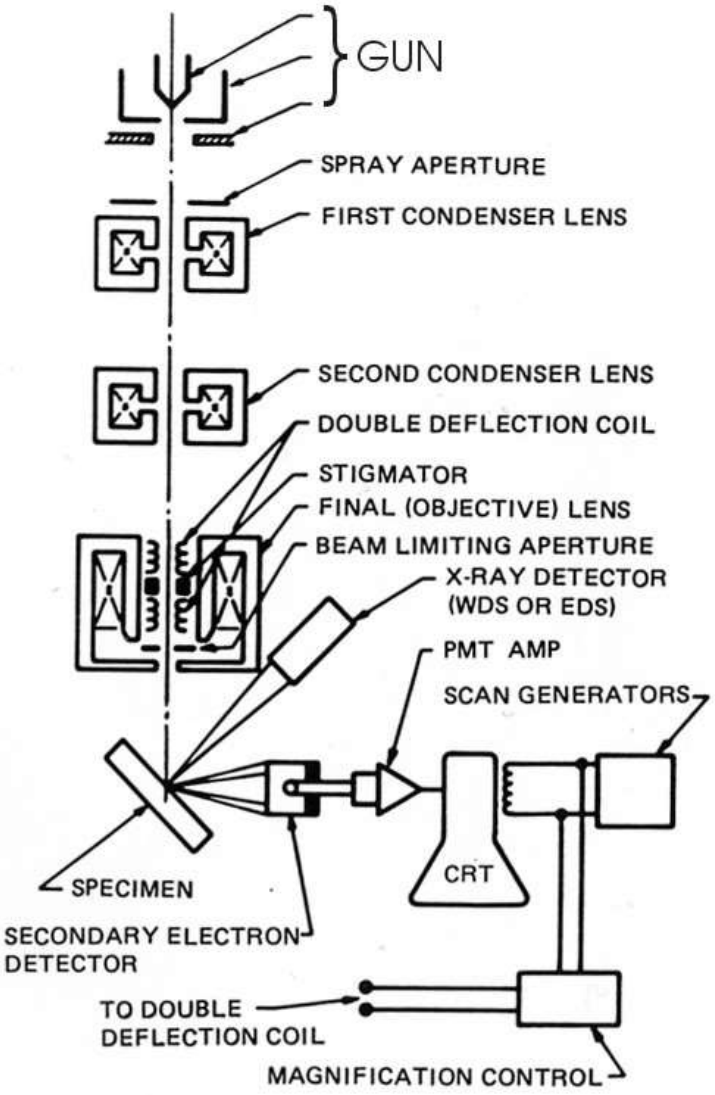

Figure 14. *Schematic representation of the scanning electron microscope:* **Credits:** *https://serc.carleton.edu/research_education/geochemsheets/techniques/SEM.html*

1.5.7. Atomic force microscopy (AFM):

Atomic force microscopy (AFM) or scanning force microscopy (SFM) is a very high-resolution scanning probe microscope (SPM) with a resolution on the order of nanometers which allows us

to analyze the structure of surface from the 3D-surface profile. The basic principle of this microscope is to make use of interatomic and molecular forces to compute the interactions between a sharp probing tip and surface of the sample under study. A schematic block diagram of AFM shown in figure 15.

In atomic force microscopy, the probing tip attached to a cantilever. Images are obtained by the lateral movement of the probing tip over the surface of the sample in a raster pattern. The cantilever deflections are digitized as a function of its lateral position by using a piezoelectric diode. There are three modes of imaging in atomic force microscopy technique.

1. Contact mode
2. Non-contact mode
3. Tapping mode or discontinuous contact mode.

The main components of an AFM are (Figure 15):

- a sharp tip mounted on a soft cantilever (AFM probe),
- a photodiode for measuring the cantilever deflections,
- a feedback loop that allows for monitoring the interaction forces between the molecules on the tip with the ones on the cell surface,
- a piezoelectric scanner that moves the tip relative to the sample in a 3D pattern,
- a conversion system from raw data acquired by the instrument into an image or other useful.

1.5.7.1. Contact mode:

Contact mode AFM works in a repulsive mode, in which tip makes a soft "physical contact" with the surface of the sample. Cantilever with low spring constant is attached with probe tip at the end. The deflection of the cantilever used as an input to a feedback circuit which moves the scanner up and down in z-direction, responding to the topography by keeping the cantilever deflection display constant. The total force applied to the sample in this mode is constant, since the cantilever deflection is held constant. During the scan across the sample, the contact force causes the cantilever to bend for adjusting the changes in topography. The topographic data obtained can be categorized into one of the two modes, *constant-height* or *constant-force* mode and used for generating the images of the sample.

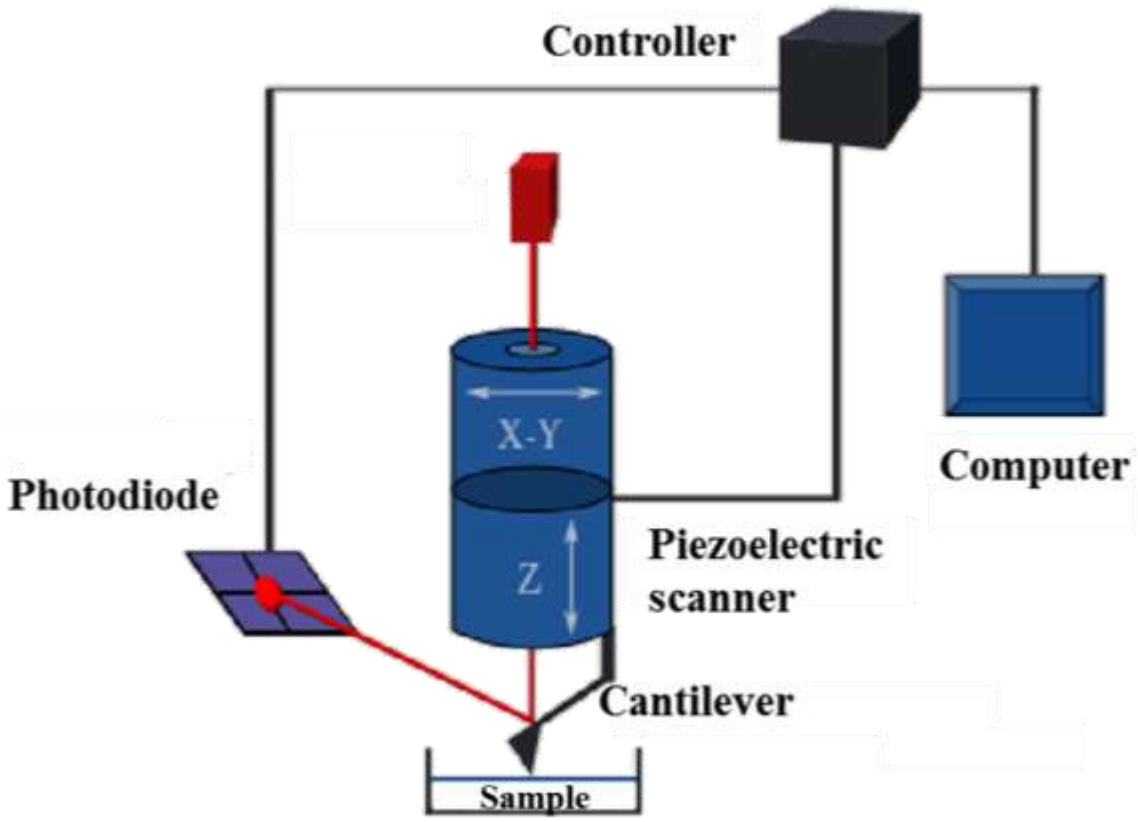

Figure 15*. Block diagram of atomic force microscope (AFM).*

(**Credits:** *https://medicine.tamhsc.edu/afm/principles.php*).

1.5.7.2. Non-contact mode:

Unlike contact mode AFM, the tip of the cantilever will not have any contact with the surface of the sample. In the case of non-contact AFM mode, the tip and sample surface are separated from each other within an order of ten to hundreds of angstroms. The cantilever is in oscillating motion at its resonant frequency during the scan. The cantilever is kept close to the sample in between 1 to 10nm range, where the sample and cantilever interact through the Van der Waals forces. Due to this interaction, there will be a decrease in the resonance frequency of the cantilever. The distance of the tip-sample is adjusted by feedback loop system thus retaining the resonant frequency of the tip. The topographic image of the sample surface is constructed by measuring the tip-sample distance at each dwell point. Since there is no contact of the tip with the sample surface, non-

contact mode AFM is a preferable technique over contact mode AFM for measuring soft samples, *e.g.*, organic thin films and biological samples.

Non-contact mode AFM is divided into two categories:

1. Frequency modulation, where a phase-locked loop keeps track of the cantilever's resonance frequency, to keep the cantilever amplitude constant.
2. Amplitude modulation, in which the oscillation amplitude or phase provide the feedback signal for imaging.

1.5.7.3. Tapping mode:

Samples absorb moisture from surroundings, which might develop liquid meniscus over the sample surface and lead to unavoidable errors during the contact mode. This problem can overcome by the use of dynamic contact mode in which cantilever is driven to oscillate up and down near its resonance frequency. The oscillation of the cantilever is controlled by a small piezo element in the system. The cantilever's frequency and amplitude are kept constant during the entire scan. As the tip gets close to the sample, there exists a small interaction like Van der Waals forces, dipole-dipole interactions, electrostatic forces, *etc.* between tip and surface of the sample. The amplitude of the cantilever changes due to these tip-sample interactions. Therefore, the images obtained in *tapping mode AFM* are generated due to the force of the discontinuous contacts of the tip with the sample surface.

1.5.8. Scanning tunneling microscopy (STM):

Scanning tunneling microscopy (STM) is a powerful tool for investigation of very small areas of surface with an extremely high level of precision. It has been extensively applied to analyze the monolayer coated surfaces, *e.g.*, thiol-coated gold substrates.

In a typical STM experiment, an atomically sharp metallic tip is brought very close to 10Å to the surface. If a small potential difference (~100mV) applied between the surface and the tip, a tunneling current will flow. This process of tunneling occurs due to the fact that the wavefunctions extend over the surface and there is an overlap between atoms on the tip and atoms on the surface. In an STM experiment, the tip is scanned over the surface even while the tunneling current monitored. Since this current decreases by one order of magnitude per ~1Å change of the electrical gap width, an accuracy of the order of 0.1Å can be achieved. There are two ways to carry out an

STM experiment, the first being the constant current and second the constant height approach. In the first method, the tip height above the sample adjusted by maintaining the current constant and the image obtained as a map of the tip height (z), versus the lateral coordinates x and y. In the latter approach, the height is kept constant, and the current (I) recorded as a function of the lateral coordinates.

While imaging the SAM-coated metals using STM, damage to the monolayer and the substrate can be prevented if prolonged scanning at high current densities avoided. For STM, the observed images are the function of surface topography and electron density, while for AFM the images combine topography with the forces between the AFM tip and the substrate. Both methods can generate images with atomic resolution on a SAM-coated substrate. Scanning probe techniques have been used to determine pinhole defect density, monolayer morphology, and monolayer structure on the substrate.

1.5.9. Contact Angle:

One of the essential properties of a monolayer is the wetting behavior. The wetting contact angle is measured by placing a small drop of a probe liquid on a horizontal substrate and measuring the angle subtended by the edge of the drop and the substrate. Both the advancing angle (drop volume increasing) and the receding angle (drop volume decreasing) are of interest since the hysteresis in the contact angle is indicative of the degree of order in the monolayer. Schematic diagram for the contact angle measurement shown in figure 16. For homogeneous monolayers, close packing and the high degree of orientation generate a surface in which effectively only the terminal group of the tail is exposed outside. These types of surfaces exhibit strong characteristic wetting properties. The highest values are observed for water in contact with alkyl monolayers of -CF_3 terminal group [95–97]. These high wetting contact angles show that the monolayer chains are well oriented so that only the terminal group exposed to the contacting liquid. Monolayers possessing very polar terminal group like -COOH show zero contact angle which indicates complete wetting.

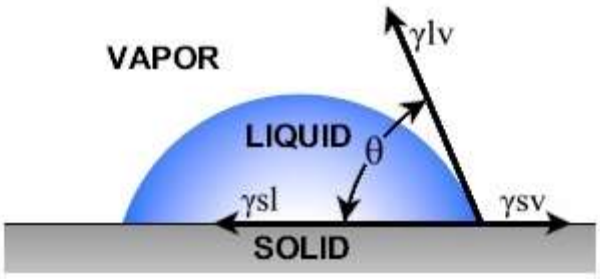

Figure 16. *Schematic diagram of contact angle measurement.*

1.5.10. Raman Spectroscopy:

Raman spectroscopy works on the principle of inelastic scattering of monochromatic light by the molecules of the sample. The wavelength of the scattered light is shifted with respect to the incident wavelength. This shift provides information regarding the molecular structure. Raman spectroscopy is highly sensitive to carbon-carbon bonds and as such is a method of choice for characterizing carbon nanomaterials like carbon nanotubes, graphene, graphene oxide, fullerenes, *etc.* Raman spectroscopy is employed in this work to characterize the electrochemically exfoliated graphite oxide material.

1.5.11. X-ray diffraction:

X-ray diffraction is a technique employed for analyzing the atomic and molecular structure of a solid in the form of a crystal or powder, in which the atoms of the sample trigger the incident X-rays to diffract into many specific directions. Crystalline samples produce sharp diffraction patterns due to their regular arrangement, whereas the nanometer-sized materials which do not have regular shape produce broad diffraction patterns. The crystallite size is determined from the FWHM of the broadened peaks.

The wavelength of an incident X-ray is related to the lattice spacing and the diffraction angle by Bragg's law,

$$n\lambda = 2d\ Sin\theta$$

where λ - wavelength of the incident X-ray,

d- distance between two crystal planes and

θ - Scattering angle.

The schematic representation of this law shown in figure 17. In our studies, XRD mainly used for the characterization of the metal nanoparticles phase composition, crystallite size, and crystallographic orientation of the metal nanoparticles. The Scherrer equation relates the size of crystallites in a solid to the broadening of a peak in a diffraction pattern.

The Scherrer equation can be written as:

$$D = k\lambda/\beta\ Cos\theta$$

D is the crystallite size, λ is the wavelength of the radiation, θ is the Bragg's angle, and β is the full width at half maximum (FWHM) of the broadened peak.

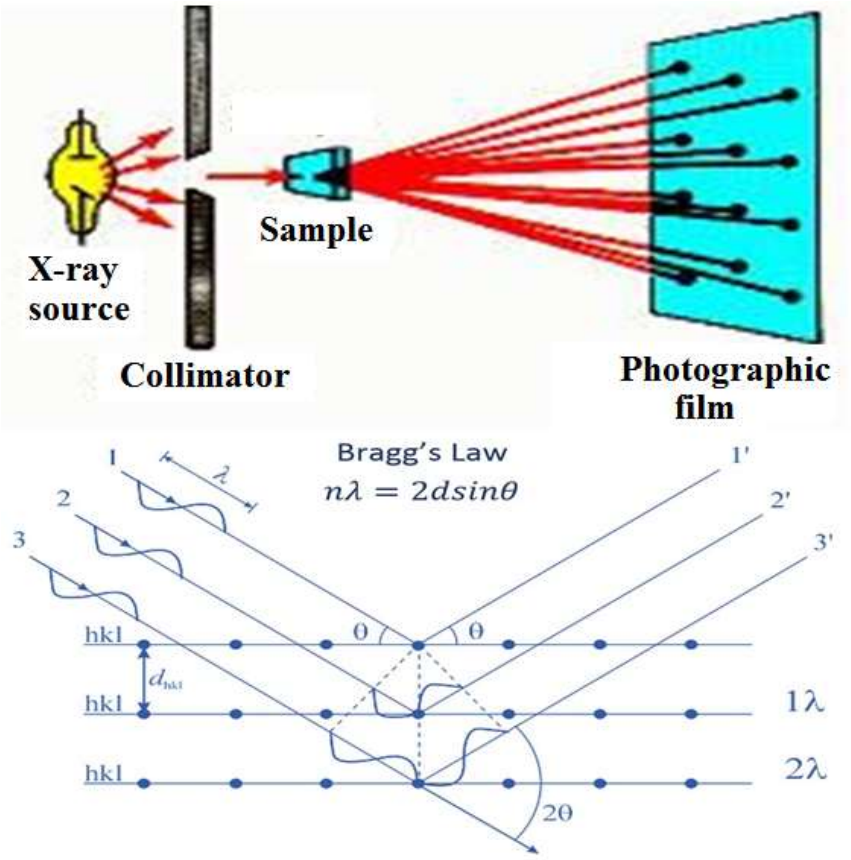

Figure 17. *Schematic representation of the scattering of X-ray leading to the Bragg's reflection.*

1.5.12. Electrochemical evaluation of self-assembled monolayers:

Cyclic voltammetry (CV) and electrochemical impedance spectroscopy (EIS) are the most widely used electroanalytical techniques for assessing the permeability of the monolayer [98]. Electron transfer at the interface can be influenced by the introduction of a monolayer between electrode and electrolyte solution since the active surface of the electrode is inaccessible to the redox species. Formation of monolayer increases the thickness of the electrochemical double layer and introduces a dielectric material at the interface which eventually leads to lowering of capacitance.

SAM acts as a barrier to the electron transfer of any redox species by blocking their access directly to the electrode surface. However, the electron transfer can still occur through the gaps present in the monolayer (pinholes) or by tunneling through the monolayer. Due to the surface modification, the electron transfer reactions occur at higher overpotentials with a reduced reaction rate. It is well known that interfacial capacitance of the gold electrode surface decreases due to the formation of alkanethiol monolayer [99]. Porter *et al.* studied the electron transfer behavior of alkanethiol modified gold with varying the chain length of the adsorbate and suggested that alkanethiols form better monolayers with increasing chain length [100]. Subramaniam *et al.* measured the adsorption kinetics and thickness of the monolayer by using electrochemical impedance spectroscopy (EIS) [101].

Cyclic voltammetry can be used to measure the capacitance of the electrode in the absence of redox active species. The interfacial capacitance of the SAM-modified electrolyte is a combination of double layer capacitance (C_{dl}) and capacitance of the monolayer film (C_f) in series. At higher electrolyte concentrations (0.1M), the interfacial capacitance is dominated by the monolayer capacitance, as the capacitance of the Gouy-Chapman layer is very high. The expression for monolayer capacitance (C_f) based on Helmholtz model which is given by [102],

$$C_f = \varepsilon_f \varepsilon_0 A/d$$

where d-thickness of the double layer, ε_f-static dielectric constant of the monolayer, A-area of the electrode, and ε_0-the permittivity of free space ($8.854 \times 10^{-12}\ F/m$).

Pinholes and defects are the patches in the SAM due to the absence of monolayer. The density of pinholes can be obtained by using cyclic voltammetry (CV) and electrochemical impedance spectroscopy (EIS) [98]. These are the areas where the redox species can directly access the

electrode surface. The blocking of electron transfer at these sites is not significant when compared to the blocking behavior of areas where the monolayer is defect free. The deviation of perfect blocking behavior by the modified electrode is an indicator for the presence of pinholes and defects in the monolayer. The pinholes in the monolayer can be analyzed using CV by following some faradaic reactions such as metal oxidation, underpotential deposition of metals or using redox species undergoing electron transfer process. The true surface area of the gold electrode can be measured by the gold oxide stripping current in acidic and alkaline medium [98,103]. The charge measured under the oxide-stripping peak is proportional to the amount of gold oxide formed during the anodic sweep. The decrease in the magnitude of the gold oxide stripping peak current gives the estimation of pinholes in the monolayer [33,104]. Peak area ratio of a bare gold electrode and SAM-modified gold electrode provides the information of the surface not covered by the monolayer on the electrode surface area (1-θ) value. A good monolayer yields the (1-θ) value between 0.001 and 0.0001 [98]. The density of pinholes increases when the SAM-coated electrode is subjected to repeated CV scan in the oxide forming regions.

The formation of close-packed hydrocarbon chains inhibits the electron transfer reaction of the redox species at the interface. Several aspects such as heterogeneous electron transfer rate constant, the size, the solubility of redox species, and mechanism of electron transfer (inner sphere and outer sphere) have significant effect on the electron transfer behavior over SAM modified surface. Inhibition of metal deposition over the electrode surface is another effect of monolayer formation. The metal deposition far from thermodynamic potentials is known as underpotential deposition (UPD) and can be used for measuring the pinhole area. The area of the stripping peak under the UPD is a measure of the pinholes on the monolayer which is an indicator for the integrity of the film.

1.6. Major objectives of the thesis:

The first objective of the thesis is to explore the optically transparent and electrically conducting surface of hydroxyl-functionalized indium tin oxide (ITO) on the glass as a viable and less expensive alternative to noble metals like gold and silver for the surface modification to form organic thin films of organosilanes, phosphonates, and carboxylates. The adsorption kinetics of the formation of monolayers and their role in inhibiting the electron transfer kinetics of some redox species were studied in this work. The surface functionalization of silanes with redox active

proteins like cytochrome *c* and lipid-like DPPC have also been investigated. It is expected that these studies can be carried forward for the development of electrochemical and enzyme-based bio-sensors.

The second objective is to exploit high surface area possessed by exfoliated graphite oxide to deposit noble metal catalyst Pd nanoparticle and Pd-PANI nanocomposite. This modified graphite oxide is used as an integral electrode material for studying the electrocatalysis of methanol and ethanol oxidation reactions in an alkaline medium which can find applications in low-temperature alkaline alcohol fuel cells.

1.7. References:

[1] S.B. Hill, C.A. Haich, F.B. Dunning, G.K. Walters, J.J. McClelland, R.J. Celotta, H.G. Craighead, J. Han, D.M. Tanenbaum, Patterning of octadecylsiloxane self-assembled monolayers on Si(100) using Ar(P-3(0 ;2)) atoms, J. Vac. Sci. Technol. B Microelectron. Process. Phenom. 17 (1999) 1087–1089. doi:10.1116/1.590699.

[2] Y. Xia, X.M. Zhao, G.M. Whitesides, Pattern transfer: Self-assembled monolayers as ultrathin resists, Microelectron. Eng. 32 (1996) 255–268. doi:10.1016/0167-9317(95)00174-3.

[3] S.A. DiBenedetto, A. Facchetti, M.A. Ratner, T.J. Marks, Molecular self-assembled monolayers and multilayers for organic and unconventional inorganic thin-film transistor applications, Adv. Mater. 21 (2009) 1407–1433. doi:10.1002/adma.200803267.

[4] A.S. Aricò, P. Bruce, B. Scrosati, J.-M. Tarascon, W. van Schalkwijk, Nanostructured materials for advanced energy conversion and storage devices, Nat. Mater. 4 (2005) 366–377. doi:10.1038/nmat1368.

[5] J. Rickert, T. Weiss, W. Goepel, Self-assembled monolayers for chemical sensors: molecular recognition by immobilized supramolecular structures, Sensors Actuators, B Chem. B31 (1996) 45–50. doi:10.1016/0925-4005(96)80015-3.

[6] T. Wink, S.J. van Zuilen, A. Bult, W.P. van Bennekom, Self-assembled Monolayers for Biosensors, Analyst. 122 (1997) 43R–50R. doi:10.1039/a606964i.

[7] K.A. Peterlinz, R. Georgiadis, In Situ Kinetics of Self-Assembly by Surface Plasmon Resonance Spectroscopy, Langmuir. 12 (1996) 4731–4740. doi:10.1021/la9508452.

[8] H. Biebuyck, C. Bain, G. Whitesides, Comparison of organic monolayers on polycrystalline gold spontaneously assembled from solutions containing dialkyl disulfides or alkanethiols, Langmuir. (1994) 1825–1831. doi:10.1021/la00018a034.

[9] J.C. Love, L.A. Estroff, J.K. Kriebel, R.G. Nuzzo, G.M. Whitesides, Self-Assembled Monolayers of Thiolates on Metals as a Form of Nanotechnology, Chem. Rev. 105 (2005) 1103–1170. doi:10.1021/cr0300789.

[10] A. Ulman, Formation and Structure of Self-Assembled Monolayers, Chem. Rev. 96 (1996) 1533–1554. doi:10.1021/cr9502357.

[11] M. Wang, K.M. Liechti, Q. Wang, J.M. White, Self-Assembled Silane Monolayers: Fabrication with Nanoscale Uniformity, Langmuir. 21 (2005) 1848–1857. doi:10.1021/la048483y.

[12] Y. Xia, G.M. Whitesides, SOFT LITHOGRAPHY, Annu. Rev. Mater. Sci. 28 (1998) 153–184. doi:10.1146/annurev.matsci.28.1.153.

[13] G.M. Whitesides, E. Ostuni, S. Takayama, X. Jiang, D.E. Ingber, Soft Lithography in Biology and Biochemistry, Annu. Rev. Biomed. Eng. 3 (2001) 335–373. doi:10.1146/annurev.bioeng.3.1.335.

[14] F. Li, W. Chen, S. Zhang, Development of DNA electrochemical biosensor based on covalent immobilization of probe DNA by direct coupling of sol-gel and self-assembly technologies, Biosens. Bioelectron. 24 (2008) 781–786. doi:10.1016/j.bios.2008.06.052.

[15] A. Sassolas, B.D. Leca-Bouvier, L.J. Blum, DNA biosensors and microarrays, Chem. Rev. 108 (2008) 109–139. doi:10.1021/cr0684467.

[16] S. Dong, J. Li, Self-assembled monolayers of thiols on gold electrodes for bioelectrochemistry and biosensors, Bioelectrochemistry Bioenerg. 42 (1997) 7–13. doi:10.1016/S0302-4598(96)05172-0.

[17] H.O. Finklea, D.A. Snider, J. Fedyk, Passivation of Pinholes in Octadecanethiol Monolayers on Gold Electrodes by Electrochemical Polymerization of Phenol, Langmuir. 6 (1990) 371–376. doi:10.1021/la00092a014.

[18] R.P. Janek, W.R. Fawcett, A. Ulman, Impedance Spectroscopy of Self-Assembled Monolayers on Au(111): Sodium Ferrocyanide Charge Transfer at Modified Electrodes, Langmuir. 14 (1998) 3011–3018. doi:10.1021/la970980+.

[19] S.R. Wasserman, Y.T. Tao, G.M. Whitesides, Structure and Reactivity of Alkylsiloxane Monolayers Formed by Reaction of Alkyltrichlorosilanes on Silicon Substrates, Langmuir. 5

(1989) 1074–1087. doi:10.1021/la00088a035.

[20] P. Silberzan, L. Leger, D. Ausserre, J.J. Benattar, Silanation of silica surfaces. A new method of constructing pure or mixed monolayers, Langmuir. 7 (1991) 1647–1651. doi:10.1021/la00056a017.

[21] J. Sagiv, Organized Monolayers by Adsorption. 1. Formation and Structure of Oleophobic Mixed Monolayers on Solid Surfaces, J. Am. Chem. Soc. 102 (1980) 92–98. doi:10.1021/ja00521a016.

[22] S. Brandriss, S. Margel, Synthesis and Characterization of Self-Assembled Hydrophobic Monolayer Coatings on Silica Colloids, Langmuir. 9 (1993) 1232–1240. doi:10.1021/la00029a014.

[23] K. Mathauer, C.W. Frank, Naphthalene Chromophore Tethered in the Constrained Environment of a Self-Assembled Monolayer, Langmuir. 9 (1993) 3002–3008. doi:10.1021/la00035a044.

[24] K. Mathauer, C.W. Frank, Binary Self-Assembled Monolayers As Prepared by Successive Adsorption of Alkyltrichlorosilanes, Langmuir. 9 (1993) 3446–3451. doi:10.1021/la00036a019.

[25] J. Gun, R. Iscovici, J. Sagiv, On the formation and structure of self-assembling monolayers. II. A comparative study of Langmuir-Blodgett and adsorbed films using ellipsometry and IR reflection-absorption spectroscopy, J. Colloid Interface Sci. 101 (1984) 201–213. doi:10.1016/0021-9797(84)90020-1.

[26] N. Tillman, A. Ulman, J.S. Schildkraut, T.L. Penner, Incorporation of Phenoxy Groups in Self-Assembled Monolayers of Trichlorosilane Derivatives: Effects on Film Thickness, Wettability, and Molecular Orientation, J. Am. Chem. Soc. 110 (1988) 6136–6144. doi:10.1021/ja00226a031.

[27] J. Gun, J. Sagiv, On the formation and structure of self-assembling monolayers. III. Time of formation, solvent retention, and release, J. Colloid Interface Sci. 112 (1986) 457–472. doi:10.1016/0021-9797(86)90114-1.

[28] G. Carson, S. Granick, Self-assembly of octadecyltrichlorosilane films on mica, J. Appl. Polym. Sci. 37 (1989) 2767–2772. doi:10.1002/app.1989.070370925.

[29] G.A. Carson, S. Granick, Self-Assembly of Octadecyltrichlorosilane Monolayers on Mica, J. Mater. Res. 5 (1990) 1745–1751. doi:10.1557/JMR.1990.1745.

[30] C.R. Kessel, S. Granick, Formation and Characterization of a Highly Ordered and Well- Anchored Alkylsilane Monolayer on Mica by Self-Assembly, Langmuir. 7 (1991) 532–538.

doi:10.1021/la00051a020.

[31] D.K. Schwartz, S. Steinberg, J. Israelachvili, J.A.N. Zasadzinski, Growth of a self-assembled monolayer by fractal aggregation, Phys. Rev. Lett. 69 (1992) 3354–3357. doi:10.1103/PhysRevLett.69.3354.

[32] H.O. Finklea, L.R. Robinson, A. Blackburn, B. Richter, D. Allara, T. Bright, Formation of an Organized Monolayer by Solution Adsorption of Octadecyltrichlorosilane on Gold: Electrochemical Properties and Structural Characterization, Langmuir. 2 (1986) 239–244. doi:10.1021/la00068a022.

[33] E. Sabatani, I. Rubinstein, R. Maoz, J. Sagiv, Organized self-assembling monolayers on electrodes. Part I. Octadecyl derivatives on gold, J. Electroanal. Chem. 219 (1987) 365–371. doi:10.1016/0022-0728(87)85054-4.

[34] C.A. Goss, D.H. Charych, M. Majda, Application of (3-Mercaptopropyl)trimethoxysilane as a Molecular Adhesive in the Fabrication of Vapor-Deposited Gold Electrodes on Glass Substrates, Anal. Chem. 63 (1991) 85–88. doi:10.1021/ac00001a018.

[35] I. Markovich, D. Mandler, Disorganised self-assembled monolayers (SAMs): the incorporation of amphiphilic molecules, Analyst. 126 (2001) 1850–1856. doi:10.1039/b107068c.

[36] I. Markovich, D. Mandler, Preparation and characterization of octadecylsilane monolayers on indium-tin oxide (ITO) surfaces, J. Electroanal. Chem. 500 (2001) 453–460. doi:10.1016/S0022-0728(00)00458-7.

[37] J. Sagiv, Organized Monolayers by Adsorption. III. Irreversible Adsorption and Memory Effects in Skeletonized Silane Monolayers, Isr. J. Chem. 18 (1979) 346–353. doi:10.1002/ijch.197900053.

[38] K. Yamamura, H. Hatakeyama, K. Naka, I. Tabushi, K. Kurihara, Guest selective molecular recognition by an octadecylsilyl monolayer covalently bound on an SnO2 electrode, J. Chem. Soc. Chem. Commun. 3 (1988) 79. doi:10.1039/c39880000079.

[39] A. Muthurasu, V. Ganesh, Electrochemical characterization of Self-assembled Monolayers (SAMs) of silanes on indium tin oxide (ITO) electrodes - Tuning electron transfer behaviour across electrode-electrolyte interface, J. Colloid Interface Sci. 374 (2012) 241–249. doi:10.1016/j.jcis.2012.02.007.

[40] S.P. Pujari, L. Scheres, A.T.M. Marcelis, H. Zuilhof, Covalent surface modification of oxide surfaces, Angew. Chemie - Int. Ed. 53 (2014) 6322–6356. doi:10.1002/anie.201306709.

[41] B.J. Brennan, M.J. Llansola Portolés, P. a Liddell, T.A. Moore, A.L. Moore, D. Gust, Comparison of silatrane, phosphonic acid, and carboxylic acid functional groups for attachment of porphyrin sensitizers to TiO2 in photoelectrochemical cells, Phys. Chem. Chem. Phys. 15 (2013) 16605. doi:10.1039/c3cp52156g.

[42] R.D. Ramsier, P.N. Henriksen, A.N. Gent, Adsorption of phosphorus acids on alumina, Surf. Sci. 203 (1988) 72–88. doi:10.1016/0039-6028(88)90195-1.

[43] T. Schulmeyer, S.A. Paniagua, P.A. Veneman, S.C. Jones, P.J. Hotchkiss, A. Mudalige, J.E. Pemberton, S.R. Marder, N.R. Armstrong, Modification of BaTiO3 thin films: adjustment of the effective surface work function, J. Mater. Chem. 17 (2007) 4563. doi:10.1039/b706949a.

[44] T.L. Breen, P.M. Fryer, R.W. Nunes, M.E. Rothwell, Patterning indium tin oxide and indium zinc oxide using microcontact printing and wet etching, Langmuir. 18 (2002) 194–197. doi:10.1021/la015543g.

[45] Y. Lu, C. Alexander, Z. Xiao, Y. Yuan, R. Zhang, J. Huang, Utilizing insulating nanoparticles as the spacer in laminated flexible polymer solar cells for improved mechanical stability, Nanotechnology. 23 (2012) 344007. doi:10.1088/0957-4484/23/34/344007.

[46] A. Vega, P. Thissen, Y.J. Chabal, Environment-controlled tethering by aggregation and growth of phosphonic acid monolayers on silicon oxide, Langmuir. 28 (2012) 8046–8051. doi:10.1021/la300709n.

[47] P. Thissen, A. Vega, T. Peixoto, Y.J. Chabal, Controlled, low-coverage metal oxide activation of silicon for organic functionalization: Unraveling the phosphonate bond, Langmuir. 28 (2012) 17494–17505. doi:10.1021/la3038457.

[48] M. Giza, P. Thissen, G. Grundmeier, Adsorption kinetics of organophosphonic acids on plasma-modified oxide-covered aluminum surfaces, Langmuir. 24 (2008) 8688–8694. doi:10.1021/la8000619.

[49] I. Felhősi, E. Kálmán, Corrosion protection of iron by α,ω-diphosphonic acid layers, Corros. Sci. 47 (2005) 695–708. doi:10.1016/j.corsci.2004.07.007.

[50] Y.T. Tao, Structural Comparison of Self-Assembled Monolayers of n-Alkanoic Acids on the Surfaces of Silver, Copper, and Aluminum, J. Am. Chem. Soc. 115 (1993) 4350–4358. doi:10.1021/ja00063a062.

[51] D.L. Allara, R.G. Nuzzo, Spontaneously Organized Molecular Assemblies. 2. Quantitative

Infrared Spectroscopic Determination of Equilibrium Structures of Solution-Adsorbed n-Alkanoic Acids on an Oxidized Aluminum Surface, Langmuir. 1 (1985) 52–66. doi:10.1021/la00061a008.

[52] D.L. Allara, R.G. Nuzzo, Spontaneously organized molecular assemblies. 1. Formation, dynamics, and physical properties of n-alkanoic acids adsorbed from solution on an oxidized aluminum surface, Langmuir. 1 (1985) 45–52. doi:10.1021/la00061a007.

[53] J.P. Folkers, C.B. Gorman, P.E. Laibinis, S. Buchholz, G.M. Whitesides, R.G. Nuzzo, Self-Assembled Monolayers of Long-Chain Hydroxamic Acids on the Native Oxide of Metals, Langmuir. 11 (1995) 813–824. doi:10.1021/la00003a024.

[54] G.A. Buckholtz, E.S. Gawalt, Effect of Alkyl Chain Length on Carboxylic Acid SAMs on Ti-6Al-4V, Materials (Basel). 5 (2012) 1206–1218. doi:10.3390/ma5071206.

[55] N.E. Schlotter, M.D. Porter, T.B. Bright, D.L. Allara, Formation and structure of a spontaneously adsorbed monolayer of arachidic on silver, Chem. Phys. Lett. 132 (1986) 93–98. doi:10.1016/0009-2614(86)80702-3.

[56] A. Raman, E.S. Gawalt, Self-Assembled Monolayers of Alkanoic Acids on the Native Oxide Surface of SS316L by Solution Deposition, Langmuir. 23 (2007) 2284–2288. doi:10.1021/la063089g.

[57] E.R. Garland, E.P. Rosen, L.I. Clarke, T. Baer, Structure of submonolayer oleic acid coverages on inorganic aerosol particles: evidence of island formation, Phys. Chem. Chem. Phys. 10 (2008) 3156. doi:10.1039/b718013f.

[58] G.E. Brown, V.E. Henrich, W.H. Casey, D.L. Clark, C. Eggleston, A. Felmy, D.W. Goodman, M. Grätzel, G. Maciel, M.I. McCarthy, K.H. Nealson, D.A. Sverjensky, M.F. Toney, J.M. Zachara, Metal Oxide Surfaces and Their Interactions with Aqueous Solutions and Microbial Organisms, Chem. Rev. 99 (1999) 77–174. doi:10.1021/cr980011z.

[59] K.D. Dobson, A.J. McQuillan, In situ infrared spectroscopic analysis of the adsorption of aromatic carboxylic acids to TiO2, ZrO2, Al2O3, and Ta2O5 from aqueous solutions, Spectrochim. Acta Part A Mol. Biomol. Spectrosc. 56 (2000) 557–565. doi:10.1016/S1386-1425(99)00154-7.

[60] I.L. Liakos, R.C. Newman, E. McAlpine, M.R. Alexander, Study of the resistance of SAMs on aluminium to acidic and basic solutions using dynamic contact angle measurement, Langmuir. 23 (2007) 995–999. doi:10.1021/la062233v.

[61] I.L. Liakos, R.C. Newman, E. McAlpine, M.R. Alexander, Comparative study of self-assembly of

a range of monofunctional aliphatic molecules on magnetron-sputtered aluminium, Surf. Interface Anal. 36 (2004) 347–354. doi:10.1002/sia.1749.

[62] E.D. Mentovich, B. Belgorodsky, I. Kalifa, S. Richter, 1-Nanometer-Sized Active-Channel Molecular Quantum-Dot Transistor, Adv. Mater. 22 (2010) 2182–2186. doi:10.1002/adma.200902431.

[63] G. Stephan, C. Näther, G. Peters, F. Tuczek, Molybdenum 17-and 18-Electron Bis-and Tris (Butadiene) Complexes: Electronic Structures, Spectroscopic Properties, and Oxidative Ligand Substitution Reactions, Inorg. Chem. 52 (2013) 5931–5942. http://pubs.acs.org/doi/abs/10.1021/ic400145f.

[64] I. Carmeli, A. Lewin, E. Flekser, I. Diamant, Q. Zhang, J. Shen, M. Gozin, S. Richter, Y. Dagan, Tuning the Critical Temperature of Cuprate Superconductor Films with Self-Assembled Organic Layers, Angew. Chemie - Int. Ed. 51 (2012) 7162–7165. doi:10.1002/anie.201201606.

[65] L.A. Martini, G.F. Moore, R.L. Milot, L.Z. Cai, S.W. Sheehan, C.A. Schmuttenmaer, G.W. Brudvig, R.H. Crabtree, Modular Assembly of High-Potential Zinc Porphyrin Photosensitizers Attached to TiO2 with a Series of Anchoring Groups, J. Phys. Chem. C. 117 (2013) 14526–14533. doi:10.1021/jp4053456.

[66] L.M. Bishop, J.C. Yeager, X. Chen, J.N. Wheeler, M.D. Torelli, M.C. Benson, S.D. Burke, J.A. Pedersen, R.J. Hamers, A Citric Acid-Derived Ligand for Modular Functionalization of Metal Oxide Surfaces via “Click” Chemistry, Langmuir. 28 (2012) 1322–1329. doi:10.1021/la204145t.

[67] S. Szillies, P. Thissen, D. Tabatabai, F. Feil, W. Fürbeth, N. Fink, G. Grundmeier, Applied Surface Science Formation and stability of organic acid monolayers on magnesium alloy AZ31 : The role of alkyl chain length and head group chemistry, Appl. Surf. Sci. 283 (2013) 339–347. doi:10.1016/j.apsusc.2013.06.113.

[68] F. Pan, Z. Cao, Q. Zhao, H. Liang, J. Zhang, Nitrogen-doped porous carbon nanosheets made from biomass as highly active electrocatalyst for oxygen reduction reaction, J. Power Sources. 272 (2014) 8–15. doi:10.1016/j.jpowsour.2014.07.180.

[69] J. Zhang, J. Zhang, Surfactant Inducing Phase Change of ZnO Nanorods to Low Friction, Tribol. Lett. 49 (2013) 77–83. doi:10.1007/s11249-012-0043-4.

[70] C. Arisio, C.A. Cassou, M. Lieberman, Loss of Siloxane Monolayers from GaN Surfaces in Water, Langmuir. 29 (2013) 5145–5149. doi:10.1021/la400849j.

[71] M.M. Islam, B. Diawara, P. Marcus, D. Costa, Synergy between iono-covalent bonds and van der Waals interactions in SAMs formation : A first-principles study of adsorption of carboxylic acids on the Zn – ZnO (0 0 0 1) surface, Catal. Today. 177 (2011) 39–49. doi:10.1016/j.cattod.2011.06.007.

[72] M.S. Lim, K. Feng, X. Chen, N. Wu, A. Raman, J. Nightingale, E.S. Gawalt, D. Korakakis, L.A. Hornak, A.T. Timperman, Adsorption and Desorption of Stearic Acid Self-Assembled Monolayers on Aluminum Oxide, Langmuir. 23 (2007) 2444–2452. doi:10.1021/la061914n.

[73] N. Emery, C. Hérold, J.-F. Marêché, P. Lagrange, Synthesis and superconducting properties of CaC 6, Sci. Technol. Adv. Mater. 9 (2008) 44102. doi:10.1088/1468-6996/9/4/044102.

[74] D.D.L. Chung, Exfoliation of graphite, J. Mater. Sci. 22 (1987) 4190–4198. doi:10.1007/BF01132008.

[75] U. Gonser, A.M.K.A. Muller, M.B.P.H. Sakaki, Graphite intercalation compounds I, Springer-Velag Berlin Heidelberg NewYork, 1990.

[76] A. Ambrosi, C.K. Chua, A. Bonanni, M. Pumera, Electrochemistry of graphene and related materials, Chem. Rev. 114 (2014) 7150–7188. doi:10.1021/cr500023c.

[77] A. Jnioui, A. Metrot, A. Storck, Electrochemical production of graphite salts using a three-dimensional electrode of graphite particles, Electrochim. Acta. 27 (1982) 1247–1252. doi:10.1016/0013-4686(82)80143-6.

[78] M. Noel, R. Santhanam, M. Francisca Flora, Effect of polypyrrole film on the stability and electrochemical activity of fluoride based graphite intercalation compounds in HF media, J. Appl. Electrochem. 24 (1994) 455–459. doi:10.1007/BF00254159.

[79] M. Inagaki, N. Iwashita, Z.D. Wang, Y. Maeda, Electrochemical synthesis of graphite intercalation compounds with nickel and hydroxides, Synth. Met. 26 (1988) 41–47. doi:10.1016/0379-6779(88)90333-5.

[80] M. Alanyalioğlu, J.J. Segura, J. Oró-Sol, N. Casañ-Pastor, The synthesis of graphene sheets with controlled thickness and order using surfactant-assisted electrochemical processes, in: Carbon N. Y., 2012: pp. 142–152. doi:10.1016/j.carbon.2011.07.064.

[81] C.Y. Su, A.Y. Lu, Y. Xu, F.R. Chen, A.N. Khlobystov, L.J. Li, High-quality thin graphene films from fast electrochemical exfoliation, ACS Nano. 5 (2011) 2332–2339. doi:10.1021/nn200025p.

[82] D.A.C. Brownson, J.P. Metters, D.K. Kampouris, C.E. Banks, Graphene electrochemistry: Surfactants inherent to graphene can dramatically effect electrochemical processes, Electroanalysis. 23 (2011) 894–899. doi:10.1002/elan.201000708.

[83] A. Bonanni, M. Pumera, Surfactants used for dispersion of graphenes exhibit strong influence on electrochemical impedance spectroscopic response, Electrochem. Commun. 16 (2012) 19–21. doi:10.1016/j.elecom.2011.12.012.

[84] C. Xu, L. Cheng, P. Shen, Y. Liu, Methanol and ethanol electrooxidation on Pt and Pd supported on carbon microspheres in alkaline media, Electrochem. Commun. 9 (2007) 997–1001. doi:10.1016/j.elecom.2006.12.003.

[85] F. Xie, Z. Tian, H. Meng, P.K. Shen, Increasing the three-phase boundary by a novel three-dimensional electrode, J. Power Sources. 141 (2005) 211–215. doi:10.1016/j.jpowsour.2004.10.002.

[86] M. Cai, D. Thorpe, D.H. Adamson, H.C. Schniepp, Methods of graphite exfoliation, J. Mater. Chem. 22 (2012) 24992. doi:10.1039/c2jm34517j.

[87] W. Yuan, Y. Zhou, Y. Li, C. Li, H. Peng, J. Zhang, Z. Liu, L. Dai, G. Shi, The edge- and basal-plane-specific electrochemistry of a single-layer graphene sheet, Sci. Rep. 3 (2013) 2248. doi:10.1038/srep02248.

[88] Y.C. Liu, X.P. Qiu, Y.Q. Huang, W.T. Zhu, Methanol electro-oxidation on mesocarbon microbead supported Pt catalysts, Carbon N. Y. 40 (2002) 2375–2380. doi:10.1016/S0008-6223(02)00115-X.

[89] D. Pletcher, R. Greff, R. Peat, L. M. Peter, J. Robinson, INSTRUMENTAL METHODS IN ELECTROCHEMISTRY, HORWOOD Publishers., 2011. https://www.sciencedirect.com/science/book/9781898563808.

[90] A.J. Bard, L.R. Faulkner, Electrochemical methods Fundamentals and Applications, second, New York, 2001. http://as.wiley.com/WileyCDA/WileyTitle/productCd-0471043729.html.

[91] N. Elgrishi, K.J. Rountree, B.D. McCarthy, E.S. Rountree, T.T. Eisenhart, J.L. Dempsey, A Practical Beginner's Guide to Cyclic Voltammetry, J. Chem. Educ. (2017) acs.jchemed.7b00361. doi:10.1021/acs.jchemed.7b00361.

[92] W. Chrzanowski, A. Wieckowski, Surface Structure Effects in Platinum/Ruthenium Methanol Oxidation Electrocatalysis, Langmuir. 14 (1998) 1967–1970. doi:10.1021/la980184j.

[93] J.O.M. Bockris, A primer on electrocatalysis, J. Serbian Chem. Soc. 70 (2005) 475–487. doi:10.2298/JSC0503475B.

[94] Z.X. Liang, T.S. Zhao, J.B. Xu, L.D. Zhu, Mechanism study of the ethanol oxidation reaction on palladium in alkaline media, Electrochim. Acta. 54 (2009) 2203–2208. doi:10.1016/j.electacta.2008.10.034.

[95] X.H. Xu, Z.Z. Zhang, W. Liu, Fabrication of superhydrophobic surfaces with perfluorooctanoic acid modified TiO2/polystyrene nanocomposites coating, Colloids Surfaces A Physicochem. Eng. Asp. 341 (2009) 21–26. doi:10.1016/j.colsurfa.2009.03.028.

[96] W. Ma, H. Wu, Y. Higaki, H. Otsuka, A. Takahara, A "non-sticky" superhydrophobic surface prepared by self-assembly of fluoroalkyl phosphonic acid on a hierarchically micro/nanostructured alumina gel film, Chem. Commun. 48 (2012) 6824. doi:10.1039/c2cc32513f.

[97] D. Ambrozewicz, F. Ciesielczyk, M. Nowacka, J. Karasiewicz, A. Piasecki, H. MacIejewski, T. Jesionowski, Fluoroalkylsilane versus alkylsilane as hydrophobic agents for silica and silicates, J. Nanomater. 2013 (2013). doi:10.1155/2013/631938.

[98] H.O. Finklea, Electrochemistry of organized monolayers of thiols and related molecules on electrodes, Electroanal. Chem. 19 (1996) 109–335.

[99] B.B. Damaskin, Adsorption of Organic Compounds At the Mercury Electrode – Solution Interface, Russ. Chem. Rev. 34 (1965) 752–759. doi:10.1070/RC1965v034n10ABEH001560.

[100] M.D. Porter, T.B. Bright, D.L. Allara, C.E.D. Chidsey, Spontaneously organized molecular assemblies. 4. Structural characterization of n-alkyl thiol monolayers on gold by optical ellipsometry, infrared spectroscopy, and electrochemistry, J. Am. Chem. Soc. 109 (1987) 3559–3568. doi:10.1021/ja00246a011.

[101] R. Subramanian, V. Lakshminarayanan, A study of kinetics of adsorption of alkanethiols on gold using electrochemical impedance spectroscopy, Electrochim. Acta. 45 (2000) 4501–4509. doi:10.1016/S0013-4686(00)00512-0.

[102] R.P. Janek, W.R. Fawcett, A. Ulman, Impedance Spectroscopy of Self-Assembled Monolayers on Au(111): Evidence for Complex Double-Layer Structure in Aqueous NaClO4 at the Potential of Zero Charge, J. Phys. Chem. B. 101 (1997) 8550–8558. doi:10.1021/jp971698e.

[103] E. Sabatani, I. Rubinstein, Organized self-assembling monolayers on electrodes. 2. Monolayer-based ultramicroelectrodes for the study of very rapid electrode kinetics, J. Phys. Chem. 91 (1987)

6663–6669. doi:10.1021/j100311a021.

[104] H.O. Finklea, S. Avery, M. Lynch, T. Furtsch, Blocking Oriented Monolayers of Alkyl Mercaptans on Gold Electrodes, Langmuir. 3 (1987) 409–413. doi:10.1021/la00075a024.

Chapter 2

Adsorption kinetics of phosphonic acids and proteins on functionalized Indium tin oxide (ITO) surfaces using electrochemical impedance spectroscopy

2.1 Introduction:

The unique property of the phosphonates to form monolayers on several metal oxides like Al_2O_3, SiO_2, Fe_2O_3, Fe_3O_4, In_2O_3, SnO_2, ITO, *etc*., opens up several possibilities usually associated with organic thiols on gold including their potential applications for developing sensors and biosensors [1]. It also provides an opportunity for surface modification with phosphonate monolayer film on optically transparent and electrically conducting substrates, which can function as a platform for adsorption and subsequent study on bio-molecules such as enzymes, proteins, and nucleic acids by spectrochemical and electrochemical techniques.

Phosphonic acids (PAs) undergo chemisorption through hetero-condensation by reacting with hydroxyl groups on metal oxide surface [2]. The chemisorption mechanism of phosphonic acids on metal oxide surface is influenced substantially by reaction conditions, such as temperature, pH, nature of the dissolving solvent, and the type of oxide substrate [2–7]. In literature, there is a lack of agreement on the deposition protocols to be employed and on the nature of the phosphonate film obtained. The process of self-assembly effected by the simple immersion of oxide substrates or using the well-known immersion procedure known as "T-BAG" method [6]. There are also reports on the development of techniques for grafting of phosphonic acids onto oxide surfaces [2,6].

Muthukumar *et al.* have studied the effect of roughness on the crystallinity and the defect density of the monolayer and concluded that the adsorption rate depends on the hydroxyl density of ITO

[8]. It was reported that the amorphous ITO provides an excellent substrate surface for well packed phosphonic acid monolayers, in contrast to the use of crystalline ITO surfaces which lead to monolayer films with several surface defects. Gardner *et al.* have studied the preferential adsorption of PAs onto ITO in the presence of carboxylic acids and thiols [9]. However, in literature, there are only a few reports on the adsorption kinetics of PAs onto ITO. For example, Paniagua *et al.* studied the adsorption kinetics of fluorine-substituted phosphonic acids using XPS by following the intensity ratio of Fluorine/Indium (F/In) at different intervals during the adsorption and also studied the tuning of the work function of ITO [7]. Jo *et al.* studied the adsorption kinetics of 3-phosphonopropionic acid (PPA), 6-phosphonohexanoic acid (PHA), and 11-phosphonoundecanoic acid (PUA) using electrochemical impedance spectroscopy (EIS). The adsorption kinetics of the carboxyl-terminated phosphonic acids were measured the by monitoring the change in charge transfer resistance (R_{ct}) value during the adsorption of PAs at different time intervals [10]. While these reports provide valuable information on adsorption process at longer time scales, information in the literature on the initial stages of adsorption kinetics at shorter time scales of the order of several seconds is however sparse. In this work, the method of measurement of double layer capacitance using the electrochemical impedance spectroscopy (EIS) technique for the study was adopted, since it has an excellent time resolution and therefore provides information on the adsorption kinetics at very short timescales. It was earlier shown by Subramanian *et al.* in case of thiol adsorption onto Au surface, that EIS as an effective method for following the kinetics of adsorption by monitoring the changes in interfacial capacitance with time which is related to the evolution of surface coverage of monolayer film [11]. It is shown here that the ITO-electrolyte interface is very well suited for such studies, since it behaves as an ideal low leakage capacitor at low-frequency ranges normally employed in EIS studies.

Also explored are the methods for the study of adsorption of proteins, which are interfacially active molecules on the phosphonate modified ITO surfaces. The study of protein adsorption on solid-support is essential for understanding the enzyme-substrate reaction leading to the development of biosensors. As the protein aggregates on the surface, the net charge of the surface adsorbed species changes at the protein-solution interface which impacts the electrical double layer close to the macromolecule. This process of structural changes in the vicinity of the double layer at the interface manifests itself in the changes of interfacial capacitance as reflected by the measured impedance.

Until recently, the protein surface interactions are being characterized using infrared spectroscopy (FT-IR), filter binding assays, circular dichroism (CD), gel-electrophoretic mobility, microscopic, NMR, UV-visible spectroscopy, and microarray techniques [12–20]. While these methods have provided valuable information on the nature of protein-surface interactions, they are however not easily adaptable for studying real-time interactions of surface immobilized macromolecules involving other ligands either in solution or at interfaces. Vladimir *et al.* [21] studied the adsorption kinetics of proteins onto carboxyl and amine terminated thiol monolayers on gold by monitoring the capacitance changes of the electrode. The presently available methods for the study of the adsorption are somewhat complicated, making use of autoradiography [14], microscopy [22], total internal reflection fluorescence spectroscopy [14], and FT-ATR [20], *etc*. Recently, Matsuda *et al.* used the measurement of absorbance of *cyt c* on the glass surface for the studies on the kinetics of adsorption using time-resolved optical waveguide spectroscopy [23]. However, it is shown that electrochemical method like electrochemical impedance spectroscopy (EIS) is simple and elegant for real-time studies and is quite amenable to the development of the stand-alone instrument for bio-sensing applications.

EIS has an advantage over other electrochemical techniques since it uses a very small amplitude voltage signals (5-10mV) without significantly perturbing the electrochemical interface thereby providing the reliable measurement of interfacial parameters such as charge transfer resistance (R_{ct}) and double layer capacitance (C_{dl}). Such a small AC voltage perturbation causes measurable variations in impedance in a way that is related to the properties of the liquid or solid under investigation.

For the study of PA adsorption on ITO surface, small chain length PAs such as PPA, BuPA, BPA, ABPA, and a long chain PA namely DecPA were employed. Also, the adsorption of a heme protein *cyt c* and an enzyme, urease on the PA modified surfaces were studied. The adsorption of these biomolecules on the PA modified surface was confirmed using scanning electron microscopy (SEM) and atomic force microscopy (AFM). The bio-molecular activity was studied using chronoamperometry (CA) and electrochemical impedance spectroscopy (EIS) measurements.

The second part of the chapter deals with the electrochemical sensing of hydrogen peroxide (H_2O_2) using hydroxylated ITO electrode. Hydrogen peroxide has a significant importance in biological systems, and therefore, an efficient and inexpensive electrochemical H_2O_2 sensor has essential

applications. In electrochemistry, H_2O_2 can either be oxidized or reduced at an electrode or modified electrode surfaces. Various materials such as Prussian Blue (PB), heme proteins, carbon nanotubes (CNTs), and transition metals have been employed in the production of hydrogen peroxide sensors [24–27]. However, these systems in electroanalytical applications limited by the slow electrode kinetics and high overpotential which might reduce the electrode performance and may suffer interferences from other electroactive species in biological samples such as ascorbate, urate, bilirubin, *etc*. On the other hand, in recent years, metal oxides have attracted significant research interest because of their desirable chemical, physical, and electronic properties that are different from those of bulk materials. Furthermore, functionalizing of the ITO surface by the hydrolysis step enhances the electrocatalytic property of the electrode making it sensitive to hydrogen peroxide detection. Herein, it is shown that ITO electrode exhibits a very good sensitivity to H_2O_2 with just a simple hydroxyl pre-treatment. The electrochemical H_2O_2 determination is carried out by using cyclic voltammetry (CV) and chronoamperometry (CA) technique.

2.2 Experimental Section:

2.2.1 Chemicals:

All chemicals used in this study were analytical grade (AR) reagents. Benzylphosphonic acid (97% purity, Aldrich), 3-phosphonopropionic acid (94% purity, Aldrich), butylphosphonic acid (Aldrich), 1-decylphosphonic acid (98% purity, Alfa Aesar), 4-aminobenzylphosphonic acid (95% purity, Aldrich), sodium fluoride (Merck), sodium phosphate monobasic (99% purity, Sigma), sodium phosphate dibasic (99% purity, Sigma), ethanol (AR. grade 99.9%, Yanguan chemical), hydrogen peroxide (30% pure, SDFCL chemicals limited), ammonia solution (25% AR SDFCL chemicals limited), *cytochrome c* extracted from horse heart (99% purity, Sigma), urease extracted from jack beans (SRL Pvt. Ltd.), were used in our study as received. Millipore water having a resistivity of 18MΩcm was used to prepare all aqueous solutions employed in this work. ITO coated glass plates purchased from Xin Yan Technology Ltd. This plate (355mm X 406mm X 1.1mm) is a single side polished, a SiO_2 passivated glass plate coated with ITO film. For electrochemical studies, this larger plate was cut into small pieces of a pre-defined geometric area and used as strips.

2.2.2 Fabrication of electrodes and electrochemical cell:

An electrochemical cell with a conventional three-electrode configuration used for the study. A platinum wire (Pt) and a saturated calomel electrode (SCE) were utilized as a counter and reference electrodes respectively. The pretreated ITO and phosphonic acid modified ITO substrates were used as working electrodes for the studies of the kinetics of adsorption of phosphonic acids and proteins respectively. Initially, ITO pieces were cleaned ultrasonically using ethanol and water for 15 minutes each. They were then removed and immersed in 10ml of an aqueous solution consisting of hydrogen peroxide, liquid ammonia, and water in the ratio of 1:3:5 for about an hour. Later, these pre-treated ITO strips were washed thoroughly with Millipore water and immediately used for the analysis. This method is known to produce well-covered hydroxyl functionalization on the surface. Fabrication of a working electrode was carried out by connecting the pre-cleaned ITO plates to the electrode holder. A distinct area of the specimen was exposed to the electrolyte with the remaining portions well insulated.

2.2.3 SAM preparation:

Monolayers prepared by keeping the pre-treated ITO substrates in 10mM aqueous solutions of BPA, PPA, BuPA, ABPA, and DecPA for 18 hours. Later, the phosphonic acid SAM-modified ITO electrodes taken out, sonicated in Millipore water three times and rinsed with Millipore water to remove any traces of loosely attached phosphonic acid molecules. Further, these ITO strips dried in an oven at 80ºC for an hour and allowed to cool to room temperature and used for electrochemical and morphological characterizations.

2.2.4 Instrumentation:

Adsorption kinetics experiments were conducted using EG&G PAR potentiostat connected to SRS Model SR830 DSP Lock-In Amplifier interfaced to a PC. The amplitude of the sinusoidal voltage kept at 10mV rms. The whole set up connected to the computer through NI-GPIB card. The program for running this experiment was written in LabVIEW 2012 software (SRS 830) and sampled at a rate of 1s per data point. All adsorption studies carried out at open circuit potential of the working electrode measured with respect to a reference electrode. The morphology of the bare ITO, phosphonic acid monolayer, and protein modified ITO substrates were recorded through FESEM (Ultra Plus, Carl Zeiss) and AFM (Agilent technologies).

2.3 Results and Discussion:

2.3.1 Adsorption kinetics studies of PAs on ITO surface:

The adsorption kinetics of PPA, BuPA, BPA, ABPA, and DecPA onto the pretreated ITO strips was followed by measuring the changes in the double layer capacitance at the selected frequency as a function of time during the adsorption process. Subramaniam *et al*. earlier reported a similar method for the measurement of adsorption kinetics of alkanethiols on a gold surface using electrochemical impedance spectroscopy [11]. The process was shown to provide interfacial capacitance changes that precisely correspond to the chain lengths of different alkanethiols adsorbed on the gold surface.

Figure 1 shows the Bode plot of phase angle (Φ) vs. log f for (a). 0.1M NaF and (b). 10mM PPA in 0.1M NaF solution respectively. From the above plot, it can be seen that the bare ITO exhibits almost ideal capacitive behavior with phase angles close to 90º at lower frequencies (10Hz-0.1Hz). Therefore, if an appropriate frequency chosen, the capacitance values can be derived directly from the imaginary component of impedance (Z"), since the electrode-solution interface behaves as an ideal capacitor at this frequency range with a capacitance given by equation (1),

$$C = 1/2\pi f Z'' \qquad (1)$$

A frequency of 10Hz was chosen to monitor the interfacial capacitance changes to study the adsorption kinetics of PAs onto hydroxylated ITO surface.

Figures 2 (a-d) shows the normalized capacitance vs. time for ITO electrode in 0.1M NaF supporting electrolyte containing 1mM, 5mM, 10mM, and 20mM PPA respectively with measurements carried out at open circuit potential. The initial capacitance values were normalized at different concentrations to unity as these values are dependent on the concentration of PPA in the solution as indicated in the parenthesis of figure 2 caption. It can be seen from the figure 2, that the capacitance decreases initially rapidly and later slowly to asymptotically reach a constant value in all the cases. This variation is due to the adsorbed molecules forming a dielectric barrier between the electrode and solution interface. As can be seen from figure 2, a little or no change in the capacitance observed beyond the duration of the experiment (3600 seconds), showing that the saturation coverage has reached. A closer observation of the plots reveals that ~70-75% of the

adsorption takes place within the first 100 to 200 seconds followed by a slower process which in any case does not extend beyond ~30-40 minutes for all the PAs studied in this work.

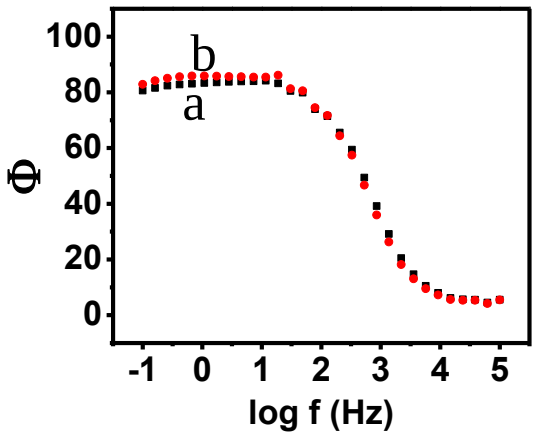

Figure 1. *Phase angle (Φ) vs. log f Bode plot for ITO in (a). 0.1M NaF and (b). 10mM .PPA + 0.1M NaF solution respectively.*

The variation of capacitance with time can be employed to study the adsorption kinetics of PAs onto the ITO substrate. Measurement of interfacial capacitance provides a convenient way of measuring the surface coverage of organic adsorbates as it is dependent on the relative areas of the covered and uncovered surface region [28]. The surface coverage (θ) is the fraction of the adsorbed surface with the monolayer. This can be obtained by using the expression:

$$\theta = (C_0 - C_t)/(C_0 - C_f) \qquad (2)$$

where C_o is the capacitance of bare ITO substrate, C_t is the capacitance at any time, and C_f is the capacitance of the fully covered monolayer.

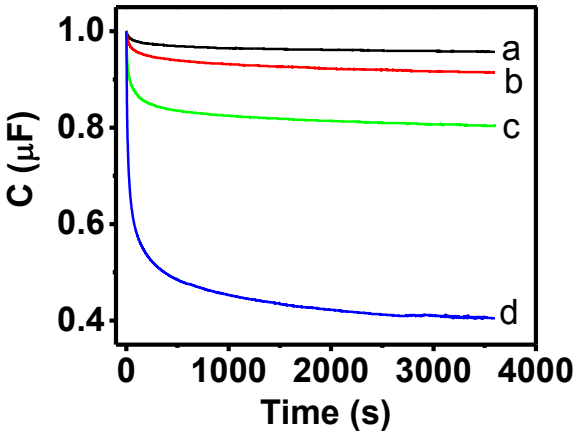

Figure 2. *Normalized Capacitance vs. time curves for ITO in 10mM PPA in 0.1M NaF electrolyte at ocp vs. SCE, (a). 1mM PPA (14.93 μF/cm^2), (b). 5mM PPA (15.67 μF/cm^2), (c). 10mM PPA (20.45 μF/cm^2), (d). 20mM PPA (22.12 μF/cm^2). The values in the parenthesis are the actual initial capacitance (μF) in each case for 1cm^2 area. The standard deviation for the initial capacitance measured for ITO electrode in 1mM PPA and 5mM PPA concentrations are respectively* $14.93 \pm 0.0585\ \mu F/cm^2$ *and* $15.67 \pm 0.1665\ \mu F/cm^2$.

The adsorption kinetics studies conducted at three different concentrations of PAs, namely, 1mM, 5mM, and 10mM with three samples and the measured rate constants reported are the mean of these measurements. The following adsorption models were considered for fitting either alone or in combination to explain the experimental data [28,29]:

1. *Langmuir model*: Here, the dependence of coverage on the time of adsorption expressed by the relation

$$\theta = 1 - exp(-kt) \qquad (3)$$

2. *Diffusion-controlled Langmuir model (DCL)*:

$$\theta = 1 - \exp\left(-k\sqrt{t}\right) \qquad (4)$$

   where θ is the fractional surface coverage at any instant of time (t) and k is the rate constant of adsorption.

3. *Purely diffusion controlled adsorption*:

$$\theta = k_d \sqrt{t} \qquad (5)$$

   where k_d is the diffusion rate constant given by

$$k_d = \left({}^{2cD^{1/2}}/_{B\pi^{1/2}}\right) \qquad (6)$$

where B is the number of molecules per unit area at fractional coverage, c is the concentration, and D is the diffusion coefficient.

Figure 3 shows the adsorption kinetics of PPA, ABPA, BPA, BuPA, and DecPA at different concentrations. While PPA and BPA are freely soluble in water, the other PAs dissolve easily only below 10mM concentration. The analysis show two different time constants that can be fitted on the coverage (θ)-time (t) plots, in all the cases except for DecPA at 1mM concentration. The two-step adsorption process was quite well studied in the case of adsorption of thiols on gold [4,11]. This behavior is reasoned as a rapid first step of adsorption forming an imperfect monolayer followed by a slower process of reorganization and enhanced packing of the film [30,31]. Similarly in the case of PAs, the adsorption kinetics initially follows the diffusion controlled Langmuir mechanism which is followed by the Langmuir adsorption isotherm. During the first step, 70-75% of the final coverage attained and the second slower step extends for the rest of the coverage. This behavior closely resembles adsorption of organic thiols on gold [32]. If it is assumed that the adsorption behavior of PAs on ITO is similar to thiols on gold, then, the first step corresponds to the rapid adsorption of PAs to the ITO surface without any organization. Since the initial adsorption of PAs on the surface is rapid, the process of diffusion of the adsorbing species through the Nernst diffusion layer to the electrode surface controls the overall rate during this initial stage. Hence, the adsorption during the initial phase follows the diffusion controlled Langmuir mechanism. Later in the second step, the adsorbed PA molecules attempt to reorganize their structure by deformation from the lying down phase to aligning phase which is normal to the surface [30,31]. During this step, PA molecules align and form an organized monolayer. During the second step, the lateral order in the monolayer increases. The adsorption rate increases with increase in the concentration of PAs as is obvious from the figure 3A. Maximum coverage is attained only at the highest concentrations of 20mM in the case of PPA and BPA, whereas it is 10mM in the case of the rest of the PAs. In fact, the maximum monolayer coverage is obtained only after 4-5 hours of adsorption (figure 4). However, at lower concentrations, there is an initial rapid rise in the coverage followed by a distinct plateau region that asymptotically reaches a surface coverage of less than one. The rate constants of PA adsorption on ITO is shown in Table 1. In the case of thiol adsorption on the gold surface, 1mM concentration is sufficient to get full

coverage in contrast to the PAs on ITO where nearly 10-20 times of this concentration are needed to get maximum surface coverage [11]. In this work, three trials were conducted for the PPA experiment at 1mM and 5mM concentrations to check the validity of the adsorption kinetics experiment and averaged out the values to get the coverage value which used for measuring the rate constants for various concentrations.

It can be seen from the Table 1 that PPA shows higher adsorption rate constant compared to the rest of the PAs. This high adsorption rate for PPA can be attributed to the high affinity of the hydrophilic interaction between hydroxylated ITO surface and the terminal carboxylic group of PA. This assumption validated by the fact that the adsorption rate constants for the rest of the PAs are comparatively less and the decrease in the adsorption rate constants follow the increasing hydrophobic nature of PAs. The concentration-dependent rate constants also show a decreasing trend with the increase in concentration. The variation in the rate constant values follow the order according to the increasing hydrophobic nature of the PAs *viz.*, PPA> ABPA> BPA~ BuPA > DecPA. The DecPA has the highest hydrophobic behavior compared to the other PAs under study, which therefore adsorbs slowly at 1mM and 5mM concentrations. Interestingly, at higher concentration of 10mM, DecPA shows higher adsorption rate constant. The reason for this counter-intuitive behavior is that above 2.7mM, DecPA forms micelles to avoid hydrophilic-hydrophobic interactions between water and decyl chains of DecPA [33]. These micelles project the hydrophilic PA group outwards and hydrophobic alkyl chains inside the aqueous medium. Since the hydrophilic PA groups are on the outside of the micelle, they show a higher affinity to bind with -OH groups of ITO resulting an increase in the rate of adsorption at this concentration.

There are very few reports in the literature on adsorption kinetics studies of PAs on ITO surface. Paniagua *et al*. studied the growth of pentafluorobenzylphosphonic acid onto ITO employing XPS studies [7]. Jo *et al.* studied the adsorption kinetics of PPA, PHA, and PUA using electrochemical impedance spectroscopy (EIS) [34]. In both of the above studies, the adsorption kinetics measurements were carried out for several hours and fitted with Langmuir adsorption isotherm with a single time constant. From our studies, we find that the 75% of adsorption of PAs takes place rapidly at short time scales of within 200s and therefore short timescale measurement is crucial for getting information on the initial stages of adsorption. Interestingly, these studies show that there are two time constants, the first of which is diffusion controlled Langmuir (DCL) which

is followed by Langmuir adsorption unlike a single time constant measured for the Langmuir kinetics in the earlier reports [7,34].

Table 1 lists the rate constants calculated for different PAs using DCL model (plot of θ vs. $t^{1/2}$) for 1mM, 5mM, 10mM, and 20mM concentrations. In the case of 1mM DecPA, the reaction fitted to pure diffusion control kinetics. The latter behavior may be due to the long chain of the DecPA molecule which needs to be at proper orientation on the surface for effective adsorption. At low concentrations, the diffusion of the molecules from the solution to the surface controls the adsorption process and therefore the rate constants.

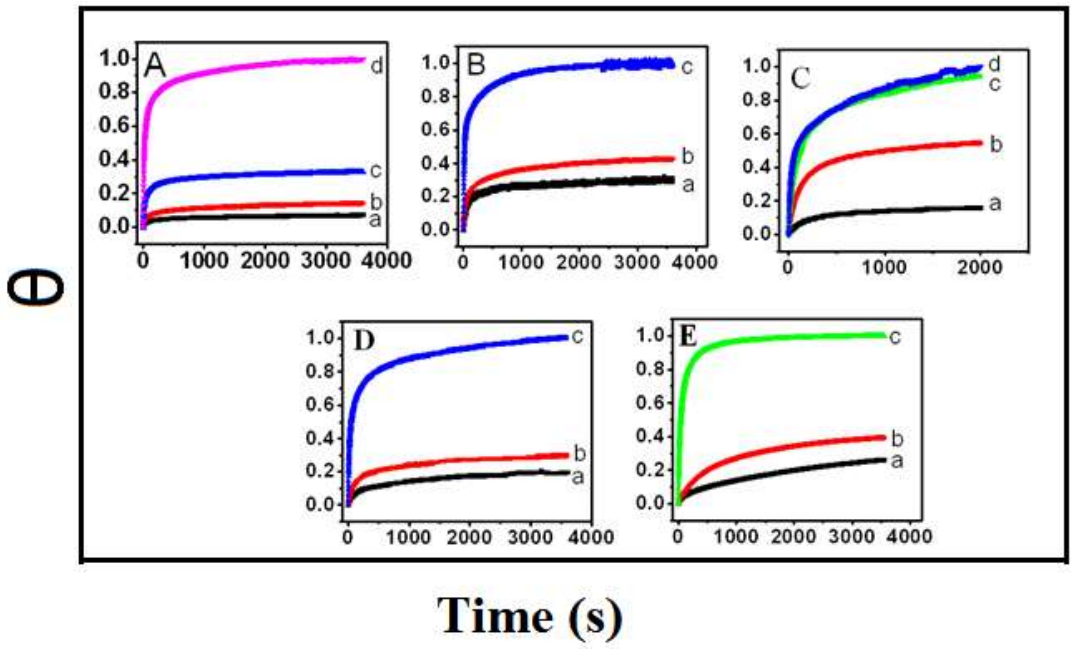

Figure 3. *Adsorption curves of different PAs with 0.1M NaF as supporting electrolyte*

A. 3-Phosphonopropionic acid (a). 1mM, (b). 5mM, (c). 10mM, (d). 20mM

B. 4-Aminobenzylphosphonic acid (a). 1mM, (b). 5mM, (c). 10mM

C. Benzylphosphonic acid (a). 1mM, (b). 5mM, (c). 10mM, (d). 20mM

D. Butylphosphonic acid (a).1mM, (b). 5mM, (c). 10mM

E. Decylphosphonic acid (a).1mM, (b). 5mM, (c). 10mM

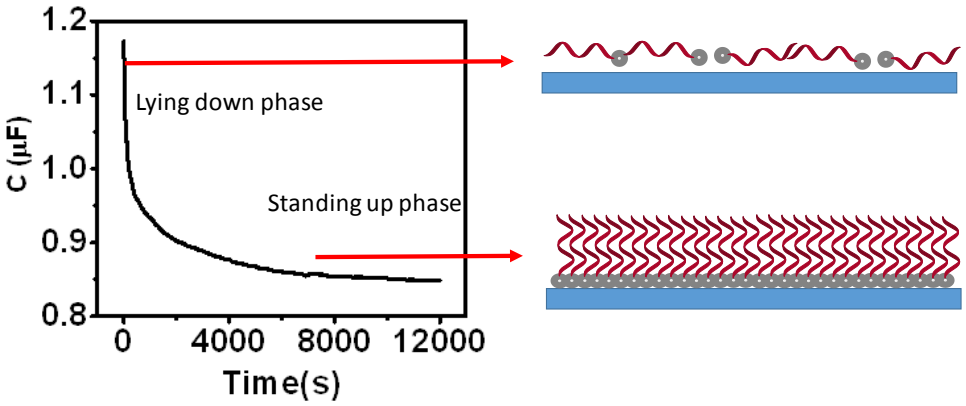

Figure 4. *A plot of capacitance vs. time for 10mM BPA in 0.1M NaF supporting electrolyte.*

Table 1. Rate constants of K_{ads} ($s^{-1/2}$), K_c ($M^{-1}\,s^{-1/2}$) PA adsorption onto ITO in 0.1M NaF solution for different PAs obtained using DCL model at 1mM and 10mM concentrations.

PA	1mM		5mM		10mM			20mM
	K_{ads}	K_c	K_{ads}	K_c	K_{ads}	K_c	K_{ads}	K_c
PPA	0.03	31.9	0.057	11.4	0.159	15.9	0.054	2.7
ABPA	0.02	26.0	0.04	7.8	0.059	5.9	---	---
BPA	0.026	26.0	0.034	6.8	0.032	3.2	0.01	0.5
BuPA	0.025	25.0	0.029	5.8	0.036	3.6	---	---
DecPA	0.005*	5.0*	0.001	0.2	0.085	8.5	---	---

* purely diffusion controlled adsorption following equation (6).

2.3.2 Immobilization of biomolecules:

Virtually all physiological processes in living matter occur in the aqueous medium, which means for immobilization study of the species by electrochemical methods, the bio-molecules need to be positioned on the surface of the electrode with the hydrophilic domain as a supporting structure. Besides, the hydrophilic support should allow penetration of water-soluble species by the process of diffusion to gain access to the immobilized bio-molecular species. For example, in the study of enzyme-catalyzed reactions, the enzyme molecules should maintain the spatial arrangements in water to retain its maximum activity. The hydrophilic support also helps to avoid any non-specific

interactions of a hydrophobic moiety which may deactivate the enzyme and denature it. The molecules containing hydrophilic groups like amide, epoxides, hydroxyl groups or even charged groups like carboxylate ions, sulfo groups, amines, *etc*. have all been used as support [35–45].

The adsorption of redox active heme protein *cyt c* and urease on ABPA and PPA modified ITO electrode is studied in this work. The surface structure of *cyt c* has been characterized by using AFM. Being a soft surface after adsorption of protein molecules, the imaging was carried out in non-contact mode and the displayed AFM images are phase contrast images that define the soft features more prominently.

2.3.3 Non-contact mode AFM studies:

Figure 5A shows the phase AFM images of (a) bare ITO, (b) ABPA/ITO, and (c) c*yt c*/ABPA/ITO. Figure 5B (a,b) shows the surface morphologies of PPA/ITO and *cyt c*/PPA/ITO surface respectively. While the bare ITO exhibits typical crystalline morphology, the ABPA modified ITO surface while retaining the essential crystalline features presents spherical and marginally larger domain structures. Figure 5A (c) corresponds to the *cyt c* immobilized ABPA/ITO electrode which shows distinct elongated and stripe-like features formed by the non-covalently immobilized *cyt c*. The average roughness (R_a) values reflecting the surface heterogeneity of the samples calculated from AFM images. These values for bare ITO, ABPA/ITO, and *cyt c*/ABPA/ITO are 0.7nm, 1nm, and 1.7nm respectively. The variation in R_a values show that there is a definitive increase in the roughness of the surface after *cyt c* adsorption on ABPA/ITO.

Figure 5B (a,b) corresponds to the AFM images of PPA/ITO and *cyt c*/PPA/ITO substrates. After immobilizing *cyt c* onto PPA/ITO, the grain morphology of the substrate vanishes producing the stripe-like features of *cyt c* on the PPA/ITO surface seen in figure 5B (b). The average roughness (R_a) values for the PPA/ITO and *cyt c*/PPA/ITO are 0.7 and 2.1nm respectively indicating a significant increase in the roughness values after *cyt c* adsorption.

The different morphological features of the *cyt c* protein on ABPA/ITO and PPA/ITO surfaces can be attributed to the different affinities of the protein towards these two monolayers.

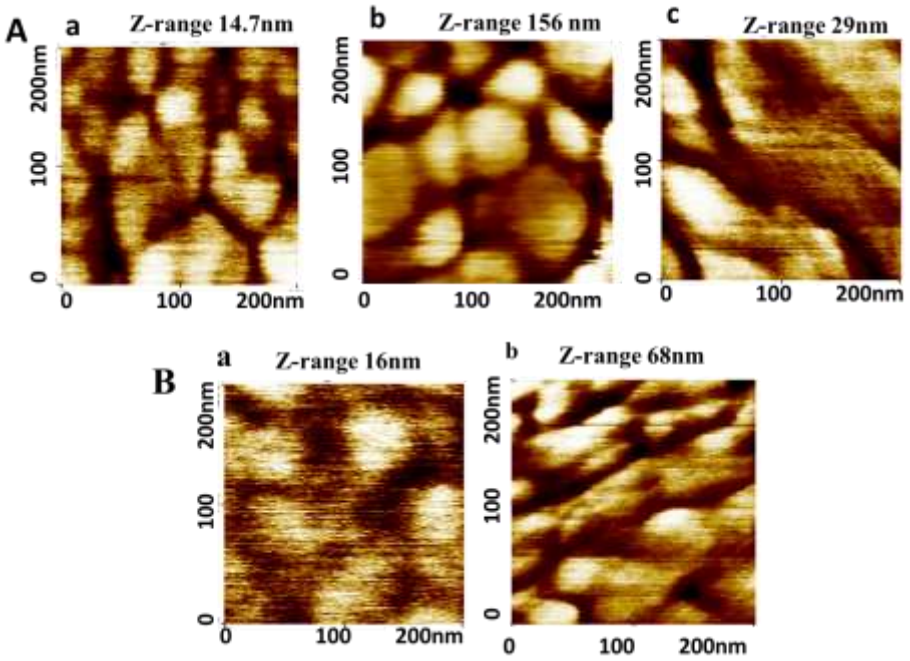

Figure 5. *Phase AFM images of (A.) (a). Bare ITO, (b). ABPA/ITO and (c). Cyt c/ABPA/ITO, (B.) (a). PPA/ITO and (b). Cyt c/PPA/ITO.*

2.3.4 Adsorption kinetic studies of *cyt c* on ABPA/ITO and PPA/ITO surfaces:

The adsorption kinetics of *cyt c* onto ABPA/ITO and PPA/ITO were studied by monitoring the capacitance changes during the adsorption of protein.

Cytochrome c is a biomolecule which is quite well characterized in electrochemistry since it is a redox protein with heme groups that can undergo electron transfer reaction after the surface immobilization. It is hydrophilic and positively charged below pH=10. Waldemar *et al.* extensively studied the immobilization of *cyt c* on amino terminated thiols and found that *cyt c* does not denature after immobilization in phosphate buffered solutions contrary to the previous reports [39]. This behavior was explained by the fact that phosphate ions specifically adsorb onto the amine-terminated SAMs, thereby creating a net negative charge on the surface. The negative charge on the surface leads to the adsorption of positively charged *cyt c* on the surface while at the same time without loss of any of its activity after immobilization. Chen *et al.* successfully immobilized *cyt c* on amino terminated thiols without denaturation of the protein [46]. Figure 7 shows the

electrochemical reduction of hydrogen peroxide on *cyt c* adsorbed ABPA/ITO and PPA/ITO surfaces which confirms that *cyt c* retains the redox activity even after surface immobilization and adsorption on PA modified surface. In both the above cases, the protein adsorbs in a conformation that allows rapid exchange of electrons between its heme group and the electrode surface. It was also suggested that carboxyl terminated SAMs have surface inhomogeneity arising due to protonation and deprotonation of carboxyl groups [39].

Figure 6A shows the coverage vs. time plots for *cyt c* onto ABPA modified ITO electrode measured using the imaginary component of impedance at a constant frequency of 10Hz. We monitored the adsorption below 100µg/ml *cyt c* concentration, as the final coverage attained corresponds to maximum adsorption for *cyt c* beyond which there is no further increase. The adsorption data were fitted to the plot using the expression proposed by Jose *et al.* which represents Langmuir adsorption kinetics with two successive times *viz.*,[43]

$$\theta = A_1(1 - \exp(-k_1 t)) + A_2(1 - \exp(-k_2 t)) \qquad (7)$$

where $k_1$and $k_2 - adsorption\ rate\ constants$

The rate constant depends on the concentration of *cyt c*, and it is directly proportional to the concentration of the adsorbing species.

$$\text{Therefore, } k_1 = k_{c1} C \ and \ k_2 = k_{c2}\ C \qquad (8)$$

where k_{c1}, k_{c2} $-$ *concentration-dependent rate constants*

This concentration-dependent rate constant changes with the concentration of protein adsorbing onto the modified surface. Since most of the adsorption occurs in the initial stages, the first adsorption rate constant corresponds to the surface anchoring of protein molecules.

Figure 6B shows the adsorption kinetics of the *cyt c* on the PPA modified ITO electrode at (a). 50µg/ml and (b). 100µg/ml concentrations respectively. In this case, too, *cyt c* adsorption follows two different rate constants. The two different rate constants attributed to initial fast adsorption followed by slower reorganization of the *cyt c* on the monolayer modified electrode.

Jose *et al.* studied the adsorption kinetics of *cyt c* onto a glass surface and measured $2.2s^{-1}$ as the rate constant for adsorption of protein using time-resolved optical waveguide spectroscopy up to

a short time scale of 10 seconds [43]. They find that after initial fast adsorption of protein, there is a slower process of rearrangement on the surface. Shrikrishnan *et al.* have earlier studied the adsorption kinetics of alkaline phosphatase enzyme onto 3-mercaptobenzoicacid (MBA) on the gold electrode in phosphate buffer and measured the adsorption rate constant to be $0.23s^{-1}$ by fitting with Langmuir adsorption isotherm with a single time constant [44].

From Table 2, it can be seen that *cyt c* adsorbs faster onto the ABPA/ITO compared to the PPA/ITO surface. ABPA which is an amine terminated phosphonic acid positively charged at pH=7, at which the study conducted. These positively charged amine groups are solvated by phosphate groups in solution, which results in a negative charge on the surface that facilitates faster adsorption of *cyt c.* However, on PPA with the carboxyl terminated monolayer being inhomogeneous the adsorption process takes place slowly.

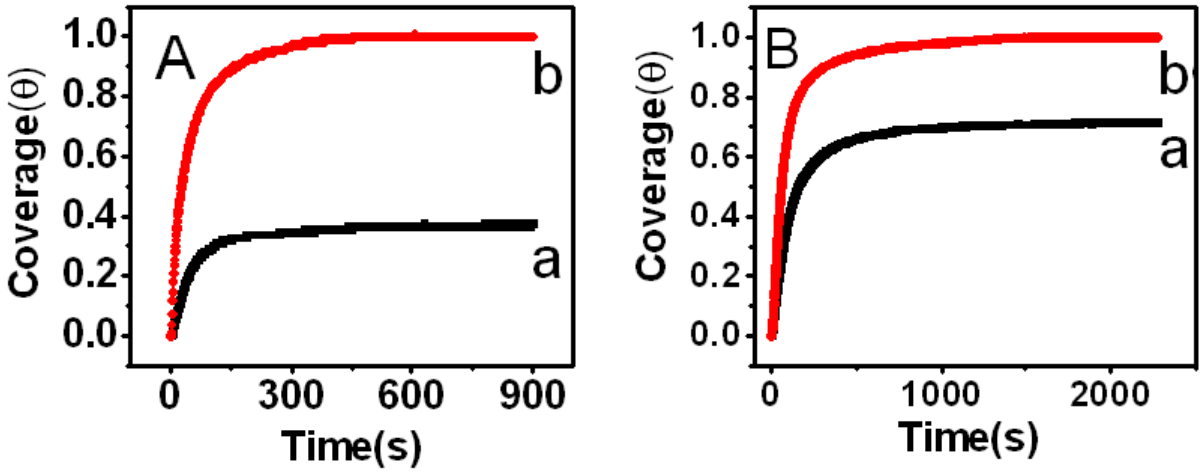

Figure 6. *Coverage (θ) vs. time (t) plot for adsorption of cyt c onto (A) ABPA modified ITO electrode (a) 50µg/mL cyt c, (b) 100µg/mL cyt c, (B) PPA modified ITO (a) 50µg/mL cyt c, (b) 100µg/mL cyt c in 0.2M phosphate buffer solution of pH=7.*

Table 2. Rate constants of adsorption of *cyt c* and urease on modified ITO.

Concentration	K_{ads} (s^{-1})		K_c (M^{-1} s^{-1})	
	ABPA	PPA	ABPA	PPA
50µg/mL *cyt c*	0.0205	0.0093	410	190
100µg/mL *cyt c*	0.0446	0.0129	446	129

Figure 7 shows the cyclic voltammetric behavior of (A). *cyt c*/ABPA/ITO and (B). c*yt c*/PPA/ITO electrodes towards the addition of 1mM H_2O_2 increments for each experiment. The current begins to increase at potentials more negative to -0.1V vs. SCE on the addition of H_2O_2 due to its reduction to HO_2^- ions by *cyt c*. The current saturation occurs for the *cyt c*/ABPA/ITO electrodes at 5mM and 4mM in the case of *cyt c*/PPA/ITO electrode.

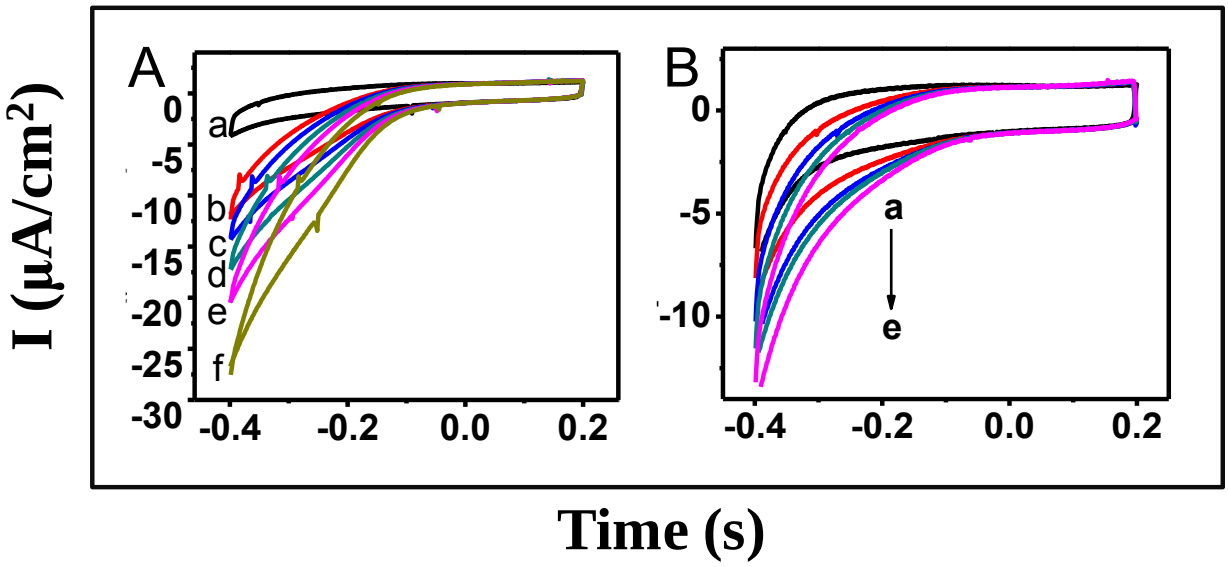

Figure 7. *Cyclic voltammograms of (A). Cyt c/ABPA/ITO and (B). Cyt c/PPA/ITO in 0.1M phosphate buffer solution of pH=7.0 on the addition of 1mM H_2O_2 in increments (b-f).*

Electrochemical sensing behavior of *cyt c* immobilized on hydrophilic terminated phosphonic acid modified electrodes were studied using chronoamperometry technique by the addition of 0.5mM

H_2O_2 at 30 seconds interval for 300 seconds. Figure 8A shows chronoamperograms obtained for *cyt c* immobilized on ABPA/ITO (figure 8A (b)) coated electrodes along with the response of the monolayer coated electrode (figure 8A (a)). A similar response also seen for PPA coated ITO electrode, with the addition of 0.5mM H_2O_2 to (a). PPA/ITO electrodes and (b). *cyt c* immobilized on PPA/ITO electrode. The response shown by the protein modified electrodes suggests that adsorbed *cyt c* protein is stable on the surface and retains its native state. *Cyt c*/ABPA/ITO electrode shows better sensitivity for the addition of H_2O_2 compared to *cyt c*/PPA/ITO which can be inferred from figures A and B in figure 8. The difference in sensing behavior can be attributed to the electrostatic attraction between positively charged *cyt c* and negatively charged ABPA (negative charge on ABPA arises due to the adsorption of negatively charged phosphate ions over positively charged monolayer) [39]. Due to the electrostatic interactions, the positively charged *cyt c* lies close to the electrode surface due to which *cyt c*/ABPA/ITO exhibits better electrochemical response. Moreover, 4-aminobenzylphosphonic acid consists of electron rich phenyl group which provides a facile pathway for the electron transfer between heme protein and electrode surface.

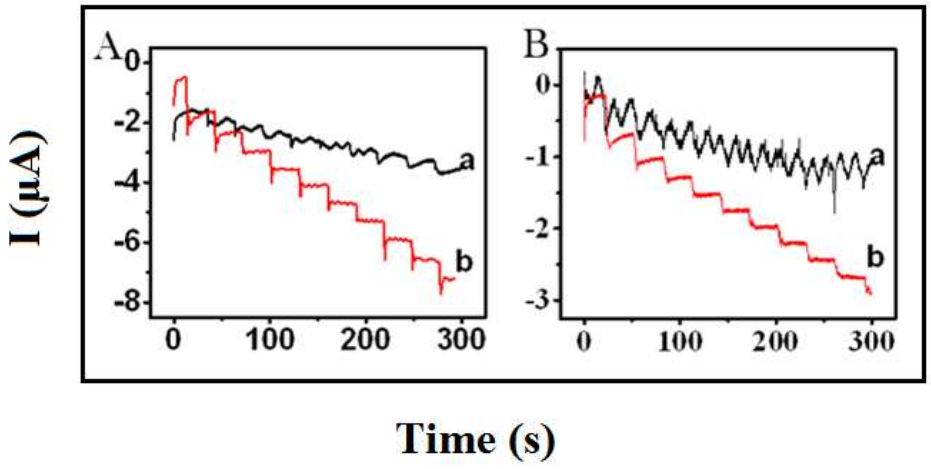

Figure 8. *Chronoamperometry curves for 0.5mM H_2O_2 standard addition (A) (a) ABPA/ITO, (b) Cyt c/ABPA/ITO, (B) (a) PPA/ITO, (b) Cyt c/PPA/ITO.*

2.3.5 Adsorption kinetic studies of urease on ABPA/ITO and PPA/ITO surfaces:

Urease, an enzyme belongs to the super family of amidohydrolases and phosphotriesterases. It is found in numerous bacteria, fungi, algae, plants, and some invertebrates, as well as in soils [47,48].

It is a nickel-containing metalloenzyme of a high molecular weight of 480kDa. It catalyzes the hydrolysis of urea into carbon dioxide and ammonia.

$$NH_2CONH_2 + H_2O \longrightarrow CO_2 + 2NH_3 \qquad (9)$$

The active site of the urease consists of dimeric nickel center, with an interatomic distance of ~3.5Å [49]. The water molecules are located towards the opening of the active site and form a tetrahedral cluster that fills the cavity site through hydrogen bonds, and the urea binds to the active site for the reaction, displacing the water molecules. The amino acid residues participate in the substrate binding, mainly through hydrogen bonding, stabilize the catalytic transition state, and accelerate the reaction.

Urease enzyme can be immobilized onto various supports through entrapment, copolymerization, encapsulation, non-covalent, and covalent binding depending on the nature of the support. Stability and retaining the activity of the enzyme is the main criterion of immobilization [50–52]. Selvamurugan *et al.* studied the stability of urease immobilized on various matrices and their applicability towards urea sensing and suggested that covalently immobilized urease on Nylon beads show better stability and activity compared to the Ca-alginate trapped urease enzyme [52]. Shrikrishnan *et al.* have studied the adsorption kinetics of urease enzyme immobilized on 3-mercaptobenzoic acid (3-MBA) on gold. The urea-urease kinetics were studied by monitoring the imaginary component of impedance with the addition of urea near the urease immobilized 3-MBA/gold electrode [44].

Figure 9 shows the coverage vs. time adsorption plot for 100 and 250µg/ml of urease in solution onto ABPA/ITO and PPA/ITO surfaces. While, for 100µg/ml, the adsorption rate constant follows diffusion controlled Langmuir (DCL) kinetics, at higher concentration of 250µg/ml it follows the Langmuir adsorption kinetics with a single time constant. It can be seen from Table 3, that the rate of adsorption of urease on PPA is comparable with that of *cyt c* (Table 2). Urease activity has been studied using urea as a substrate at different concentrations.

Figure 10 gives a schematic representation of the reaction between urea and urease enzyme. Urea sensing studies were carried out by monitoring the interfacial capacitance changes by the addition of different quantities of urea near the (A). urease/ABPA/ITO and (B). urease/PPA/ITO electrodes in 0.1M phosphate buffer solution at a constant frequency of 10Hz (figure 11). Addition of urea to

electrolyte system in the presence of non-covalently immobilized enzyme electrode resulted in the production of ammonium and carbonate ions at the surface of these membranes. These ions alter the electrostatic fields at the electrode/electrolyte interface of membranes. The increased electrostatic attraction between the protein and the substrate results in variation of interfacial capacitance at the interfaces. Therefore, there is a reduction in the number of trap-sites causing a decrease in the interfacial capacitance of the electrode [53].

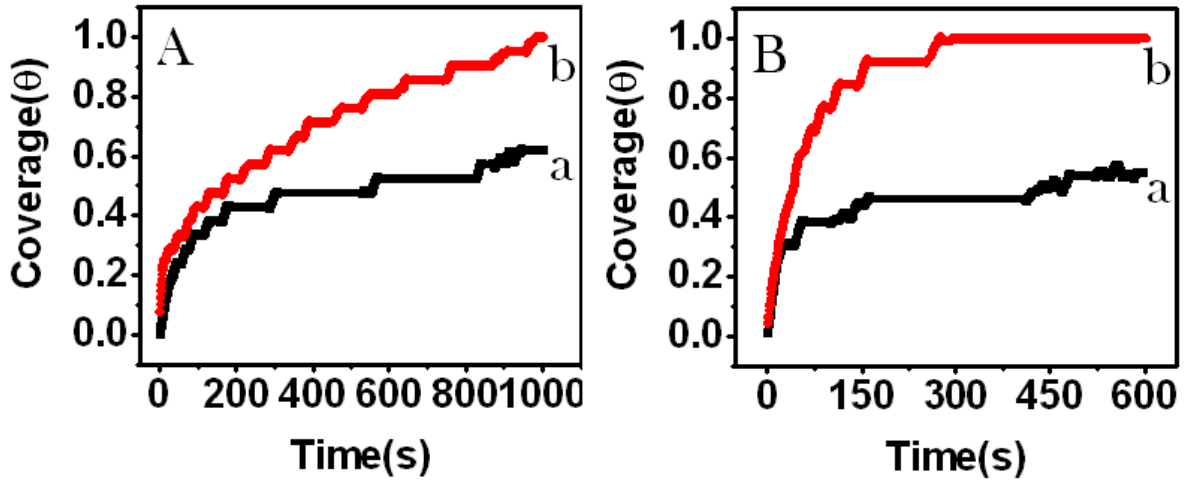

Figure 9. *Urease adsorption kinetics onto ABPA and PPA modified ITO electrode in 0.1M phosphate buffer (A) (a). 100µg/ml urease, (b). 250µg/ml urease addition on ABPA/ITO, (B) (a). 100µg/ml urease, (b). 250µg/ml urease addition on PPA/ITO.*

It can be seen from the figure 11, that the net change in capacitance increases with increasing amount of urea in the electrolyte. Urease immobilized on PPA/ITO causes large changes even at low concentration of urea, whereas urease on ABPA/ITO electrode needs a much large amount of additions for significant variations to be observed. The difference in sensing behavior might be attributed to the configuration obtained by urease after immobilization onto these substrates. The minimum amount of urea detected is 0.2mM and 1mM respectively in the case of urease/PPA/ITO and urease/ABPA/ITO electrodes.

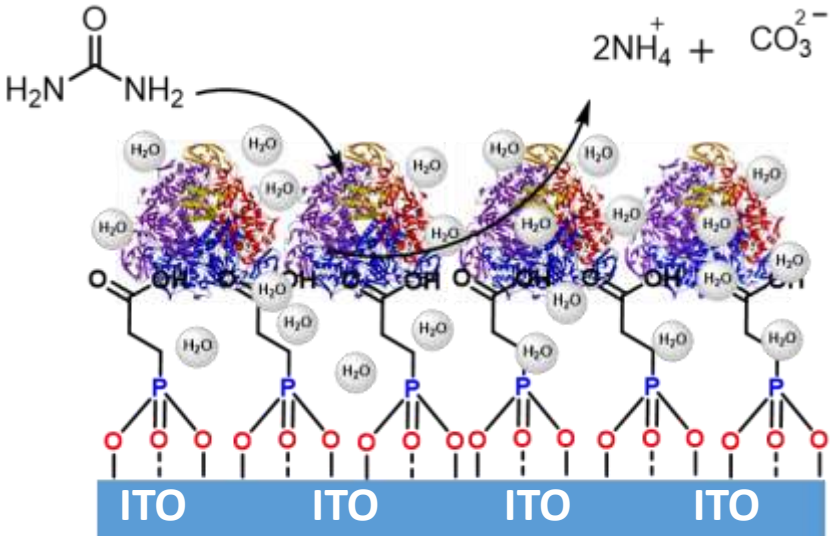

***Figure10**. Schematic representation of urea-urease reaction.*

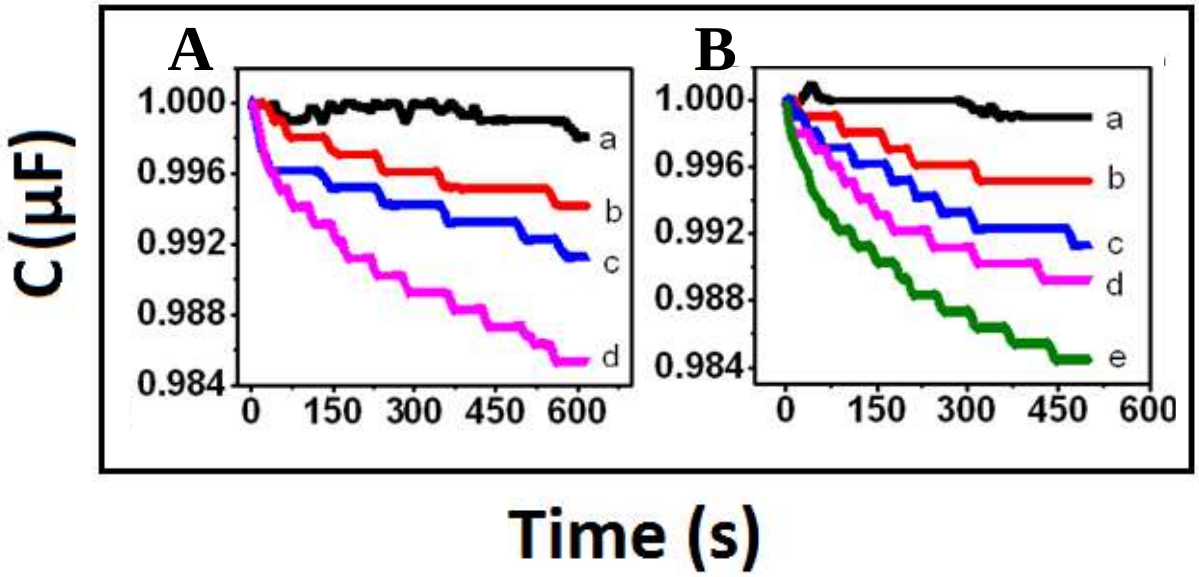

***Figure 11.** Capacitance vs. time curves on (A). urease/ABPA/ITO (a). 0mM urea, (b). 1mM urea, (c). 5mM urea, and (d). 10mM urea, and (B). urease/PPA/ITO, (a) 0mM urea, (b).0.2mM urea, (c). 0.3mM urea, (d).0.4mM urea, and (e). 0.5mM urea.*

2.3.6 Hydrogen peroxide sensor studies on ITO:

The interaction of hydrogen peroxide (H_2O_2) with metal surfaces is significant because it is a byproduct of various biological processes such as enzyme reactions of glucose oxidase [54],

cholesterol oxidase [55], pyranose oxidase [56], xanthine peroxidase enzymes [57], and acts as a substrate for reaction with proteins such as cytochrome *c* [58], catalase [59], *etc*. The reaction of H_2O_2 with the metal surfaces are largely mediated by hydrogen bonding between H_2O_2 and surface hydroxyl groups of the electrodes. Thus, a close interaction between the oxygen atoms of hydrogen peroxide and the metal atoms are also present in the oxide [60]. Stewart *et al.* suggested that peroxide undergoes reduction on surface hydroxyls of copper oxides by the dissociative adsorption of peroxide forming $HO_2^{\cdot}$ radicals [61]. One of these radicals can further abstract an H atom initially bound to surface oxygen and form H_2O. Cai *et al.* earlier reported that indium tin oxide film coated glass substrates can be used as a non-enzymatic amperometric hydrogen peroxide sensor. The peroxide sensitivity of the ITO substrate determined through chronoamperometric technique [62]. Reddy *et al.* studied the electrocatalytic behavior of template electrodeposited copper/copper oxide nanoparticles formed on pencil graphite lead substrate towards hydrogen peroxide sensing [63].

To evaluate the catalytic efficiency of indium tin oxide towards hydrogen peroxide (H_2O_2), cyclic voltammetric (CV) and chronoamperometry experiments were performed. Figure 12 shows cyclic voltammetry and chronoamperometry response curves for the successive addition of 1mM H_2O_2 in 0.1M phosphate buffer solution at pH 7. Indium tin oxide (ITO) reduces hydrogen peroxide to water at -0.15V vs. SCE. As observed from the figure 12A, CV shows increasing current response with the hydrogen peroxide addition at the negative potential region.

Chronoamperometric studies were carried out with the successive addition of 1mM H_2O_2 for the 30-second interval at a constant applied potential of -0.2V vs. SCE in a solution containing 0.1M phosphate buffer at pH 7.0 (Figure 12B). The sensitivity of ITO substrate for H_2O_2 is measured to be.1.75µA/mM.

Figure 13 shows the cyclic voltammograms of bare ITO electrode in 1mg/ml of GO_x solution using 0.1M phosphate buffer by increasing the concentration of glucose by 0.5mM during each addition. Glucose oxidase in the presence of oxygen converts glucose to gluconic acid and hydrogen peroxide. Hydrogen peroxide which is a by-product of this enzyme-substrate reaction undergoes electrochemical reduction at the ITO surface. The current increase during each experiment is the result of the production of the equivalent amount of hydrogen peroxide evolved due to the enzyme-substrate reaction. The reaction becomes saturated over the concentration of 5mM of glucose

addition to the electrolyte solution. The enzyme kinetics of glucose oxidase and glucose reaction is followed by monitoring the hydrogen peroxide concentration near the electrode surface.

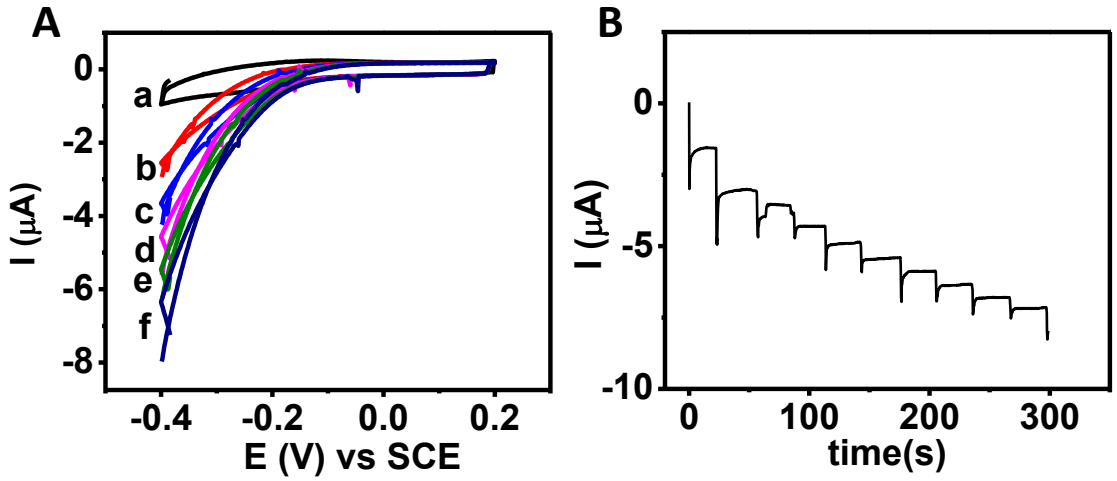

Figure 12. *(A). Cyclic voltammetric and (B). Chronoamperometric curves for ITO electrode in 0.1M phosphate buffer solution with increments of 1mM H_2O_2.*

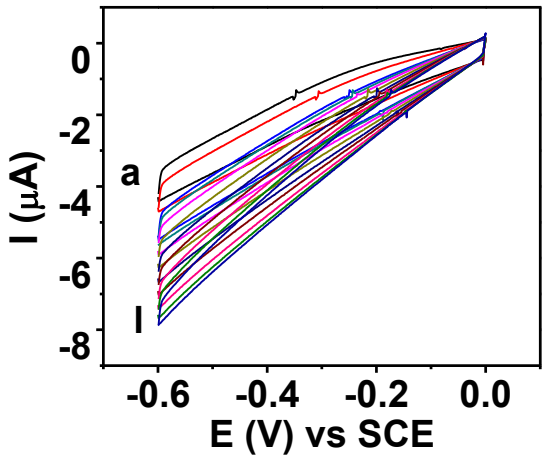

Figure 13. *Cyclic voltammetric curves for bare ITO electrode in 1mg/ml GO_x solution of 0.1M phosphate buffer with increments in addition of glucose by 0.5mM each experiment.*

$$Glucose + O_2 \longrightarrow Gluconic\ acid + H_2O_2 \qquad (10)$$

$$H_2O_2 \longrightarrow O_2 + H_2O \qquad (11)$$

Figure 14 shows the (A). chronoamperometric response curves with the incremental addition of glucose to the electrolyte solution and (B). Michaelis-Menten curve for calculation of Michaelis-Menten constant (k_m) value for the glucose oxidase enzyme kinetics. The electrolyte solution

consists of 1mg/ml concentrated glucose oxidase solution and is continuously stirred using a magnetic stirrer. The byproduct of glucose oxidase-glucose reaction is hydrogen peroxide. The released peroxide is electrochemically reduced on the ITO surface which results in the corresponding increase in the current. The increase in currents reaches saturation after the addition of 5mM glucose suggesting the saturation of the enzyme activity. Figure 14B shows the Michaelis-Menten curve for the reaction. The rate of generation of H_2O_2 measured from figure 14A. The Michaelis-Menten curve shown in figure 14B, where the rate of generation of H_2O_2 plotted against H_2O_2 concentration.

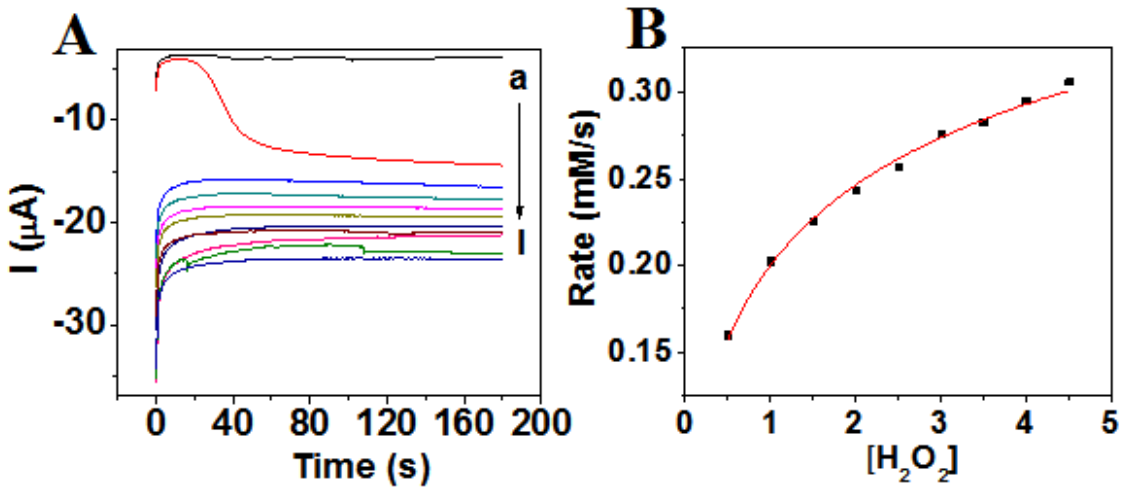

Figure 14. *(A). Chronoamperometric curves of sequential concentration increments (5 x 10^{-4} mol/l) at an ITO electrode which is immersed in 1mg/ml concentrated GO_x solution in 0.1M phosphate buffer solution; operating potential -200mV (B). Michaelis-Menten curve obtained for glucose oxidase-glucose enzyme kinetics. (k_m=2.16mM).*

2.4 Conclusions:

The adsorption kinetics of different phosphonic acids and proteins on functionalized ITO were studied. It is found that the adsorption kinetics of PAs correlate very well with the nature of the terminal functional groups and their hydrophobic nature. It is further demonstrated that the enzyme, such as urease and heme protein *cyt c* can be immobilized onto the modified surface while retaining their protein activity, thereby providing a completely stabilized monolayer/enzyme or monolayer systems. Except for DecPA at lower concentrations, all PAs follow two rate constants for adsorption onto ITO electrode. The adsorption kinetics of a heme protein *cyt c* and an enzyme

urease onto ABPA/ITO and PPA/ITO surfaces have also studied. The *cyt c* adsorption follows two rate constants, Langmuir adsorption in both the steps In the case of urease, it follows diffusion Langmuir adsorption at low concentration and Langmuir adsorption at high concentrations with a single time constant.

Finally, it is shown that hydroxylated ITO surface can be very sensitive to H_2O_2 detection as demonstrated by using cyclic voltammetry and chronoamperometry studies. This method has been applied for sensing glucose in the presence of glucose oxidase enzyme, and the Michaelis-Menten constant was determined using hydroxylated ITO electrode surface.

2.5 References:

[1] S.P. Pujari, L. Scheres, A.T.M. Marcelis, H. Zuilhof, Covalent surface modification of oxide surfaces, Angew. Chemie - Int. Ed. 53 (2014) 6322–6356. doi:10.1002/anie.201306709.

[2] A. Vega, P. Thissen, Y.J. Chabal, Environment-controlled tethering by aggregation and growth of phosphonic acid monolayers on silicon oxide, Langmuir. 28 (2012) 8046–8051. doi:10.1021/la300709n.

[3] X. Chen, E. Luais, N. Darwish, S. Ciampi, P. Thordarson, J.J. Gooding, Studies on the effect of solvents on self-assembled monolayers formed from organophosphonic acids on indium tin oxide, Langmuir. 28 (2012) 9487–9495. doi:10.1021/la3010129.

[4] P. Thissen, A. Vega, T. Peixoto, Y.J. Chabal, Controlled, low-coverage metal oxide activation of silicon for organic functionalization: Unraveling the phosphonate bond, Langmuir. 28 (2012) 17494–17505. doi:10.1021/la3038457.

[5] B. Nowack, A.T. Stone, Adsorption of phosphonates onto the Goethite-Water interface, J. Colloid Interface Sci. 214 (1999) 20–30. doi:10.1006/jcis.1999.6111.

[6] E.L. Hanson, J. Schwartz, B. Nickel, N. Koch, M.F. Danisman, Bonding Self-Assembled, Compact Organophosphonate Monolayers to the Native Oxide Surface of Silicon, J. Am. Chem. Soc. 125 (2003) 16074–16080. doi:10.1021/ja035956z.

[7] S.A. Paniagua, E.L. Li, S.R. Marder, Adsorption studies of a phosphonic acid on ITO:

film coverage, purity, and induced electronic structure changes, Phys. Chem. Chem. Phys. 16 (2014) 2874. doi:10.1039/c3cp54637c.

[8] M. Chockalingam, N. Darwish, G. Le Saux, J.J. Gooding, Importance of the indium tin oxide substrate on the quality of self-assembled monolayers formed from organophosphonic acids, Langmuir. 27 (2011) 2545–2552. doi:10.1021/la104464w.

[9] T.J. Gardner, C.D. Frisbie, M.S. Wrighton, Systems for orthogonal self-assembly of electroactive monolayers on Au and ITO: An approach to molecular electronics, J. Am. Chem. Soc. 117 (1995) 6927–6933. doi:10.1021/ja00131a015.

[10] K. Jo, H.Z. Yu, H. Yang, Formation kinetics and stability of phosphonate self-assembled monolayers on indium-tin oxide, Electrochim. Acta. 56 (2011) 4828–4833. doi:10.1016/j.electacta.2011.03.021.

[11] R. Subramanian, V. Lakshminarayanan, A study of kinetics of adsorption of alkanethiols on gold using electrochemical impedance spectroscopy, Electrochim. Acta. 45 (2000) 4501–4509. doi:10.1016/S0013-4686(00)00512-0.

[12] D.J. Fink, T.B. Hutson, K.K. Chittur, R.M. Gendreau, Quantitative surface studies of protein adsorption by infrared spectroscopy. II. Quantification of adsorbed and bulk proteins, Anal. Biochem. 165 (1987) 147–154. doi:10.1016/0003-2697(87)90213-2.

[13] H.P. Jennisen, Immobilization of residues on agarose gels: effects on protein adsorption isotherms and chromatographic parameters, J. Chromatogr. A. 215 (1981) 73–85. doi:10.1016/S0021-9673(00)81387-4.

[14] V. Hlady, J. Buijs, H.P. Jennissen, [26] Methods for studying protein adsorption, Vitr. PROTIEN Depos. 309 (1999) 402–429. doi:10.1016/S0076-6879(99)09028-X.

[15] C. Mathé, S. Devineau, J.-C. Aude, G. Lagniel, S. Chédin, V. Legros, M.-H. Mathon, J.-P. Renault, S. Pin, Y. Boulard, J. Labarre, Structural Determinants for Protein adsorption/non-adsorption to Silica Surface, PLoS One. 8 (2013) e81346. doi:10.1371/journal.pone.0081346.

[16] C.H. Ho, D.W. Britt, V. Hlady, Human low density lipoprotein and human serum albumin adsorption onto model surfaces studied by total internal reflection fluorescence and

scanning force microscopy, J. Mol. Recognit. 9 (1996) 444–455. doi:10.1002/(SICI)1099-1352(199634/12)9:5/6<444::AID-JMR281>3.0.CO;2-I.

[17] M.F.M. Engel, A.J.W.G. Visser, C.P.M. Van Mierlo, Adsorption of Bovine α-Lactalbumin on Suspended Solid Nanospheres and Its Subsequent Displacement Studied by NMR Spectroscopy, Langmuir. 20 (2004) 5530–5538. doi:10.1021/la049834b.

[18] S. Kumar, V.K. Aswal, J. Kohlbrecher, SANS and UV-vis spectroscopy studies of resultant structure from lysozyme adsorption on silica nanoparticles, Langmuir. 27 (2011) 10167–10173. doi:10.1021/la201291k.

[19] A.F. Runge, S.S. Saavedra, Comparison of Microcontact-Printed and Solution-Adsorbed Cytochrome c Films on Indium Tin Oxide Electrodes, Langmuir. 19 (2003) 9418–9424. doi:10.1021/la0350507.

[20] J. Xie, C. Riley, M. Kumar, K. Chittur, FTIR/ATR study of protein adsorption and brushite transformation to hydroxyapatite, Biomaterials. 23 (2002) 3609–3616. doi:10.1016/S0142-9612(02)00090-X.

[21] H.V. Buijs Jos, Adsorption kinectics, confromation, and mobility of the growth hormone and lysozyme on solid surfaces, studied with TIRF, J. Colloid Interface Sci. 190 (2012) 171–181.

[22] C. Mathé, S. Devineau, J.C. Aude, G. Lagniel, S. Chédin, V. Legros, M.H. Mathon, J.P. Renault, S. Pin, Y. Boulard, J. Labarre, Structural determinants for protein adsorption/non-adsorption to silica surface, PLoS One. 8 (2013) 1–13. doi:10.1371/journal.pone.0081346.

[23] Z. Qi, N. Matsuda, A. Takatsu, K. Kato, A Kinetic Study of Cytochrome c Adsorption to Hydrophilic Glass by Broad-Band, Time-Resolved Optical Waveguide Spectroscopy, J. Phys. Chem. B. 107 (2003) 6873–6875. doi:10.1021/jp034901g.

[24] A.A. Karyakin, Prussian Blue and Its Analogues: Electrochemistry and Analytical Applications, Electroanalysis. 13 (2001) 813–819. doi:10.1002/1521-4109(200106)13:10<813::AID-ELAN813>3.0.CO;2-Z.

[25] W. Wang, T.J. Zhang, D.W. Zhang, H.Y. Li, Y.R. Ma, L.M. Qi, Y.L. Zhou, X.X. Zhang,

Amperometric hydrogen peroxide biosensor based on the immobilization of heme proteins on gold nanoparticles-bacteria cellulose nanofibers nanocomposite, Talanta. 84 (2011) 71–77. doi:10.1016/j.talanta.2010.12.015.

[26] W. Chen, S. Cai, Q.-Q. Ren, W. Wen, Y.-D. Zhao, Recent advances in electrochemical sensing for hydrogen peroxide: a review, Analyst. 137 (2012) 49–58. doi:10.1039/C1AN15738H.

[27] Y.E. Miao, S. He, Y. Zhong, Z. Yang, W.W. Tjiu, T. Liu, A novel hydrogen peroxide sensor based on Ag/SnO2 composite nanotubes by electrospinning, Electrochim. Acta. 99 (2013) 117–123. doi:10.1016/j.electacta.2013.03.063.

[28] B.B. Damaskin, Adsorption of Organic Compounds At the Mercury Electrode – Solution Interface, Russ. Chem. Rev. 34 (1965) 752–759. doi:10.1070/RC1965v034n10ABEH001560.

[29] J. Liu, U. Messow, Diffusion-controlled adsorption kinetics at the air/solution interface, Colloid Polym. Sci. 278 (2000) 124–129. doi:10.1007/s003960050021.

[30] M. Grunze, Preparation and Characterization of Self-Assembled Organic Films on Solid Substrates, Phys. Scr. T49b (1993) 711–717. doi:10.1088/0031-8949/1993/T49B/056.

[31] M. Himmelhaus, F. Eisert, M. Buck, M. Grunze, Self-Assembly of n -Alkanethiol Monolayers. A Study by IR−Visible Sum Frequency Spectroscopy (SFG), J. Phys. Chem. B. 104 (2000) 576–584. doi:10.1021/jp992073e.

[32] K.A. Peterlinz, R. Georgiadis, In Situ Kinetics of Self-Assembly by Surface Plasmon Resonance Spectroscopy, Langmuir. 12 (1996) 4731–4740. doi:10.1021/la9508452.

[33] C. V. Di Anibal, M.A. Moroni, V. Verdinelli, J.L. Rodríguez, R. Minardi, P.C. Schulz, B. Vuano, Critical micelle concentration of tridecane, tetradecane and hexadecane phosphonic acids and their mono- and disodium salts, Colloids Surfaces A Physicochem. Eng. Asp. 348 (2009) 276–281. doi:10.1016/j.colsurfa.2009.07.042.

[34] K. Jo, H. Yang, Comparative study of stability of phosphonate self-assembled monolayers on indium-tin oxide electrodes prepared using different methods, J. Electroanal. Chem. 712 (2014) 8–13. doi:10.1016/j.jelechem.2013.10.022.

[35] V.A. Ivan, McLean J.C. Robert, Immobilized Biosystems, Springer Netherlands, Dordrecht, 1994. doi:10.1007/978-94-011-1334-2.

[36] M.T.W. Hearn, Application of 1,1′-carbonyldiimidazole-activated matrices for the purification of proteins, J. Chromatogr. B Biomed. Sci. Appl. 376 (1986) 245–257. doi:10.1016/S0378-4347(00)80841-5.

[37] M.T. De Groot, T.H. Evers, M. Merkx, M.T.M. Koper, Electron transfer and ligand binding to cytochrome c′ immobilized on self-assembled monolayers, Langmuir. 23 (2007) 729–736. doi:10.1021/la062308v.

[38] F. Li, W. Chen, S. Zhang, Development of DNA electrochemical biosensor based on covalent immobilization of probe DNA by direct coupling of sol-gel and self-assembly technologies, Biosens. Bioelectron. 24 (2008) 781–786. doi:10.1016/j.bios.2008.06.052.

[39] D.A. Capdevila, W.A. Marmisollé, F.J. Williams, D.H. Murgida, Phosphate mediated adsorption and electron transfer of cytochrome c. A time-resolved SERR spectroelectrochemical study, Phys. Chem. Chem. Phys. 15 (2013) 5386–5394. doi:10.1039/C2CP42044A.

[40] D.H. Nagaraju, R.K. Pandey, V. Lakshminarayanan, Electrocatalytic studies of Cytochrome c functionalized single walled carbon nanotubes on self-assembled monolayer of 4-ATP on gold, J. Electroanal. Chem. 627 (2009) 63–68. doi:10.1016/j.jelechem.2008.12.020.

[41] X. Chen, R. Ferrigno, J. Yang, G.M. Whitesides, Redox properties of cytochrome c adsorbed on self-assembled monolayers: A probe for protein conformation and orientation, Langmuir. 18 (2002) 7009–7015. doi:10.1021/la0204794.

[42] M.D.K. Kumaraswamy, K.P. Rao, K.T. Joseph, M. Santappa, Immobilization of enzymes on alginic acid-polyacrylamide copolymers, Biotechnol. Bioeng. 23 (1981) 1889–1892. doi:10.1002/bit.260230815.

[43] J.H. Santos, N. Matsuda, Z.-M. Qi, T. Yoshida, A. Takatsu, K. Kato, Time-Resolved Optical Waveguide Spectroscopy for Studying Protein Adsorption Kinetics, Mater. Trans. 45 (2004) 1015–1018. doi:10.2320/matertrans.45.1015.

[44] S. Shrikrishnan, K. Sankaran, V. Lakshminarayanan, Electrochemical impedance analysis of adsorption and enzyme kinetics of calf intestine alkaline phosphatase on SAM-modified gold electrode, J. Phys. Chem. C. 116 (2012) 16030–16037. doi:10.1021/jp3027463.

[45] E. Delamarche, Patterned Delivery of Immunoglobulins to Surfaces Using Microfluidic Networks, Science (80-.). 276 (1997) 779–781. doi:10.1126/science.276.5313.779.

[46] X. Chen, R. Ferrigno, J. Yang, G.M. Whitesides, Redox properties of cytochrome c adsorbed on self-assembled monlayers: a probe for protein confrmation and orientation, Langmuir. 18 (2002) 7009–7015.

[47] L. Holm, C. Sander, An evolutionary treasure: unification of a broad set of amidohydrolases related to urease, Proteins Struct. Funct. Genet. 28 (1997) 72–82. doi:10.1002/(SICI)1097-0134(199705)28:1<72::AID-PROT7>3.0.CO;2-L.

[48] I. Konieczna, P. Zarnowiec, M. Kwinkowski, B. Kolesinska, J. Fraczyk, Z. Kaminski, W. Kaca, Bacterial Urease and its Role in Long-Lasting Human Diseases, Curr. Protein Pept. Sci. 13 (2012) 789–806. doi:10.2174/138920312804871094.

[49] P.A. Karplus, M.A. Pearson, R.P. Hausinger, 70 Years of Crystalline Urease: What Have We Learned?, Acc. Chem. Res. 30 (1997) 330–337. doi:10.1021/ar960022j.

[50] B. Sahoo, S.K. Sahu, P. Pramanik, A novel method for the immobilization of urease on phosphonate grafted iron oxide nanoparticle, J. Mol. Catal. B Enzym. 69 (2011) 95–102. doi:10.1016/j.molcatb.2011.01.001.

[51] S. Kumar, A. Dwevedi, A.M. Kayastha, Immobilization of soybean (Glycine max) urease on alginate and chitosan beads showing improved stability: Analytical applications, J. Mol. Catal. B Enzym. 58 (2009) 138–145. doi:10.1016/j.molcatb.2008.12.006.

[52] A. Maaref, H. Barhoumi, M. Rammah, C. Martelet, N. Jaffrezic-Renault, C. Mousty, S. Cosnier, Comparative study between organic and inorganic entrapment matrices for urease biosensor development, Sensors Actuators B Chem. 123 (2007) 671–679. doi:10.1016/j.snb.2006.10.010.

[53] C. Selvamurugan, A. Lavanya, B. Sivasankar, A comparative study on immobilization of

urease on different matrices, J Sci Ind Res. 66 (2007) 655–659. http://hdl.handle.net/123456789/1299.

[54] J.D. Brennan, K.M.R. Kallury, U.J. Krull, Transduction of the reaction between urea and covalently immobilized urease by fluorescent amphiphilic membranes, Thin Solid Films. 244 (1994) 898–904. doi:10.1016/0040-6090(94)90596-7.

[55] R. Wilson, A.P.F. Turner, Glucose oxidase: an ideal enzyme, Biosens. Bioelectron. 7 (1992) 165–185. doi:10.1016/0956-5663(92)87013-F.

[56] L. Pollegioni, G. Wels, M.S. Pilone, S. Ghisla, Kinetic mechanisms of cholesterol oxidase from Streptomyces hygroscopicus and Brevibacterium sterolicum, Eur. J. Biochem. 264 (1999) 140–151. doi:10.1046/j.1432-1327.1999.00586.x.

[57] M. Prongjit, J. Sucharitakul, T. Wongnate, D. Haltrich, P. Chaiyen, Kinetic mechanism of pyranose 2-oxidase from Trametes multicolor, Biochemistry. 48 (2009) 4170–4180. doi:10.1021/bi802331r.

[58] M.P. Silva, L. Mira, J. Lima, C.F. Manso, Kinetics of the inhibition of xanthine dehydrogenase and of the reversible and irreversible forms of xanthine oxidase by silibinin and bendazac, Environ. Toxicol. Pharmacol. 1 (1996) 279–284. doi:10.1016/1382-6689(96)00021-X.

[59] K. De Wael, Q. Bashir, S. Van Vlierberghe, P. Dubruel, H. a Heering, A. Adriaens, Electrochemical determination of hydrogen peroxide with cytochrome c peroxidase and horse heart cytochrome c entrapped in a gelatin hydrogel., Bioelectrochemistry. 83 (2012) 15–8. doi:10.1016/j.bioelechem.2011.07.001.

[60] K.J. Huang, D.J. Niu, X. Liu, Z.W. Wu, Y. Fan, Y.F. Chang, Y.Y. Wu, Direct electrochemistry of catalase at amine-functionalized graphene/gold nanoparticles composite film for hydrogen peroxide sensor, Electrochim. Acta. 56 (2011) 2947–2953. doi:10.1016/j.electacta.2010.12.094.

[61] T. Poux, A. Bonnefont, A. Ryabova, G. Kéranguéven, G.A. Tsirlina, E.R. Savinova, Electrocatalysis of hydrogen peroxide reactions on perovskite oxides: experiment versus kinetic modeling, Phys. Chem. Chem. Phys. 16 (2014) 13595–13600.

doi:10.1039/C4CP00341A.

[62] K.L. Stewart, A.A. Gewirth, Mechanism of electrochemical reduction of hydrogen peroxide on copper in acidic sulfate solutions, Langmuir. 23 (2007) 9911–9918. doi:10.1021/la7013557.

[63] X. Cai, B. Ogorevc, G. Tavčar, J. Wang, Indium–tin oxide film electrode as catalytic amperometric sensor for hydrogen peroxide, Analyst. 120 (1995) 2579–2583. doi:10.1039/AN9952002579.

[64] G.R.K. Reddy, M. Hyder, P.S. Kumar, Facile Preparation of High-Performance Copper Oxide Sensors for Electroanalysis of Hydrogen Peroxide, Mater. Today Proc. 4 (2017) 12457–12469. doi:10.1016/j.matpr.2017.10.016.

Chapter 3

Adsorption kinetics and electron transfer reactions on self-assembled monolayers (SAMs) of long chain alkylphosphonic acids, silanes, and carboxylic acids on Indium Tin Oxide (ITO) surface

3.1. Introduction:

Electron transfer behavior at the electrode/solution interface can be controlled by chemically modifying the electrode surface. For example, organic thiol molecules can be used for modifying the noble metal surfaces due to their high affinity towards them. Thiol-modified surfaces have been extensively studied for the application towards bio-sensors, molecular electronics, micro arrays, *etc* [1–5]. Recently, there have been several reports of using cheaper alternatives to gold as a substrate for similar applications [6–8]. For example, transparent conducting oxides (TCOs) show excellent affinity towards phosphonic acids (PAs), silanes, and carboxylic acids (CAs). They form monolayers which adsorb onto surface through bidentate binding [9–11]. It was reported that, thiols can be removed by putting a load of 80nN on the modified surface, whereas to remove the monolayers on oxide substrates a larger force of 400nN was required [12]. This shows that the monolayers formed on ITO surfaces are strongly bound and quite stable.

Jo *et al.* [13] studied the formation kinetics and electrochemical behavior of phosphonic acids of three different alkyl chain lengths by using CV and EIS, with $[Fe(CN)_6]^{3-/4-}$ as a redox probe and suggested that blocking behavior of PA monolayer increases with increasing its chain length. Binding behavior of siloxane and phosphonate monolayers were compared by using dynamic contact angle experiments on Ti alloy [14]. Gardner *et al.* studied the coverage of the phosphonic acid and carboxylic acid monolayers onto indium tin oxide substrates and found that phosphonic acid covers the substrate four times more compared to its counterpart [15]. Xiao *et al.* studied the frictional properties of alkylsilanes of various chain lengths on mica substrate [16]. Felhősi *et al.*

studied the formation kinetics of alkyl phosphonic acids on mica [17] substrate and oxides of iron using AFM technique [18]. Lim *et al.* fabricated In_2O_3 nanowires by modifying with ODPA to improve the quality of the nanowire transistors [19]. Okahata *et al.* studied the electron transfer reactions on silane modified SnO_2 electrode [20].

Several surface sensitive experimental techniques like infrared spectroscopy (IR), surface plasmon resonance (SPR), quartz crystal microbalance (QCM), ellipsometry, second harmonic generation (SHG), atomic force microscopy (AFM), electrochemical impedance spectroscopy (EIS), and cyclic voltammetry (CV) have been used for following the *in situ* adsorption behavior of self-assembled monolayers [21–28].

There have been several reports on the modification of work function of ITO surface by using phosphonic acid SAMs. Paniagua *et al.* and wood *et al.* studied the work function changes of ITO on modifying it with fluorine substituted benzyl phosphonic acids [11,29]. Li *et al.* described a systematic study of PA/ITO interface by considering a variety of binding sites and coverage densities which provides a very good insight into the modification of ITO by PA molecules [30]. It was also reported that crystalline structure of ITO plays an important role in defining the order of the monolayer [31,32].

Till now, there are no reports on electrochemical studies of the monolayers formed by PAs, silanes, and CAs on ITO in terms of their electron transfer kinetics to understand their blocking behavior using different redox species. There is also no reference to any comparative study of the three different monolayers in terms of their wetting behavior, adsorption kinetics, and electron transfer blocking properties. In this work, we report the results of our study using different redox probes on the monolayers formed by PAs, silanes, and CAs on ITO surface. Such a study is important from the point of view of applications ranging from bio-sensors to organic electronics.

The electrochemical behavior of modified ITO electrode is studied by using cyclic voltammetry (CV) and electrochemical impedance spectroscopy (EIS). Morphological properties of the modified ITO were characterized by using atomic force microscopy (AFM). Compactness of the monolayers was studied using contact angle (CA) experiments. By using CV and EIS, the blocking behavior of monolayers was studied towards ferro/ferricyanide redox couple on modified electrodes.

3.2. Experimental Section:

3.2.1. Chemicals:

All chemicals used in this study were analytical grade (AR) reagents hexadecylphosphonic acid (97% purity, Aldrich), octadecylphosphonic acid (97% purity, Aldrich), hexadecyltrimethoxysilane (85% purity technical grade, Aldrich), octadecyltrimethoxysilane (90% purity technical grade), palmitic acid (99% purity, Aldrich), and stearic acid (95% purity reagent grade Aldrich). Solvents used are toluene (AR grade, SDFCL), hexane (AR grade, SDFCL), and ethanol (absolute for analysis, Merck chemical). Hydrogen peroxide (30% pure, SDFCL), ammonia solution (25% AR Grade, SDFCL chemicals limited), were used in our study as received. Millipore water having a resistivity of 18MΩcm was used to prepare all aqueous solutions employed in this work. ITO coated glass plates were purchased from Xin Yan Technology Ltd. This plate (355mm X 406mm X 1.1mm) is a single side polished, SiO_2 passivated float glass coated with ITO film. For electrochemical studies, this large plate was cut into small pieces of pre-defined geometric area and was used as strips.

3.2.2. Fabrication of electrodes and electrochemical cell:

An electrochemical cell with a conventional three electrode configuration was used for the adsorption and electrochemical study. A platinum foil (Pt) and a saturated calomel electrode (SCE) were utilized as counter and reference electrodes respectively. The pre-treated ITO and modified ITO substrates were used as working electrodes for studying the kinetics of adsorption of molecules under study and their electron transfer behavior. Initially, ITO pieces were cleaned ultrasonically using acetone, ethanol and Millipore water for 15 minutes each. These were then removed and immersed in aqueous solution consisting of hydrogen peroxide, liquid ammonia and water in the ratio of 1:3:10 about an hour. Later, these strips washed thoroughly with Millipore water and immediately used for analysis. This method is known to produce well covered hydroxyl functionalization on the surface. The specimen was held by an electrode holder with a well-defined area exposed to the electrolyte with the remaining portions well insulated by covering with parafilm and Teflon.

3.2.3. SAM preparation:

Monolayers were prepared by immersing the pre-treated ITO substrates in 10mM solutions of HDPA, ODPA, HDTMS, ODTMS, PTA, and STA of ethanol, hexane, toluene, and neat adsorbate (except for phosphonic acids) for 12 hours. Later the SAM modified ITO electrodes were taken out, sonicated in respective solvents to remove any traces of loosely attached adsorbates. Further, these modified ITO strips (except PA/ITO and SA/ITO) were dried in an oven at 80°C for an hour and allowed to cool to room temperature for few hours and used for electrochemical and morphological characterizations.

3.2.4. Instrumentation:

Adsorption kinetics experiments were conducted using EG&G PAR potentiostat connected to SRS Model SR830 DSP lock-in amplifier. The whole set up is connected to the computer through NI-GPIB card. The program for monitoring the impedance changes with time was written using LabVIEW 2012 software and sampled at a rate of 1s per data point.

The contact angle (VCA Optima XE) measurements were carried out using different volumes of water. The values presented here are for an optimized volume of 5µl. The morphology of the bare ITO and modified ITO substrates were imaged using AFM (Molecular Imaging). Cyclic voltammetric experiments were conducted using EG&G PAR potentiostat. Electrochemical impedance spectroscopy (EIS) studies were carried out using an EG&G potentiostat (Model 263A) interfaced to a model 5210 lock-in-amplifier and controlled using PowerSine software and computer.

Measurement of initial capacitance at time $t = 0$ is similar to our earlier work on the kinetics of adsorption of alkanethiols on gold surfaces and formation of PAs onto ITO [26,33]. First, bare ITO of 10mm^2 area was dipped in 0.1M TBATFB solution and allowed to attain a constant impedance value which normally takes about 10 minutes. The change in capacitance observed in absence of adsorbate was negligible compared to the capacitance changes observed in the presence of adsorbate. The procedure adopted for measurement of capacitance during adsorption of PAs, CAs, and silane species is as mentioned above. The ITO electrode is dipped in the specific SAM solution of a given concentration in 0.1M TBATFB and the capacitance is followed as a function of time

(t) till the value reaches a plateau or the change in the value of capacitance (C_f) with time is at a minimum.

3.3. Results and discussion:

Indium tin oxide (ITO) electrode is modified with two homologues of longer alkyl chain phosphonic, silanes, and carboxylic acids of similar chain lengths. Adsorption kinetics studies were conducted by using impedance spectroscopy at constant frequency. The electrochemical behavior of modified ITO is studied using negatively charged redox couple *i.e.* potassium ferro/ferricyanide redox species. The blocking behavior of corresponding monolayers were studied using cyclic voltammetry (CV) and electrochemical impedance spectroscopy (EIS).

3.3.1. Contact Angle measurements:

Surface wettability of the bare ITO and SAM modified ITO electrodes were analyzed using contact angle measurements. A static sessile drop method was employed for the measurement of contact angle and the values reported were the maximum value of contact angles measured at three different locations of the sample. The equilibrium water contact angle of bare ITO (before modification) exhibits a strong dependence on the pre-treatment method adapted for cleaning the surface. As received ITO surface provides a contact angle of $80 \pm 1°$, which reflects a higher degree of hydrophobic nature of the substrate and upon pre-treatment by the method explained in the material and methods, contact angle was found to decrease to $48 \pm 2°$ implying a hydrophilic nature. This change indicates a significant increase in the composition of hydroxyl groups on ITO surface as a result of pre-treatment method. The contact angle values obtained for bare ITO show some deviation from the earlier reported values [28,34–36]. This change in contact angle can be attributed to the adsorption of atmospheric carbon dioxide onto the pre-treated ITO surface which makes the surface hydrophobic [37]. After the formation of monolayers, contact angle values found to increase significantly depending on the molecular structure of SAM formation on ITO electrodes. Static water contact angles on ODPA/ITO, ODTMS/ITO, and STA/ITO are measured to be $95.2 \pm 0.1°$, $104.5 \pm 0.1°$, and $93.9 \pm 0.1°$ respectively. ODTMS monolayer exhibits a higher contact angle value compared to all the other SAMs due to the formation of a compact monolayer with a methyl group termination as in the case of SAMs of alkanethiols on gold surface. ODPA/ITO and STA/ITO also show a relatively higher contact angle due to the presence of

terminal methyl group implying the formation of an ordered hydrophobic SAM. The difference mainly arises from the order of the monolayers. Based on our results, it can be considered that SAM formation using PAs, silanes, and CAs on ITO electrodes and their surface wettability can be strongly influenced by their molecular structure.

3.3.2. Morphological analysis using phase imaging AFM:

Morphological characterization of the bare ITO and modified ITO surfaces were carried out by using phase imaging mode in atomic force microscopy. Figure 1 shows the phase images of (A) bare ITO, (B) ODPA/ITO, (C) ODTMS/ITO, and (D) STA/ITO surfaces. Figure 1A shows that, ITO surface features are in the form of grains with distinct boundaries in between individual grains. Figure 1B shows that ODPA/ITO morphology in the form of thread shaped bundles arranged compactly in a unidirectional order with very few voids on the surface. Figure 1C shows the surface of ODTMS/ITO being covered in the form of layers almost following the crystalline arrangement of ITO. STA/ITO surface (Figure 1D) morphology shows that the molecules of stearic acid adsorb in the form of randomly oriented aggregates with numerous voids within the monolayer. The phase AFM images support the results of electrochemical studies which show that PA monolayers possess the most compact and the least permeable surface morphology, while carboxylic acids form very poor film on ITO. The monolayers formed by silanes are quite compact and better than carboxylic acid monolayers in terms of surface coverage and compact morphologies, which is also reflected in good electron transfer blocking property of these films.

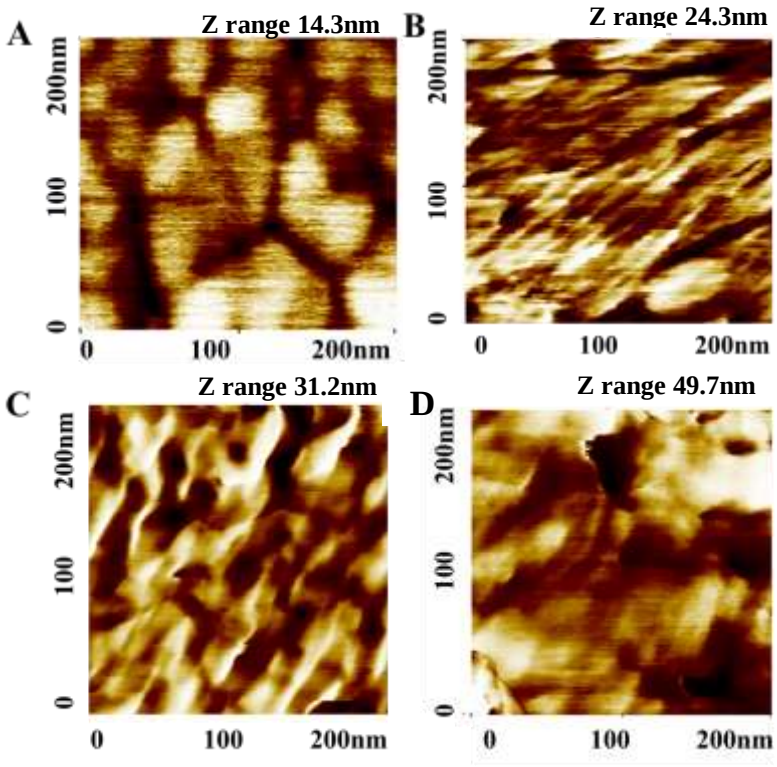

Figure 1. *Phase images of (a) Bare ITO, (b) ODPA/ITO, (c) ODTMS/ITO, and (d) STA/ITO surfaces prepared from ethanol solvent.*

3.3.3. Adsorption kinetics studies:

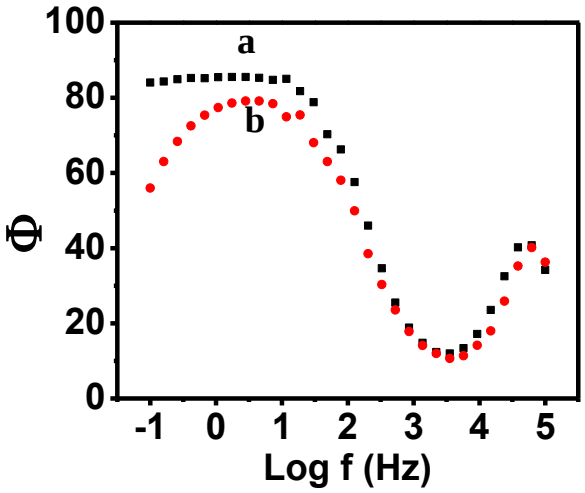

Figure 2. *Phase angle (Φ) vs. log f Bode phase plot of ITO in (a). 0.1M TBATFB electrolyte and (b). 0.01M ODPA + 0.1M TBATFB solution respectively.*

Figure 2 shows the phase angle (Φ) vs. logarithm of frequency (f) plot for bare ITO in (a) 0.1M TBATFB and (b) 0.01M ODPA + 0.1M TBATFB solution in ethanol using Ag/Ag^+ ion reference electrode. At higher frequencies, the phase angle behavior of ITO gives similar response on the application of applied 10mV AC voltage. However, at lower frequencies starting from 10Hz to 100mHz there is a significant deviation as seen in figure 2. The adsorption kinetics experiments were carried out at 10Hz by keeping the working electrode potential constant at open circuit potential *i.e.,* -0.365V vs. Ag/Ag^+ ion reference electrode during the entire experiment. This ensures that the choice of frequency is valid for all the monolayers.

Figure 3 shows the capacitance (C) vs. time (t) plots for 0.01M HDPA, ODPA, HDTMS, ODTMS, PTA, and STA respectively in 0.1M TBATFB supporting electrolyte dissolved in ethanol. The capacitance values are normalized to $1cm^2$ area of the electrode, since the ITO surface is not atomically smooth and the roughness factor of the electrode was not considered for the area correction. The initial capacitance values differ from each experiment depending upon the hydroxyl density on ITO surface [31]. Thus, we followed a similar procedure for pre-treatment of ITO surface in all monolayer cases to produce similar hydroxyl density. Electrochemical experiments were carried out using $10mm^2$ ITO strips and the capacitance values were normalized to $1cm^2$ area. The initial capacitance value obtained for each adsorbate on an average is around $12\pm1\mu F/cm^2$. From figure 3, it is shown that adsorption reaches its maximum coverage within an hour for all the monolayer cases.

There are some reports on the adsorption kinetics studies of monolayers onto hydroxyl functionalized ITO surfaces. They have mostly studied the kinetics in the time scale of hours and days [13,33,38]. Whereas in this work, the adsorption kinetics studies have been carried out at shorter intervals as it provides critical information on the initial stages of adsorption. It will be shown here, that adsorption of these monolayers takes place in two distinct kinetic steps. The first kinetic step of SAM formation represents, (i) the spontaneous growth of low-density lying down phase where the molecular axes of the adsorbed molecules are parallel to the substrate, and (ii) the transition from lying down phase to the dense standing-up phase where the molecular axes tilt is ~30-45° in the case of phosphonic acids and silanes while in the case of carboxylic acid monolayers, the molecular tilt is around ~15-25° from the surface normal [39–41]. The second

step, advances *via* the interaction of neighboring molecules in order to form a new island nucleus or incorporation of a molecule at the boundary of an already formed island.

The development of PAs, silanes, and CAs of n = 16, 18 alkyl chain lengths on ITO surfaces from ethanol solutions in 0.1M TBATFB supporting electrolyte were studied over a period of 1 hour. In figure 4, the coverage vs. time curves for adsorption of 10mM concentrated solution of HDPA, ODPA, HDTMS, ODTMS, PTA, and STA are presented. A fast first kinetic step that lasts for about 600s and a second much slower step that leads to a maximum coverage. In the first step, 80% of the maximum coverage is reached for C_{16} monolayer, while in the case of C_{18} monolayer, 60% of the maximum coverage is attained during this period. The monolayer coverage is the fraction of the surface adsorbed with the monolayer film. It can be calculated using the expression [26,42]:

$$\theta = (C_0 - C_t)/(C_0 - C_f) \qquad (1)$$

where C_0 is the bare ITO electrode capacitance, C_t is the capacitance of the electrode at any time t, and C_f is the capacitance of the maximum coverage of the monolayer.

The kinetics of the adsorption is fitted with two models, diffusion Langmuir adsorption (DL) and Langmuir adsorption. The DL model involves the diffusion of the molecule towards the favorable site for surface anchoring and subsequent growth of the lying-down phase while the organization of the standing up phase explains the Langmuir adsorption kinetics. Table 1 show the rate constant of adsorption for the HDPA, ODPA, HDTMS, ODTMS, PTA, and STA monolayers. The rate constant of C_{16} monolayer is larger compared to its C_{18} homologues. From Table 1, it can be seen that the formation rate constant decreases with increase in the chain length of the adsorbate molecule which can be assumed from the solubility of the adsorbate in ethanol solvent with increase in its chain length.

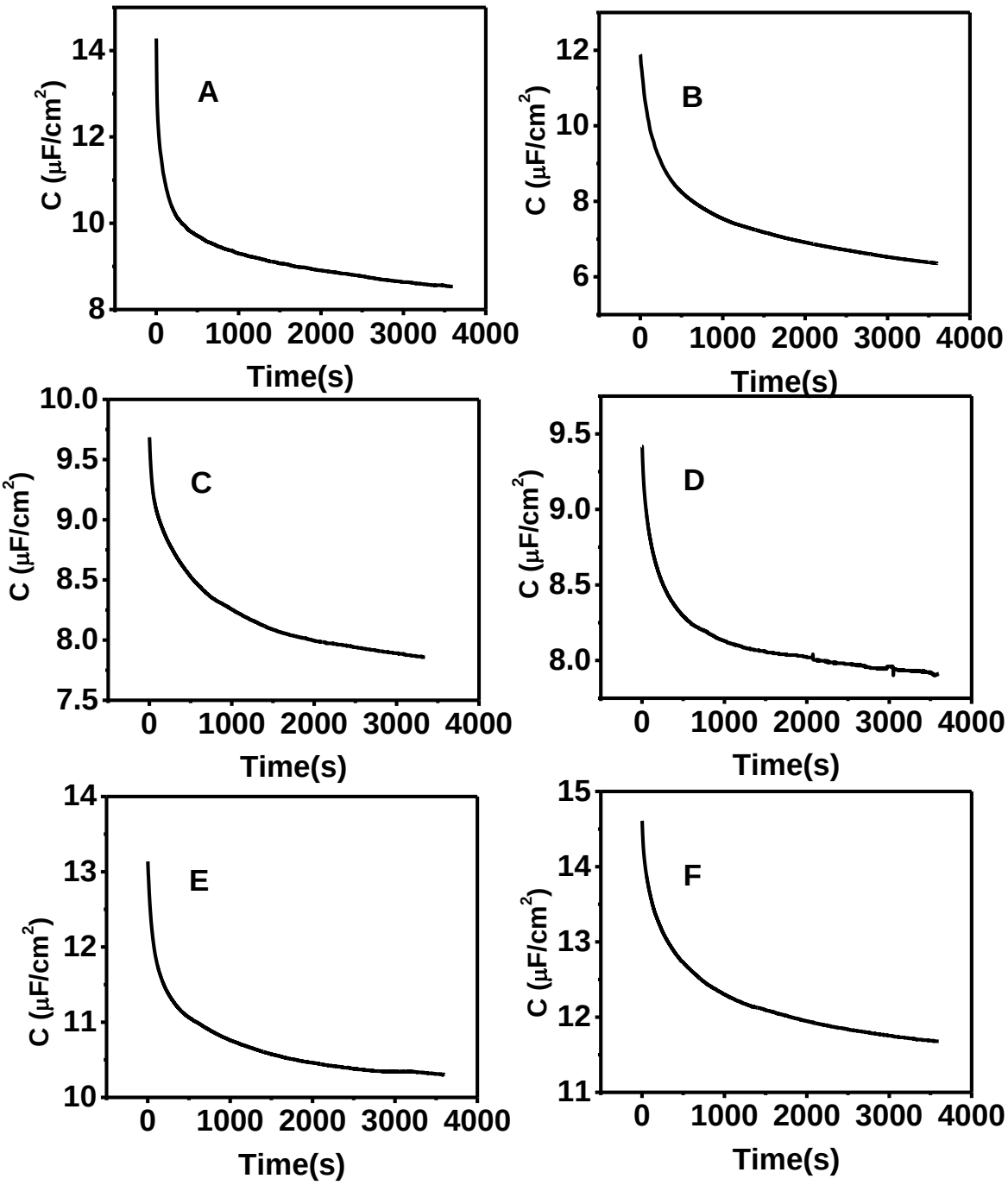

Figure 3. *Capacitance (C) vs. time (t) curves for 0.01M (A) HDPA, (B) ODPA, (C) HDTMS, (D) ODTMS, (E) PTA and (F) STA respectively in ethanol using 0.1M TBATFB as supporting electrolyte.*

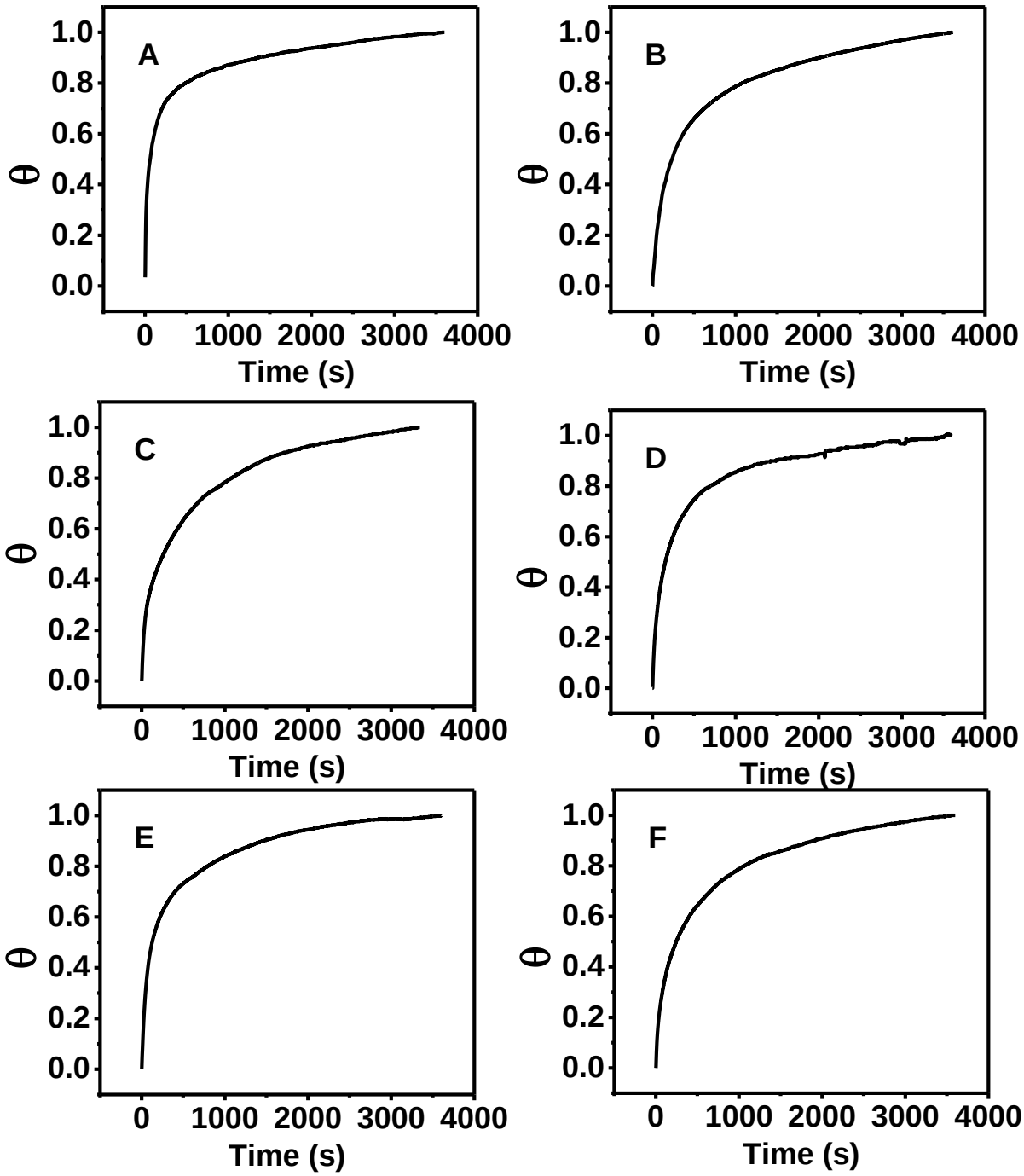

Figure 4. *Coverage (θ) vs. time (t) curves for (A) HDPA, (B) ODPA, (C) HDTMS, (D) ODTMS, (E) PTA and (F) STA respectively in ethanol using 0.1M TBATFB as supporting electrolyte.*

Table 1. Concentration dependent rate constants for adsorption of PAs, silanes and CAs in ethanol solvent.

Substrate	K_{c1} (M^{-1} $s^{-1/2}$)	K_{c2} (M^{-1} s^{-1})
HDPA	3.83	2.91
ODPA	1.85	0.53
HDTMS	4.68	0.09
ODTMS	0.16	0.67
PTA	3.95	0.48
STA	0.11	0.48

3.3.4. Electron transfer studies:

3.3.4.1. Bare ITO:

Figure 5 represents the (A) cyclic voltammogram and (B) Nyquist plot at half peak potential of the $[Fe(CN)_6]^{3-/4-}$ (1mM) redox couple using 0.1M NaF supporting electrolyte on bare ITO. From figure 5A, the CV of the redox couple on bare ITO shows quasi-reversible electron transfer behavior with a peak separation of 100mV. The Nyquist plot of the redox couple in figure 5B shows a small semi-circle at high frequencies which is followed by a straight line at lower frequencies suggesting that electron transfer is controlled by diffusion of redox species in the solution. The charge transfer resistance (R_{ct}) value for the electron transfer reaction of ferro/ferricyanide redox couple on bare ITO is measured to be 5.1Ωcm^2 obtained by fitting the impedance data with Randles equivalent circuit.

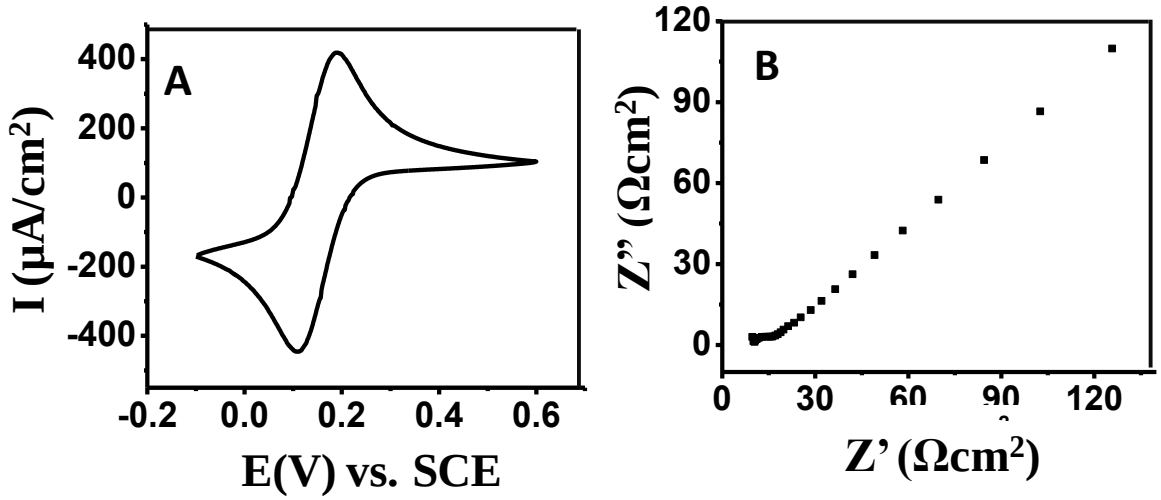

Figure 5*. (A) CV and (B) EIS plots of 1mM $[Fe(CN)_6]^{3-/4-}$ redox couple using 0.1M NaF as supporting electrolyte on bare ITO electrode.*

3.3.4.2. Phosphonic acid modified ITO:

From the CVs shown in figure 6 (A-D), it is seen that HDPA/ITO monolayer exhibits an irreversible electron transfer behavior in all the solvents under study but to a varying extent in each case. The ODPA/ITO (figure 6 (E-H)) electrodes show S-shaped sigmoidal cyclic voltammograms corresponding to a microelectrode array type of behavior. This shows that PAs adsorb quite well onto the ITO surface. Phosphonic acid monolayers prepared from ethanol solvent show better blocking behavior compared to the monolayers prepared from water, toluene, and hexane solvents. The reason behind such a behavior can be attributed to the hydrophilic nature of $-PO_3H_2$ head group which is solvated very well by polar solvent like ethanol. This makes the phosphonic acid molecules to be well separated by solvation sheath around the polar functional group leaving a significant space for adsorption of individual PA molecules onto ITO surface. On the other hand, the solvents like water, hexane, and toluene show low solubility for PAs. In these solvents, during adsorption process there can be a competition between individual PA molecules and its aggregates, which cause several defects in the monolayer when the substrate is rinsed or sonicated to remove loosely attached particles.

Figure 7 show Nyquist plots of 1mM ferro/ferricyanide redox couple on HDPA/ITO and ODPA/ITO electrode prepared in (A,E) ethanol, (B,F) water, (C,G) toluene, and (D,H) hexane

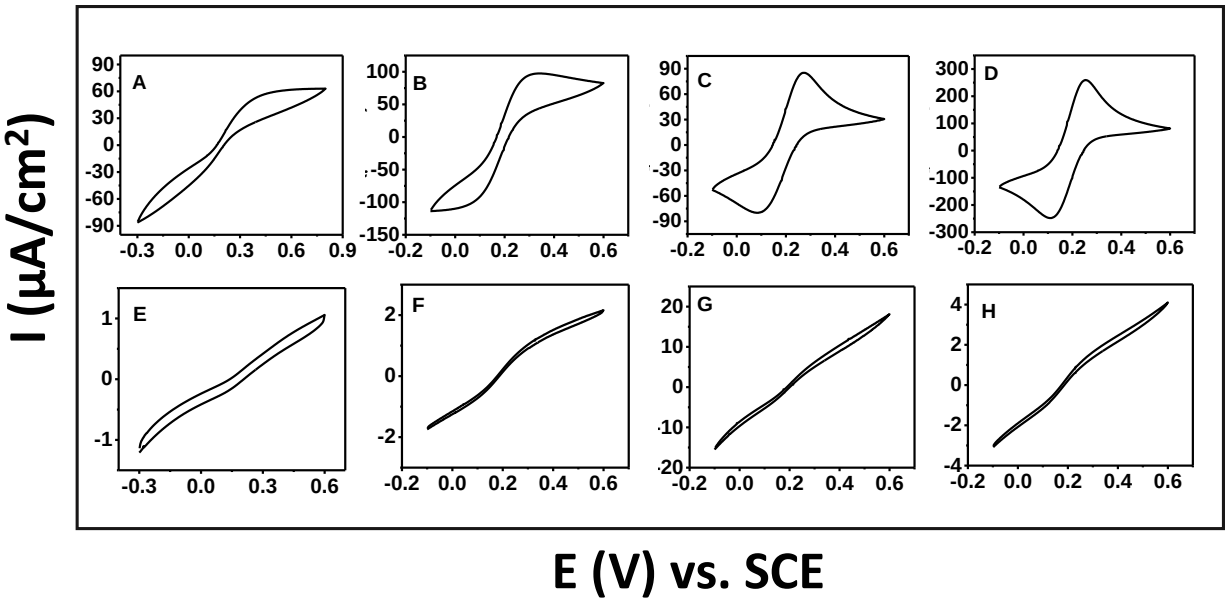

Figure 6. *CVs of HDPA/ITO electrode prepared from (A) ethanol, (B) water (C) toluene and (D) hexane and ODPA/ITO from (E) ethanol, (F) water, (G) toluene and (H) hexane in 1mM $K_{3/4}[Fe(CN)_6]$ using 0.1M NaF supporting electrolyte.*

solvents. The Nyquist plots show a semi-circle behavior in the case of HDPA/ITO prepared in ethanol, whereas HDPA/ITO monolayer prepared from water, toluene, and hexane solvents show a semi-circle followed by a straight line at lower frequencies. ODPA/ITO monolayer prepared from water, toluene, and hexane solvents, a semi-circle is seen in the entire frequency range of Nyqusit plot suggesting that the charge transfer controlled electron transfer at the ODPA/ITO solution interface. From EIS results, it is evident that ODPA/ITO monolayer shows excellent blocking behavior for ferro/ferricyanide redox couple. The impedance data obtained for $[Fe(CN)_6]^{3-/4-}$ redox couple shown in figure 7 were studied using equivalent circuit analysis. The measured impedance values were fitted by using a standard Randles equivalent circuit consisting of a double layer capacitance (C_{dl}) connected in parallel with the charge transfer resistance (R_{ct}) and together in series with solution resistance (R_u). The Warburg diffusion element (W) in equivalent circuit for ODPA/ITO was excluded in all the cases, since the electron transfer is completely blocked by the monolayer. The values were acquired using the above mentioned equivalent circuit fitting of the impedance data as shown in Table 2. The blocking behavior of ODPA/ITO electrode follows the order ethanol>water>toluene>hexane.

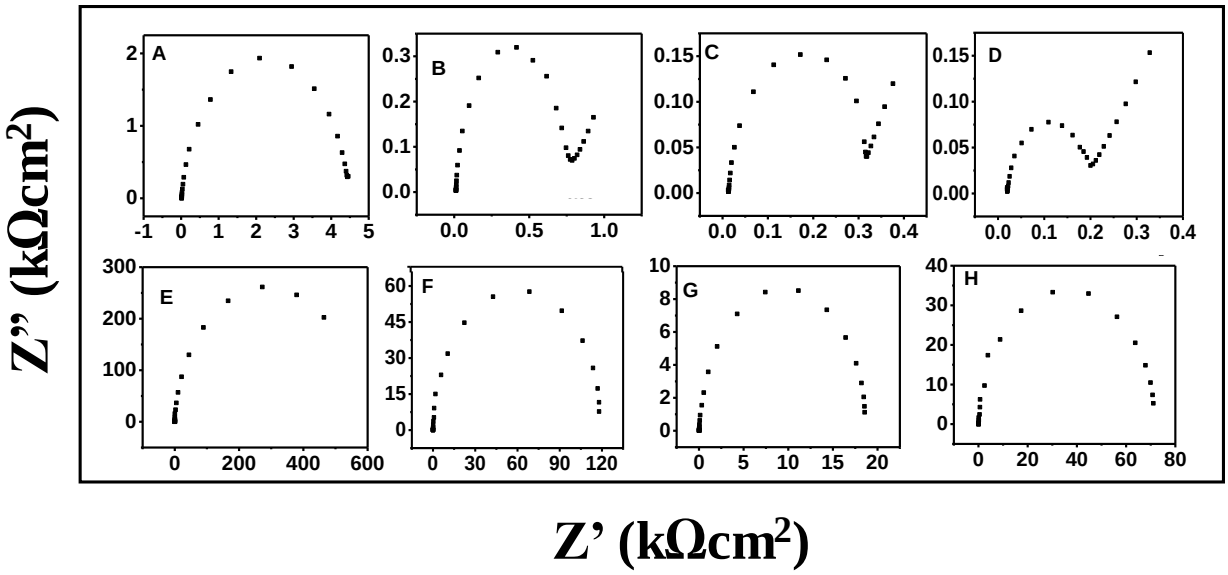

Figure 7. *(A-H) Nyquist plots of 1mM $[Fe(CN)_6]^{3-/4}$ using 0.1M NaF for HDPA/ITO electrode prepared from (A) ethanol, (B) water, (C) toluene, and (D) hexane and ODPA/ITO prepared in (E) ethanol, (F) water, (G) toluene, and (H) hexane.*

The equivalent circuit fitting done on HDPA monolayer prepared from ethanol shows a charge transfer resistance (R_{ct}) value of 4366Ωcm^2 with no diffusion component. The HDPA monolayer prepared in water, hexane, and toluene show R_{ct} values of 740, 169 and 285Ωcm^2 respectively. The results obtained here fits quite well with the Randles equivalent circuit where the double layer capacitance (C_{dl}) is replaced with constant phase element (Q). HDPA/ITO prepared from ethanol is however an exception. ODPA monolayer prepared from ethanol gives the highest R_{ct} value of around $5.5x10^5$ Ωcm^2 for the $[Fe(CN)_6]^{3-/4-}$ redox couple. The R_{ct} values for the redox couple on ODPA/ITO monolayer prepared from water, toluene, and hexane are $1.2x10^5$, $7.2x10^4$, and 4834Ωcm^2 respectively.

From the charge transfer resistance (R_{ct}) values, the surface coverage (θ) was calculated for the HDPA/ITO and ODPA/ITO monolayer surfaces using the following expression which assumes that the faradaic current is due to the presence of defects and pinholes within the monolayer through which the redox species can access the surface. The fractional surface coverage (θ) can be measured by the following expression:

$$\theta = 1 - (R_{ct} - R'_{ct}) \qquad (2)$$

where R_{ct}-charge transfer resistance for bare ITO electrode and R'_{ct}-charge transfer resistance of modified ITO electrode. The surface coverage values determined for the SAMs are above 97% in case of HDPA/ITO and around 99.9% for ODPA/ITO electrodes.

Table 2. Charge transfer resistance values measured for HDPA/ITO and ODPA/ITO electrodes for $[Fe(CN)_6]^{3-/4-}$ redox couple (R_{ct} of bare ITO =5.1Ωcm^2).

Substrate	R_{ct} (Ωcm^2)			
	Ethanol	Water	Toluene	Hexane
HDPA/ITO	4366.0	740.5	285.3	169.3
ODPA/ITO	$5.5x10^5$	$1.2x10^5$	$7.2x10^4$	$1.7x10^4$

Table 3 show the fractional surface coverage (θ) values of HDPA/ITO and ODPA/ITO substrates which is derived from the respective R_{ct} values. From the fractional surface coverage values, it can be concluded that HDPA monolayer prepared from ethanol shows the best coverage compared to that prepared in water, toluene, and hexane solvents. However, in the case of ODPA/ITO, the monolayers prepared in all the four solvents have very low defect density. The excellent surface coverage of HDPA/ITO and ODPA/ITO shows that they are comparable to alkanethiol monolayers on noble metal surfaces like gold.

Table 3. Surface coverage (θ) values determined using equation 2 for the HDPA/ITO and ODPA/ITO electrodes prepared from various solvents using $[Fe(CN)_6]^{3-/4-}$ redox probe.

Solvent	Θ	
	HDPA/ITO	ODPA/ITO
Ethanol	0.9988	0.9999
Water	0.9940	0.9999
Toluene	0.9820	0.9999
Hexane	0.9700	0.9992

3.3.4.2.1. Pore size analysis of the ODPA modified SAM:

From cyclic voltammetry and electrochemical impedance spectroscopy studies, it is inferred that the ODPA modified ITO electrode blocks the electron transfer completely. The sigmoidal curve obtained for CV in 1mM $[Fe(CN)_6]^{3-/4-}$ using 0.1M NaF supporting electrolyte (figures 6 (E-H)) suggests that ODPA/ITO electrodes show microelectrode array type of behavior towards electron transfer of redox species. By the use of electrochemical impedance spectroscopy, valuable information on the pinholes and defects in the monolayer can be obtained. A model of the monolayer/solution interface was developed by Finklea *et al.* for analyzing the impedance response of a perfectly blocking electrode [44]. Fawcett and co-workers used electrochemical impedance data for studying the integrity of the monolayer using the method of pore size analysis within the film [45–47]. In order to understand the faradaic electron transfer at the pinholes and defects of the monolayer and distribution of pinholes within the monolayer, a model was developed by Amatore and Matsuda. By assuming the total pinhole area fraction (1-θ), where θ is the fractional surface coverage of the monolayer, which is <0.1, impedance expressions have been derived. Both the real and imaginary parts of the faradaic impedance values are plotted as a function of $\omega^{-1/2}$ [48,49]. Diffusion profiles of the microelectrode constituents of monolayer are very well separated at higher frequencies, whereas these constituents overlap at lower frequencies. The presence of pinholes and defects are analyzed for ODPA monolayer on ITO using the above model. Figure 8 (A-E) show the real part of the faradaic impedance of bare ITO and ODPA/ITO systems prepared from various solvents plotted as a function of $\omega^{-1/2}$. Figure 9 (A-D) shows the plots of imaginary component of faradaic impedance for ODPA/ITO electrodes prepared from ethanol, water, hexane, and toluene. Bare ITO shows a single straight line for a large frequency range which corresponds to the diffusion controlled electron transfer behavior at the electrode surface. Whereas, in case of ODPA/ITO, the respective Z_f' vs. $\omega^{-1/2}$ plots show features similar to that of an array of microelectrodes [43,44]. Two linear domains were observed in the plot, one at high frequencies and another one at lower frequencies in Z_f' vs. $\omega^{-1/2}$ plot (figures 8 (B-E)) and a peak formation in the case of Z_f'' vs. $\omega^{-1/2}$ plot.

The surface coverage of the monolayer can be obtained from slope of the Z_f' vs. $\omega^{-1/2}$ plot at a higher frequency region and is given by,

$$m = \sigma + \sigma(1 - \theta) \qquad (3)$$

where m is the slope, θ is the fractional surface coverage of the monolayer, and σ is the Warburg component, which can be obtained from the bare ITO electrode.

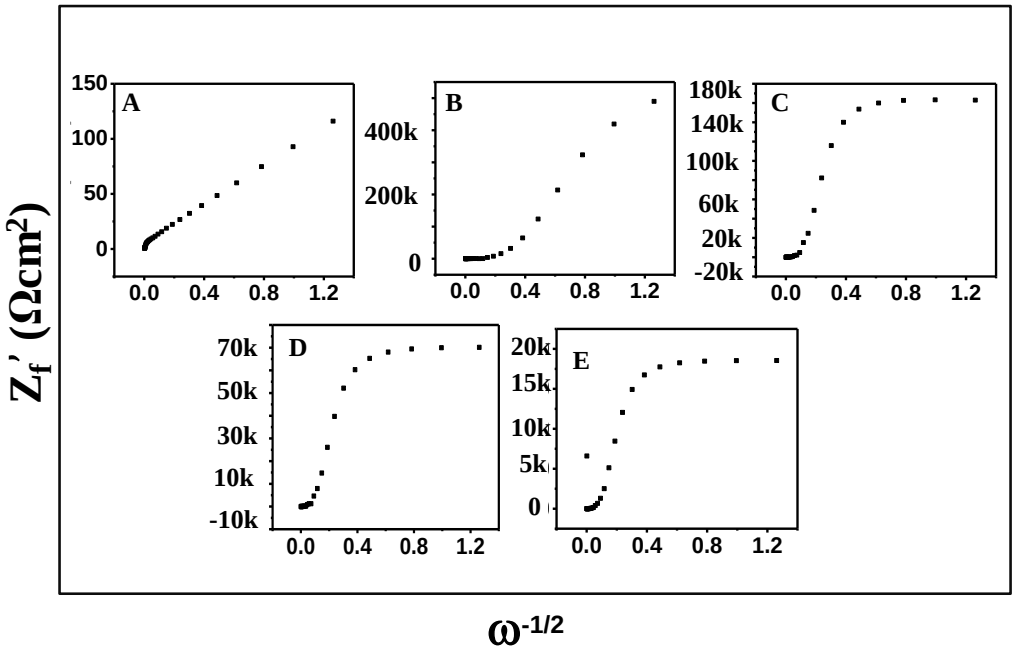

Figure 8. *Plots of real part of the faradaic impedance Z_f' vs. $\omega^{-1/2}$ for (a). Bare ITO and (b). ODPA/ITO electrode in 1mM $[Fe(CN)_6]^{3-/4-}$ using 0.1M NaF supporting electrolyte.*

From the analysis of figure 8 and equation 3, a surface coverage value of >95 % were calculated in case of ODPA/ITO electrode prepared from various solvents under study. It is also to be noted from the comparison of the data presented in Table 3 and Table 4, the method of pinhole analysis provides more precise values where the surface coverage values are related to the nature of the solvents used for monolayer formation. In this study ethanol and water being polar, it can effectively solvate the polar phosphonate head group and effectively facilitate binding with hydroxylated ITO surface.

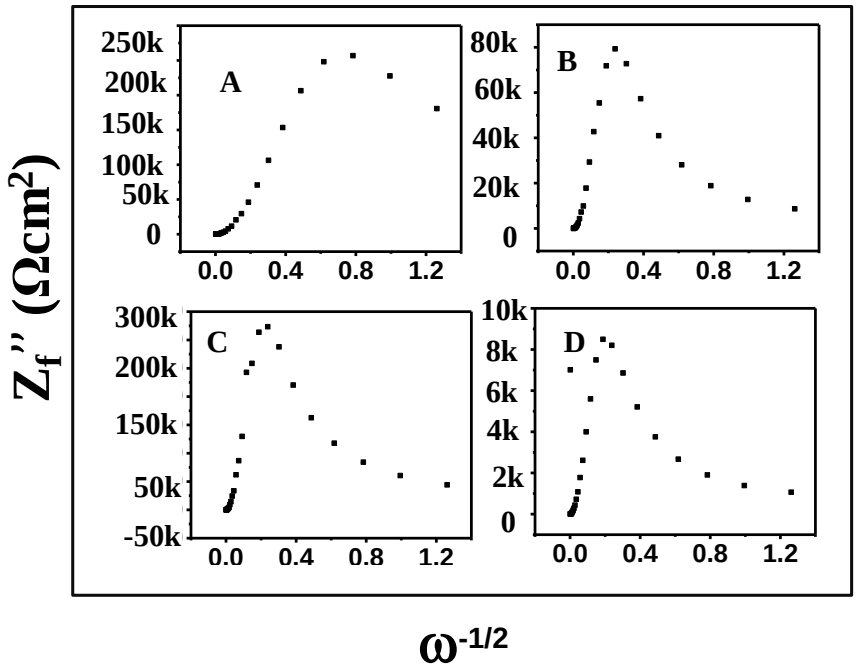

Figure 9. *Plots of imaginary part of impedance (Z_f'' vs. $\omega^{-1/2}$) of ODPA/ITO electrode prepared from various solvents in 1mM $[Fe(CN)_6]^{3-/4-}$ using 0.1M NaF supporting electrolyte.*

Table 4. Surface coverage (θ) values determined for ODPA/ITO electrodes, from the pinhole and defects analysis using impedance data obtained for $[Fe(CN)_6]^{3-/4-}$ redox couple as a probe molecule.

ODPA/ITO	θ
Ethanol	0.9971
Water	0.98650
Toluene	0.9220
Hexane	0.9530

3.3.4.3. Silane modified ITO:

Figure 10 (A-D) represent the cyclic voltammograms of 1mM $[Fe(CN)_6]^{3-/4-}$ redox couple using 0.1M NaF supporting electrolyte on HDTMS/ITO and ODTMS/ITO electrodes, prepared from (A,E) neat silane, (B,F) ethanol, (C,G) toluene, and (D,H) hexane. From the figure 10A, it can be seen that C_{16} silane shows slightly larger peak separation compared to its higher homologue of C_{18} chain. The CVs of HDTMS/ITO and ODTMS/ITO prepared from hexane solvent (figure 10 (D,H)) show high irreversibility with a peak separation of 258 and 500mV (Table 5) for $[Fe(CN)_6]^{3-/4-}$ redox couple which agrees very well agreed with the literature reports [13,34]. Silane monolayers prepared from neat silane, ethanol, and toluene solvents show quasi reversible electron transfer characteristics (figure 10 (B-D), (F-H)).

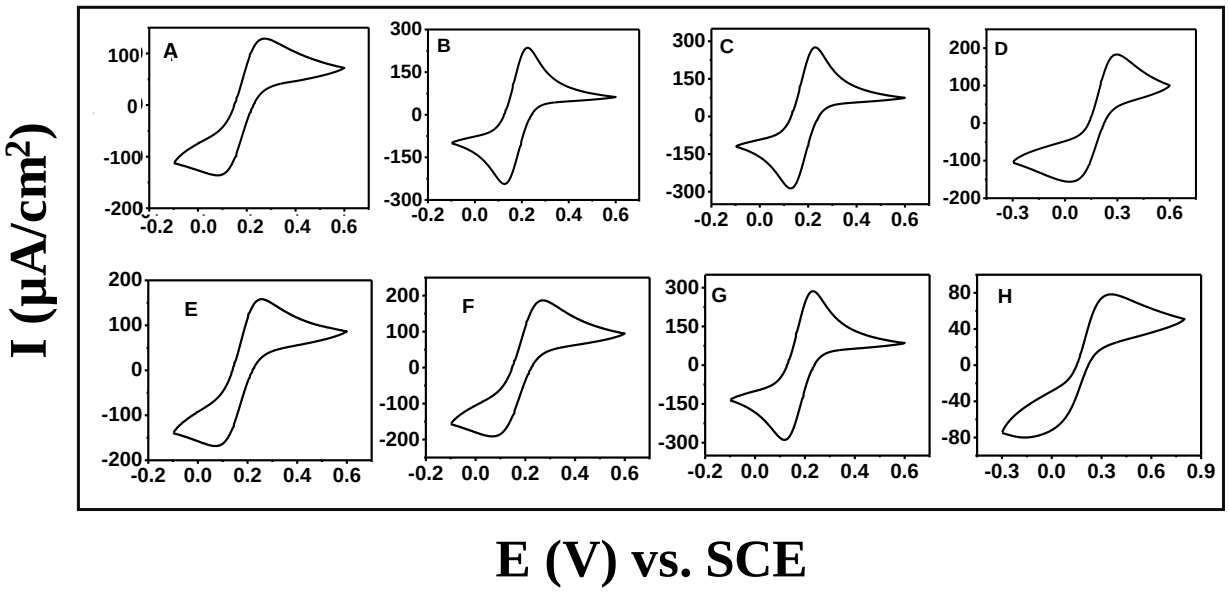

Figure 10. *Cyclic voltammograms of HDTMS/ITO electrode prepared from (A) neat HDTMS, (B) ethanol (C) toluene and (D) hexane and ODTMS/ITO electrode from (E) neat ODTMS, (F) ethanol, (G) toluene and (H) hexane in 1mM $K_{3/4}[Fe(CN)_6]$ using 0.1M NaF supporting electrolyte.*

Figure 11 shows the Nyquist plots of HDTMS/ITO and ODTMS/ITO electrodes prepared from (A,E). neat silane, (B,F). ethanol, (C,G). toluene, and (D,H). hexane solution in 1mM $[Fe(CN)_6]^{3-/4-}$ redox couple using 0.1M NaF supporting electrolyte. Nyquist plots of HDTMS/ITO

electrode show a slightly depressed semi-circle along with a straight line which suggests that electron transfer at the interface corresponds to a charge transfer behavior at high frequencies and is diffusion controlled at low frequencies. It can be seen from the Table 5 that the monolayer prepared from hexane shows higher R_{ct}, when compared to the monolayer prepared from neat silane, ethanol, and toluene solvents. Impedance behavior of the modified electrode is complementary to their cyclic voltammetric behavior. The data obtained were fitted with Randles equivalent circuit, in which the double layer capacitance is replaced by constant phase element to account for the deviation in the semi-circle behavior. HDTMS/ITO and ODTMS/ITO monolayers prepared in hexane show the highest blocking behavior. This may be explained by the fact that hexane molecules are loosely attached and not blocking the hydroxyl sites of ITO due to the non-polar nature of the solvent. Due to this reason the silane molecules from solution can easily replace the hexane molecules present on the surface during the chemisorption. In addition to this, hexane has very low miscibility in water which restricts the interaction of chemisorbed surface water molecules with the silane in solution and avoids homo-condensation polymerization.

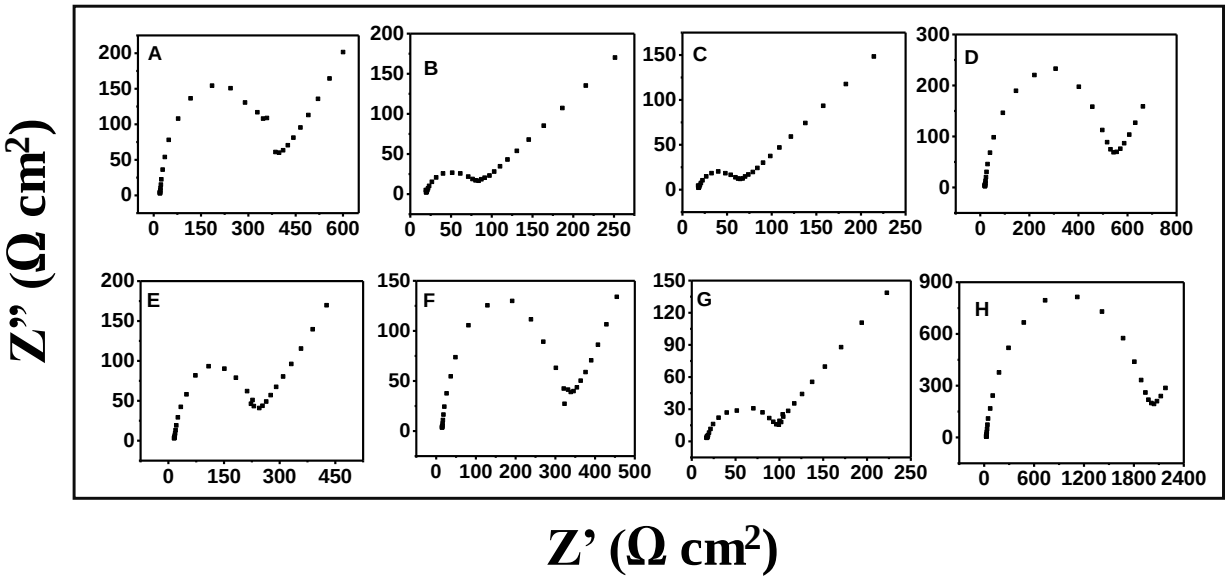

Figure 11. *Nyquist plots of HDTMS/ITO prepared from (A) Neat HDTMS, (B) ethanol, (C) toluene, and (D) hexane and ODTMS/ITO prepared from (E) Neat ODTMS, (F) ethanol, (G) toluene, and (H) hexane in 1mM* $[Fe(CN)_6]^{3-/4-}$ *in 0.1M NaF supporting electrolyte.*

Even though, toluene is a non-polar solvent, the silane film prepared in it shows very poor blocking behavior. This behavior can be explained due to the fact that, toluene shows partial miscibility with water. Due to this, during the process of adsorption, the chemisorbed water molecules after displacement from the surface diffuse in the solvent and react with the silane molecules resulting in the formation of silanols [50]. Since the silanols are very reactive, they undergo homo-condensation reaction and form oligomers inside the solution and adsorb onto the surface. The adsorbed oligomeric silanes contain defects which explain the poor electron transfer blocking behavior of silane monolayers prepared from toluene. The monolayers prepared from ethanol show intermediate blocking behavior in-between hexane and toluene.

Table 5 Peak separation and charge transfer resistance values measured from CV and EIS plots of HDTMS/ITO and ODTMS/ITO electrodes in $[Fe(CN)_6]^{3-/4-}$ redox couple (R_{ct} of bare ITO=5.1Ωcm^2).

Solvent	HDTMS/ITO		ODTMS/ITO	
	ΔE_p (mV)	R_{ct} (Ωcm^2)	ΔE_p (mV)	R_{ct} (Ωcm^2)
Neat	187.8	249.3	170.6	218.3
Ethanol	98.9	59.8	197.2	284.9
Toluene	103.2	44.5	111.8	64.7
Hexane	257.8	507.6	498.5	1931.0

3.3.4.4. Carboxylic acid modified ITO:

Palmitic acid (PTA) and stearic acid (STA) are saturated carboxylic acids with -COOH head group and exist in the form of solid flakes. Melting temperatures for PTA is 61-62°C whereas for STA it is 53-59°C. For modification of neat PTA and neat STA on ITO surface, the flakes of the carboxylic acids were heated on a hot plate by controlling the temperature at 75°C in both the cases.

Figure 12 represents the cyclic voltammetric behavior of PTA/ITO prepared in (A) neat PTA, (B) ethanol, (C) toluene, and (D) hexane and STA/ITO prepared from (E) Neat STA, (F) ethanol, (G) toluene, and (H) hexane in 1mM $[Fe(CN)_6]^{3-/4-}$ redox couple using 0.1M NaF as supporting electrolyte. Carboxylic acid modified ITO substrates show poor blocking behavior compared to the phosphonic acids and silanes of similar chain length. It can be seen that, there is a slight increase in the peak separation for the redox couple at STA/ITO prepared from its neat solution, comapared to its homologue prepared from neat PTA/ITO (Table 6).

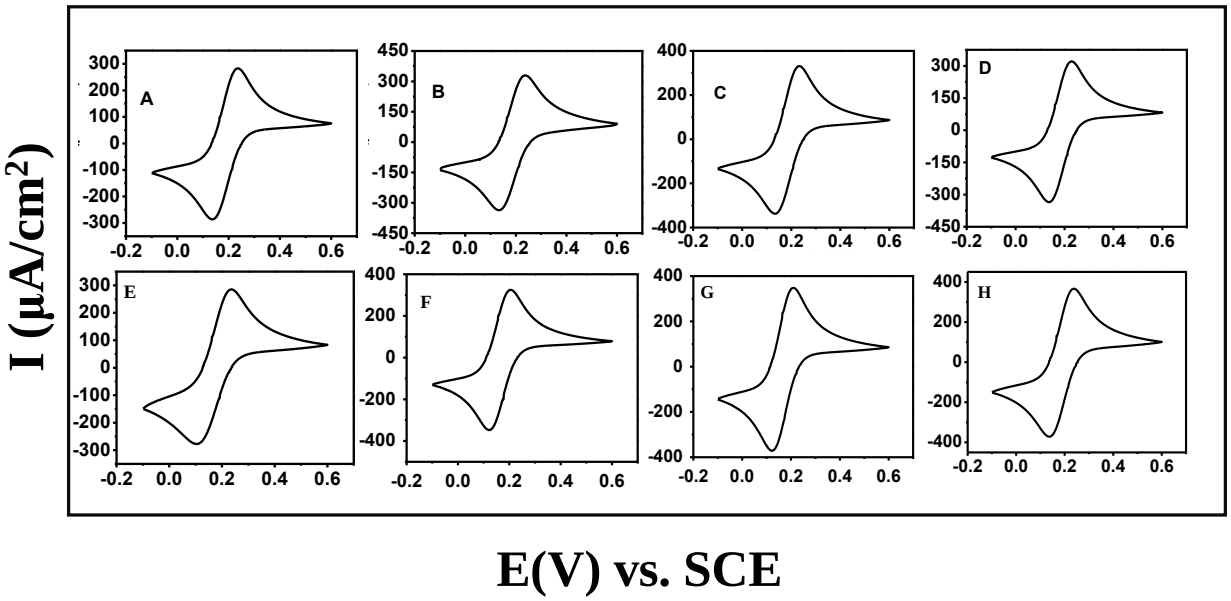

Figure 12*. Cyclic voltammograms of 1mM $K_{3/4}[Fe(CN)_6]$ using 0.1M NaF supporting electrolyte on PTA/ITO monolayer prepared from (A) Neat PTA, (B) ethanol (C) toluene and (D) hexane and on STA/ITO monolayer prepared from (E) Neat STA, (F) ethanol, (G) toluene and (H) hexane solvent.*

Figure 13 represents the Nyquist behavior of PTA/ITO and STA/ITO electrodes prepared from (A,E). neat PTA/STA, (B,F). ethanol, (C,G). toluene, and (D,H). hexane solvents in 1mM $[Fe(CN)_6]^{3-/4-}$ using 0.1M NaF supporting electrolyte. The results obtained for impedance studies of carboxylic acid modified ITO electrodes are complementary to their corresponding cyclic voltammograms (figure 13). There is an increase in R_{ct} value of the carboxylic acid modified ITO

electrodes compared to the bare ITO which is 5.1Ωcm^2 (Table 6). However, this increase is much less than that of PA and silane modified surfaces (Table 2 and 5).

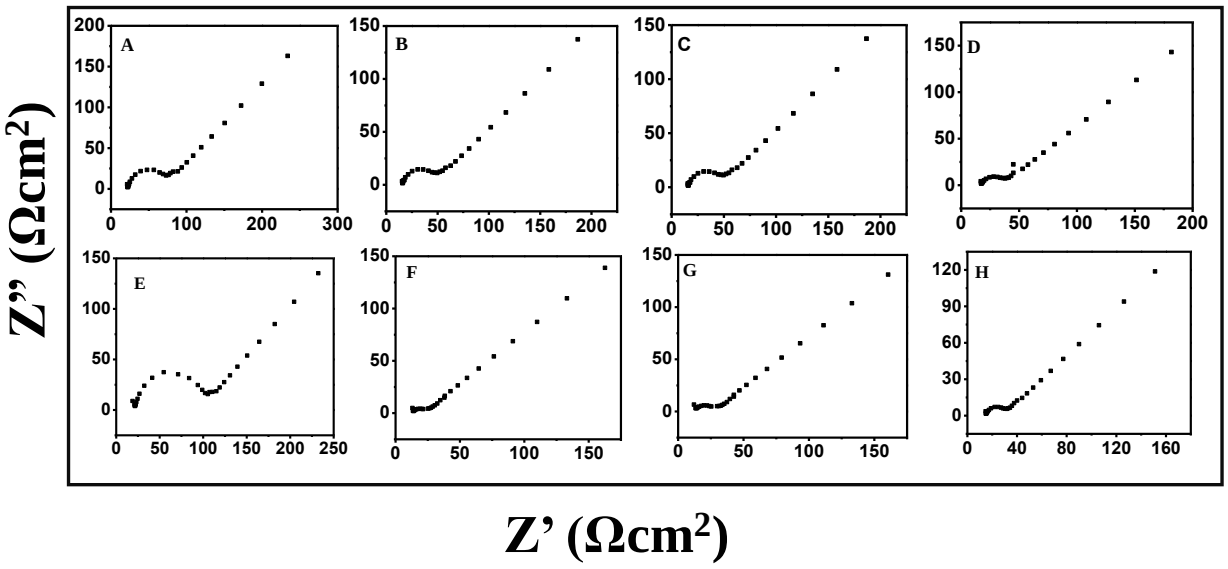

Figure 13. *Nyquist plots of PTA/ITO prepared from (A) Neat PTA, (B) ethanol, (C) toluene, and (D) hexane and STA/ITO prepared from (E). Neat STA, (F) ethanol, (G). toluene, and (H). hexane in 1mM $[Fe(CN)_6]^{3-/4-}$ using 0.1M NaF as supporting electrolyte.*

Table 6. Peak separation (ΔE_p) and charge transfer resistance (R_{ct}) values measured from CV of $[Fe(CN)_6]^{3-/4-}$ redox couple towards PTA/ITO and STA/ITO electrodes (Bare ITO, R_{ct}=5.1Ωcm^2).

Solvent	PTA/ITO		STA/ITO	
	ΔE_p (mV)	R_{ct} (Ωcm^2)	ΔE_p (mV)	R_{ct} (Ωcm^2)
Neat	100.2	46.0	132.7	80.1
Ethanol	97.5	32.6	83.3	19.8
Toluene	90.6	40.3	87.2	16.9
Hexane	104.4	20.3	83.3	18.7

From the obtained CV and EIS data in case of bare ITO, PA/ITO, silane/ITO, and CA/ITO surfaces, it can be seen that, by increasing the chain length of the monolayer the electron transfer blocking behavior of the modified electrode is also enhanced except in the case of carboxylic acid monolayers. Blocking behavior of monolayers is very much dependent on the head groups of the molecule. The variation in blocking behavior of the monolayers can be due to two reasons, (i) the difference in density of binding sites on ITO surface during the adsorption or (ii) different extent of compactness of the monolayers. Since the procedure for pre-treatment of ITO surface for modification was similar for all monolayer formations, the possibility of difference in the density of binding sites can be ruled out. Thus, the difference in blocking behavior can be explained based on the strong affinity of the molecules of phosphonic acids to the metal hydroxides [14,15]. The solvent used for adsorption also plays a key role in the formation of compact monolayer in the case of PAs, silane, and CA monolayers. HDPA/ITO and ODPA/ITO monolayers prepared from ethanol solvent show better blocking behavior compared to the water, toluene, and hexane solvents. This can be attributed to the better solvation of phosphonic acid groups by polar ethanol molecules compared to water, toluene, and hexane solvents. Longer chain alkyl phosphonic acid monolayer forms a more compact monolayer due to Van der Waals interactions among the alkyl chains of the methylene groups in ODPA. It was also earlier reported that at high coverage of phosphonic acids, the monodentate binding is more energetically favorable [51].

Whereas the silanes dissolve quite well in all solvents used in our study, the monolayer show varied blocking behavior towards electron transfer of $[Fe(CN)_6]^{3-/4-}$ redox couple when prepared from neat silane, ethanol, toluene, and hexane solvents. HDTMS/ITO and ODTMS/ITO films prepared from hexane show large peak separations of 258mV and 500mV compared to the silane films prepared from ethanol, toluene, and respective neat silane solutions (Table 5). It can be seen from figures 10 (D,H) and figures 11 (D,H), that silane films prepared from hexane show better blocking (as seen from larger peak separation, low peak currents, and large R_{ct}) for electron transfer of $[Fe(CN)_6]^{3-/4-}$ redox couple, when compared to the silane film prepared from its neat solution. Formation of better silane film on ITO surface when it is prepared from hexane can be explained in terms of low miscibility of the solvent towards water and its weak interactions with polar hydroxyl surfaces since it is a non-polar molecule. These two properties of hexane effectively play a crucial role in the formation of a better silane film on ITO surface. This is in contrast to ethanol and toluene solvents, which show higher affinity for hydrophilic hydroxyl groups on ITO surface,

[52] and therefore more difficult to displace. Peak separation for redox couple in neat C_{18} silane is very much less when compared to its neat C_{16} homologue, which can be attributed to the formation of more disordered monolayer in the case of C_{18} silane.

The STA/ITO electrodes prepared in ethanol, toluene, and hexane solvents exhibited a lower R_{ct} when compared to PTA/ITO (Table 6). In contrast to this, a higher R_{ct} was observed for neat STA which can be accounted by the fact that the high density of adsorbate molecules per ml solvent dissolved STA can lead to a maximum coverage of carboxyl monolayer.

The EIS studies show that the carboxylic acid monolayers show poor blocking to the electron transfer for $[Fe(CN)_6]^{3-/4-}$ redox couple compared to PA and silane films in agreement to that obtained by CV. The poor blocking of the monolayer can be attributed to the fact that carboxylic acid head group does not form a fully covered and compact monolayer on metal oxide substrates [14,15,53–56]. Liakos *et al* has compared the stability of carboxylic acid and phosphonic acid derivatives using PM-IRRAS and XPS techniques on aluminum metal by following their ability to displace carbonaceous contamination. Phosphonic acids remove the contamination better compared to carboxylic acids.[57]. They also studied the hydrolytic stability of alkyl phosphonic acid and carboxylic acid monolayers and concluded that phosphonic acids show better stability than carboxylic acid monolayers [55]. This can be attributed to the strong binding of phosphonic acids onto aluminum surface compared to the carboxylic acids. Foster *et al.* studied the adsorption of phosphonic acid and carboxylic acid onto aluminum using FFM and reported that phosphonic acids form a closely packed monolayer compared to carboxylic acids [56]. Gardner *et al.* showed that -COOH head groups adsorb relatively slowly compared to phosphonic acids. Further, the coverage of the carboxylic acids was observed to be only 25% when compared to that of other monolayers [15]. Thus, the previous studies of carboxylic acid monolayers on various oxide surfaces indicate that the poor blocking for electron transfer reactions. Poor blocking shown by the carboxylic acid based monolayers in the present study can be attributed to the low coverage and weak binding of these monolayers over hydroxylated ITO surface.

3.4. Conclusions:

Adsorption kinetics of HDPA/ITO, ODPA/ITO, HDTMS/ITO, ODTMS/ITO, PTA/ITO, and STA/ITO were studied by electrochemical impedance spectroscopy technique. The rate of

adsorption on the ITO surface depends upon the chain length of the monolayer. Electron transfer behavior of the modified electrodes was studied by using CV and EIS techniques. Since the solvents play a key role in the quality of the monolayer, modification of ITO surfaces was carried out in various solvents apart from the neat compound in the case of silanes and carboxylic acids. In the case of phosphonic acids, high dielectric solvents such as water and ethanol lead to the formation of a very good blocking monolayer. In the case of silane, the solvents of low dielectric constant are a good choice for getting a SAM with fewer number of defects. The studies carried out in this work, clearly demonstrate that, the phosphonic acids form the most compact monolayer followed by silanes of similar chain length, while carboxylic acids form very poor monolayer with numerous voids and defects. The electron transfer blocking behavior towards redox species follows the order of PA > silane > carboxylic acid which is also correlated to the surface morphological studies carried out using AFM.

3.5. References:

[1] S. Dong, J. Li, Self-assembled monolayers of thiols on gold electrodes for bioelectrochemistry and biosensors, Bioelectrochemistry Bioenerg. 42 (1997) 7–13. doi:10.1016/S0302-4598(96)05172-0.

[2] P. Morf, Self-assembled monolayers beyond thiols : Dithiocarbamates – from pure layers to ternary assembly systems, (2007). doi:10.5451/unibas-004237467.

[3] T.J.J. Müller, U.H.F. Bunz, Functional Organic Materials: Syntheses, Strategies and Applications, 2007. doi:10.1002/9783527610266.

[4] J. Escorihuela, M.J. Bañuls, S. Grijalvo, R. Eritja, R. Puchades, Á. Maquieira, Direct covalent attachment of DNA microarrays by rapid thiol-ene "click" chemistry, Bioconjug. Chem. 25 (2014) 618–627. doi:10.1021/bc500033d.

[5] N. Gupta, B.F. Lin, L.M. Campos, M.D. Dimitriou, S.T. Hikita, N.D. Treat, M. V. Tirrell, D.O. Clegg, E.J. Kramer, C.J. Hawker, A versatile approach to high-throughput microarrays using thiol-ene chemistry, Nat. Chem. 2 (2010) 138–145. doi:10.1038/nchem.478.

[6] C. Queffélec, M. Petit, P. Janvier, D.A. Knight, B. Bujoli, Surface modification using

phosphonic acids and esters, Chem. Rev. 112 (2012) 3777–3807. doi:10.1021/cr2004212.

[7] S. Attavar, M. Diwekar, M.R. Linford, M.A. Davis, S. Blair, Passivation of aluminum with alkyl phosphonic acids for biochip applications, Appl. Surf. Sci. 256 (2010) 7146–7150. doi:10.1016/j.apsusc.2010.05.041.

[8] H. Ma, O. Acton, D.O. Hutchins, N. Cernetic, A.K.-Y. Jen, Multifunctional phosphonic acid self-assembled monolayers on metal oxides as dielectrics, interface modification layers and semiconductors for low-voltage high-performance organic field-effect transistors, Phys. Chem. Chem. Phys. 14 (2012) 14110. doi:10.1039/c2cp41557g.

[9] S.P. Pujari, L. Scheres, A.T.M. Marcelis, H. Zuilhof, Covalent surface modification of oxide surfaces, Angew. Chemie - Int. Ed. 53 (2014) 6322–6356. doi:10.1002/anie.201306709.

[10] G.E. Fryxell, S. V. Mattigod, Y. Lin, H. Wu, S. Fiskum, K. Parker, F. Zheng, W. Yantasee, T.S. Zemanian, R.S. Addleman, J. Liu, K. Kemner, S. Kelly, X. Feng, Design and synthesis of self-assembled monolayers on mesoporous supports (SAMMS): The importance of ligand posture in functional nanomaterials, J. Mater. Chem. 17 (2007) 2863. doi:10.1039/b702422c.

[11] P.J. Hotchkiss, S.C. Jones, S.A. Paniagua, A. Sharma, B. Kippelen, N.R. Armstrong, S.R. Marder, The modification of indium tin oxide with phosphonic acids: Mechanism of binding, tuning of surface properties, and potential for use in organic electronic applications, Acc. Chem. Res. 45 (2012) 337–346. doi:10.1021/ar200119g.

[12] O. El Zubir, I. Barlow, G.J. Leggett, N.H. Williams, oxide surfaces by nanoshaving of self-assembled monolayers of alkylphosphonates, (2013) 11125–11131. doi:10.1039/c3nr04701f.

[13] K. Jo, H. Yang, Comparative study of stability of phosphonate self-assembled monolayers on indium-tin oxide electrodes prepared using different methods, J. Electroanal. Chem. 712 (2014) 8–13. doi:10.1016/j.jelechem.2013.10.022.

[14] B.M. Silverman, K.A. Wieghaus, J. Schwartz, Comparative properties of siloxane vs phosphonate monolayers on a key titanium alloy, Langmuir. 21 (2005) 225–228. doi:10.1021/la0482271.

[15] T.J. Gardner, C.D. Frisbie, M.S. Wrighton, Systems for orthogonal self-assembly of electroactive monolayers on Au and ITO: An approach to molecular electronics, J. Am. Chem. Soc. 117 (1995) 6927–6933. doi:10.1021/ja00131a015.

[16] X. Xiao, J. Hu, D.H. Charych, M. Salmeron, Chain Length Dependence of the Frictional Properties of Alkylsilane Molecules Self-Assembled on Mica Studied by Atomic Force Microscopy, Langmuir. 12 (1996) 235–237. doi:10.1021/la950771u.

[17] A. Paszternák, A. Pilbáth, Z. Keresztes, I. Felhősi, J. Telegdi, E. Kálmán, Atomic Force Microscopy Studies of Alkyl-Phosphonate SAMs on Mica, Mater. Sci. Forum. 589 (2008) 257–262. doi:10.4028/www.scientific.net/MSF.589.257.

[18] I. Felhősi, J. Telegdi, G. Pálinkás, E. Kálmán, Kinetics of self-assembled layer formation on iron, Electrochim. Acta. 47 (2002) 2335–2340. doi:10.1016/S0013-4686(02)00084-1.

[19] T. Lim, J. Han, K. Seo, M.-K. Joo, J.-S. Kim, W.-Y. Kim, G.-T. Kim, S. Ju, Fabrication of controllable and stable In_2O_3 nanowire transistors using an octadecylphosphonic acid self-assembled monolayer, Nanotechnology. 26 (2015) 145203. doi:10.1088/0957-4484/26/14/145203.

[20] Y. Okahata, M. Yokobori, Y. Ebara, H. Ebato, K. Ariga, Electrochemical Properties of Covalently Bonded Silane Amphihile Monolayers on a SnO2 Electrode, Langmuir. 6 (1990) 1148–1153.

[21] A.G. Young, A.J. McQuillan, Adsorption/desorption kinetics from ATR-IR spectroscopy. Aqueous oxalic acid on anatase TiO2, Langmuir. 25 (2009) 3538–3548. doi:10.1021/la803116n.

[22] D.B. Parry, J.M. Harris, Attenuated total reflection FT-IR spectroscopy to measure interfacial reaction kinetics at silica surfaces, Appl. Spectrosc. 42 (1988) 997–1004. doi:10.1366/0003702884430146.

[23] M. Giza, P. Thissen, G. Grundmeier, Adsorption kinetics of organophosphonic acids on plasma-modified oxide-covered aluminum surfaces, Langmuir. 24 (2008) 8688–8694. doi:10.1021/la8000619.

[24] M. Bieri, T. Bürgi, Adsorption kinetics, orientation, and self-assembling of N-acetyl-L-cysteine on gold: A combined ATR-IR, PM-IRRAS, and QCM study, J. Phys. Chem. B.

109 (2005) 22476–22485. doi:10.1021/jp052409m.

[25] M. Buck, M. Grunze, F. Eisert, J. Fischer, F. Träger, Adsorption kinetics of n - alkyl thiols on gold studied by second harmonic generation and x- ray photoelectron spectroscopy, J. Vac. Sci. Technol. A Vacuum, Surfaces, Film. 10 (1992) 926–929. doi:10.1116/1.577879.

[26] R. Subramanian, V. Lakshminarayanan, A study of kinetics of adsorption of alkanethiols on gold using electrochemical impedance spectroscopy, Electrochim. Acta. 45 (2000) 4501–4509. doi:10.1016/S0013-4686(00)00512-0.

[27] M. Yang, H.C.M. Yau, H.L. Chan, Adsorption Kinetics and Ligand-Binding Properties of Thiol-Modified Double-Stranded DNA on a Gold Surface, Langmuir. 14 (1998) 6121–6129. doi:10.1021/la980577i.

[28] B.L. Kropman, D.H.. Blank, H. Rogalla, Atomic force microscopic studies on the growth of self-assembled monolayers on SrTiO3-surfaces, Thin Solid Films. 327–329 (1998) 185–190. doi:10.1016/S0040-6090(98)00625-7.

[29] S.A. Paniagua, P.J. Hotchkiss, S.C. Jones, S.R. Marder, A. Mudalige, F.S. Marrikar, J.E. Pemberton, N.R. Armstrong, Phosphonic Acid Modification of Indium-Tin Oxide Electrodes: Combined XPS/UPS/Contact Angle Studies, J. Phys. Chem. C. 112 (2008) 7809–7817. doi:10.1021/jp710893k.

[30] H. Li, P. Paramonov, J.-L. Bredas, Theoretical study of the surface modification of indium tin oxide with trifluorophenyl phosphonic acid molecules: impact of coverage density and binding geometry, J. Mater. Chem. 20 (2010) 2630. doi:10.1039/b921768a.

[31] M. Chockalingam, N. Darwish, G. Le Saux, J.J. Gooding, Importance of the indium tin oxide substrate on the quality of self-assembled monolayers formed from organophosphonic acids, Langmuir. 27 (2011) 2545–2552. doi:10.1021/la104464w.

[32] M. Cerruti, C. Rhodes, M. Losego, A. Efremenko, J.-P. Maria, D. Fischer, S. Franzen, J. Genzer, Influence of indium–tin oxide surface structure on the ordering and coverage of carboxylic acid and thiol monolayers, J. Phys. D. Appl. Phys. 40 (2007) 4212–4221. doi:10.1088/0022-3727/40/14/016.

[33] R.V. Jagadeesh, V. Lakshminarayanan, Adsorption kinetics of phosphonic acids and

proteins on functionalized Indium tin oxide surfaces using electrochemical impedance spectroscopy, Electrochim. Acta. 197 (2016) 1–9. doi:10.1016/j.electacta.2016.03.008.

[34] A. Muthurasu, V. Ganesh, Electrochemical characterization of Self-assembled Monolayers (SAMs) of silanes on indium tin oxide (ITO) electrodes - Tuning electron transfer behaviour across electrode-electrolyte interface, J. Colloid Interface Sci. 374 (2012) 241–249. doi:10.1016/j.jcis.2012.02.007.

[35] T.B. Carmichael, S.J. Vella, A. Afzali, Selective Electroless Metal Deposition Using Microcontact Printing of Phosphine−Phosphonic Acid Inks, Langmuir. 20 (2004) 5593–5598. doi:10.1021/la049870a.

[36] C. Yan, M. Zharnikov, A. Gölzhä, M. Grunze, Preparation and Characterization of Self-Assembled Monolayers on Indium Tin Oxide, Langmuir. 16 (2000) 6208–6215. doi:10.1021/la000128u.

[37] J.L. Dickson, G. Gupta, T.S. Horozov, B.P. Binks, K.P. Johnston, Wetting phenomena at the CO2/water/glass interface, Langmuir. 22 (2006) 2161–2170. doi:10.1021/la0527238.

[38] S.A. Paniagua, E.L. Li, S.R. Marder, Adsorption studies of a phosphonic acid on ITO: film coverage, purity, and induced electronic structure changes, Phys. Chem. Chem. Phys. 16 (2014) 2874. doi:10.1039/c3cp54637c.

[39] A.G. Koutsioubas, N. Spiliopoulos, D.L. Anastassopoulos, A.A. Vradis, G.D. Priftis, Formation of alkane-phosphonic acid self-assembledmonolayers on alumina: An in situ SPR study, Surf. Interface Anal. 41 (2009) 897–903. doi:10.1002/sia.3116.

[40] C. Zhang, J. Wang, J. Jasensky, Z. Chen, Molecular orientation analysis of alkyl methylene groups from quantitative coherent anti-Stokes Raman scattering spectroscopy, J. Phys. Chem. Lett. 6 (2015) 1369–1374. doi:10.1021/acs.jpclett.5b00394.

[41] Y.T. Tao, Structural Comparison of Self-Assembled Monolayers of n-Alkanoic Acids on the Surfaces of Silver, Copper, and Aluminum, J. Am. Chem. Soc. 115 (1993) 4350–4358. doi:10.1021/ja00063a062.

[42] B.B. Damaskin, Adsorption of Organic Compounds At the Mercury Electrode – Solution Interface, Russ. Chem. Rev. 34 (1965) 752–759. doi:10.1070/RC1965v034n10ABEH001560.

[43] V. Ganesh, R.R. Pandey, B.D. Malhotra, V. Lakshminarayanan, Electrochemical characterization of self-assembled monolayers (SAMs) of thiophenol and aminothiophenols on polycrystalline Au: Effects of potential cycling and mixed SAM formation, J. Electroanal. Chem. 619–620 (2008) 87–97. doi:10.1016/j.jelechem.2008.03.015.

[44] H.O. Finklea, D.A. Snider, J. Fedyk, E. Sabatani, Y. Gafni, I. Rubinstein, Characterization of octadecanethiol-coated gold electrodes as microarray electrodes by cyclic voltammetry and ac impedance spectroscopy, Langmuir. 9 (1993) 3660–3667. doi:10.1021/la00036a050.

[45] L. V. Protsailo, W.R. Fawcett, Electrochemical impedance spectroscopy at alkanethiol-coated gold in propylene carbonate, Langmuir. 18 (2002) 8933–8941. doi:10.1021/la0201218.

[46] L. V. Protsailo, W.R. Fawcett, D. Russell, R.L. Meyer, Electrochemical characterization of the alkaneselenol-based SAMs on Au(111) single crystal electrode, Langmuir. 18 (2002) 9342–9349. doi:10.1021/la0203483.

[47] R.P. Janek, W.R. Fawcett, A. Ulman, Impedance Spectroscopy of Self-Assembled Monolayers on Au(111): Sodium Ferrocyanide Charge Transfer at Modified Electrodes, Langmuir. 14 (1998) 3011–3018. doi:10.1021/la970980+.

[48] K. Tokuda, T. Gueshi, H. Matsuda, Voltammetry at partially covered electrodes, J. Electroanal. Chem. Interfacial Electrochem. 102 (1979) 41–48. doi:10.1016/S0022-0728(79)80027-3.

[49] C. Amatore, J.M. Savéant, D. Tessier, Charge transfer at partially blocked surfaces. A model for the case of microscopic active and inactive sites, J. Electroanal. Chem. 147 (1983) 39–51. doi:10.1016/S0022-0728(83)80055-2.

[50] M.E. McGovern, K.M.R. Kallury, M. Thompson, Role of Solvent on the Silanization of Glass with Octadecyltrichlorosilane, Langmuir. 10 (1994) 3607–3614. doi:10.1021/la00022a038.

[51] D.M. Spori, N. V. Venkataraman, S.G.P. Tosatti, F. Durmaz, N.D. Spencer, S. Zürcher, Influence of alkyl chain length on phosphate self-assembled monolayers, Langmuir. 23

(2007) 8053–8060. doi:10.1021/la700474v.

[52] X. Chen, E. Luais, N. Darwish, S. Ciampi, P. Thordarson, J.J. Gooding, Studies on the effect of solvents on self-assembled monolayers formed from organophosphonic acids on indium tin oxide, Langmuir. 28 (2012) 9487–9495. doi:10.1021/la3010129.

[53] M. Grunze, Preparation and Characterization of Self-Assembled Organic Films on Solid Substrates, Phys. Scr. T49b (1993) 711–717. doi:10.1088/0031-8949/1993/T49B/056.

[54] R.D. Ross, L.E. Cole, R.K. Roeder, Relative binding affinity of carboxylate-, phosphonate-, and bisphosphonate-functionalized gold nanoparticles targeted to damaged bone tissue, J. Nanoparticle Res. 14 (2012). doi:10.1007/s11051-012-1175-z.

[55] I.L. Liakos, R.C. Newman, E. McAlpine, M.R. Alexander, Study of the resistance of SAMs on aluminium to acidic and basic solutions using dynamic contact angle measurement, Langmuir. 23 (2007) 995–999. doi:10.1021/la062233v.

[56] T.T. Foster, M.R. Alexander, G.J. Leggett, E. McAlpine, Friction force microscopy of alkylphosphonic acid and carboxylic acids adsorbed on the native oxide of aluminum, Langmuir. 22 (2006) 9254–9259. doi:10.1021/la061082t.

[57] I.L. Liakos, R.C. Newman, E. McAlpine, M.R. Alexander, Comparative study of self-assembly of a range of monofunctional aliphatic molecules on magnetron-sputtered aluminium, Surf. Interface Anal. 36 (2004) 347–354. doi:10.1002/sia.1749.

Chapter 4

Electron transfer studies on short chain phosphonic acid (PA) modified Indium Tin Oxide (ITO) surfaces

4.1. Introduction:

Surface modification of self-assembled monolayers (SAMs) has provided a novel route for altering the physical and chemical properties of surfaces resulting in several potential applications [1,2]. Traditionally, noble metal surfaces were studied extensively, especially with organothiol molecules as a modifier. However, it is well known that short chain organic thiols (<5 methylene groups) from very poor monolayers [3]. Moreover, the short chain organic thiols are highly volatile and not easily amenable for monolayer formation. However, short chain phosphonic acids are non-volatile and quite soluble in aqueous medium. In this work, as described in earlier chapters, indium tin oxide (ITO) surface is studied as a platform for surface modification with phosphonic acid monolayer [4].

Functionalization of electrodes using SAMs alter the electrode-electrolyte interface and therefore influences the electron transfer behavior of the electrodes in a profound way. This aspect of the monolayers has been studied extensively on thiol modified surfaces [5,6]. However, there is a very little study on modified transparent conducting oxide surfaces (TCOs) towards electron transfer behavior [7,8]. Amphiphilic molecules like phosphonic acids (PAs), silanes, and carboxylic acids (CAs) show good affinity towards hydroxyl terminated surfaces [1]. Adsorption of PA and carboxylic acid (CA) monolayers onto a hydroxylated surface is an acid-base reaction with water as a byproduct. Whereas silanes adsorb onto metal oxide surfaces by reacting with hydrogen atom of metal hydroxide with its hydroxyl group resulting in the removal of water. Simultaneously, silanes can undergo homocondensation by reacting with other silane monomers and forms a polymeric film. PA monolayers can be prepared from aqueous medium which make them environmentally benign unlike CAs and silanes [9]. The high stability of PA modified metal oxide surfaces result in the use of this surface for further modifications and extended applications [10–12]. According to the previous reports, PA monolayers show higher stability compared to silane and carboxylic acid monolayers. PAs adsorb on metal oxide surfaces strongly, have high

hydrolytic stability and also resist homocondensation polymerization [13,14]. Hotchkiss *et al*. analyzed the binding characteristics of phosphonic acids on ZnO substrates by using x-ray photoelectron spectroscopy (XPS) and infrared reflection absorption spectroscopy (IRRAS) [15]. Felhősi *et al.* studied the corrosion protection properties of alkylphosphonic acids on iron surface and suggested that a layer of iron oxide plays a role in enhancing the stability of the monolayer [16]. Levine *et al*. compared and analyzed the charge transport behavior of MOx-SAM-M junction with increasing the thickness of the SAM [17]. Brennan *et al.* studied the stability of $-PO_3H_2$, $-Si(OH)_3$, -COOH functionalized porphyrins and binding to TiO_2 substrates. They showed that $-PO_3H_2$ binds more strongly [13]. Silverman *et al.* compared the hydrolytic stability of phosphonates and silanes on titanium alloy [10]. Liakos *et al.* studied the stability of long chain carboxylic acids and phosphonic acids on alumina [18].

However, a relatively less attention has been paid to the study of electron transfer blocking properties of short chain phosphonic acid SAMs [8,19] on metal oxide surfaces and more specifically on ITO surfaces. It is known that, PAs provide a wide range of unique properties which can be usefully exploited for various applications involving SAMs. In this chapter, the electrochemical properties of four different short chain phosphonic acid monolayer modified ITO surfaces using CV and EIS were studied. By tailoring the end group of the molecules constituting the monolayer, variation in the electrochemical properties were monitored using various ferrocene redox probes like ferrocene (Fc), ferrocenemethanol (FcOH), ferroceneacetic acid (FcAc), and 1,1'-ferrocenedicarboxylic acid (Fcdc) in addition to the standard redox probe, $[Fe(CN)_6]^{3-/4-}$. The purpose of such a study is for understanding the effect of the functional groups of redox species like ferrocene on the electron transfer rate on a monolayer with polar and non-polar properties. The phosphonic acids chosen for the study are benzylphosphonic acid (BPA), butylphosphonic acid (BuPA), 3-phosphonopropionic acid (PPA), and 4-aminobenzylphosphonic acid (ABPA). The first two form a surface monolayer which is non-polar and hydrophobic while the latter two are polar and hydrophilic.

4.2. Experimental Section:

4.2.1. Chemicals:

All chemicals used in this study were analytical grade (AR) reagents. The phosphonic acids studied are benzylphosphonic acid (97%, Aldrich), 3-phosphonopropionic acid (94%, Aldrich), butylphosphonic acid (>88%, Aldrich,) and 4-aminobenzylphosphonic acid (95%, Sigma-Aldrich). Solvents used are acetonitrile (HPLC grade, Merck Limited), ethanol (absolute for analysis, Merck Limited), hydrogen peroxide (30% pure, SDFCL), and ammonia solution (25% AR, SDFCL), which are all used as received. Redox probes used are potassium ferricyanide (III) (assay 99%, Merck Limited), potassium ferrocyanide (II) trihydrate (assay 99%, Merck Limited), ferrocenemethanol (97%, Aldrich), ferroceneacetic acid (98%, Aldrich), 1, 1'-ferrocenedicarboxylic acid (96%, Aldrich), and ferrocene (98%, ACROS), potassium chloride (AR grade, SDFCL), sodium fluoride (assay 99%, Merck Limited), and tetrabutylammonium tetrafluoroborate (99%, Aldrich) are used as supporting electrolyte. Millipore water was used to prepare all aqueous solutions employed in this work. ITO coated glass is purchased from Xin Yan technology Limited. This plate (355mm X 406mm X 1.1mm) is a single side polished, SiO_2 passivated float glass coated with ITO film. For electrochemical studies, this larger plate was cut into small pieces of pre-defined geometrical area and was used as strips.

4.2.2. SAM preparation:

The monolayers were prepared by keeping the pre-treated ITO substrates in 10mM solutions of benzylphosphonic acid (BPA), 3-phosphonopropionic acid (PPA), butylphosphonic acid (BuPA), and 4-aminobenzylphosphonic acid (ABPA) for 12 hours using water as solvent. Later, the SAM modified ITO electrodes were taken out, ultra-sonicated in water to remove any traces of loosely attached adsorbates. Further, these modified ITO strips were annealed in an oven at 80°C for an hour, then allowed to cool to room temperature for few hours and finally used for electrochemical studies.

4.3. Results and Discussion:

Electrochemical properties of phosphonic acid modified ITO surfaces are reported in this section as studied by cyclic voltammetry (CV) and electrochemical impedance spectroscopy (EIS). The structures of phosphonic acids used for the formation of monolayers are shown in figure 1.

4.3.1. Phosphonic acids and Redox active probes:

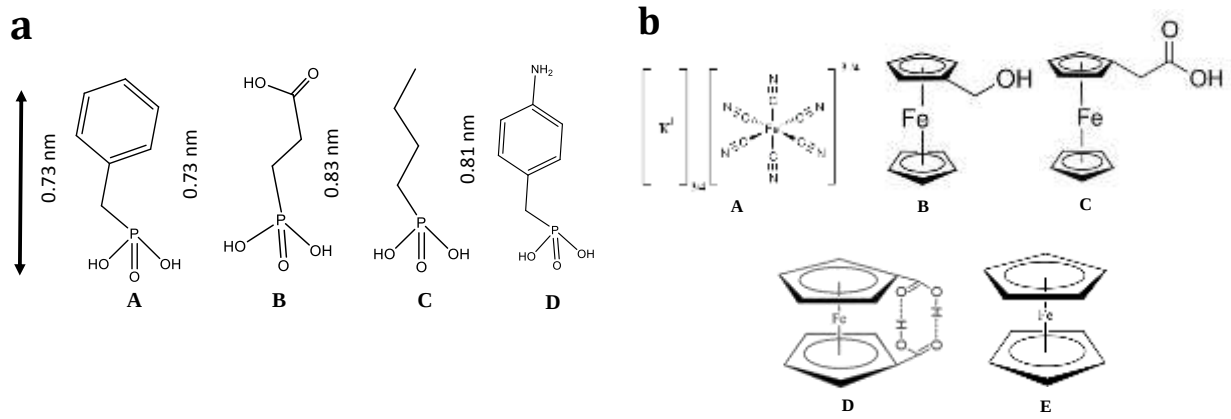

Figure 1. (a). *Chemical structure of phosphonic acid (PA) molecules under study (A) benzylphosphonic acid (BPA), (B) 3-phosphonopropionic acid (PPA) (C) butylphosphonic acid (BuPA), and (D) 4-aminobenzylphosphonic acid (ABPA) respectively used for SAM formation on ITO electrodes.* ***1 (b).*** *Redox species employed for electron transfer studies (A). potassium ferro/ferricyanide, (B). ferrocenemethanol (FcOH), (C). ferroceneacetic acid (FcAc), (D). ferrocenedicarboxylic acid (Fcdc), and (E). ferrocene (Fc).*

4.3.2. Electrochemical studies on Bare ITO:

Figure 2. shows the CV and EIS behavior of 1mM (A,B) $[Fe(CN)_6]^{3-/4-}$ (0.1M NaF), (C,D) ferrocene (0.1M TBATFB), (E,F) ferrocenemethanol (0.1M NaF), (G,H) ferroceneacetic acid (0.1M NaF), and (I,J) ferrocenedicarboxylic acid (0.1M NaF) redox species in their respective supporting electrolyte on hydroxylated ITO surface. The CV of $[Fe(CN)_6]^{3-/4-}$ redox couple on bare ITO (figure 2A) shows a peak separation of about 82mV (Table 1) .[20]. However, in the case of ferrocene a peak separation of about 370mV (Table 1) is seen, which implies that it undergoes an irreversible electron transfer process on ITO surface. The CVs (figure 2E, G and I) of ferrocenemethanol (FcOH), ferrocene acetic acid (FcAc), and ferrocenedicarboxylic acid (Fcdc)

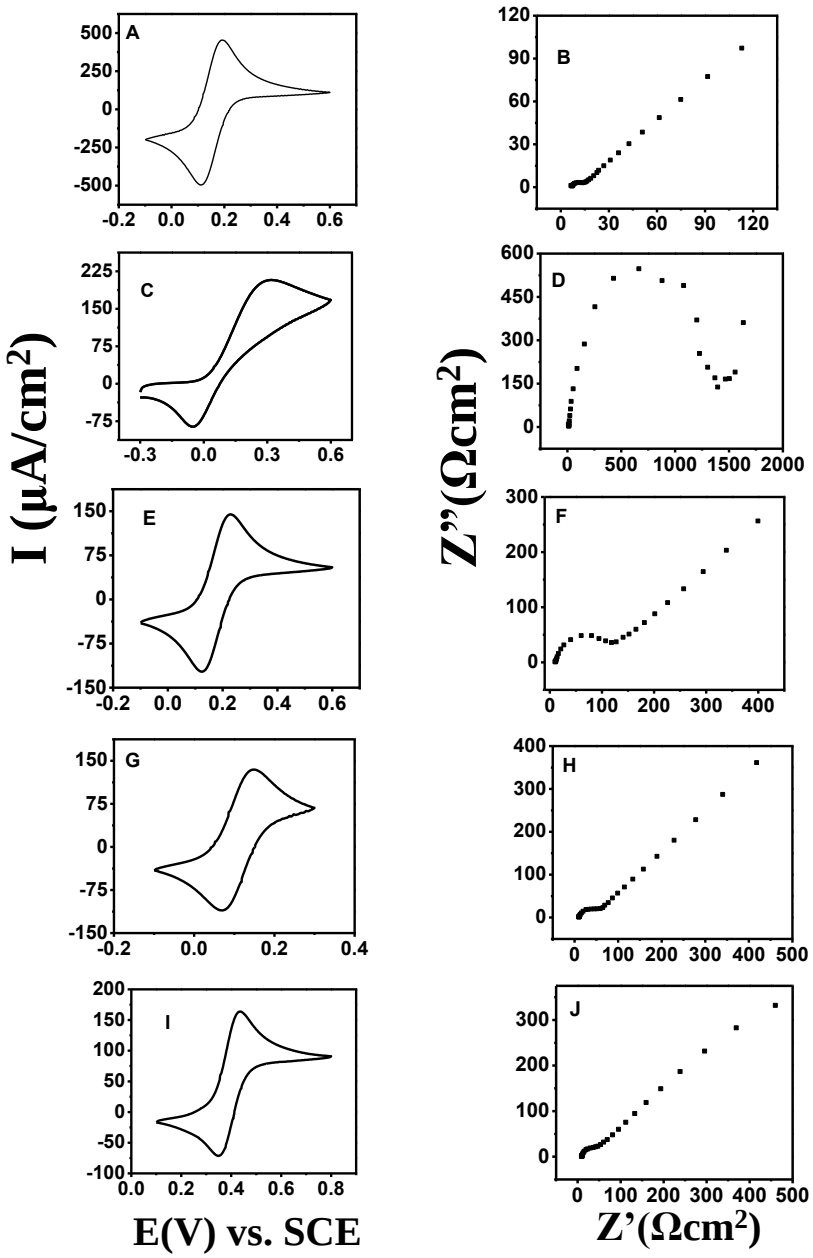

Figure 2. *CV and EIS plots of hydroxylated ITO in 1mM of (A,B) $[Fe(CN)_6]^{3-/4-}$ (0.1M NaF), (C,D) ferrocene (0.1M TBATFB), (E,F) ferrocenemethanol (0.1M NaF), (G,H) ferroceneacetic acid (FcAc), and ferrocenedicarboxylic acid (Fcdc) (0.1M NaF) ferrocenemethanol (FcOH), acid (0.1M NaF) and (I,J) ferrocenedicarboxylic acid (0.1M NaF) redox species in their respective supporting electrolyte.*

exhibit peak separations of 104, 81 and 97mV respectively, corresponding to the quasi-reversible electron transfer behavior (Table 1). The irreversible electron transfer behavior of ferrocene, a non-

polar redox molecule, can be attributed to the fact that its interaction with hydrophilic ITO surface is inhibited due to its hydrophobic property. However, in the case of redox species like FcOH, FcAc, and Fcdc which contain hydrophilic functional groups, the reaction is facilitated on the hydrophilic ITO surface.

It can be seen from figure 2B, that the Nyquist plot for $[Fe(CN)_6]^{3-/4-}$ electron transfer on pre-treated ITO surface shows a straight line at a low frequency and a very small semi-circle at a high-frequency region, indicating that the process is essentially diffusion-controlled for the redox couple (figure 2B). It is to be noted that the surface of ITO is hydrophilic and polar due to the hydroxylation which facilitate the electron transfer of charged redox species like $[Fe(CN)_6]^{3-/4-}$ and therefore the reaction is largely diffusion controlled. The measured equivalent circuit parameters from EIS were fitted with Randle's model which shows a charge transfer resistance (R_{ct}) value of $5.1\Omega cm^2$ (Table 1). Figure 2D shows Nyquist plot of pre-treated ITO for 1mM ferrocene using 0.1M TBATFB supporting electrolyte. A large semi-circle followed by a straight line at narrow range of low frequencies shows that electron transfer is under charge transfer control over the whole frequency ranges. The high R_{ct} value for ferrocene redox reaction on hydroxylated ITO surface is due to the inhibition of the electron transfer process of the highly hydrophobic species on hydrophilic ITO surface. Similar behavior is expected by FcOH, FcAc, and Fcdc, whereas the relatively low R_{ct} values show that the electron transfer process is facilitated in these cases unlike that of ferrocene. This can be attributed to the hydrophilic nature of functional groups like hydroxyl, acetate, and dicarboxylate attached to the ferrocene redox moiety.

In the case of Fcdc, the half-peak potential (figure 2I) is 390mV which is 200mV more positive when compared to that of FcAc. This can be explained by the fact that in Fcdc, the two carboxylic groups attached to cyclopentadiene (cp_2) rings conform in *cis* position to form intramolecular hydrogen bond. Oxidation of the ferrocene group to ferricenium results in breaking of the intramolecular hydrogen bond due to positively charged ferricenium group pulling the electrons away from carboxyl groups. Since breaking of hydrogen bond is energetically unfavorable it becomes necessary to apply more positive potential to accomplish this process. Hence, the half-peak potential shifts more positive potential in this case [21]. It is also earlier reported that the 'electromeric effect' of the –COOH group in Fcdc withdraws the electrons from ferrocene and causes a positive shift in the oxidation potential [21,22].

Table 1. Peak separation (mV), peak current ($\mu A/cm^2$) and charge transfer resistance (Ωcm^2) values of bare ITO electrode towards various redox species.

Redox species	ΔE_p	I_p	R_{ct} From EIS
$[Fe(CN)_6]^{3-/4-}$	82	473	5.9
Fc	370.1	147	1295.0
FcOH	104.4	146	105.9
FcAc	80.7	123	33.4
Fcdc	96.8	118	33.2

I_p average peak current

4.3.3. Electron transfer studies on BPA/ITO:

Figure 3 shows the CV and EIS behavior of 1mM (A,B). $[Fe(CN)_6]^{3-/4-}$ (0.1M NaF), (C,D). Fc (0.1M TBATFB), (E,F). FcOH (0.1M NaF), (G,H). FcAc (0.1M NaF), and (I,J). Fcdc (0.1M NaF) redox species in their respective supporting electrolyte on BPA/ITO. Figure 3A shows CV of BPA/ITO in $[Fe(CN)_6]^{3-/4-}$ redox couple with a peak separation of 182mV (Table 2) which corresponds to the irreversible electron transfer behavior of the redox couple at the modified electrode. This value is quite high compared to the pre-treated ITO (82mV). The increase in peak separation is due to the compact monolayer formation of BPA by lateral π interactions between neighboring phenyl rings which inhibits the electron transfer on the modified ITO surface. Whereas in the case of ferrocene, the CV shows a lower peak separation of around 164mV (Figure 3C) compared to the value obtained for pre-treated ITO. In non-polar solvents like acetonitrile, BPA monolayer disorganizes due to the permeation of acetonitrile solvent through the monolayer and can provide access to the electrode surface for the redox reaction to occur [23]. In the case of FcOH and FcAc, a peak separation of around 81 and 78mV (Table 2) were obtained on BPA/ITO (figures 3E and G) which is quite less compared to the values obtained for pre-treated ITO (Table 1). The decrease in peak separation is due to the non-polar nature of the phenyl ring, which allows the non-polar ferrocene moiety to move freely to access the electrode. In addition to this, favorable π-π interaction between phenyl rings of the BPA monolayer and cyclopentadienyl (cp_2) rings of

redox moieties further facilitates the electron transfer [24]. This assumption is further supported by the average peak (I_p) currents obtained for the respective redox species at the BPA/ITO electrode surface (Table 2). Electron transfer behavior of ferrocenedicarboxylic acid (Fcdc) on BPA/ITO is well inhibited by BPA/ITO monolayer which can be assessed from the lower peak currents of 78μA/cm^2 (figure 3I and Table 2). It shows that a peak separation of 217mV corresponds to the irreversible electron transfer behavior of redox species at BPA modified electrode. A closer access to the hydrophobic electrode surface of BPA is inhibited for Fcdc due to the steric hindrance of bulky hydrophilic carboxyl moieties.

In the case of $[Fe(CN)_6]^{3-/4-}$, the Nyquist plot of Figure 3B shows a large semi-circle at high frequencies which is followed by a low frequency straight line that corresponds to the partial charge transfer and diffusion controlled electron transfer behavior. The charge transfer resistance (R_{ct}) for the redox couple 234Ωcm^2 (Table 2) is increased when compared to the pre-treated ITO. Since BPA is a non-polar molecule, it forms a highly organized monolayer in aqueous solutions due to the hydrophobic effect thereby blocking the diffusion of redox species to the electrode surface resulting in an increase of R_{ct}. For Fc, FcOH, and FcAc redox moieties, the R_{ct} values obtained are around 156, 34, and 9Ωcm^2 (Table 2). These values are significantly less compared to the values obtained for pre-treated ITO. The decrease in R_{ct} values can be attributed to the extended π-conjugation between phenyl rings of BPA monolayer and cp_2 rings of ferrocene redox moieties due to which redox species moves closer to the electrode surface [5]. Ferrocenedicarboxylic acid (Fcdc) redox moiety (figure 3J) shows a higher R_{ct} value, due to the steric hindrance caused by two hydrophilic -COOH groups which therefore cannot access closely to the non-polar BPA/ITO surface.

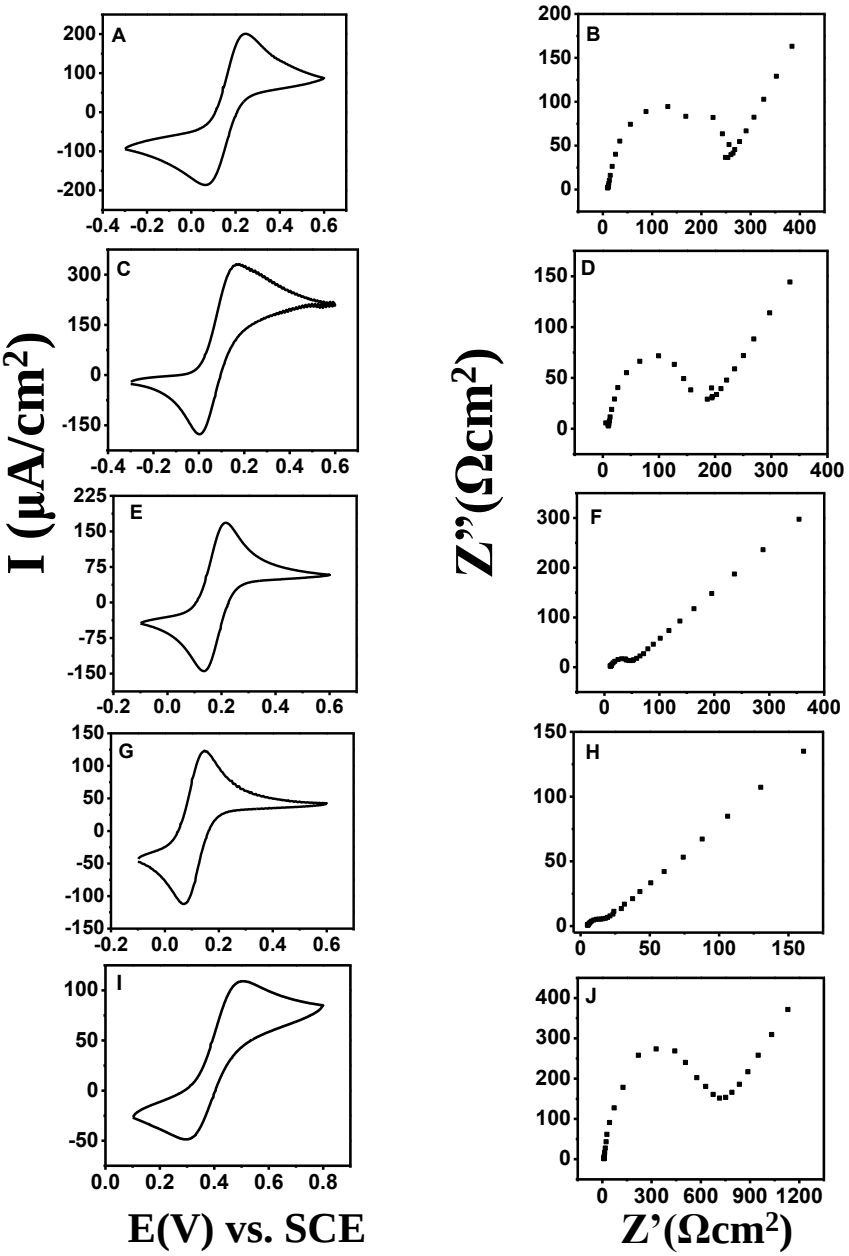

Figure 3. *CV and EIS plots of BPA/ITO in 1mM (A,B) $[Fe(CN)_6]^{3-/4-}$ (0.1M NaF), (C,D) Fc (0.1M TBATFB), (E,F) FcOH (0.1M NaF), (G,H) FcAc (0.1M NaF), and (I,J) Fcdc (0.1M NaF) redox species in their respective supporting electrolyte.*

Table 2 Peak separation (mV), peak current ($\mu A/cm^2$) and charge transfer resistance (Ωcm^2) values of BPA/ITO electrode towards various redox species.

Redox species	**ΔE_p**	**I_p**	**R_{ct} From EIS**
$[Fe(CN)_6]^{3-/4-}$	182.5	148	234
Fc	164.1	253	156.7
FcOH	81.0	243	33.6
FcAc	78.2	117	9.4
Fcdc	217.8	78	655.3

4.3.4. Electron transfer studies on PPA/ITO:

Figure 4 shows the CV and EIS behavior of 1mM (A,B) $[Fe(CN)_6]^{3-/4-}$ (0.1M NaF), (C,D) Fc (0.1M TBATFB), (E,F) FcOH (0.1M NaF), (G,H) FcAc (0.1M NaF), and (I,J) Fcdc (0.1M NaF) redox species in their respective supporting electrolyte at PPA/ITO electrode. Figure 4A shows an increase in peak separation and reduced peak currents for $[Fe(CN)_6]^{3-/4-}$ redox species towards PPA/ITO electrode (Table 3) indicating the inhibition of electron transfer process at the modified electrode. PPA/ITO surface shows higher peak currents for $[Fe(CN)_6]^{3-/4-}$ redox couple when compared to non-polar monolayers but is still less than on ABPA monolayer (Table 3). The higher peak currents are due to the disorganization of the monolayer of PPA in aqueous solutions. Terminal hydrophilic -COOH groups of PPA and ionic redox species like $[Fe(CN)_6]^{3-/4-}$ is solvated by water molecules. Thus $[Fe(CN)_6]^{3-/4-}$can easily permeate through the disorganized monolayer and can undergo redox process [25]. From figure 4C, it can be seen that the electron transfer process of ferrocene in acetonitrile is not inhibited at the PPA/ITO surface. However, there is a significant decrease in peak separation and increase in peak currents (Table 3) when compared to the CV in the case of bare ITO surface (Table 1). The diffusion of non-polar redox species, ferrocene and subsequent electron transfer can only occur at the defects and pinholes in the monolayer. The decrease in peak separation and increase in peak currents (Table 3) on PPA/ITO surface is due to the decrease in hydrophilic hydroxyl concentration on ITO surface after the

formation of monolayer. Though carboxyl group of PPA is hydrophilic, there is an overall increase in non-polar character of the film which facilitate the permeation of ferrocene molecule. From Table 3, it can be seen that there is a decrease in peak separation for the functionalized ferrocene moieties on PPA/ITO. In the case of ferrocene derivatives (FcOH, FcAc, and Fcdc), electron transfer is facile due to the interaction of attached hydrophilic groups with the carboxyl group of the monolayer with the hydrophobic cp_2 group in the molecule orienting farther away from the electrode surface [26,27].

Figure 4B shows the impedance plots for $[Fe(CN)_6]^{3-/4-}$ redox couple on PPA/ITO electrode. It can be seen that, the charge transfer resistance has increased compared to ITO for the redox couple as shown in Table 3. The charged carboxylate groups repel each other and create more spaces in between the molecules for redox species to access the gaps, where the ferro/ferricyanide redox couple can access the electrode surface. This results in the PPA monolayer being not quite effective in inhibiting the electron transfer process (Table 3). Chidsey *et al.* have observed a fluid-like peak position for the 11-carbon homologue of carboxylic acid terminated thiol which suggests that the presence of the carboxylic acid group decreases the crystalline-like packing of the monolayer [25].

In contrast, for ferrocene, the PPA monolayer shows a higher R_{ct} value of around $1842 \Omega cm^2$ (Table 3) which indicates that the electron transfer process is significantly inhibited by the monolayer. This can be attributed to highly organized PPA monolayer through lateral hydrogen bonding between the neighboring carboxylic end groups of PPA. The ferrocene molecule has unfavorable hydrophobic-hydrophilic interaction with PPA monolayer. Because of this ferrocene cannot orient favorably towards the hydrophilic PPA film to undergo facile electron transfer. This results in an increase in the charge transfer resistance. Moreover, in non-polar acetonitrile solvent, the hydrophilic carboxylic acid group of PPA monolayer at the terminal aligns together quite tightly in domains resulting in the creation of voids in the interdomain spaces. The electron transfer can still occur through the gaps in the disordered monolayer which is responsible for the distinct current peak observed in figure 4C.

Figures 4F and H show the Nyquist plots of FcOH and FcAc redox moiety showing diffusion controlled features at low frequency region. Table 3 shows that the charge transfer resistance (R_{ct}) values for FcOH and FcAc redox reactions are less in PPA/ITO surface compared to the pre-treated ITO (see Table 1). Due to the favorable orientation of functionalized ferrocene (FcOH and FcAc)

redox moieties, they get close access to PPA/ITO surface resulting in an increase in reaction rate and decrease in charge transfer resistance. The high charge transfer resistance for Fcdc redox couple (Table 3) is due to the steric hindrance caused by the presence of two carboxylic acid groups resulting in an unfavorable orientation of redox moiety on the electrode surface. The hydrophobic ferrocene group cannot interact with the hydrophilic PPA monolayer film resulting in a slower reaction kinetics as reflected in high R_{ct} (Table 3).

Table 3. Peak separation (mV), peak current ($\mu A/cm^2$), and charge transfer resistance (Ωcm^2) values of PPA/ITO electrode towards various redox species.

Redox species	**ΔE_p**	**I_p**	**R_{ct} From EIS**
$[Fe(CN)_6]^{3-/4-}$	182.5	200	72.1
Fc	158.8	192	1842.0
FcOH	101.6	123	70.1
FcAc	79.6	155	24.6
Fcdc	109.8	95	564.0

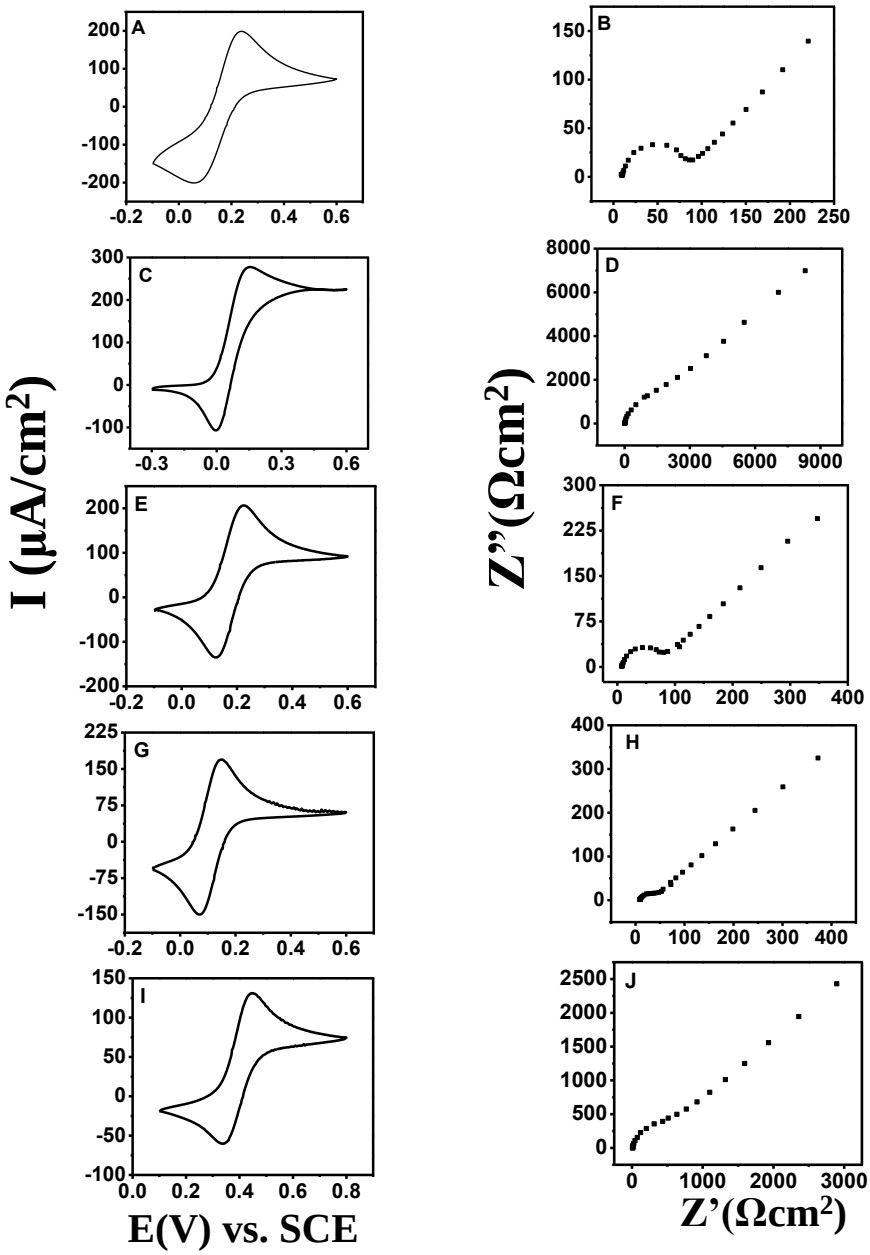

Figure 4. *CV and EIS of PPA/ITO in 1mM (A,B) $[Fe(CN)_6]^{3-/4-}$ (0.1M NaF), (C,D) Fc (0.1M TBATFB), (E,F) FcOH (0.1M NaF), (G,H) FcAc (0.1M NaF) and (I,J) Fcdc (0.1M NaF) redox species in their respective supporting electrolyte.*

4.3.5. Electron transfer studies on BuPA/ITO:

Figure 5 shows the CV and Nyquist plots of BuPA/ITO in 1mM (A,B) $[Fe(CN)_6]^{3-/4-}$ (0.1M NaF), (C,D) Fc (0.1M TBATFB), (E,F) FcOH (0.1M NaF), (G,H) FcAc (0.1M NaF), and (I,J) Fcdc

(0.1M NaF) redox species in their respective supporting electrolyte. For the redox process of $[Fe(CN)_6]^{3-/4-}$ on the SAM of BuPA/ITO (figure 4 A) an irreversible CV behavior with a large peak separation of around 170mV (Table 4) is obtained. This implies that BuPA/ITO significantly blocks the electron transfer, though not entirely hindering it. This behavior is due to the sequential arrangement of monolayer on the nanostructures of pre-treated ITO. In the case of ferrocene redox molecule at the BuPA/ITO surface, the peak currents are higher than pre-treated ITO. The favorable hydrophobic interactions between methyl terminated monolayer and ferrocene redox species combined with the disorganization of monolayer by the acetonitrile solvent facilitates the closer access of ferrocene to the electrode surface thus enhancing the electron transfer rate. However, the decrease in peak separation in the case of BuPA/ITO is less compared to the BPA/ITO, since in the case of latter, the electron transfer is facilitated by the strong π-π interactions, whereas in the case of former much weaker hydrophobic interactions are involved.

Due to the hydrophobic interactions, functionalized ferrocene derivatives of FcOH and FcAc tend to stay close to the BuPA modified electrode surface due to which the electrode vicinity is enriched with the redox species. A facile electron transfer takes place in this case as seen from the two clear peaks and a relatively low peak separation (101 and 79mV). In the case of Fcdc redox molecule (figure 5I), the observed decrease in peak currents is due to the steric hindrance of two carboxyl groups which avoid a close approach of redox species to the BuPA modified interface.

From figure 5B, we observe that the BuPA monolayer shows higher R_{ct} value for $[Fe(CN)_6]^{3-/4-}$ redox couple (Table 4) compared to that of pre-treated ITO surface. The inhibition of the electron transfer process is due to the hydrophobic nature of the surface film to which the charged polar $[Fe(CN)_6]^{3-/4-}$ couple do not have close access. In contrast, charge transfer resistance of hydrophobic and non-polar ferrocene redox moiety is decreased when compared to the pre-treated ITO which can be attributed to the closer access of the redox moiety to the electrode surface due to the favorable hydrophobic interactions between BuPA monolayer and cp_2 rings of ferrocene.

The dominance of diffusion controlled electron transfer behavior for FcOH and FcAc (figures 5F and H) redox moieties show that electron transfer is facilitated for the species at BuPA/ITO electrode interface which can be attributed to the favorable hydrophobic interactions with ferrocene groups of these two species. Figure 5J shows that electron transfer for Fcdc redox reaction is under charge transfer controlled process at high frequencies. The two carboxyl groups

in Fcdc are intra molecularly hydrogen bonded. This hydrogen bonding will be broken if the ferrocene group in Fcdc is oxidized to ferricenium and acquire net positive charge. Therefore, the process of oxidation of Fcdc not favored which makes charge transfer resistance larger than FcAc with single carboxylic group as shown in Table 4. The R_{ct} values are obtained by equivalent circuit fitting and are tabulated in Table 4 for different monolayers.

Table 4. Peak separation (mV), peak current ($\mu A/cm^2$), and charge transfer resistance (Ωcm^2) values of BuPA/ITO electrode towards various redox species.

Redox species	**ΔE_p**	**I_p**	**R_{ct} From EIS**
$[Fe(CN)_6]^{3-/4-}$	170.2	166	299.3
Fc	220.6	239	246.1
FcOH	101.6	123	70.1
FcAc	90.5	126	57.1
Fcdc	113.7	65	553.0

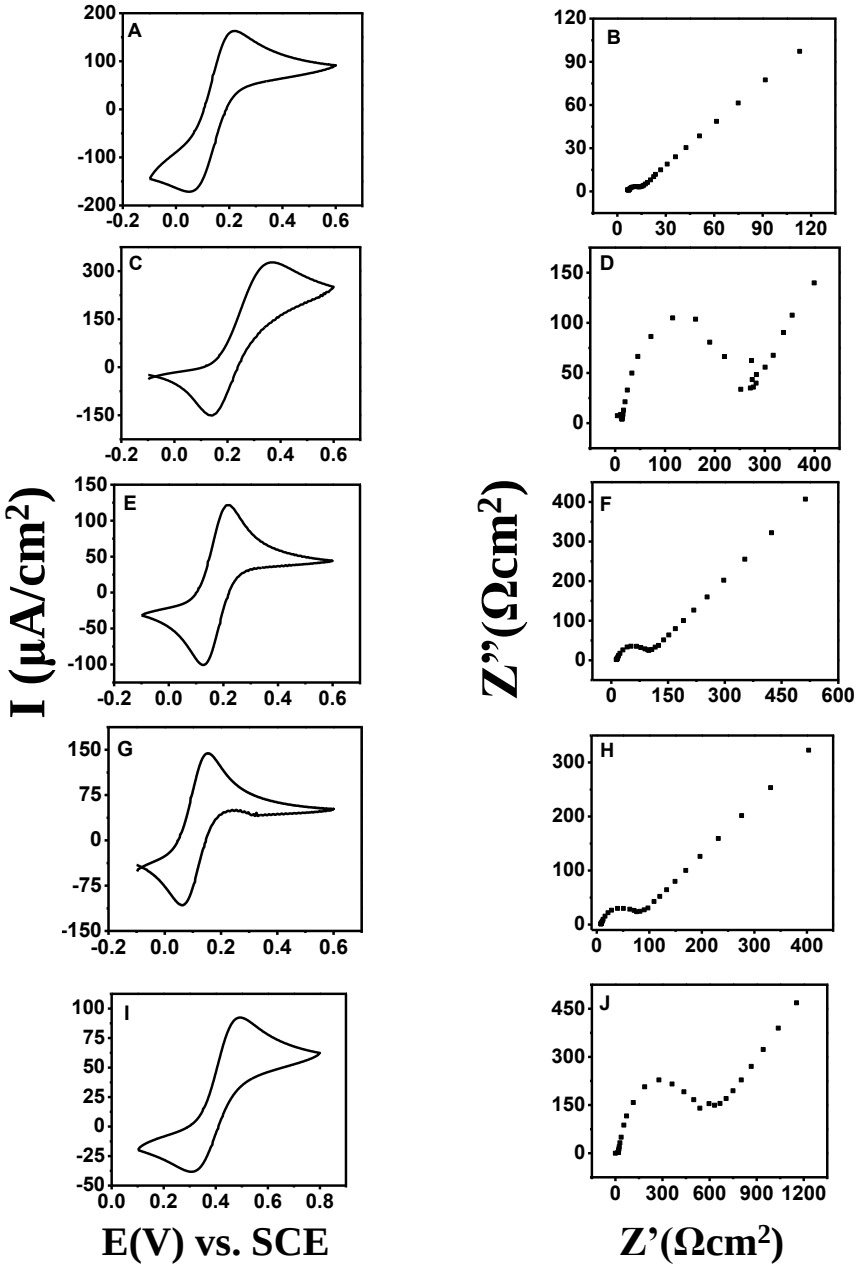

Figure 5. *CV and EIS of BuPA/ITO in 1mM (A,B) $[Fe(CN)_6]^{3-/4-}$ (0.1M NaF), (C,D) Fc (0.1M TBATFB), (E,F) FcOH (0.1M NaF), (G,H) FcAc (0.1M NaF) and (I,J) Fcdc (0.1M NaF) redox species in their respective supporting electrolyte.*

4.3.6. Electron transfer studies on ABPA/ITO:

Figure 6 shows CV and EIS plots of ABPA/ITO in 1mM (A,B) $[Fe(CN)_6]^{3-/4-}$ (0.1M NaF), (C,D) Fc (0.1M TBATFB), (E,F) FcOH (0.1M NaF), (G,H) FcAc (0.1M NaF) and (I,J) Fcdc (0.1M NaF)

redox species in their respective supporting electrolyte. Figure 6A shows the CV of $[Fe(CN)_6]^{3-/4-}$ redox couple at the ABPA modified ITO surface. It shows higher peak currents compared to the BPA, PPA, and BuPA monolayers (Table 5). This behavior can be attributed to the electrostatic attraction between positively charged ABPA monolayer and negatively charged $[Fe(CN)_6]^{3-/4-}$ redox couple which enriches the redox species in the vicinity of the electrode surface. In the case of ferrocene redox reaction (figure 6C, Table 5), a favorable π-π interaction between the phenyl groups present in the ABPA monolayer and the cyclopentadiene groups of the redox couple leads to an increase in the currents when compared to PPA monolayer surface. A favorable π-π interaction also increases the closest approach of FcOH, FcAc, and Fcdc redox species to the electrode interface. The increased peak currents are also observed in the case of FcOH and FcAc redox moieties which can be explained by the extended π-π interaction between the ferrocene redox moiety and ABPA monolayer.

Figure 6B shows a semi-circle followed by a straight line which corresponds to the partial charge transfer and diffusion controlled electron transfer behavior of the ABPA/ITO electrode towards $[Fe(CN)_6]^{3-/4-}$ redox couple. From Table 5, it can be seen that there is an increase in the R_{ct} value (Table 5) for redox couple compared to pre-treated ITO. This is due to the compact monolayer formation of ABPA monolayer due to lateral π-π interactions. In the case of ferrocene, the R_{ct} value ($233.8\Omega cm^2$) is much lower than on PPA/ITO surface ($1842\Omega cm^2$). This can be ascribed to the conducive π-π interactions originated between the phenyl rings of ABPA monolayer and cp_2 rings of redox molecule. Ferrocenedicarboxylic acid (Fcdc) shows lowest R_{ct} in ABPA/ITO monolayer compared to BPA, PPA and BuPA monolayer films. This is due to the favorable hydrophilic and electrostatic interactions between positively charged amino groups of monolayer and negatively charged carboxylate functional group of Fcdc redox species.

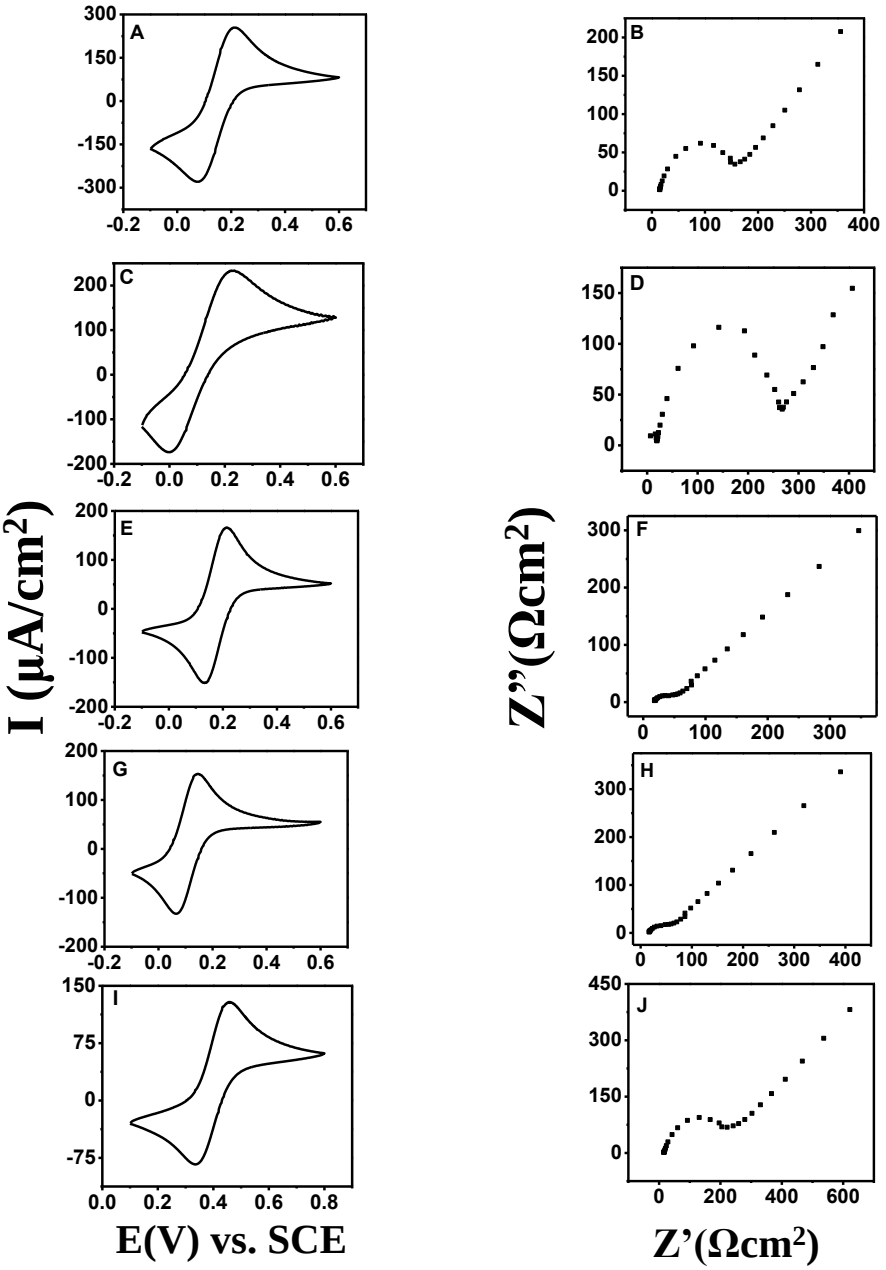

Figure 6. *CV and EIS of ABPA/ITO in 1mM (A,B) $[Fe(CN)_6]^{3-/4-}$ (0.1M NaF), (C,D) Fc (0.1M TBATFB), (E,F) FcOH (0.1M NaF), (G,H) FcAc (0.1M NaF) and (I,J) Fcdc (0.1M NaF) redox species in their respective supporting electrolyte.*

Table 5. Peak separation (mV), peak current ($\mu A/cm^2$), and charge transfer resistance (Ωcm^2) values of ABPA/ITO electrode towards various redox species.

Redox species	ΔE_p	I_p	R_{ct} From EIS
$[Fe(CN)_6]^{3-/4-}$	137.2	266	133.4
Fc	230.1	201	233.8
FcOH	80.8	158	32.4
FcAc	90.5	126	57.1
Fcdc	120.7	106	196.9

4.4. Conclusions:

Indium tin oxide (ITO) surface is modified with phosphonic acid monolayers of carboxylic (PPA), amino (ABPA), benzyl (BPA), and methyl (BuPA) terminal end groups. The interactions between these terminal groups of short chain phosphonic acids and different redox species like $[Fe(CN)_6]^{3-/4-}$ (polar, hydrophilic), ferrocene (non-polar, hydrophobic), ferrocenemethanol (neutral, non-polar redox group, and polar functional group), ferroceneacetic acid (non-polar redox group, polar functional group), and ferrocenedicarboxylic acid (non-polar redox group, polar intramolecular hydrogen bonded functional groups) are studied. The terminal functional groups of the monolayer have been shown to exert significant influence on the electron transfer behavior in the case of ferrocene redox couples. Extended π-π interactions play a key role in controlling the electron transfer behavior of functionalized ferrocene on BPA/ITO monolayer. PPA monolayer which has a carboxylic acid terminal group shows very good blocking of ferrocene redox reaction in acetonitrile solvent, in contrast to its poor blocking behavior of redox reactions in aqueous medium. This is due to the fact that PPA forms a disorganized monolayer in aqueous solutions due to the solvation of hydrophilic -COOH groups, whereas in non-aqueous solvents like acetonitrile, it forms a close packed monolayer due to the intermolecular hydrogen bonding between neighboring carboxyl groups. In the case of BPA and BuPA monolayers, excellent blocking towards $[Fe(CN)_6]^{3-/4-}$ redox couple was observed, whereas for ferrocene redox moieties the

electron transfer process is facilitated. This behavior can be attributed to the formation of highly organized monolayers of BPA and BuPA in aqueous solutions due to the hydrophobic effect, whereas in non-aqueous solvents like acetonitrile, BPA, and BuPA form disorganized monolayer due to the solvation of terminal phenyl and methyl groups. It is shown in this chapter that, the nature of the solvent, monolayer surface, functional group, and redox species altogether play a key role in electron transfer behavior of phosphonic acid modified ITO surfaces. Such a study helps to understand the role of various interactions such as polar, non-polar, hydrophobic, and hydrophilic effects existing among the monolayer film, solvent, and the redox species in influencing the kinetics of electron transfer process.

4.5. References:

[1] S.P. Pujari, L. Scheres, A.T.M. Marcelis, H. Zuilhof, Covalent Surface Modification of Oxide Surfaces, Angew. Chemie Int. Ed. 53 (2014) 6322–6356. doi:10.1002/anie.201306709.

[2] C. Queffélec, M. Petit, P. Janvier, D.A. Knight, B. Bujoli, Surface Modification Using Phosphonic Acids and Esters, Chem. Rev. 112 (2012) 3777–3807. doi:10.1021/cr2004212.

[3] L.L. Rouhana, M.D. Moussallem, J.B. Schlenoff, Adsorption of short-chain thiols and disulfides onto gold under defined mass transport conditions: Coverage, kinetics, and mechanism, J. Am. Chem. Soc. 133 (2011) 16080–16091. doi:10.1021/ja2041833.

[4] A. Ulman, Formation and Structure of Self-Assembled Monolayers, Chem. Rev. 96 (1996) 1533–1554. doi:10.1021/cr9502357.

[5] V. Ganesh, V. Lakshminarayanan, Scanning Tunneling Microscopy, Fourier Transform Infrared Spectroscopy, and Electrochemical Characterization of 2-Naphthalenethiol Self-Assembled Monolayers on the Au Surface: A Study of Bridge-Mediated Electron Transfer in $Ru(NH_3)_6^{2+}$ |$Ru(NH_3)_6^{3+}$, J. Phys. Chem. B. 109 (2005) 16372–16381. doi:10.1021/jp052489u.

[6] R.P. Janek, W.R. Fawcett, A. Ulman, Impedance Spectroscopy of Self-Assembled

Monolayers on Au(111):Sodium Ferrocyanide Charge Transfer at Modified Electrodes, Langmuir. 14 (1998) 3011–3018. doi:10.1021/la970980+.

[7] A. Muthurasu, V. Ganesh, Electrochemical characterization of Self-assembled Monolayers (SAMs) of silanes on indium tin oxide (ITO) electrodes - Tuning electron transfer behaviour across electrode-electrolyte interface, J. Colloid Interface Sci. 374 (2012) 241–249. doi:10.1016/j.jcis.2012.02.007.

[8] K. Jo, H. Yang, Comparative study of stability of phosphonate self-assembled monolayers on indium-tin oxide electrodes prepared using different methods, J. Electroanal. Chem. 712 (2014) 8–13. doi:10.1016/j.jelechem.2013.10.022.

[9] R.V. Jagadeesh, V. Lakshminarayanan, Adsorption kinetics of phosphonic acids and proteins on functionalized Indium tin oxide surfaces using electrochemical impedance spectroscopy, Electrochim. Acta. 197 (2016) 1–9. doi:10.1016/j.electacta.2016.03.008.

[10] B.M. Silverman, K.A. Wieghaus, J. Schwartz, Comparative properties of siloxane vs phosphonate monolayers on a key titanium alloy, Langmuir. 21 (2005) 225–228. doi:10.1021/la0482271.

[11] C. Yan, M. Zharnikov, A. Golzhauser, M. Grunze, Preparation and characterization of self-assembled monolayers on indium tin oxide, Langmuir. 16 (2000) 6208–6215. doi:10.1021/La000128u.

[12] X. Han, X. Sun, T. He, S. Sun, Formation of highly stable self-assembled alkyl phosphonic acid monolayers for the functionalization of titanium surfaces and protein patterning, Langmuir. 31 (2015) 140–148. doi:10.1021/la504644q.

[13] B.J. Brennan, M.J. Llansola Portolés, P. a Liddell, T.A. Moore, A.L. Moore, D. Gust, Comparison of silatrane, phosphonic acid, and carboxylic acid functional groups for attachment of porphyrin sensitizers to TiO_2 in photoelectrochemical cells, Phys. Chem. Chem. Phys. 15 (2013) 16605. doi:10.1039/c3cp52156g.

[14] T.J. Gardner, C.D. Frisbie, M.S. Wrighton, Systems for orthogonal self-assembly of electroactive monolayers on Au and ITO: An approach to molecular electronics, J. Am. Chem. Soc. 117 (1995) 6927–6933. doi:10.1021/ja00131a015.

[15] P.J. Hotchkiss, M. Malicki, A.J. Giordano, N.R. Armstrong, S.R. Marder, Characterization of phosphonic acid binding to zinc oxide, J. Mater. Chem. 21 (2011) 3107–3112. doi:10.1039/c0jm02829k.

[16] A. Paszternák, I. Felhosi, Z. Pászti, E. Kuzmann, A. Vértes, E. Kálmán, L. Nyikos, Surface analytical characterization of passive iron surface modified by alkyl-phosphonic acid layers, Electrochim. Acta. 55 (2010) 804–812. doi:10.1016/j.electacta.2009.09.023.

[17] I. Levine, S.M. Weber, Y. Feldman, T. Bendikov, H. Cohen, D. Cahen, A. Vilan, Molecular length, monolayer density, and charge transport: Lessons from Al-AlOx/alkyl-phosphonate/Hg junctions, Langmuir. 28 (2012) 404–415. doi:10.1021/la2035664.

[18] I.L. Liakos, R.C. Newman, E. McAlpine, M.R. Alexander, Study of the resistance of SAMs on aluminium to acidic and basic solutions using dynamic contact angle measurement, Langmuir. 23 (2007) 995–999. doi:10.1021/la062233v.

[19] M. Chockalingam, N. Darwish, G. Le Saux, J.J. Gooding, Importance of the indium tin oxide substrate on the quality of self-assembled monolayers formed from organophosphonic acids, Langmuir. 27 (2011) 2545–2552. doi:10.1021/la104464w.

[20] J. Stotter, Y. Show, S. Wang, G. Swain, Comparison of the electrical, optical, and electrochemical properties of diamond and indium tin oxide thin-film electrodes, Chem. Mater. 17 (2005) 4880–4888. doi:10.1021/cm050762z.

[21] M.E. N.P.R.A. Silva, A.J.L. Pombeiro, J.J.R. Fraústo da Silva, R. Herrmann, N. Deus, R. E.Bozak, Redox potential and substituent effects in ferrocene derivatives: II, J. Organomet. Chem. 480 (1994) 81–90. doi:10.1016/0022-328X(94)87105-1.

[22] S.M. Batterjee, M.I. Marzouk, M.E. Aazab, M.A. El-Hashash, The electrochemistry of some ferrocene derivatives: Redox potential and substituent effects, Appl. Organomet. Chem. 17 (2003) 291–297. doi:10.1002/aoc.414.

[23] M.R. Anderson, M.N. Evaniak, M. Zhang, Influence of Solvent on the Interfacial Structure of Self-Assembled Alkanethiol Monolayers, Langmuir. 12 (1996) 2327–2331. doi:10.1021/la950294f.

[24] A. Fitch, Apparent formal potential shifts in ion exchange voltammetry, J. Electroanal.

Chem. 284 (1990) 237–244. doi:10.1016/0022-0728(90)87076-V.

[25] C.E.D. Chidsey, D.N. Loiacono, Chemical Functionality in Self -Assembled Monolayers: Structural and Electrochemical Properties, Langmuir. 6 (1990) 682–691. doi:10.1021/la00093a026.

[26] S. Shrikrishnan, V. Lakshminarayanan, Electron transfer studies of redox probes in bovine milk, J. Colloid Interface Sci. 370 (2012) 124–131. doi:10.1016/j.jcis.2011.12.070.

[27] P.S. Kumar, S.K. Pal, S. Kumar, V. Lakshminarayanan, Dispersion of thiol stabilized gold nanoparticles in lyotropic liquid crystalline systems, Langmuir. 23 (2007) 3445–3449. doi:10.1021/la063318z.

Chapter 5

Electron transfer studies on 3-Aminopropyltrimethoxy silane (APTMS) modified Indium Tin Oxide (ITO) at various pH

5.1. Introduction:

Self-assembled monolayers (SAMs) are formed by the spontaneous adsorption of small or long-chain, terminally functionalized amphiphilic molecules with a specific affinity of the head group to a solid substrate and organize into a more or less ordered domains [1–3]. SAMs can be used to suitably tailor the work function of surfaces, thereby minimizing the energy barriers for injection or extraction of charge carriers into or out of an active silane layer [4–6]. The precise control of surface parameters, ease of preparation, and ability to couple with the electrodes by the monolayer have led to many studies directing to scientific and technological applications like corrosion protection, surface adhesion, and wetting of bio- and analytical sensors, colloidal nanostructures, ligand stabilized metal nanostructures, biological immobilization of DNA, proteins, fabrication of nanodevices, and controlling the alignment, and orientation of liquid crystals, growth, and deposition of polymer films [3,7–9]. Trifunctional organosilanes ($RSiX_3$, X= -OR, -Cl) are sensitive to the presence of water. These three functional groups react with water on the surface of the adsorbate resulting in the formation of silanol. These silanols are very reactive and are polymerized by the homo-condensation reaction to form of Si-O-Si bond. The silanes also directly bind to hydroxyl terminated exteriors covalently by the formation of Si-O-M bond. This bond stabilizes the monolayer and also enables further chemical modification, without diminishing the quality of the monolayer. Silanes can form SAMs by solution or vapor phase deposition process. 3-aminopropyltrimethoxy silane (APTMS) modified solid surfaces are widely used to prepare substrates for applications using immobilized proteins and to prepare selective absorbents or organic/inorganic hybrid materials [10,11]. Chemisorbed APTMS on an inorganic surface provides a platform for further chemical reactions through terminal amine group of the silane. Due

to the presence of hydrophilic amino terminal functional group, APTMS modified surfaces can act as a platform for immobilization of bio-molecules like proteins and can be fixed onto the platform by non-covalent or covalent adsorption over the surface.

It has been shown previously that the surface inhomogeneities on the silane modified surfaces can trap macromolecules, dyes, and redox species and can act as soft embedding material for biological compounds [12–14]. Sagiv reported that silanes form disorganized monolayers with large pores and has the ability to reversibly adsorb macromolecules like dyes inside the film [13]. Tabushi *et al.* and Yamamura *et al*. silanized SnO_2 surface with a mixture of OTS and hexadecane followed by removal of the intercalated hexadecane by chloroform. This process resulted in the formation of a monolayer that was permeable by adsorbing vitamins K_1, K_2, and E into its vacant sites [15,16]. Markovich *et al.* studied the electron transfer behavior of OTS modified ITO towards $[Fe(CN)_6]^{3-/4-}$ and found that the redox species gets trapped in the monolayer during the voltammetric scan. It was suggested that OTS forms a disorganized monolayer film over the ITO surface and the gaps within the film are large enough to trap the redox species [17]. These adsorbed redox species can be identified by CV with a small peak separation indicating that the trapped redox species diffuses laterally inside the monolayer. The effect of long alkyl chain on the electron transfer behavior of various silane modified ITO surfaces was studied by Muthurasu *et al.* They showed that long chain alkyl silanes form better monolayer film by inhibiting the diffusion of redox species [18].

The interfacial properties of a monolayer surface are dependent on the nature of the terminal functional groups of the adsorbed species. Silanes adsorb readily onto the hydroxylated surfaces like silica, glass, TiO_2, and ITO by covalent bond can function as a support for immobilizing certain bio molecules like proteins. By maintaining certain hydrous conditions, it is possible to polymerize the adsorbed silane monolayer and the electron transfer studies on the films can provide new insights on the nature of the modified surfaces. The polymer film can acts as a soft surface for immobilizing the bio-molecules like lipids, proteins, *etc.*

There are only a few reports on the electron transfer studies on silane modified surfaces in literature [17,18]. In this work, the silane modification was carried out on a pre-treated semi-conducting ITO substrates using APTMS and the resulting surface was used for further studies. The electrochemical behavior of the APTMS/ITO was studied using cyclic voltammetry (CV) and

electrochemical impedance spectroscopy (EIS). The redox probes taken for the study are distinct in terms of their charge, ferro/ferricyanide $[Fe(CN)_6]^{3-/4-}$ (negative), ruthenium hexamine $[Ru(NH_3)_6]^{3+/2+}$ (positive), and ferrocene methanol (FcOH) (neutral). The electrochemical behavior of these redox species on the APTSM/ITO surface when studied by CV and EIS can provide some valuable information on the surface properties. It is to be noted that, APTMS film acts as a positively charged surface in acidic or neutral pH, which can influence the electron transfer process of a charged redox species. An analysis of pinholes and defects will be undertaken with the EIS studies, as it will help in better understanding of the electron transfer processes through the pores of the monolayer film. With this in view, experiments were performed in buffer at three different pH values namely at pH 4.1 (acidic), 7.0 (neutral), and 9.2 (basic).

The other part of this chapter deals with the immobilization of 1,2-dipalmitoyl-*sn*-glycero-3-phosphocholine (DPPC) and cytochrome *c* (*cyt c*) protein onto the APTMS/ITO electrode surface where α-cyclodextrin (α-CYD) is used as a promoter for better adhesion of *cyt c* to the surface. The effect of lipophiles like cholesterol, tetraphenylphosphonium iodide (TPP^+), and sodiumtetraphenylborate ($TPhB^-$) on DPPC immobilized surface was investigated. Electrocatalytic behavior of protein immobilized surfaces was studied using cyclic voltammetry. The morphological characteristics of the modified surface were studied by scanning electron microscopy (SEM) and atomic force microscopy (AFM).

5.2. Experimental Section:

5.2.1. Chemicals:

3-aminopropyltrimethoxy silane, (97%, Aldrich), toluene (SD fine), monosodium dihydrogen phosphate, (>99%, Aldrich), and disodium hydrogen phosphate, (>99.5%, Aldrich) were employed to prepare required solutions for our studies. In addition, potassium ferrocyanide trihydrate (98.5%, Aldrich), potassium ferricyanide (99.98%, Aldrich), hexamine ruthenium (III) chloride, (99.9%, Aldrich), hexamine ruthenium (II) chloride, (99.9%, Aldrich), and ferrocene methanol, (97%, Aldrich), α-cyclodextrin (98%, Aldrich) were used for our studies. 1,2-dipalmitoyl-*sn*-glycero-3-phosphocholine (>99%, Sigma Aldrich), tetraphenylphosphonium iodide (>98%, Aldrich), cholesterol (>99%, Aldrich), and sodium teteraphenylborate (>99.5%, Aldrich) were used for microscopy studies. Cytochrome *c* from bovine heart were purchased from

Sigma Aldrich. All these chemicals were used as received without any further purification. Millipore water having a resistivity of 18MΩcm was used to prepare all the aqueous solutions. For electrochemical studies, this ITO plates of geometric area of 4mm X 10mm and were used as strips.

5.2.2. Electrode pre-treatment and electrochemical cell:

Prior to the surface modification of ITO strips with APTMS, they were cleaned ultrasonically using acetone, ethanol, and water in succession for 15 minutes. Later, they were immersed in an aqueous solution, for pre-treatment, consisting of hydrogen peroxide, liquid ammonia, and water in the ratio of 1:3:10 for about an hour. Finally, the pre-treated ITO strips were rinsed with Millipore water several times and immediately used for further studies. A three-electrode electrochemical cell was used for electrochemical characterization. A platinum foil and saturated calomel electrode (SCE) were used as counter and reference electrodes, respectively. Bare ITO and APTMS/ITO modified electrodes were employed as working electrodes.

5.2.3. SAM formation on ITO electrodes:

Pre-cleaned ITO strips were used as electrodes for modification and subsequent characterization. Phosphate buffers of different pH has been used in order to investigate the effect of pH on the electron transfer process across electrode–electrolyte interface. The corresponding monolayer films prepared by immersing the pre-cleaned ITO electrodes into 10mM solution of APTMS in toluene for about 14–15 hours. Next, the APTMS/ITO electrodes were taken out, ultra-sonicated in toluene three times for five minutes each. Later these strips were rinsed with excess of toluene and washed thoroughly with Millipore water. Finally, these electrodes were dried under a stream of nitrogen gas and immediately used for morphological and electrochemical characterizations.

1mg of 1,2-dipalmitoyl-*sn*-glycero-3-phosphocholine (DPPC) was taken in a 10ml glass beaker and dissolved in 5ml of Millipore water, sonicated for fifteen minutes to get the right dispersion of phospholipid. Immediately, after sonication, the beaker is transferred to a thermostat at 41°C for an hour and removed. APTMS modified ITO substrates were immersed in DPPC solution for 6 hours and later washed vigorously with Millipore water to remove any loosely adhering lipid molecules.

1mg of cholesterol, tetraphenylphosphonium iodide, and sodium tetraphenylborate were dissolved in chloroform solvent using separate beakers for each. DPPC modified APTMS/ITO substrates were transferred into each compartment and kept for an hour for adsorption. The substrates were later removed and washed with chloroform to remove loosely attached species. These substrates were analyzed by atomic force microscopy (AFM) for morphological characterization.

1mg of α-cyclodextrin (α-CYD) is dissolved in 1ml of water and the APTMS/ITO substrate is kept immersed in the solution for 4 hours at room temperature. Adsorption of α-CYD on APTMS/ITO is non-specific which adheres to the underlayer by physisorption. Cytochrome *c* (*cyt c*) immobilization is carried out by immersion of APTMS/ITO and α-CYD/APTMS/ITO electrodes in 0.2mg/ml concentrated *cyt c* solution for 12 hours at 4°C. The *cyt c* solution is prepared by dissolving 1mg of *cyt c* in 5ml of 0.1M phosphate buffer of pH=7. The *cyt c* is immobilized onto APTMS/ITO surface by immersion of substrate in *cyt c* solution for 12 hours at 4°C.

5.2.4. Electrochemical characterization of SAMs on ITO:

The electron transfer behavior of APTMS/ITO electrode was investigated using electrochemical techniques, namely CV and EIS. The CV studies were carried out at a scan rate of 50mV/s in an aqueous solution of phosphate buffer of pH 4.1, 7, and 9.2 prepared by mixing 0.2M Na_2HPO_4 and 0.2M NaH_2PO_4 appropriately. The barrier to electron transfer process by APTMS film was analyzed using standard redox probes with negative, positive, and neutral charges. Impedance measurements were carried out by applying an AC signal of 10mV amplitude at formal potential of the respective redox probes using a wide frequency ranging from 100 kHz to 0.1 Hz. The electrolyte solution containing equal concentrations of both the oxidized and reduced forms, namely 1mM $[Fe(CN)_6]^{3-/4-}$ and 1mM $[Ru(NH_3)_6]^{3+/2+}$ in 0.2M phosphate buffer medium was employed for the study. A neutral redox probe of ferrocene methanol was also used for the study.

5.2.5. Instrumentation:

CV and EIS measurements were carried out using EG&G potentiostat model 263A and Perkin-Elmer Lock-In-Amplifier Model 5210. The CV experiments and the analysis of data were performed using PowerSUITE software provided by EG&G Inc. The potential ranges and scan

rates used for the study were shown in the respective diagrams. The impedance data were fitted to an appropriate equivalent circuit model using ZSimpWin software developed on the basis of Boukamp's model.

5.3. Results and discussion:

5.3.1. Surface morphological studies of bare ITO, APTMS/ITO unannealed, and annealed using SEM and AFM:

Figure 1 (A-C) shows the scanning electron microscopy (SEM) and figure 1 (D-F) shows the atomic force microscopy (AFM) images of bare ITO, APTMS/ITO (unannealed), and APTMS/ITO (annealed) substrates. Bare ITO shows crystallite features of various sizes with well demarcated boundaries (figure 1D). The adsorption of APTMS onto ITO is carried out by solution deposition technique in which pre-treated ITO strips were immersed for 12 hours in 1mM APTMS/toluene solution. Figure 1B shows the SEM image of the unannealed APTMS surface consisting of globular shaped domains of different sizes, whereas the annealed APTMS shows herring bone structures which clearly distinguishes it from the former. The phase contrast AFM images in figure 1 (D-F) show much finer features for the corresponding samples whose SEM images are shown in figure 1 (A-C).

From SEM image of figure 1C, where worm like features are seen, it is inferred that APTMS is adsorbed onto the ITO surface in the polymeric form. Due to the presence of moisture in solution and on the surface of ITO substrate, APTMS undergoes condensation reaction with adjacent silanol groups to form Si-O-Si linkage [19]. Iwasa *et al.* and Woodward *et al.* individually studied the *in situ* SAM formation of octadecyltrimethoxysilane (ODTMS) onto silicon oxide surface using AFM. They suggested that the adsorption of ODTMS proceeds in clusters which act as nucleation centers, on which additional reactive molecules aggregate [20,21].

The APTMS molecules adsorb on the chemisorbed water layer present on the hydrated ITO substrate and diffuse towards the primary island. These molecules after immobilization aggregate around the perimeter of the primary island [22]. This reaction occurs in parallel along with the hetero-condensation of silanes where the APTMS molecules react with the hydroxyl groups of the pre-treated ITO surface. Therefore, the APTMS molecules adsorb as monomer in some regions

while predominantly forming a polymer which appear as thread like features in the SEM image (Figure 1C). Heat treatment of APTMS/ITO surface changes the surface morphology of the polymer, since at a temperature range of 100-200°C, silanes undergo hydrolysis faster [23].

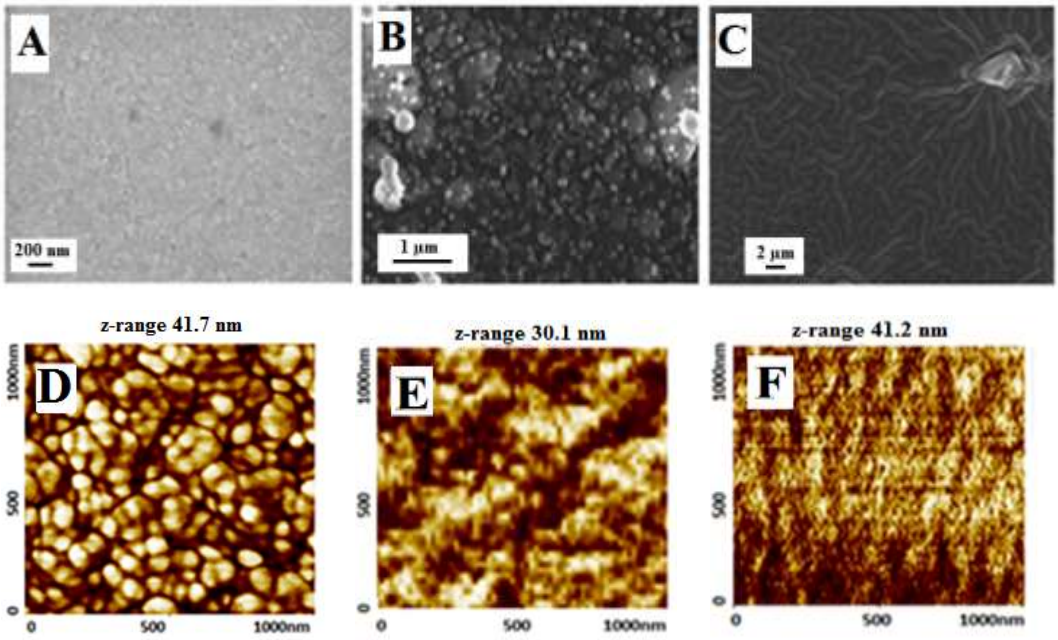

Figure 1. *SEM images of (A). Bare ITO, (B). APTMS unannealed and (C). APTMS annealed phase AFM images of (D). Bare ITO, ©. APTMS unannealed and (F). APTMS annealed of 1µm* x *1µm area.*

According to the earlier reports, silanization of silicon oxide substrates with 3-aminopropyltriethoxysilane (APTES) have shown that the *in situ* deposition at elevated temperatures (~70 °C) enhanced the hydrolysis of ethoxy groups which increases the number of binding functional groups of the silane [24]. This suggests that APTMS is a soft polymer that has a tendency to change its structure during the process of heat treatment. APTMS consists of unreacted silanol groups even after adsorption and these silanols are also very reactive. During the annealing process, neighboring silanol groups undergo homocondensation and form a Si-O-Si cross linkage [25]. Due to the integrated aggregation of the adjacent APTMS fragments, the chain length of the polymer increases resulting the worm like features.

Figure 2 shows the topographical AFM images of bare ITO, APTMS/ITO unannealed, and annealed samples at 10µm x 10µm resolution. APTMS/ITO shows a vast contrast in its

morphology depending on the surface treatment, whereas the bare ITO consists of a fine grain structures. The height profiles of the substrates are given below the respective phase images. The average grain size of bare ITO surface is around 10-15nm, while unannealed APTMS surface shows height profiles of 160nm and the annealed APTMS is around 200-250nm. This substantial change in the surface height after annealing takes place owing to the surface polymerization of APTMS on ITO.

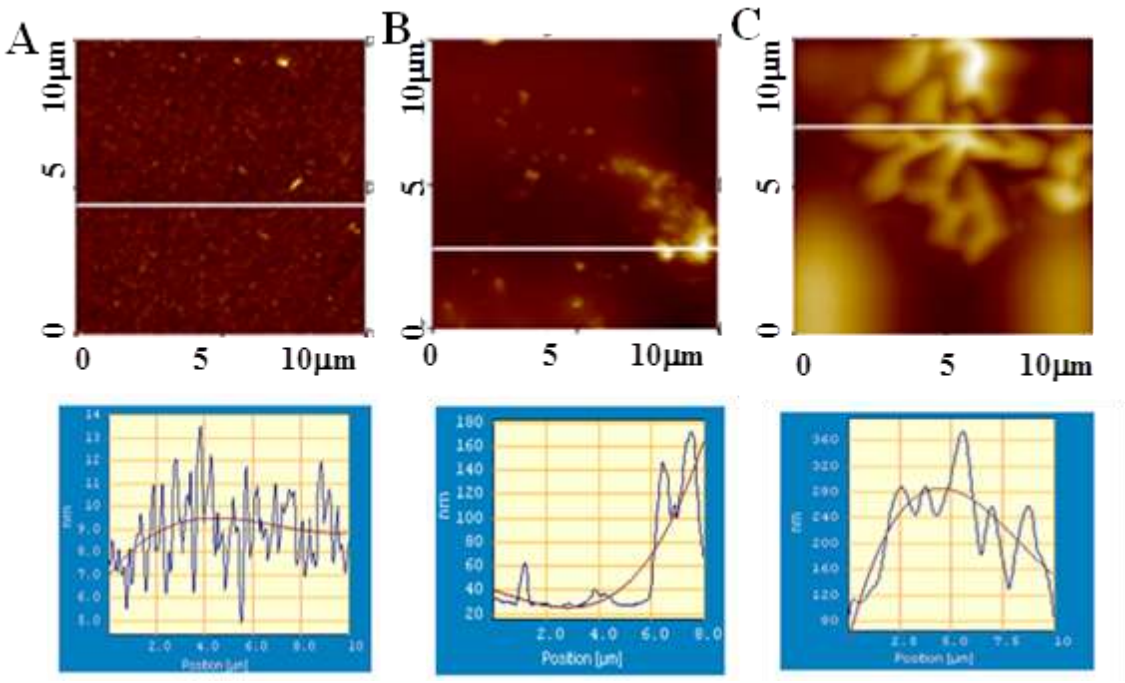

Figure 2. *Topography images of (A). Bare ITO, (B). APTMS/ITO unannealed, and (C). APTMS/ITO annealed and the respective height profiles are given below the individual images.*

5.3.2. Electron transfer studies:

The electron transfer behavior of three redox species *viz.*, ferro/ferricyanide $[Fe(CN)_6]^{3-/4-}$, hexammineruthenium $[Ru(NH_3)]^{3+/2+}$, and ferrocene methanol species were studied on the bare ITO, APTMS/ITO electrodes as well as at different pH conditions in order to understand the effect of surface protonation of APTMS on the electron transfer process.

5.3.2.1. Potassium ferri/ferrocyanide:

5.3.2.1.1. Cyclic voltammetry studies:

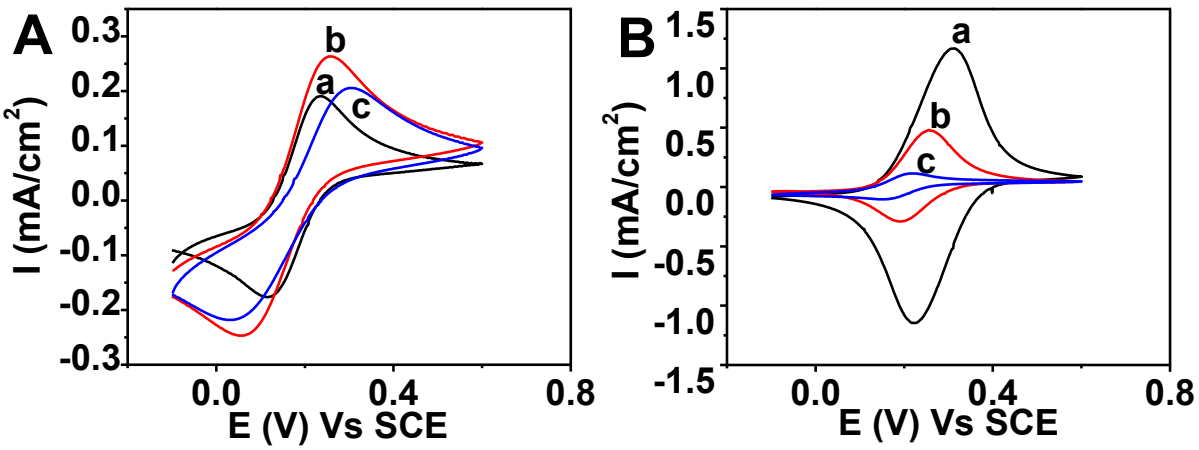

Figure 3. *Cyclic voltammograms of 1mM potassiumferri/ferrocyanide $K_{3/4}[Fe(CN)_6]$ redox couple using 0.2M phosphate buffer solution as a supporting electrolyte on (A) bare ITO, (B) APTMS/ITO in (a) acidic, (b) neutral, and (c) basic pH conditions.*

Figure 3 shows the CVs of bare ITO and APTMS/ITO electrodes in 1mM $[Fe(CN)_6]^{3-/4-}$ redox couple at a scan rate of 50mV/s using 0.2M phosphate buffer as a supporting electrolyte. Phosphate ions have high affinity towards hydroxylated metal surfaces [19]. They bind to the metal oxide by the removal of hydroxyl group from the oxide surface by the reaction of proton to form a P-O-M covalent bond. Due to the formation of phosphate layer on ITO surface, the access of the negatively charged redox couple towards the electrode surface is inhibited by the phosphate monolayer at the ITO electrode [26]. As can be seen in figure 3A, the electron transfer process is quasi-reversible at the pre-treated ITO surface. From Table 1, we observe that electron transfer behavior at the bare ITO surface is irreversible for the redox couple. Figure 3B (a), shows the CV of 1mM $[Fe(CN)_6]^{3-/4-}$ towards APTMS/ITO electrode in acidic pH conditions. The peak currents are higher by nearly five times in acidic buffer with the modification of APTMS onto the ITO surface. Moreover, the half peak potentials for the redox couple are shifted positive and peak separation is also lowered. The positive potential shift can be attributed to the electrostatic binding interactions between negatively charged redox couple and positively charged APTMS film. The bound species needs more positive potential to dissociate and undergo redox reaction. However, a negative shift in the

half peak potential with a decrease in peak currents is observed with increase in pH of phosphate buffer. This behavior can be attributed to the deprotonation of the surface amino groups and consequent reduction of the positive surface charges, thereby lowering the coulombic binding with the negatively charged $[Fe(CN)_6]^{3-/4-}$. Evidently, the electrostatic binding is more pronounced at acidic pH due to the large number of positively charged amino groups of APTMS on the surface.

Table 1. Half peak potential ($E_{1/2}$) (mV), Peak separation (ΔE_p) (mV), and average peak current (I_p) (mA/cm^2) values obtained for $[Fe(CN)_6]^{3-/4-}$ redox couple on bare ITO and APTMS/ITO electrodes

pH	Bare ITO			APTMS		
	$E_{1/2}$	ΔE_p	I_p	$E_{1/2}$	ΔE_p	$I_p^{\#}$
Acidic	173.2	129.7	0.2	221.0	82.3	1.1
Neutral	156.7	200.4	0.2	178.7	63.1	0.2
Basic	167.0	263.0	0.2	170.2	66.6	0.1

$^{\#}I_p = (I_p^a + I_p^c)/2$

5.3.2.1.2. Electrochemical Impedance spectroscopy studies:

Figure 4 shows Nyquist plots of 1mM $[Fe(CN)_6]^{3-/4-}$ on (A). bare ITO and (B). APTMS/ITO electrodes in 0.2M phosphate buffer supporting electrolyte at (a) acidic, (b) neutral, and (c). basic pH solutions. Charge transfer resistance (R_{ct}) and double layer capacitance (C_{dl}) were measured by fitting the measured data with Randles equivalent circuit that consists of electrolyte resistance (R_s) in series with the parallel combination of the double-layer capacitance (C_{dl}) and faradaic impedance. In figure 4A, the bare ITO shows a semi-circle followed by a straight line indicating a partial charge transfer and diffusion controlled electron transfer process.

5.3.2.1.3. Effects of surface charge density of APTMS on the redox process:

Modification of ITO with APTMS shows a significant decrease in R_{ct} at all pH conditions studied here. However, the R_{ct} value is lowest in acidic pH and the C_{dl} value is also quite large compared to basic and neutral medium. The changes observed in R_{ct} and C_{dl} values, with increase in pH are due to the decrease in positive charges of APTMS polymer. At low pH, positive charge density of the APTMS polymer is high as it is highly protonated such that a significant amount of negatively

charged redox species can be trapped within the polymer film. Due to this phenomenon, a substantial decrease in R_{ct} and increase in C_{dl} were observed. The effect of electrostatic attractions in neutral and basic pH conditions is significantly lower as the polymer surface charge density is diminished. At acidic pH conditions, a significant amount of negatively charged $[Fe(CN)_6]^{3-/4-}$ redox species is trapped onto the positively charged polymer film (Table 7) thereby creating a high interfacial capacitive component. However, with increase in pH, there is a large decrease in capacitance of the modified surface, as the amount of redox species trapped within the film decreases significantly at higher pH levels (Table 2). Consequently, the current decreases and the charge transfer resistance (R_{ct}) values increase with pH of the solution. It is therefore clear that, the electrostatic interactions play a key role in determining the electron transfer behavior of different redox species at the APTMS modified ITO surface.

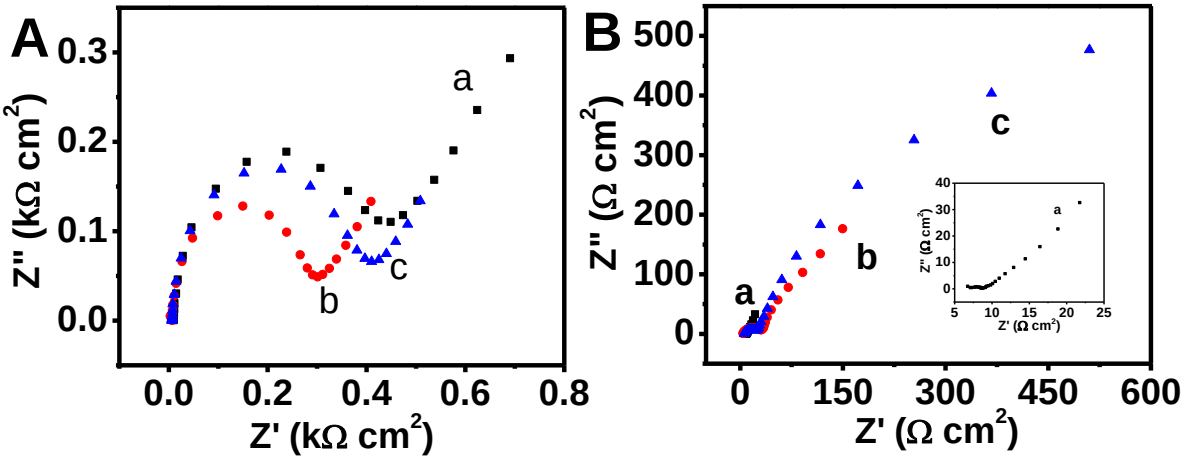

Figure 4. *Nyquist plots of (A). Bare ITO and (B) APTMS/ITO substrates in 1mM* $[Fe(CN)_6]^{3-/4-}$ at (a). acidic, (b) neutral, and (c) basic pH using 0.2M phosphate buffer supporting electrolyte.

Table 2. Charge transfer resistances (R_{ct}) (Ωcm^2), Interfacial capacitance (C_{dl}) ($\mu F/cm^2$) values obtained for $[Fe(CN)_6]^{3-/4-}$ at various pH conditions

pH	Bare ITO		APTMS/ITO	
	R_{ct}	C_{dl}	R_{ct}	C_{dl}
Acidic	367.5	15.7	0.006	1251.0
Neutral	260.8	17.0	17.4	8.3
Basic	351.5	16.4	7.7	5.3

5.3.2.2. Ruthenium hexammine $[Ru(NH_3)_6]^{3+/2+}$:

5.3.2.2.1. Cyclic voltammetry studies:

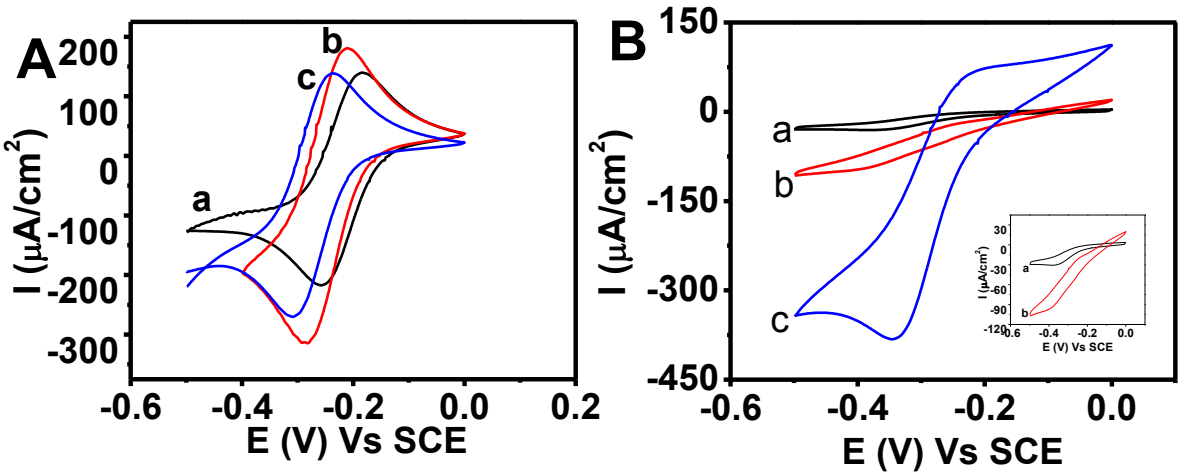

Figure 5. *Cyclic voltammograms of (A) bare ITO, (B) APTMS/ITO in 1mM $[Ru(NH_3)_6]^{3+/2+}$ using 0.2M phosphate buffer at (a) acidic, (b) neutral, and (c) basic pH conditions.*

Figure 5 shows the CV of bare ITO and APTMS/ITO electrodes at a scan rate of 50 mV/s in 1mM $[Ru(NH_3)_6]^{3+/2+}$ redox couple using 0.2M phosphate buffer supporting electrolyte. The electron transfer at bare ITO shows two distinct redox peaks corresponding to ruthenium hexamine (III/II) redox couple (figure 5A (a-c)). The peak separation values of about 78mV obtained from the cyclic voltammogram suggests a quasi-reversible electron transfer behavior of the redox couple at the bare ITO electrode surface. While APTMS/ITO shows no oxidation peak during the positive scan in acidic and neutral pH conditions, well resolved redox peaks were observed in basic pH

conditions. CVs of $[Ru(NH_3)_6]^{3+/2+}$ in acidic and neutral pH show sigmoidal shaped curves corresponding to microelectrode array type behavior of the APTMS/ITO electrode. The peak currents are lower at acidic pH conditions and increase at higher pH. The poor electron transfer blocking of the APTMS film at basic conditions suggest a disorganized nature of the surface film [27,28]. In the case of $[Ru(NH_3)_6]^{3+/2+}$ redox couple, the electron transfer at APTMS/ITO surface can occur in two ways: (1) electron transfer through the film *via* a tunneling process, and (2) permeation of electroactive species through the film and followed by electron transfer at the electrode surface [29]. Since, the tunneling phenomenon can be excluded due to the large thickness of (Figure 3) the APTMS film, electron transfer can occur mainly by diffusion through the film [30]. The permeation of a $[Ru(NH_3)_6]^{3+/2+}$ redox couple through APTMS film is restricted in acidic and neutral pH conditions due to the electrostatic repulsions between positively charged film and redox couple. However, it is not hindered at basic pH conditions due to deprotonation and negligible surface charge density.

$[Ru(NH_3)_6]^{3+/2+}$ can undergo outer sphere electron transfer on a simple monolayer covered electrode surface which therefore should not cause any decrease in peak currents if the film is of molecular thickness [28]. The observed reduction of peak currents in this case can therefore be attributed to the blocking by polymeric film of APTMS on ITO which has a thickness of about 250 nm (from height profiles of figures 2B and C). In addition to this, lower current is also caused by the electrostatic repulsion between APTMS/ITO surface and positively charged $[Ru(NH_3)_6]^{3+/2+}$ redox couple.

Table 3. Half peak potential ($E_{1/2}$) (mV), peak separation (ΔE_p) (mV) and average peak current (I_p) ($\mu A/cm^2$) values for $[Ru(NH_3)_6]^{3+/2+}$ obtained for bare ITO and APTMS/ITO electrodes.

pH	Bare ITO			APTMS		
	$E_{\frac{1}{2}}$	ΔE_p	I_p	$E_{\frac{1}{2}}$	ΔE_p	I_p
Acidic	-218.8	71.9	175.2	N/A	N/A	N/A
Neutral	-248.1	78.4	247.3	N/A	N/A	N/A
Basic	-274.3	70.6	203.6	-284.3	108.9	223.0

5.3.2.2.2. Electrochemical impedance spectroscopy studies:

Nyquist plots of bare ITO and APTMS/ITO in 1mM $[Ru(NH_3)_6]^{3+/2+}$ at (a) acidic, (b) neutral, and (c) basic pH using 0.2M phosphate buffer at half peak potential of -0.19V vs. SCE for ruthenium hexamine (III/II) redox couple are shown in figure 6. It can be seen that the impedance plot shows a straight line for bare ITO in all pH conditions which suggests that electron transfer is fully under diffusion control (Figure 6A). Modification of ITO with APTMS leads to a full semi-circle in the Nyquist plot, which suggests that diffusion of redox species through the film is completely blocked. Therefore, the reaction is entirely under charge transfer control in the case of acidic and neutral pH conditions. In basic conditions, APTMS/ITO shows a semi-circle at high frequencies followed by a straight line at low frequencies suggesting the electron transfer at the electrode surface is partially controlled by charge transfer and rest by mass transfer of the redox species. Solution resistance (R_s) values follow a decreasing trend with increasing pH conditions of the solution in case of APTMS/ITO (zoomed portion of figure 6). The measured R_s values are 11.5, 7.7 and 6.9Ω for acidic, neutral and basic buffer solutions respectively.

Nyquist plots of $[Ru(NH_3)_6]^{3+/2+}$ on bare ITO is fitted with Randles equivalent circuit, (Figure 6A inset) while that on APTMS/ITO with the same equivalent circuit along with the inclusion of parallel RC element which represents the film resistance and capacitance of the APTMS film which is connected in parallel to the charge transfer resistance and faradaic impedance (Figure 6B inset). Due to the surface modification of ITO with APTMS polymer film, there is an increase in R_{ct} value and a corresponding decrease in C_{dl} values. The increase in R_{ct} value is due to the formation of thick polymeric film of APTMS onto ITO and also due to the electrostatic repulsion between positively charged APTMS and positively charged ruthenium hexamine redox couple, which inhibits the diffusion of the redox species to the electrode surface through the film. The charge transfer resistance (R_{ct}) and interfacial capacitance (C_{dl}) of the APTMS film for the modified electrodes are measured to be 2731, 1070, and 112.5Ωcm^2, 48.7, 98.9, and 26.5μF/cm^2 in acidic, neutral, and basic pH conditions respectively. The high electrostatic repulsion between the positively charged APTMS film and similarly charged redox couple results in higher charge transfer resistance due to the coulombic repulsions within the film which is reflected in R_s values. The C_{dl} value increases from acidic to neutral pH and decreases again from neutral to basic pH. This can be attributed to the high positive charge density on the APTMS film at low pH, which

increases the separation gap between the electrode surface and the positively charged redox species. Due to this large separation gap, there is a decrease in capacitance observed. However, the separation between redox species and the electrode is less in neutral medium compared to the acidic medium which again increases the capacitance. The low capacitance values at basic pH conditions correspond to the decreased charge density on the APTMS film (Table 4).

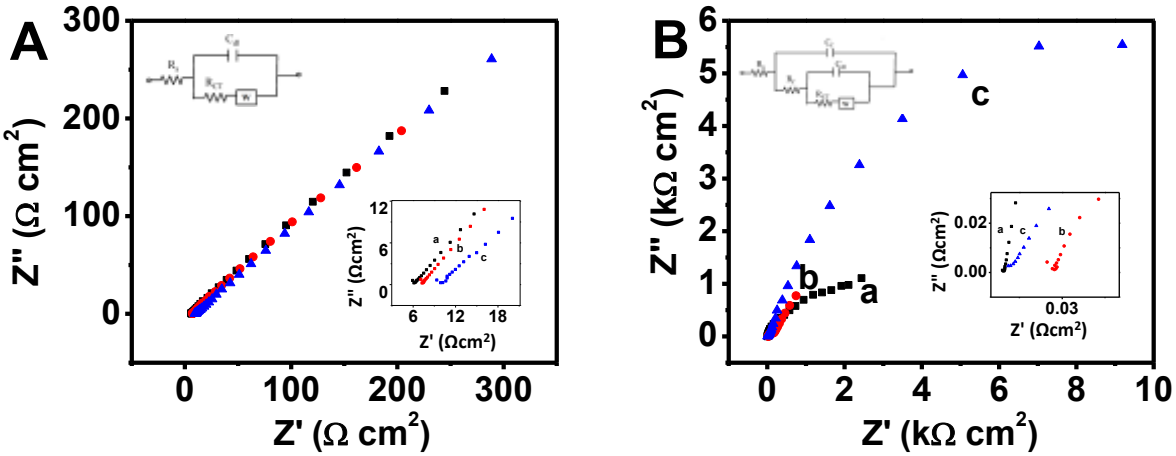

Figure 6. *Nyquist plots of 1mM $[Ru(NH_3)_6]^{3+/2+}$ at (A). Bare ITO, (B). APTMS/ITO at (a) acidic, (b) neutral and (c) basic pH using 0.2M phosphate buffer supporting electrolyte at half peak potentials vs. SCE (**Inset:** High frequency regions of Nyquist plots).*

Table 4. Charge transfer resistance (R_{ct}) (Ωcm^2), Interfacial capacitance (C_{dl}) ($\mu F/cm^2$) values obtained for $[Ru(NH_3)_6]^{3+/2+}$ at various pH conditions.

pH	Bare ITO		APTMS/ITO	
	R_{ct}	C_{dl}	R_{ct}	C_{dl}
Acidic	0.01	24.8	2731	48.7
Neutral	0.01	34.5	1070	98.9
Basic	1.0	7.3	112.5	26.5

5.3.2.3. Ferrocenemethanol (FcOH):

5.3.2.3.1. Cyclic voltammetry studies:

Figure 7 show CVs of bare ITO and APTMS/ITO in 1mM FcOH using 0.2M phosphate buffer as a supporting electrolyte. In previous cases, the electron transfer behavior of ionic redox species $[Fe(CN)_6]^{3-/4-}$ and $[Ru(NH_3)_6]^{3+/2+}$ were studied to understand their electron transfer behavior on charged surfaces. In this case, a neutral redox species, ferrocenemethanol, a neutral charged redox species, is chosen as a candidate for studying the electron transfer process on the APTMS modified ITO surface. Figure 7A shows a CV exhibiting irreversible electron transfer behavior of FcOH species in (a) acidic, (b) neutral, and (c) basic pH conditions on the bare ITO surface (Table 5). Modification of ITO by APTMS results in blocking the electron transfer of redox species at all the pH conditions. In acidic conditions, two redox peaks were observed with a small peak separation, while in neutral pH conditions, a single oxidation peak is observed. However, at basic pH conditions, both the redox peaks are observed but with relatively larger currents. The electron transfer reaction for ferrocene methanol is completely blocked at acidic and neutral pH conditions. This behavior can be explained by the fact that non-polar ferrocene group in ferrocene methanol stays away from the polar APTMS surface, thereby inhibiting the electron transfer process. In acidic pH solution, the APTMS film is highly charged and polar which inhibits the approach of non-polar part of the ferrocene methanol close to the electrode. The charge density of APTMS, however, decreases with increase in the pH of the solution as more redox species accesses the electrode surface in basic pH conditions. This decrease in charge density over APTMS surface results an increase in redox current as seen in a larger peak current at basic pH (Figure 7B (c)).

However, in basic conditions, the film is uncharged and there is a favorable orientation of -OH group with $-NH_2$ groups of APTMS due to the formation of hydrogen bond. The distinct peaks observed at basic pH for ferrocene redox reaction is due to the closest approach of redox species to the electrode surface due to the H-bonding. However, the large peak separation observed for the redox couple shows that the electron transfer process is under charge transfer control at this pH. The decrease in currents, when compared to that of bare ITO surface (figure 7A, 7B), in basic pH also suggests that APTMS film acts as an effective barrier for the electron transfer reaction through the film.

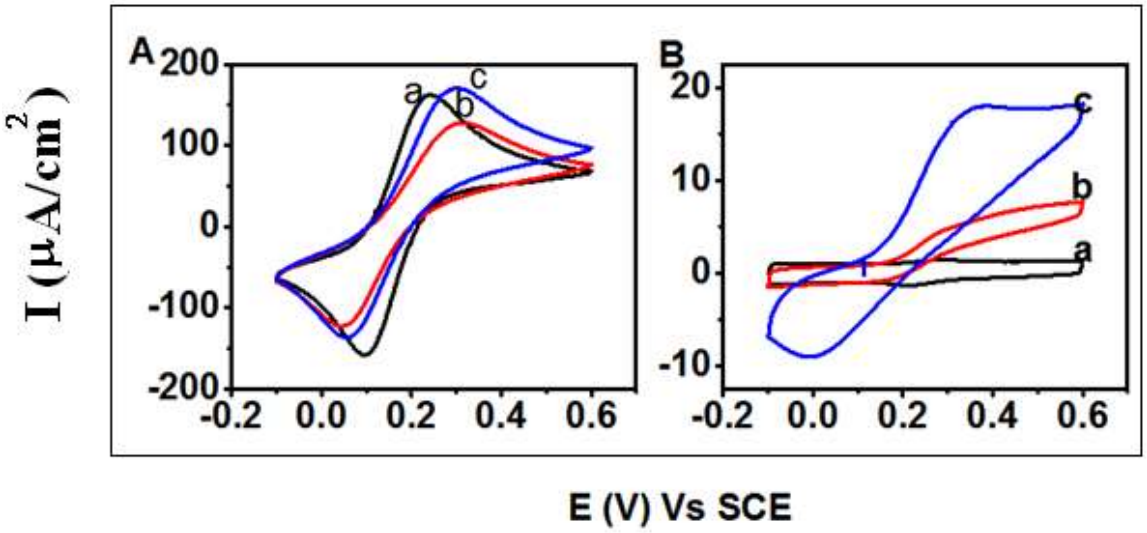

Figure 7. *Cyclic voltammograms of (A) Bare ITO, (B) APTMS/ITO in 1mM ferrocene methanol (FcOH) using 0.2M phosphate buffer at (a) acidic pH, (b) neutral pH, and (c) basic pH conditions.*

Table 5. Half peak potential ($E_{1/2}$) (mV), peak separation (ΔE_p) (mV), and average peak current (I_p) ($\mu A/cm^2$) values obtained for ferrocene methanol on bare ITO and APTMS modified ITO.

pH	Bare ITO			APTMS		
	$E_{\frac{1}{2}}$	ΔE_p	I_p	$E_{\frac{1}{2}}$	ΔE_p	I_p
Acidic	168.2	141.7	160.0	N/A	N/A	N/A
Neutral	179.3	267.6	120.4	N/A	N/A	N/A
Basic	174.5	242.7	152.7	168.3	352.7	13.5

5.3.2.3.2. Electrochemical impedance spectroscopy studies:

Nyquist plots obtained for 1mM ferrocenemethanol at (a) acidic, (b) neutral, and (c) basic pH conditions at half peak potential of the redox species (0.18V) are shown in figure 8. Bare ITO (figure 8A) shows a semi-circle followed by a rising imaginary component of impedance implying that electron transfer is charge transfer as well diffusion controlled. However, the APTMS/ITO

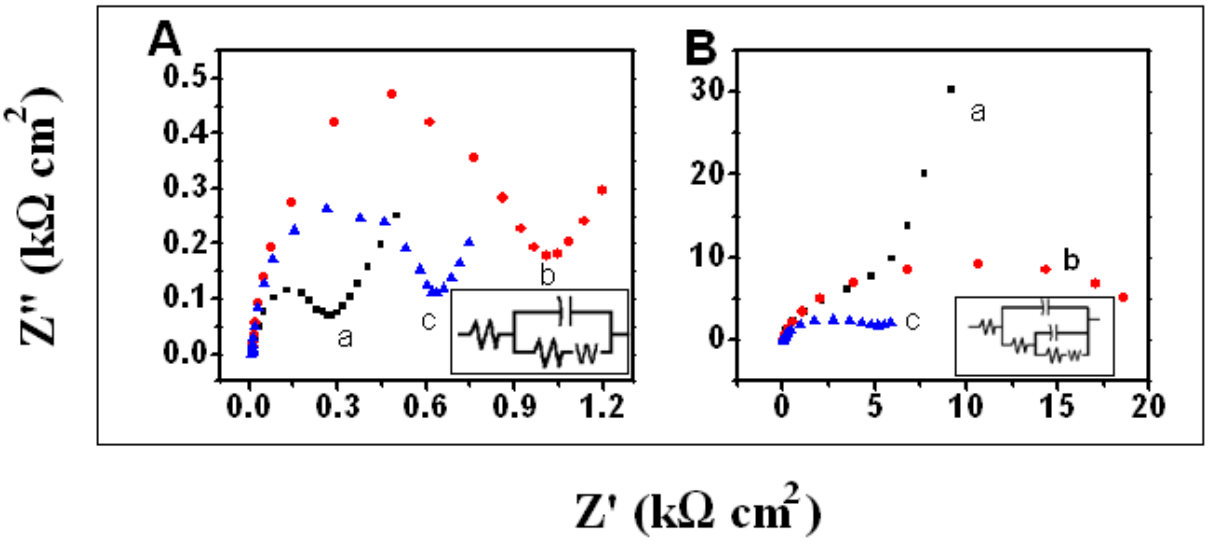

Figure 8. *Nyquist plots obtained for 1mM ferrocene methanol at (A). bare ITO and (B). APTMS/ITO using 0.2M phosphate buffer solution at (a). acidic pH, (b). neutral pH, and (c). basic pH.*

electrode shows depressed semi-circles in the case of acidic and neutral pH conditions. The rising portion at lower frequencies at acidic pH conditions corresponds to the second incomplete semi-circle. Nyquist plots obtained for bare ITO substrate are fitted to a simple Randles equivalent circuit, while for APTMS/ITO an additional RC component (R_f,C_f) is added in parallel. The R_{ct} and C_{dl} values obtained for bare ITO and APTMS/ITO are shown in Table 6. R_f and C_f values attained for bare ITO and APTMS/ITO are 1.4 x 10^4 and 4239Ωcm^2, 16 and 11.5μF/cm^2 for acidic and neutral pH conditions, respectively. Modification of ITO with APTMS film shows an increase in R_{ct} and C_{dl}. This can be attributed to the positive charges on the APTMS film by the polar amino group. The large R_{ct} values seen in acidic pH conditions decreases with increase in pH for the same reason as explained in the case of cyclic voltammetry (figure 7B). A highly polar and charged APTMS film inhibits the close access of the non-polar ferrocene methanol in acidic conditions. However, with increase in pH, there is a decrease in the charge density of the APTMS film which allows closer access of the redox species. This is also facilitated by the hydrogen bonding between amino groups of APTMS and hydroxyl groups of ferrocene methanol. This results in the lower R_{ct} values at higher pH.

Table 6. Charge transfer resistances (R_{ct}) (Ω cm^2), Interfacial capacitance (C_{dl}) ($\mu F/cm^2$) values obtained for ferrocene methanol at various pH conditions.

pH	Bare ITO		APTMS/ITO			
	R_{ct}	C_{dl}	R_{ct}	C_{dl}	R_f	C_f
Acidic	221.9	14.0	$4.9x10^5$	34.1	$1.4x10^4$	16.0
Neutral	7236	1.6	$1.5x10^4$	7.5	4239.0	11.5
Basic	4489	1.8	4120	12.5	--	--

5.3.4. Adsorption of $[Fe(CN)_6]^{3-/4-}$:

It should be pointed out that, a large amount of $[Fe(CN)_6]^{3-/4-}$ redox species is trapped within APTMS film which undergo a surface confined electron transfer. This can be seen from the cyclic voltammograms of the electrode in the corresponding supporting electrolyte alone after scanning in the presence of the redox species (figure 9). It shows that the positively charged APTMS has the ability to adsorb and incorporate within itself the negatively charged redox species of $[Fe(CN)_6]^{3-/4-}$ onto the polymeric film. This adsorbed redox species diffuse through the film and undergoes electron transfer which can be seen from the redox peaks of figure 9. By integrating the cyclic voltammetric peak obtained by APTMS/ITO electrode in supporting electrolyte, it is possible to measure the amount of $[Fe(CN)_6]^{3-/4-}$ adsorbed or incorporated in APTMS film.

Markovich *et al*. observed that disorganized octadecyltrichlorosilane (OTS) films on ITO has the ability to trap redox active amphiphiles like methylviologen and these trapped redox species diffuse laterally in the monolayer and interact with the analyte [12]. Harder *et al.* co-adsorbed 17-aminoheptadecyltrimethoxysilane (AHTMS) onto OTS modified Si (100) substrate and characterized the presence of AHTMS using XPS. Adsorption of AHTMS onto OTS/ITO is due to the presence of voids formed in the monolayer due to its disorganized structure [31].

Amount of redox species adsorbed into the silane film can be determined by using the following expression:

$$\Gamma = \frac{Q}{nFA} \longrightarrow (1)$$

Γ = amount of species adsorbed (moles/cm^2), Q = charge produced by the adsorbed species from the solution, n = number of electrons, F = faraday (1F =96,500 Coulomb), and A = area of the electrode (cm^2).

From Table 7, it can be observed that at low pH values where APTMS film is positively charged, a relatively large amount of the negatively charged redox species is adsorbed (5.2 x 10^{-8} F/cm^2). The amount of redox species getting incorporated within the polymer film decreases with the increase in pH of the phosphate buffer as the electrostatic interaction also decreases due to the reduced surface charges at higher pH.

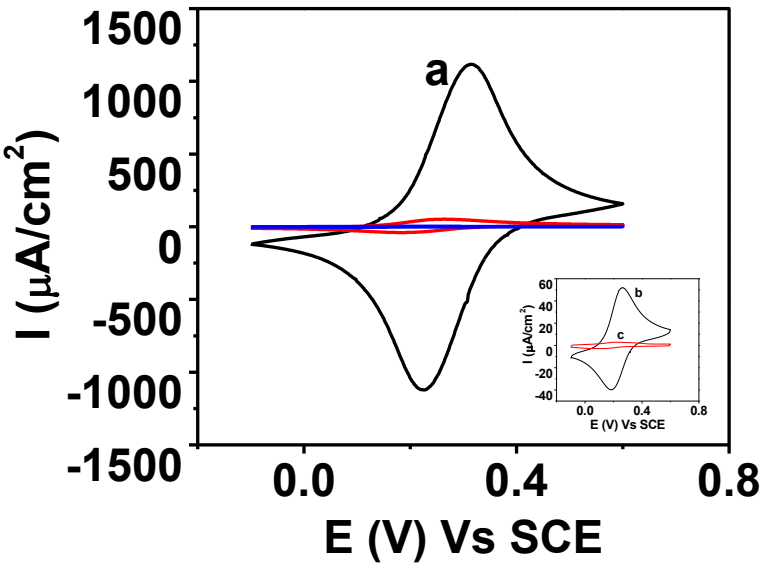

Figure 9. *Cyclic voltammograms of APTMS/ITO electrode in supporting electrolyte (0.1M NaF) after scanning in 1mM* $[Fe(CN)_6]^{3-/4-}$ *in (a). acidic pH, (b). neutral pH, and (c). basic pH solution.* ***Inset:*** *CVs of ferrocyanide on APTMS in neutral and basic pH conditions.*

Table 7. Amount of redox species (Γ) adsorbed onto APTMS is measured from the charge obtained from CV of supporting electrolyte after scanning redox species at different pH

pH	APTMS
	Γ (moles/cm^2)
Acidic	5.2×10^{-8}
Neutral	5.2×10^{-9}
Basic	2×10^{-10}

5.4. Adsorption of DPPC and lipophilic molecules:

Major component of the cell membranes are phospholipids. The phospholipids are amphipathic molecules which consist of hydrophilic phosphate head group with two long hydrocarbon tails along with quaternary ammonium salt bonded to phosphate head group. Due to the presence of hydrophilic phosphate and hydrophobic tails, phospholipids self-assemble to form micelles, reverse micelles, bilayers, and vesicles in aqueous solutions depending on their critical micellar concentration (cmc). Lipophilic substances like fatty acids, sterol, *etc.* can be interspersed among the phospholipids and together they provide the cell membrane fluidity and mechanical strength (figure 11). These substances have affinity towards lipid membranes and have the ability to modify its structure. Principal effect of sterols on phospholipid membrane organization is that they can restrict the motion of fatty acyl chains due to their rigid shape. They are able to modulate the physical properties and the phase behavior of lipid bilayers depending on the structure of the sterol. Bernsdorff and Winter [32] introduced a double bond at C_7 position in the sterol fused ring, due to which the order of lipid chain increases considerably. Leenhouts *et al.* have studied the interaction of TPP^+ ion with DOPC and suggested that the ions reorient the phosphocholine headgroups through quadrupolar interactions [33]. Moncelli *et al.* studied the interaction of TPP^+ and $TPhB^-$ ions through the lipid membrane by monitoring the membrane potential changes during the translocation of ions [34].

The physical and chemical properties of biological membranes are crucial for understanding membrane functions [32,35–39]. The main biological role of bilayers is to provide a barrier that divides the fluids in the inner and outer cell regions. Therefore, the effect of different biological

species on lipid membranes is of great importance and has generated wide interest in this area of research.

5.4.1. Characterization of bare ITO and lipid modified APTMS/ITO:

Figure 10A shows the phase image of bare ITO surface carried out through non-contact mode. It consists of crystalline domains of size around 50nm which are separated by distinct boundaries. Figure 10B shows the phase image of APTMS, which shows a granular domains with gaps in between them. AFM image after modification of APTMS with DPPC lipid is shown in figure 10C. From the figure, it can be seen that several lipid clusters cover almost fully over the APTMS/ITO surface. The surface is covered with a large number of micro sized domains which are aggregated leading to a short range order. There are a few cracks in between the clusters and these gaps are formed during the process of drying of phospholipid on APTMS/ITO similar to mud cracks. Lipophiles such as cholesterol (chol), tetraphenylphosphoniumiodide (TPP^+), and sodiumtetraphenylborate ($TPhB^-$) show strong affinity to DPPC and bind to the lipid membranes at the hydrocarbon-water interface. A schematic model for the intercalation of the lipophile within the membrane is depicted in figure 11. In addition to this, these lipophiles have the ability to disrupt the hydrogen bonding network between water molecules and reduce the lipid stability by weakening the hydrophobic effect. Figures10 (D-F) shows the AFM phase images of cholesterol, TPP^+, and $TPhB^-$ modified DPPC/APTMS/ITO substrates. It can be seen from the images that lipophiles have an effect on the structural organization of DPPC. This is due to the interaction of lipophiles with the phospholipids which rearranges the order of the lipid membrane. The short range order is disrupted by the presence of lipophiles in the phospholipid membranes. Though, analyzing the phospholipid-lipophile interactions is not an objective of this work, the surface studies throw some critical insight on the effect of lipophile on phospholipid organization.

The effect of tetraphenylphosphonium and tetraphenylborate ion on DPPC membrane has been studied in order to understand the ion permeation property of large hydrophobic species. The AFM phase image of TPP^+ and $TPhB^-$ on DPPC/APTMS/ITO surface are shown in figure 10 (E-F). The image shows that the ordered arrangement of DPPC on APTMS/ITO is disrupted by TPP^+ and $TPhB^-$ molecules. An experimental study on how cholesterol and hydrophobic ion binding affects DPPC lipid membrane are demonstrated here by using AFM technique. These results are in

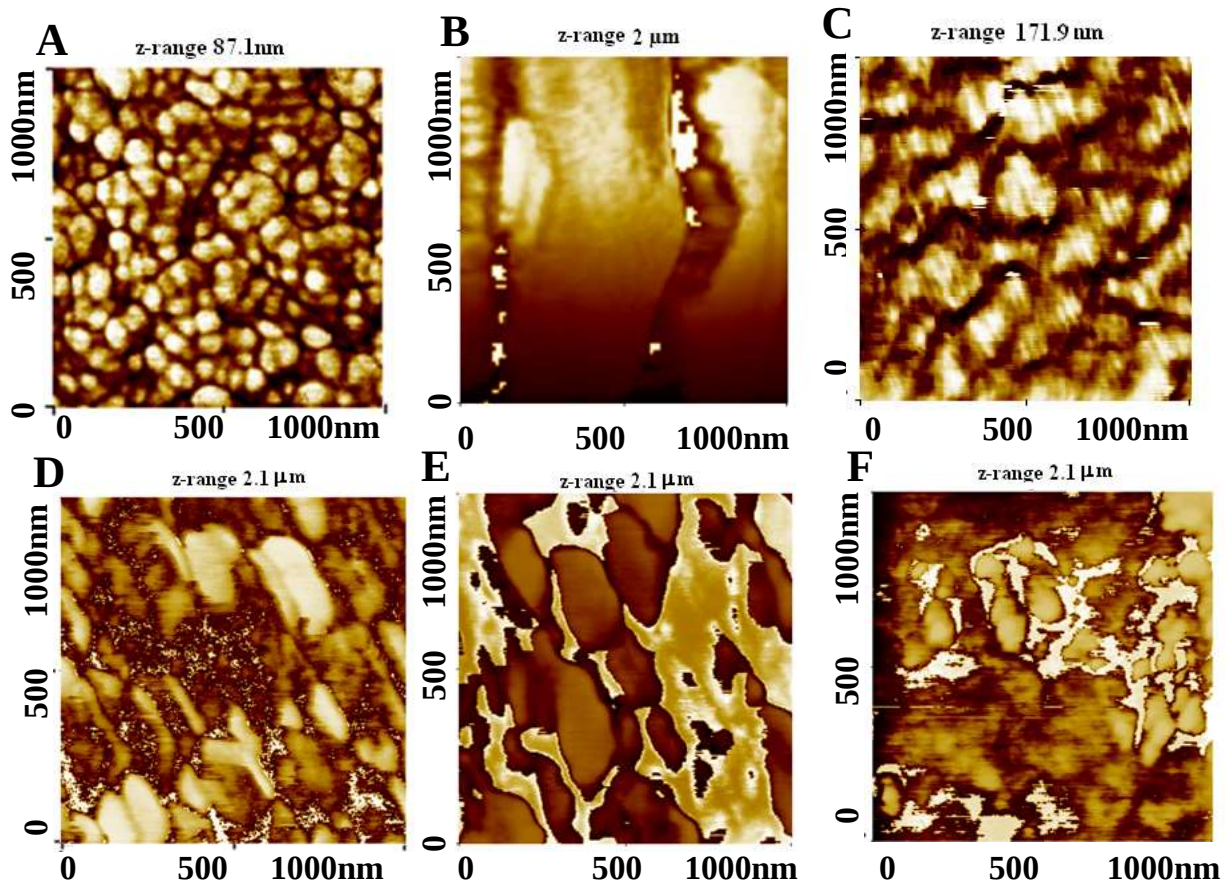

Figure 10. *AFM phase images of (A). Bare ITO, (B). APTMS/ITO, (C). DPPC/APTMS/ITO, (D). Chol/DPPC/APTMS/ITO, (E). TPP^+/DPPC/APTMS/ITO and (F). $TPhB^-$/DPPC/APTMS/ITO surfaces.*

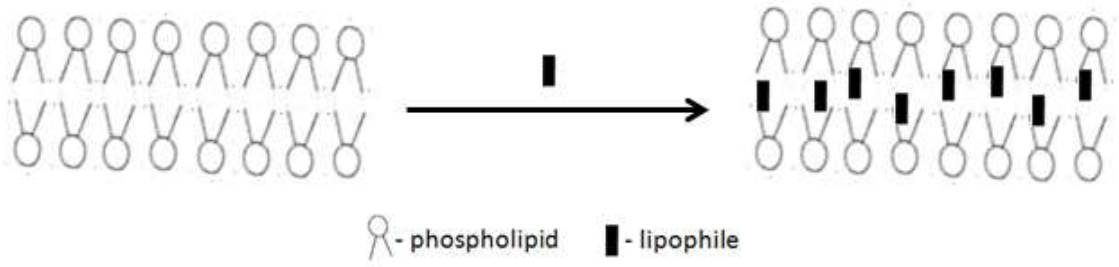

Figure 11. *Representation of phospholipid membrane and lipophile interaction.*

agreement with recent works that have shown both experimentally and theoretically that these lipophiles penetrate the head groups of phospholipid molecules, giving rise to a disrupted layer [34,40].

5.5. Adsorption of cytochrome *c:*

Immobilizing the bio-molecules like proteins onto an appropriate solid surface provides a means of studying their properties and has the potential to be used for bio-sensing. The proteins are generally unstable on bare solid surfaces and therefore it is necessary to provide soft supports to avoid denaturation of proteins. In order to overcome this problem, the proteins can be immobilized onto a soft matter platform such as organic monolayer, polymeric films, surfactants, or Langmuir films which can be formed on solid surfaces.

Cytochromes are electron-transfer proteins having one or more electroactive heme groups, bound to the protein along with two thio ether bonds involving sulphydryl groups of cysteine residues. It is a heme *c* protein with molecular weight of around 12,400 daltons, made up of single polypeptide chain containing 104 amino acid residues and centered with heme group. It is highly water-soluble and is an essential component of the electron transport chain in cell membranes. The periphery of *cyt c* contains lysine and arginine residues which are positively charged. It has been used as an ideal protein for immobilization on modified electrodes by many research groups. The *cyt c* immobilized electrodes also serve as the potential biosensors to detect hydrogen peroxide, nitrate, and superoxide *etc.* [41]. Cytochrome *c* (*cyt c*) has been widely studied as a model system to investigate the electron transfer of typical metalloproteins owing to its high stability and electrochemical activity in the wide pH range of 2 to 11 [42].

Immobilization of *cyt c* onto a solid surface while retaining its electrocatalytic activity is crucial to the preparation of bio-sensors. Adsorption of protein onto the electrode surface makes the protein structurally strained due to the deformation of 3D configuration of protein resulting in its denaturation. Prior chemical modification of surface provides a more suitable environment which can overcome the denaturation problem of protein by providing structural stability after immobilization. Thiols, silanes, phosphonic acids, and carboxylic acids are ideal modifiers of the solid surfaces that can be potentially used for immobilization of *cyt c*. The chemical surface

modifier provides anchoring regions where the adsorbed *cyt c* can retain their structural stability after immobilization. Direct electron transfer from the electrode surface to the protein occurs only when prosthetic group (heme) of *cyt c* lies in close proximity to the electrode surface.

Silane films with their three-dimensional network could be used for encapsulation of metalloproteins. Due to the hydrophilic nature of Si-O-Si network, the film can extend H-bonding with water through amino groups of APTMS which can facilitate the electron transfer process. These proteins are stabilized on the film due to the hydrophilic environment created by amino groups and siloxane groups leading to enrichment of water inside the polymer [43].

5.5.1. Cyclic voltammetric investigation of activity of immobilized *cyt c* modified ITO:

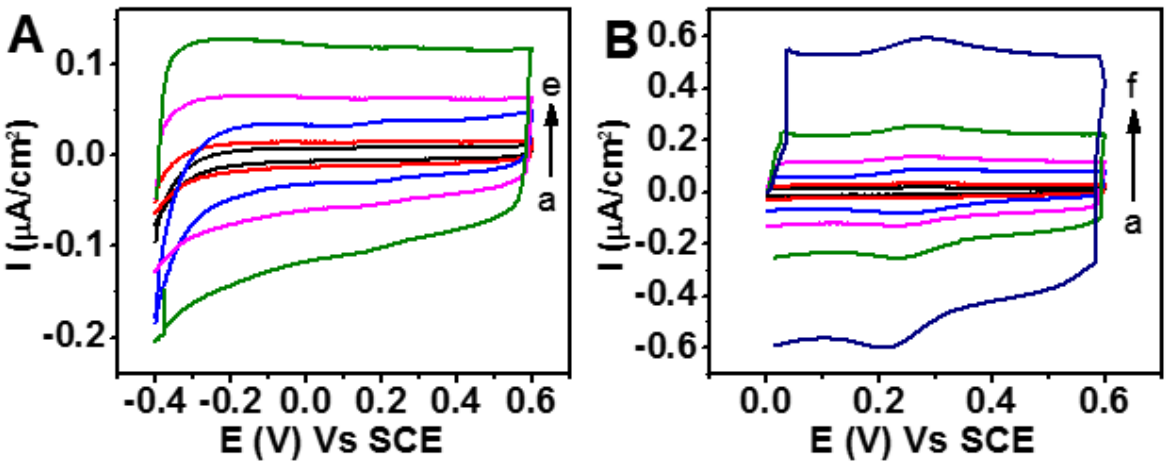

Figure 12. *Cyclic voltammograms of (A). Cyt c/APTMS/ITO and (B). Cyt c/α-CYD/APTMS/ITO in 0.1M phosphate buffer pH 7 at various scan rates.*

The APTMS/ITO surface used for immobilizing the *cyt c* protein to expose the surface confined electron transfer reaction. In addition, the effect of adsorbing negatively charged cyclodextrin on the APTMS surface followed by immobilization of *cyt c* is also investigated. Figure 12 shows the cyclic voltammograms of non-specifically adsorbed *cyt c* on APTMS/ITO and α-CYD/APTMS/ITO electrode surfaces in pH 7 buffer carried out at different scan rates. While the cyclic voltammograms of *cyt c*/APTMS/ITO show broad ill-defined humps, the *cyt c*/α-CYD/APTMS/ITO show broad, but distinct redox peaks. The co-adsorption of negatively charged

α-CYD with *cyt c* on APTMS film increase the charging currents as can be seen from peak separation of forward and reverse scans. The half peak potential values obtained for APTMS/ITO and α-CYD/APTMS/ITO are 183.2 and 266mV, whereas peak separation values obtained for the APTMS/ITO is 66.2mV and α-CYD/APTMS/ITO is 37.5mV. The half peak potentials for the oxidation and reduction of heme group of *cyt c* have shifted more positive due to the incorporation of *cyt c* within the α-CYD film formed on APTMS while the peak separation has decreased. The half peak potential shifts after inclusion of α-CYD in between APTMS and *cyt c* protein are due to the electrostatic interaction between negatively charged α-CYD and positively charged *cyt c* protein due to which the surface charges are lowered. This lets *cyt c* molecules to adsorb more effectively on the hydrophilic surface [44]. The broad hump seen in CV indicates that the immobilized protein experience changes in the native state [45]. The ΔE_p value is higher in the case of *cyt c*/APTMS/ITO electrode which can be due to the electrostatic repulsion between identical charges of the protein and the APTMS film. However, in the case of *cyt c*/α-CYD/APTMS/ITO surface, the electron transfer from the heme group to the electrode surface leads to distinct and less broadened redox peaks indicating that the conformation of protein is not affected significantly after adsorption. The peak separation values indicate diffusion less surface confined electron transfer processes and the peak current can be related to surface concentration of protein by the expression:

$$i_p = n^2F^2\upsilon A\Gamma/4RT \longrightarrow (2)$$

n=number of electrons, F=Faraday constant, Γ=the amount of redox active molecules on the surface, A=area of the electrode, and υ=scan rate. The amount of *cyt c* adsorbed onto the electrode surface is calculated to be 3.5 X 10^{-11} mol/cm^2 from equation (2).

The distinct redox peaks obtained for heme group of protein adsorbed onto the α-CYD shows that electrostatic interactions play a prominent role in stabilizing the *cyt c* protein over the surface [14]. The positively charged lysine residues that are on the outer regions of the *cyt c* molecule are repelled by the positively charged groups on the surface of the electrode and therefore, direct electron transfer of the heme groups is inhibited. α-CYD (pKa=10) consists of carboxylic acid groups which contribute negative charges to the surface. Due to the favorable electrostatic interactions, the cytochrome *c* molecules stay close to the electrode surface thus enhancing the direct electron transfer between electrode and electroactive heme group of the protein. The above

results show that the negatively charged α-CYD provides a favorable environment for *cyt c* as seen from the distinct redox peaks of figure 12B.

Figure 13 shows the peak currents (I_p) vs. scan rate (υ) (mV/s) graph α-CYD for *cyt c*/α-CYD/APTMS/ITO electrode at (a) anodic and (b) cathodic peak potential. The magnitude of peak currents increases with increase in scan rate. The straight line plots obtained (figure 13) indicates that the redox species is surface confined as per equation (2).

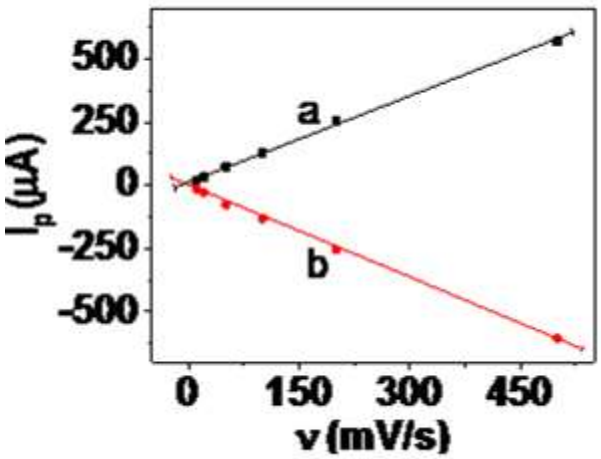

***Figure 13**. Peak current (I_p) vs. scan rate (mV/s) for cyt c/ /APTMS/ITO electrode.*

5.6. Conclusions:

APTMS adsorbs onto ITO surface by forming a polymeric film on the surface. The amino group of APTMS is protonated at acidic and neutral pH leading to a positively charged surface. The effect of pH and influence of the surface charges on the electron transfer process were studied using negative and positively charged redox couple. This study explores the vital role of electrostatic interactions in determining the electron transfer behavior of different charged redox probes at modified surfaces. However, in case of the neutral redox species like ferrocenemethanol, the electron transfer process is largely governed by H-bonding interaction. The APTMS forms a disordered film over the ITO surface creating pores and gaps in between the film where it can trap redox species like $[Fe(CN)_6]^{3-/4-}$ and cytochrome *c* in between the film.

The APTMS modified ITO is used as a support for immobilization of bio-molecules like DPPC and cytochrome *c*. The DPPC modified surface was used as a test bed for understanding the effect

of lipophiles like cholesterol, TPP^+ and $TPhB^-$ on the structural integrity of the lipid membrane. The impact of lipophiles over the organization of phospholipids was studied using atomic force microscopy in phase contrast mode. It was found that lipophiles have disrupting effect over the lipid organization through the process of intercalation within the lipid domains. Immobilization of the heme protein *cyt c* on APTMS/ITO surface does not show any redox peaks during CV scan. However, co-adsorption of α-CYD over the APTMS/ITO increases the amount of protein adsorbed over the surface which is indicated by distinct redox peaks in the cyclic voltammograms corresponding to the surface confined electron transfer processes of *cyt c*. This can be explained as a result of the favorable electrostatic interactions between negatively charged α-CYD and positively charged *cyt c*.

5.7. References:

[1] F. Schreiber, Structure and growth of self-assembling monolayers, Prog. Surf. Sci. 65 (2000) 151–257. doi:10.1016/S0079-6816(00)00024-1.

[2] A. Ulman, Formation and Structure of Self-Assembled Monolayers, Chem. Rev. 96 (1996) 1533–1554. doi:10.1021/cr9502357.

[3] J.C. Love, L. a. Estroff, J.K. Kriebel, R.G. Nuzzo, G.M. Whitesides, Self-Assembled Monolayers of Thiolates on Metals as a Form of Nanotechnology, Chem. Rev. 105 (2005) 1103–1170. doi:10.1021/cr0300789.

[4] S.A. Paniagua, P.J. Hotchkiss, S.C. Jones, S.R. Marder, A. Mudalige, F.S. Marrikar, J.E. Pemberton, N.R. Armstrong, Phosphonic Acid Modification of Indium-Tin Oxide Electrodes: Combined XPS/UPS/Contact Angle Studies, J. Phys. Chem. C. 112 (2008) 7809–7817. doi:10.1021/jp710893k.

[5] S.E. Koh, K.D. McDonald, D.H. Holt, C.S. Dulcey, J.A. Chaney, P.E. Pehrsson, Phenylphosphonic acid functionalization of indium tin oxide: Surface chemistry and work functions, Langmuir. 22 (2006) 6249–6255. doi:10.1021/la052379e.

[6] M. Gliboff, L. Sang, K.M. Knesting, M.C. Schalnat, A. Mudalige, E.L. Ratcliff, H. Li, A.K. Sigdel, A.J. Giordano, J.J. Berry, D. Nordlund, G.T. Seidler, J.L. Brédas, S.R. Marder, J.E. Pemberton, D.S. Ginger, Orientation of phenylphosphonic acid self-

assembled monolayers on a transparent conductive oxide: A combined NEXAFS, PM-IRRAS, and DFT study, Langmuir. 29 (2013) 2166–2174. doi:10.1021/la304594t.

[7] G.M. Whitesides, E. Ostuni, S. Takayama, X. Jiang, D.E. Ingber, Soft Lithography in Biology and Biochemistry, Annu. Rev. Biomed. Eng. 3 (2001) 335–373. doi:10.1146/annurev.bioeng.3.1.335.

[8] M. Mrksich, G.M. Whitesides, Using Self-Assembled Monolayers That Present Oligo(ethylene glycol) Groups To Control the Interactions of Proteins with Surfaces, in: J.M. Harris (Ed.), ACS Symp. Ser. Am. Chem. Soc., Washington D C, 1997: pp. 361–373. doi:10.1021/bk-1997-0680.ch023.

[9] M. Daniel, D. Astruc, Gold Nanoparticles : Assembly , Supramolecular Chemistry , Quantum-Size-Related Properties , and Applications toward Biology , Catalysis , and Nanotechnology, (2004).

[10] G.-J. Zhang, T. Tanii, T. Zako, T. Hosaka, T. Miyake, Y. Kanari, T. Funatsu, I. Ohdomari, Nanoscale Patterning of Protein Using Electron Beam Lithography of Organosilane Self-Assembled Monolayers, Small. 1 (2005) 833–837. doi:10.1002/smll.200500091.

[11] E. Vandenberg, H. Elwing, A. Askendal, I. Lundström, Protein immobilization of 3-aminopropyl triethoxy silane glutaraldehyde surfaces: Characterization by detergent washing, J. Colloid Interface Sci. 143 (1991) 327–335. doi:10.1016/0021-9797(91)90266-B.

[12] I. Markovich, D. Mandler, Preparation and characterization of octadecylsilane monolayers on indium-tin oxide (ITO) surfaces, J. Electroanal. Chem. 500 (2001) 453–460. doi:10.1016/S0022-0728(00)00458-7.

[13] J. Sagiv, Organized Monolayers by Adsorption. III. Irreversible Adsorption and Memory Effects in Skeletonized Silane Monolayers, Isr. J. Chem. 18 (1979) 346–353. doi:10.1002/ijch.197900053.

[14] C. Bin Gong, C.C. Guo, D. Jiang, Q. Tang, C.H. Liu, X.B. Ma, Graphene-cyclodextrin-cytochrome c layered assembly with improved electron transfer rate and high

supramolecular recognition capability, Mater. Sci. Eng. C. 39 (2014) 281–287. doi:10.1016/j.msec.2014.03.010.

[15] I. Tabushi, K. Kurihara, K. Naka, K. Yamamura, H. Hatakeyama, Supramolecular sensor based on SnO2 electrode modified withoctadecylsilyl monolayer having molecular binding sites, Tetrahedron Lett. 28 (1987) 4299–4302. doi:10.1016/S0040-4039(00)96490-6.

[16] K. Yamamura, H. Hatakeyama, K. Naka, I. Tabushi, K. Kurihara, Guest selective molecular recognition by an octadecylsilyl monolayer covalently bound on an SnO2 electrode, J. Chem. Soc. Chem. Commun. 3 (1988) 79. doi:10.1039/c39880000079.

[17] I. Markovich, D. Mandler, Disorganised self-assembled monolayers (SAMs): the incorporation of amphiphilic molecules, Analyst. 126 (2001) 1850–1856. doi:10.1039/b107068c.

[18] A. Muthurasu, V. Ganesh, Electrochemical characterization of Self-assembled Monolayers (SAMs) of silanes on indium tin oxide (ITO) electrodes - Tuning electron transfer behaviour across electrode-electrolyte interface, J. Colloid Interface Sci. 374 (2012) 241–249. doi:10.1016/j.jcis.2012.02.007.

[19] S.P. Pujari, L. Scheres, A.T.M. Marcelis, H. Zuilhof, Covalent surface modification of oxide surfaces, Angew. Chemie - Int. Ed. 53 (2014) 6322–6356. doi:10.1002/anie.201306709.

[20] J. Iwasa, K. Kumazawa, K. Aoyama, H. Suzuki, S. Norimoto, T. Shimoaka, T. Hasegawa, In Situ Observation of a Self-Assembled Monolayer Formation of Octadecyltrimethoxysilane on a Silicon Oxide Surface Using a High-Speed Atomic Force Microscope, J. Phys. Chem. C. 120 (2016) 2807–2813. doi:10.1021/acs.jpcc.5b11460.

[21] J.T. Woodward, A. Ulman, D.K. Schwartz, Self-Assembled Monolayer Growth of Octadecylphosphonic Acid on Mica, Langmuir. 12 (1996) 3626–3629. doi:10.1021/la9510689.

[22] C. Carraro, O.W. Yauw, M.M. Sung, R. Maboudian, Observation of three growth mechanisms in self-assembled monolayers, J. Phys. Chem. B. 102 (1998) 4441–4445.

doi:10.1021/jp981019f.

[23] J.J. Benkoski, E.J. Kramer, H. Yim, M.S. Kent, J. Hall, The effects of network structure on the resistance of silane coupling agent layers to water-assisted crack growth., Langmuir. 20 (2004) 3246–3258. doi:Doi 10.1021/La035920k.

[24] R.M. Pasternack, S.R. Amy, Y.J. Chaba, Attachment of 3- Aminopropyl triethoxysilane on Silicon Oxide Surfaces: Dependence on Solution Temperature, Langmuir. 24 (2008) 12963–12971. doi:10.1021/la8024827.

[25] G. Jakša, B. Štefane, J. Kovač, Influence of different solvents on the morphology of APTMS-modified silicon surfaces, Appl. Surf. Sci. 315 (2014) 516–522. doi:10.1016/j.apsusc.2014.05.157.

[26] R.D. Ross, L.E. Cole, R.K. Roeder, Relative binding affinity of carboxylate-, phosphonate-, and bisphosphonate-functionalized gold nanoparticles targeted to damaged bone tissue, J. Nanoparticle Res. 14 (2012). doi:10.1007/s11051-012-1175-z.

[27] F. Sun, Y. Lei, D.W. Grainger, Ultrathin self-assembled polymer films on solid surfaces 4. Electrochemical analysis of film microstructure on gold electrodes, Colloids Surfaces A Physicochem. Eng. Asp. 93 (1994) 191–200. doi:10.1016/0927-7757(94)02893-1.

[28] V. Ganesh, S.K. Pal, S. Kumar, V. Lakshminarayanan, Self-assembled monolayers (SAMs) of alkoxycyanobiphenyl thiols on gold surface using a lyotropic liquid crystalline medium, Electrochim. Acta. 52 (2007) 2987–2997. doi:10.1016/j.electacta.2006.09.037.

[29] M. Niwa, T. Mori, N. Nigashi, 2-Dimensional Photopolymerization at Adsorbed Monolayers on Gold, J. Mater. Chem. 2 (1992) 245–251.

[30] A.J. Bard, L.R. Faulkner, Electrochemical methods Fundamentals and Applications, second, New York, 2001. http://as.wiley.com/WileyCDA/WileyTitle/productCd-0471043729.html.

[31] P. Harder, K. Bierbaum, C. Woell, M. Grunze, S. Heid, F. Effenberger, Induced Orientational Order in Long Alkyl Chain Aminosilane Molecules by Preadsorbed Octadecyltrichlorosilane on Hydroxylated Si(100) †, Langmuir. 13 (1997) 445–454. doi:10.1021/la9604947.

[32] C. Bernsdorff, R. Winter, Differential Properties of the Sterols Cholesterol, Ergosterol, β-Sitosterol, *trans* -7-Dehydrocholesterol, Stigmasterol and Lanosterol on DPPC Bilayer Order, J. Phys. Chem. B. 107 (2003) 10658–10664. doi:10.1021/jp034922a.

[33] J.M. Leenhouts, V. Chupin, J. de Gier, B. de Kruijff, The membrane potential has no detectable effect on the phosphocholine headgroup conformation in large unilamellar phosphatidylcholine vesicles as determined by 2H-NMR, BBA - Biomembr. 1153 (1993) 257–261. doi:10.1016/0005-2736(93)90413-T.

[34] M.R. Moncelli, R. Herrero, L. Becucci, R. Guidelli, Adsorption of tetraphenylphosphonium and tetraphenylborate in self-assembled phosphatidylcholine and phosphatidylserine monolayers deposited on mercury electrodes, J. Phys. Chem. 99 (1995) 9940–9951. doi:10.1021/j100024a042.

[35] S. Garcia-Manyes, G. Oncins, F. Sanz, Effect of ion-binding and chemical phospholipid structure on the nanomechanics of lipid bilayers studied by force spectroscopy, Biophys. J. 89 (2005) 1812–1826. doi:10.1529/biophysj.105.064030.

[36] G. Cevc, Membrane electrostatics, BBA - Rev. Biomembr. 1031 (1990) 311–382. doi:10.1016/0304-4157(90)90015-5.

[37] H. Binder, O. Zschörnig, The effect of metal cations on the phase behavior and hydration characteristics of phospholipid membranes, Chem. Phys. Lipids. 115 (2002) 39–61. doi:10.1016/S0009-3084(02)00005-1.

[38] S. Ohki, N. Düzgüneş, K. Leonards, Phospholipid Vesicle Aggregation: Effect of Monovalent and Divalent Ions, Biochemistry. 21 (1982) 2127–2133. doi:10.1021/bi00538a022.

[39] S. Ohki, S. Roy, H. Ohshima, K. Leonards, Monovalent Cation-Induced Phospholipid Vesicle Aggregation: Effect of Ion Binding, Biochemistry. 23 (1984) 6126–6132. doi:10.1021/bi00320a035.

[40] R.F. Flewelling, W.L. Hubbell, Hydrophobic ion interactions with membranes. Thermodynamic analysis of tetraphenylphosphonium binding to vesicles, Biophys. J. 49 (1986) 531–540. doi:10.1016/S0006-3495(86)83663-3.

[41] Z.S. Aghamiri, M. Mohsennia, H.-A. Rafiee-Pour, Immobilization of cytochrome c and its application as electrochemical biosensors, Talanta. 176 (2018) 195–207. doi:10.1016/j.talanta.2017.08.039.

[42] A.K. Yagati, T. Lee, J. Min, J.W. Choi, Electrochemical performance of gold nanoparticle-cytochrome c hybrid interface for H2O2detection, Colloids Surfaces B Biointerfaces. 92 (2012) 161–167. doi:10.1016/j.colsurfb.2011.11.035.

[43] D.L. Angst, G.W. Simmons, Moisture Absorption Characteristics of Organosiloxane Self-Assembled Monolayers, Langmuir. 7 (1991) 2236–2242. doi:DOI 10.1021/la00058a043.

[44] V. Zia, R.A. Rajewski, V.J. Stella, Effect of cyclodextrin charge on complexation of neutral and charged substrates: comparison of (SBE)7M-beta-CD to HP-beta-CD., Pharm. Res. 18 (2001) 667–673.

[45] R.A. Clark, E.F. Bowden, Voltammetric Peak Broadening for Cytochrome c /Alkanethiolate Monolayer Structures: Dispersion of Formal Potentials, Langmuir. 13 c(1997) 559–565. doi:10.1021/la960650+.

c

Chapter 6

Electrochemically intercalated graphite substrates for immobilization of metal nanostructures and their application for alcohol oxidation

6.1. Introduction:

While earlier chapters describe the electrochemical properties and application potentials of indium tin oxide (ITO) electrode, this chapter describes the work carried out with exfoliated graphite oxide (GrO) as a potential substrate for immobilizing the noble metal nanoparticles. While ITO surface lends itself for functionalization with hydroxyl groups for modification with SAMs, the graphite can be functionalized with hydroxyl, carboxyl, and epoxy groups for further applications. The electrochemical exfoliation process described in this chapter, produces surface functionalities which are conducive for electrochemical oxidation of alcohols. In this work, the utility of such a functionalized surface with large surface area is explored as a solid support for noble metal nanoparticles for electrocatalytic oxidation of alcohols that can be used in low temperature polymer membrane alkaline fuel cells [1,2].

Low temperature fuel cells such as direct alcohol fuel cells (DAFCs) using methanol/ethanol have been emerging as a green technology alternative and is drawing considerable interest worldwide. However, commercialization of these technologies pose significant challenges due to the high cost involved in loading of precious metals for the effective electrocatalytic activity of the device. Researchers have been aiming to optimize the amount of metal to be used without compromising the electrocatalytic activity of the electrode. There are various carbon supports such as graphite, Vulcan XC-72 carbon black, highly oriented pyrolytic graphite, and pencil graphite for deposition of noble catalyst materials [3–7]. During the past several years, many carbonaceous graphite materials such as natural graphite, coke, and graphitized carbon have been widely investigated as a support for noble metal catalysts and metal composites [8–10].

An inexpensive but effective electrode support material where optimum metal loading can be achieved with large electroactive surface area along with considerable electrocatalytic activity is an important requirement for DAFCs. However, the high loading of noble metal catalyst of the electrodes remains a major concern towards the development of commercially viable fuel cells. The smooth solid supports lack anchoring ability for the metal nanoparticles which might lead to Ostwald ripening eventually. This can create sluggishness for the reactants to diffuse through the electrode which in turn will affect the electrocatalytic activity. Ehrburger *et al.* have suggested that prior gasification of graphite particles provide a better dispersion of metal nanoparticles. It is due to the surface heterogeneity created on the graphite substrate after pyrolysis step which creates defects on graphite surface. These defects serve as nucleation sites for metal atoms [11]. There are well established methods for producing high metal dispersions on carbon, but the resulting materials are not suitable for preparation of catalytic material as it involves sintering process for fabrication. This issue had motivated numerous studies to improve metal dispersions on carbons, mainly through optimization of the metal-supporting procedures or functionalization of the carbon surface.

Flexible graphite is made by compression of stacks of graphite flakes without a binder, thus the flakes adhere due to pressure thereby forming a flexible sheet that resembles a piece of thin paper which can be cut easily through scissors. These sheets contain a lot of edges and defects within the surface which in this case serve the purpose of high metal loading. These substrates have the capability of not only to disperse the catalyst particles but also play an important role in enhancing the overall performance. It also offers the advantage of shapability. Conventionally, the flake graphite consists of a lot of edge planes due to which it possess high conductivity [12,13]. A high surface area for the flexible graphites when compared to the other forms of graphite with similar geometric area can be attributed to the edge planes of the graphite flakes. Due to the presence of large number of edges/defects, functional groups such as carbonyl and phenolic hydroxyl exists on the surface which increases the probability of interactions between the substrate and the deposited/dispersed metal. In fact, various attempts are being made to improve the electrocatalytic behavior of potential electrocatalysts. This can be achieved by the exfoliation of flexible graphite substrate by the electrochemical method described in this work. The process introduces lactone, carboxyl, and quinone structure moieties which are formed on the edge surface during the electrochemical treatment [14].

Researchers have been exploring new routes to enhance the electrocatalytic activity of deposited nanomaterials. This can be achieved by the coating of another reactive metal or metal oxide over the nanomaterial, wiring of nanoparticles within the conducting polymers, and functionalizing the support. Xu *et al.* carried out electrochemical oxidation of methanol and ethanol at Pt and Pd on carbon and carbon microspheres (CMS) in alkaline medium. Metal dispersed on CMS shows better electrocatalytic activity compared to the metal dispersed on carbon substrate [15]. Liang *et al.* studied the mechanism of ethanol electrooxidation in alkaline medium and suggested that the rate determining step for ethanol oxidation is removal of the adsorbed ethoxy group by the adsorbed hydroxyl group. Ghosh *et al.* studied the enhanced electrocatalytic activity of Pd nanoplatelets dispersed on conducting polymers towards ethanol oxidation in alkaline medium [16]. Pandey *et al.* studied the electrocatalytic behavior of gold dispersed in various conducting polymers like polypyrrole, polyaniline, poly(3,4-ethylenedioxythiophene), and polythiophene towards electrooxidation of ethanol, methanol, and formic acid [17]. In this work, the application of electrochemically exfoliated graphite sheet as an integrated support for deposition of Pd nanoparticle and Pd-PANI nanocomposite is explored. The Pd-PANI nanocomposite dispersed electrode shows better electrocatalytic activity compared to just Pd on graphite support. Electrochemically exfoliated graphite substrates provides better support for the nanocomposite compared to the flexible graphite sheet (GS). The electrocatalytic activity of these electrodes was studied using cyclic voltammetry and chronoamperometry. The activation energy studies and the effect of surface coverage by reaction intermediates are investigated using Tafel polarization plots.

6.2. Experimental section:

6.2.1. Materials and methods:

Acetonitrile (HPLC grade, SDFCL limited), aniline (AR grade, SDFCL limited), ethanol (Merck grade), methanol (Merck grade), and 0.5M hydrochloric acid and Millipore water are the solvents used for our electrochemical studies. Tetrabutylammonium tetrafluoroborate (TBATFB) and sodium hydroxide are the salts used for carrying electrochemical exfoliation and electrocatalytic studies.

Exfoliation of flexible graphite sheet (GS) was carried out by using chronoamperometry (CA) technique at positive and negative potentials. Pd nanoparticle and Pd-PANI nanocomposite electrodes are prepared by galvanostatic deposition in a two electrode configuration using an EG&G potentiostat (model 263A) equipped with PowerSuite software in chronopotentiometry (CP) mode and interfaced to a PC through a GPIB card (National Instruments). The electrochemical cell was maintained at specific temperatures for kinetic studies using Julabo temperature control systems (F25). For electroanalytical techniques, Pt foil was used as a counter electrode while the nanoparticle modified graphite and exfoliated graphite were used as the working electrode. Saturated calomel electrode (SCE) and Hg/HgO/1M NaOH (MMO) were used as reference electrodes in acidic and alkaline medium respectively. SEM images and EDAX spectra were recorded with a field emission scanning electron microscope (Ultra plus, Carl Zeiss). Raman spectra measurements were obtained with a high resolution triple Raman spectrometer (T64000, Horiba JobinYvon), using a He–Ne Laser (λ = 632.0 nm) with a 50 X objective. Laser power was maintained at 23mW. XRD studies were carried out using out using Cu K_α (λ = 1.54 Å) radiation from a Rigaku Ultrax 18 rotating anode generator (5.4kW) monochromated with a graphite crystal.

6.2.2. Synthesis of the Pd and Pd-PANI:

Pd nanoparticles are synthesized from 1mM $PdCl_2$ in 0.1M HCl solution. Graphite rod of diameter 3mm is used as working electrode and flexible graphite sheet (GS) and electrochemically exfoliated graphite sheets ((+/-) IGS) are used as counter electrodes for deposition of nanoparticle and nanocomposites. Deposition of Pd nanoparticle is carried out by the application of 10mA/cm^2 from 1mM $PdCl_2$ solution, whereas deposition of Pd-PANI is carried out by dissolution of 5µL aniline+1mM $PdCl_2$+0.1M HCl solution by the application of 10mA/cm^2 current density corresponding to graphite rod respectively.

6.3. Results and Discussion:

The electrochemical techniques used for the studies are chronoamperometry (CA), chronopotentiometry (CP), cyclic voltammetry (CV), and Tafel plots. The characterization of the materials were carried out using Raman spectroscopy, x-ray diffraction (XRD), scanning electron microscopy (SEM), and scanning tunneling microscopy (STM) techniques.

6.3.1. Electrochemical exfoliation of graphite sheets:

Electrochemical exfoliation of the flexible graphite sheet (GS) was carried out in a 3 electrode compartment at a constant potential mode. The platinum (Pt) wire was used as counter electrode and silver wire as a reference electrode. Flexible graphite (GS) sheet was used as working electrode for the study. The exfoliation was carried out in acetonitrile solvent and tetrabutylammonium tetrafluoroborate (TBATFB) is used as a supporting electrolyte. According to the earlier reports, acetonitrile is the preferred solvent for carrying the electrochemical intercalation process [18]. Accordingly, the exfoliation process was carried out in acetonitrile at both positive and negative potentials namely, by the application of +2.5 or –2.5 V vs. silver wire [19,20]. Both the processes cause intercalation of the ionic species inside the graphite stacks [21]. Exfoliation process occurs through intercalation of ionic species in between the stacks of graphite sheet by increasing the width of the electrode. During this process, electrode swelling occurs. Schematic representation of electrochemical exfoliation of graphite is shown in figure 1. Loosely attached fragments of the electrode falls down due to the small disturbances like tapping and shaking of the exfoliated electrode. The swelling of the electrode diminishes after the removal of electrode from solution [19]. This can be attributed to the restacking of the graphite layers [22]. Though a large number of defects are created on the graphite layers during the exfoliation process. This integral electrode can be exfoliated electrode was quite stable and maintain structural integrity during experiments was used as substrate for immobilization of nanostructures. Depending upon the positive or negative applied potentials, a positively or negatively exfoliated integral graphite [(+)IGS or (-)IGS] substrate can be obtained [23].

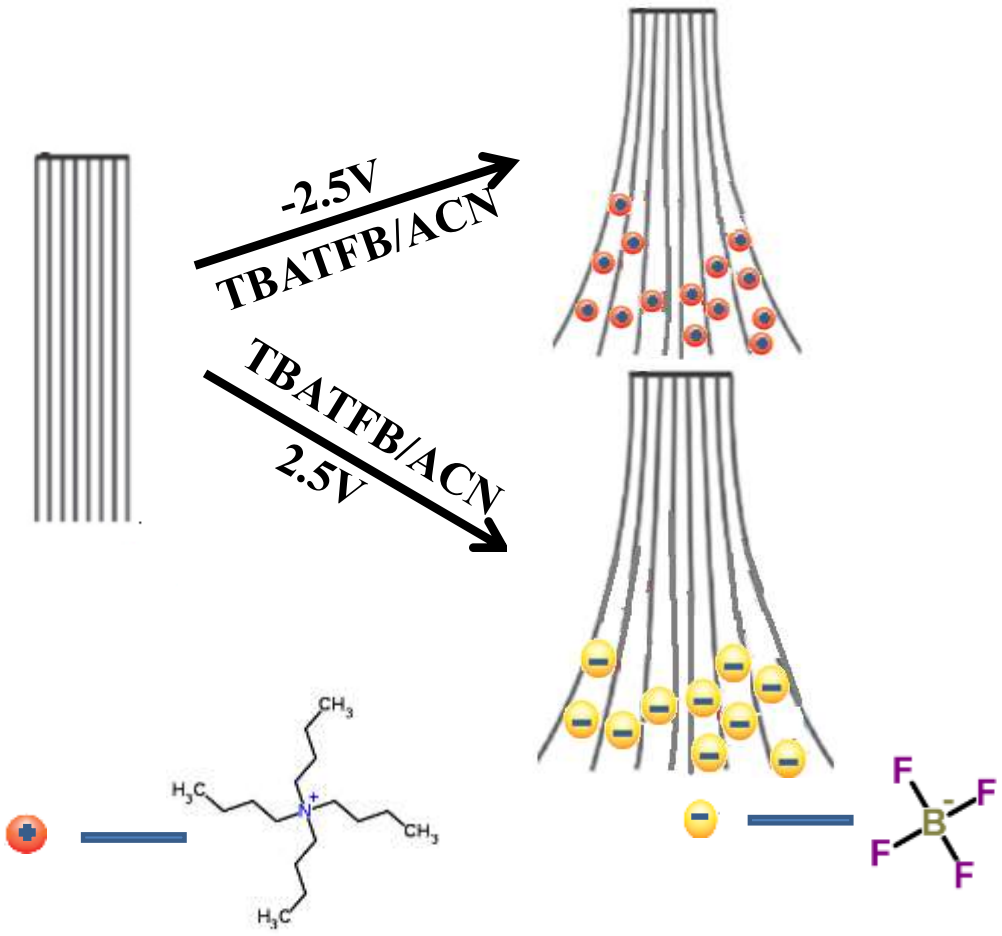

Figure 1. *Schematic mechanism of intercalation process by the application of -2.5V and +2.5V respectively using tetrabutylammonium tetrafluoroborate (TBATFB) in acetonitrile solvent.*

6.3.2. AFM and STM analysis of flexible graphite sheet:

Figure 2A shows the phase AFM image of flexible graphite sheet at 5µm x 5µm resolution obtained in constant height mode. Figure 2B shows the current profile STM image of the flexible graphite sheet at 0.63nm x 0.56nm resolution obtained in constant height mode at a tunneling current of 1nA and bias voltage of 100mV. From the figure 2A, graphite sheet is made up of several basal plane graphite layers of various sizes stacked together. A lot of step edges can be seen on graphite sheet which suggests that it is a rough surface. In contrast, STM imaging of graphite shows clear hexagonal bright spots corresponding to the high local density of state in several regions. One of the scanned portion is shown in Figure 2B where the distance between two bright spots correspond to about 0.28nm close to the reported value of 0.25nm in literature [24,25]. From the AFM and

STM images it is clear that the surface is atomically smooth but with a lot edge defects. In other words, the graphite sheet is macroscopically rough but atomically smooth.

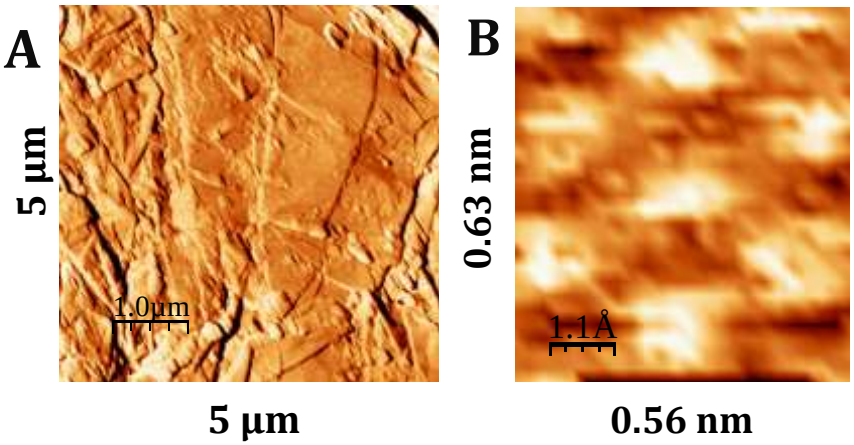

Figure 2. *(A). Phase AFM image of flexible graphite sheet at 5µmx5µm resolution in constant height mode (B). STM image of flexible graphite sheet at 0.63nm x 0.56nm obtained in constant height mode at a tunneling current of 1nA and bias voltage of 100mV.*

6.3.3. SEM and XRD analysis of flexible graphite and exfoliated graphite sheet:

The morphologies of the flexible graphite sheet (figure 3A) and the electrochemically exfoliated graphite substrates (figures 3B and C) are examined using SEM. As shown in figure. 3A, the surface of the graphite sheet is smooth which reveals a flaky structure with variously sized graphite sheet stacked together along their basal planes [4]. It also consists of highly-oriented graphite layers which are very thin and in the micrometer (µm) range [28]. It is also observed that a few gaps are present on the surface which means these bundles are not stacking uniformly. On the contrary, figures 3B and C show the images after exfoliation which comprise of wrinkled or folded thin sheets. This is due to the intercalation of ions in between graphite layers which reduces the planarity of basal planes thereby revealing a large amount of edge planes of graphite substrate. The surface roughness increases due to the formation of folds and corrugations on graphite substrates after electrochemical exfoliation.

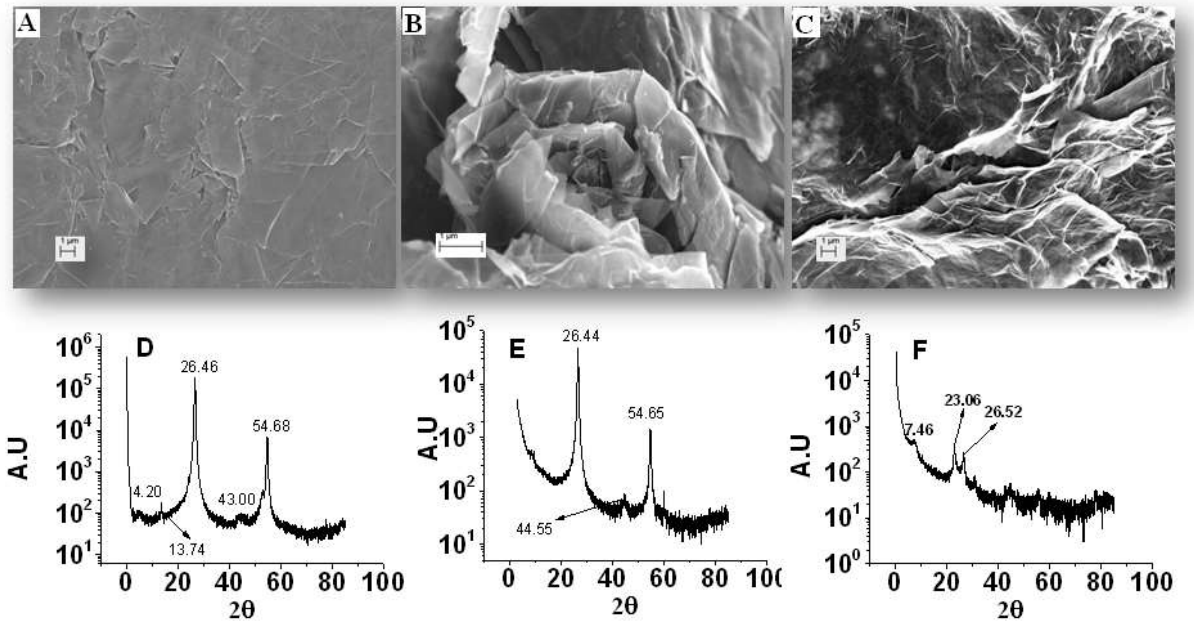

Figure 3. *SEM images and XRD plots of (A,D) GS, (B,E) (+)IGS and (C,F) (-)IGS substrates.*

Figures 3 (D–F) show XRD graphs of GS, (+)IGS, and (-)IGS respectively. Figure 3D shows two prominent sharp peaks around positions (2θ) 26.5° (002) and 54.6° (004) respectively which reflect the order and polycrystallinity of the substrate [29]. The peaks around 26.5° and 54.6° are retained after electrochemical intercalation. The sharp and highly intense (002) peak in figure 3A shows that GS is highly ordered. However, after exfoliation there is a decrease of peak intensity. This is due to the decrease in the thickness of the GS along the stacking direction of basal planes of graphite during intercalation process. The sharp peaks in all the cases indicate that the crystallinity of the substrate is still retained even after exfoliation of graphite sheet [6]. The microstructure of the graphite, however, will differ in the size and extent of the crystals that make up the polycrystalline structure of synthetic graphite.

By using Bragg's equation $n\lambda = 2d\,\mathrm{Sin}\theta$, the interlayer distances of the substrates were measured, where n is a positive integer, and λ is the wavelength of incident wave, d is the interplanar distance, and θ is the angle of incidence.

The values obtained for GS, (+)IGS, and (-)IGS are 0.337, 0.338, and 0.338 nm respectively. These interlayer spacing values obtained for exfoliated graphite sheets show very small increase compared to the graphite sheet. This is due to the restacking of exfoliated graphite layers.

6.3.4. Raman Studies on GS, (+)IGS and (-)IGS:

Figure 4 shows the Raman spectra of (a) GS, (b) (+)IGS and (c) (-)IGS substrates obtained by the incidence of 632nm laser with 15s exposure. Four bands can be seen in all the spectra: the D band (A_{1g} vibrational mode) around 1330cm^{-1}, G-band (E_{2g} vibrational mode) at around 1585cm^{-1}, 2D-band around 2670cm^{-1}, and D+G band around 2890cm^{-1} (Table 1). The G-band is an inherent Raman band for the ideal graphite structure [30]. The D-band is usually absent for the two-dimensional pristine graphite. This band is assigned to the break in symmetry at the edges of graphite particles and linked to imperfections such as defects, discontinuity in crystallites, and stacking disorder in the crystal structure [26,30]. It can be noted from figure 4, that the intensities of the D-bands increase due to the positive potential exfoliation. It is known that electrochemical exfoliation increases the defect density on graphite sheets which is reflected in the D band [31].

Table 1 shows Raman shift values for GS, (+)IGS, and (-)IGS samples where I_D/I_G ratio is also shown. It is known that ratio of I_D/I_G reflects the surface defect density of graphite. It can be seen that the (+)IGS shows largest I_D/I_G ratio implying the presence of large number of defects. However, in the negative potential exfoliated graphite (-)IGS the surface defects have increased compared to graphite substrate. However, it is very much less than that of positive exfoliated graphite.

This is because of the fact that the surface oxidation at positive potentials introduce several functional groups causing large number of defect sites which is not the case in negative exfoliation.

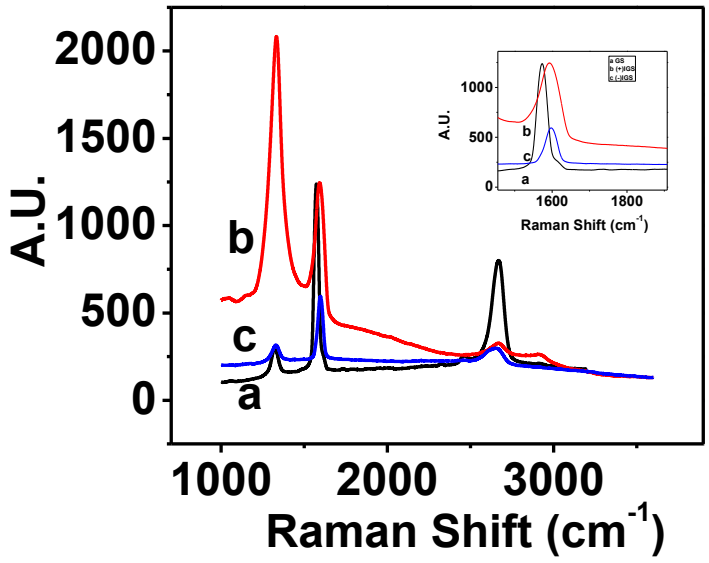

Figure 4*. Raman peaks of (a) GS, (b) (+)IGS, and (c) (-)IGS substrates.*

Table 1. Raman shift values obtained for GS and electrochemically intercalated graphite sheets (+/-)IGS at +2.5V and –2.5V using 0.1M TBATFB in acetonitrile solvent.

Substrate	**D band (cm^{-1})**	**G band (cm^{-1})**	**2D band (cm^{-1})**	**I_D/I_G**
GS	1325	1571	2667	0.20
(+)IGS	1328	1591	2635	1.69
(-)IGS	1325	1572	2635	0.53

6.3.5. Preparation of Pd-PANI nanocomposite:

Homogenous solution of 1mM $PdCl_2$ is prepared by the addition of 8.5mg of palladium salt to 100ml of 0.1M HCl solution followed by sonication for 5 minutes. 20µl of aniline is added to the 20ml of the solution and stirred well by a magnetic stirrer. A 3mm diameter graphite rod is chosen as anode and the counter electrode while a smooth flexible graphite sheet was chosen for exfoliation at both positive and negative potentials as working electrode. The dissolved palladium ions form hexachloropalladate complex in the acid solution. Highly oxidizing tendency of this palladium complex initiates the polymerization of aniline which in turn gets reduced to palladium

metal atoms. The reduced Pd metal atoms cluster together and adhere to the PANI film resulting in the Pd-PANI nanocomposite [7]. Pd-PANI nanocomposite is positively charged due to the protonation of hydrogen ions from HCl solution, which then electrophoretically deposit on to the electrode substrate as a thin film.

Deposition of Pd-PANI nanocomposite was carried out by chronopotentiometry technique by applying a 10mA/cm^2 current density with respect to the anode. This value of current density was chosen for the deposition as it provides an integrated electrode with optimum mechanical integrity. We have carried out the deposition in the galvanostatic mode for one hour with different current values to study the effect of current on the nature of coating.

A schematic representation of polymerization of aniline in the presence of palladium is shown in figure 7 [32].

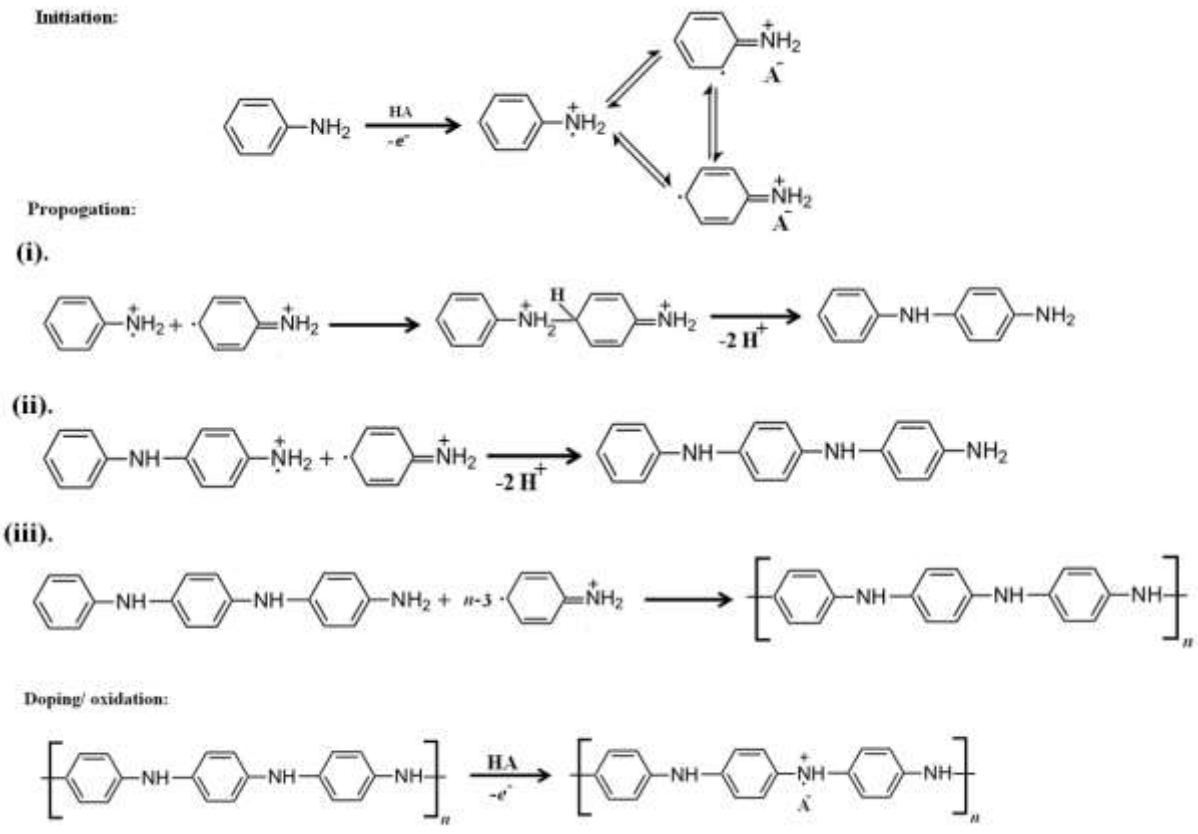

Figure 5. *Schematic representation of mechanism of electro polymerization of aniline.*

6.3.6. Morphological Characterization of Pd GS substrate, Pd-PANI GS, Pd-PANI (+)IGS, and Pd-PANI (-)IGS substrates:

Figure 6 shows the SEM image and EDAX analysis of Pd electrodeposited onto graphite sheet (GS) substrate from 1mM $PdCl_2$ + 0.5M HCl solution by the application of 10mA/cm^2 current density to a 40mm^2 area graphite sheet substrate. SEM image shows that Pd metal of less than 5nm has deposited and aggregated to form disc shaped structures. The corresponding EDAX image confirms the high content of Pd on the surface.

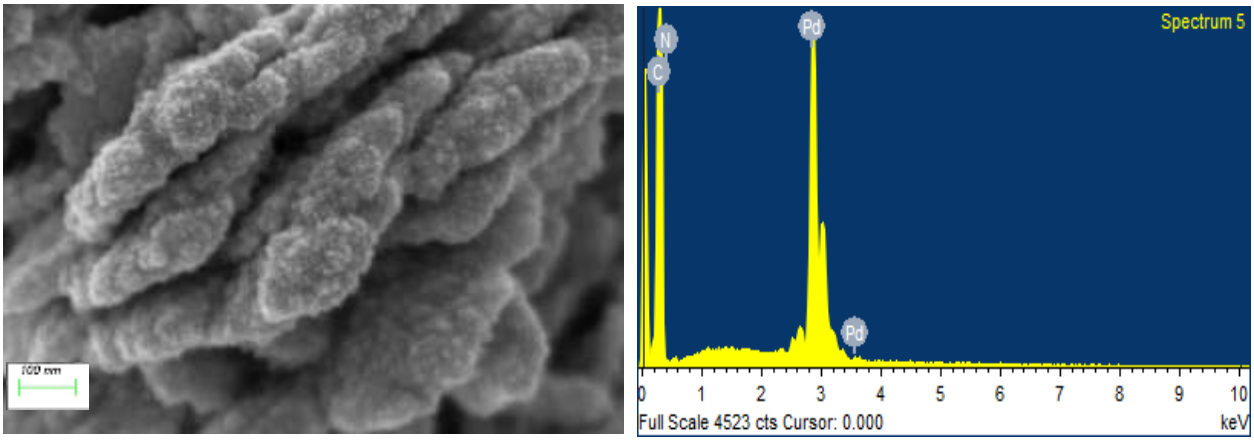

Figure 6. *(A). Scanning electron microscopy (SEM) and (B). Energy dispersive x-ray (EDAX) analysis images of Pd deposited on GS electrode by using chronopotentiometry technique.*

Figure 7 shows the high resolution SEM images and corresponding EDAX obtained for electrodeposited Pd-PANI nanocomposite on GS, (+)IGS, and (-)IGS respectively. Figure 7A shows that the nanocomposite deposited on the surface contains several clusters and are aggregated in the form of cauliflower shaped domains. These PANI clusters have Pd metal nanoparticles embedded on them. One can observe the aggregated nanoparticles by zooming the globular part of the flower shaped aggregates as can be seen from the zoomed portion of the image. Figure 7B shows globular shaped structures of different sizes when Pd-PANI is deposited on (+)IGS substrate. Figure 7C shows cylindrical shaped aggregated structures for the NC dispersed on (-)IGS substrate. These cylindrical structures were spread all over the surface. The shapes of these structures suggest a diffusion controlled aggregation growth [33]. The corresponding energy dispersive x-ray (EDAX) plots show that these substrates are mainly composed of Pd. The peaks

corresponding to C, N, and O elements are from the polymer matrix as well as from the oxygen functionalities developed on the surface during the electrochemical exfoliation.

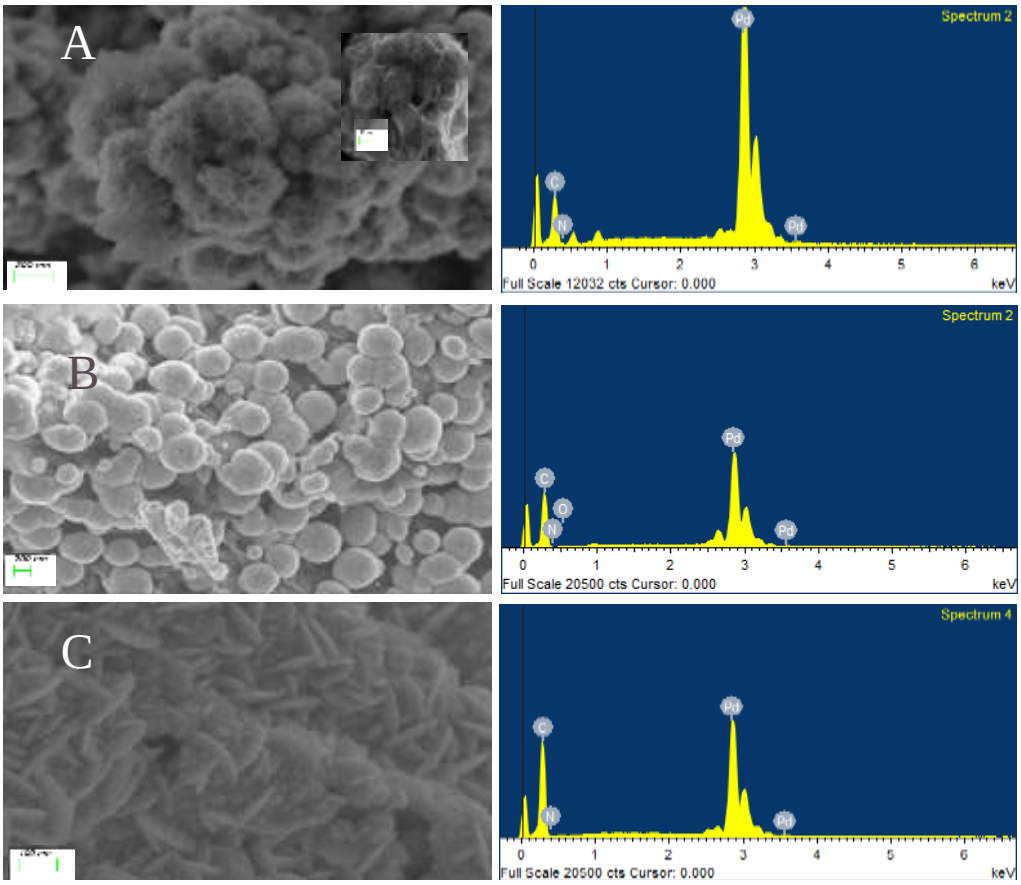

Figure 7. *Scanning electron micrographs (SEM) and energy dispersive x-ray analysis (EDAX) images of (A) Pd-PANI GS, (B) Pd-PANI (+)IGS and (C) Pd-PANI (-)IGS substrates.*

6.3.7. XRD studies of GS, (+)IGS, and (-)IGS:

Figure 8 shows the diffraction patterns of Pd-PANI nanocomposite deposited on (A) GS, (B) (+)IGS, and (C) (-)IGS substrates respectively in the θ range of 1-80° for an exposure time of one hour. The sharp peak patterns show that the nanocomposite deposits have highly crystalline features. The Pd-PANI deposited on all the three substrates show respective peaks at 40.13° (111), 46.90° (200), 68.30° (220), and 82.50° (311) angles which can be indexed to fcc nanostructure [34]. The additional sharp peaks are due to the respective substrate on which the nanocomposite was deposited. The calculated crystallite size values for the deposited composite are shown in

Table 2. It can be seen that Pd crystallite size changes with the substrate. The crystallite size (D) can be calculated using Debye-Scherrer equation:

$$D= k\lambda/\beta \, Cos\theta$$

k is a dimensionless shape factor (0.94) with a value close to unity, λ is the x-ray wavelength, β is the line broadening at half the maximum intensity (FWHM) (radians), and θ is the Bragg angle (in degrees).

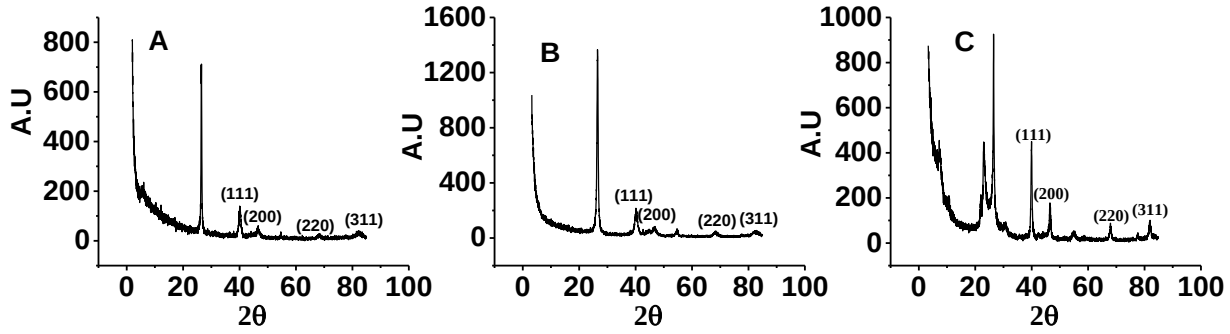

Figure 8. *X-ray diffraction graphs of Pd-PANI nanocomposites deposited on (A) GS, (B) (+)IGS, and (C) (-)IGS substrate respectively.*

Table 2. Crystallite sizes of Pd-PANI nanocomposite deposited on GS, (+)IGS and (-)IGS substrates.

Peak position (2θ)	Crystallite size (nm)		
	Pd-PANI GS	Pd-PANI (+)IGS	Pd-PANI (-)IGS
40.1	8.5	7.3	4.7
46.9	7.3	8.1	17.2
68.3	8.8	5.2	14.4
82.5	6.3	3.5	9.6

6.3.8. Cyclic voltammetric studies on exfoliated graphite:

Figure 9 shows the voltammetric behavior of the (A). Pd-PANI GS, (B). Pd-PANI (+)IGS, and (C). Pd-PANI (-)IGS electrode in 0.5M H_2SO_4 at a scan rate of 100mV/s. The voltammograms show two prominent peaks which were common in all the cases, one peak around (-0.2V) during the anodic scan which corresponds to the oxidation of adsorbed hydrogen and another peak around

+0.4V during the cathodic scan which represents the reduction of PdO to Pd [17]. Since Pd has the ability to adsorb as well as absorb H_2 onto it, the area measured by calculating the charge under the peak I does not reflect the true surface area of the Pd in the nanocomposite [35]. Nevertheless the electrocatalytic surface area (ECSA) of Pd can be calculated from the PdO stripping peak [35,36]. The charge values calculated by the integration of PdO stripping peak are 28, 87.8, and 97.5mC for Pd-PANI nanocomposite electrodes deposited onto GS, (+)IGS, and (-)IGS substrates respectively. The true ECSA calculated for Pd-PANI deposited on GS, (+)IGS, and (-)IGS are 66, 207 and 230cm^2. Exfoliation of the graphite sheet results an increase in the loading of palladium which can be attributed to the increase of surface sites for deposition of Pd-PANI nanocomposite. Figure 9C shows a peak at positive potentials above 0.8V vs. Hg/HgO. This peak can be attributed to the formation of PdO at positive potentials [37]. It is worth noting that the increase in true surface area of Pd is almost the same during the positive and negative exfoliation processes.

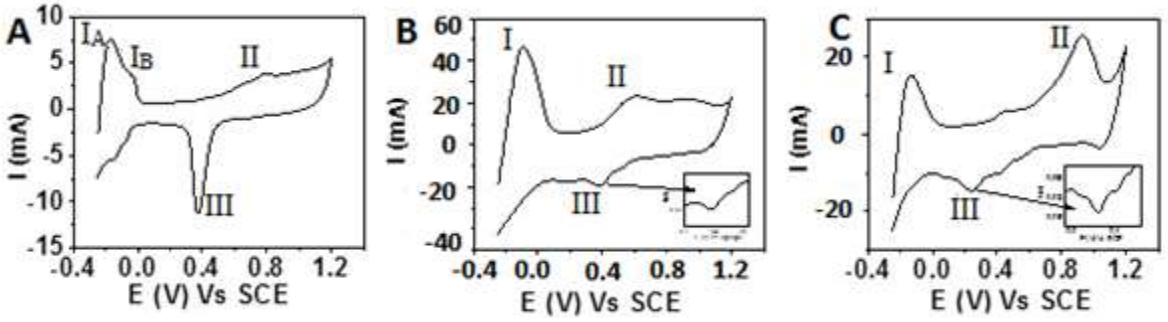

Figure 9. *Cyclic voltammograms of (A) Pd-PANI GS, (B) Pd-PANI (+)IGS, and (C) Pd-PANI (-)IGS in 0.5M H_2SO_4 solution. Geometrical surface area-40mm^2.*

6.3.9. Electrocatalytic oxidation of ethanol and methanol on exfoliated graphite oxide surface:

6.3.9.1. Ethanol oxidation studies:

Ethanol oxidation in alkaline media has been studied extensively by various groups due to its potential applications in alkaline fuel cells based on ethanol [38–40]. The mechanism of electrooxidation of ethanol is depicted in equations 1-4 given below. Complete oxidation of ethanol takes place through three intermediate steps by the formation of acetaldehyde and acetic acid as the intermediates and carbon dioxide as the final product [17,41]. The complete oxidation

of ethanol to CO_2 is not a straight forward process because of the poisoning of the electrode by the reaction intermediates. Ethanol oxidation in alkaline medium involves adsorption of reactants and intermediates through the hydroxyl group on the electrode surface [42,43]. The intermediates adsorb onto the electrode strongly and inhibit further reaction thereby bringing down the electrocatalytic activity of the electrode.

$$C_2H_5OH + 3OH^- \longrightarrow CH_3CO_{ads} + 3H_2O \quad (1)$$

$$OH^- \longrightarrow OH_{ads} \quad (2)$$

$$CH_3CO_{ads} + OH_{ads} \longrightarrow CH_3COOH \quad (3)$$

$$CH_3COOH + OH^- \longrightarrow CH_3COO^- + H_2O \quad (4)$$

6.3.9.2. CV studies for ethanol oxidation reaction (EOR):

Figure 10 shows CV of (A) Pd GS, (B) Pd-PANI GS, (C) Pd-PANI (+)IGS and (D) Pd-PANI (-)IGS electrodes at various ethanol concentrations using 0.1M NaOH at a scan rate of 50mV/s. Figures 10 (A-D) (a) show the cyclic voltammograms of 0.1M NaOH solution, which shows an oxide stripping reduction peak of PdO to Pd around -350mV vs. MMO. The effects of ethanol concentration on the cyclic voltammetric response due to the oxidation of ethanol on the porous Pd GS (0.1-0.4M), Pd-PANI GS (0.05-0.2M), Pd-PANI (+)IGS (0.01-0.04M), and Pd-PANI (-)IGS (0.01-0.04M) substrates are also shown in figure 10. The peak currents due to oxidation of ethanol during the forward scan is normally used to analyze the catalytic activity of an active material [44]. From figure 10, it can be seen that the peak potential in the anodic scan shifts towards positive direction with the increase in concentration of ethanol. The positive shift in peak potential can be attributed to the increase in coverage by reactant molecules at Pd sites at higher ethanol concentrations [45]. According to the previous reports, adsorbed hydroxyl ions play a key role in enhancing the electrocatalytic activity of the electrode [42]. The concentration of ethanol has been optimized to 0.4M for the studies on Pd GS electrode and 0.2M for Pd-PANI GS, 0.04M for Pd-PANI (+)IGS, and 0.04M for Pd-PANI (-)IGS electrodes. The cyclic voltammograms show a typical ethanol oxidation peak during the anodic scan while the reverse positive current peak during the cathodic cycle is associated with the oxidation of intermediate species adsorbed on Pd surface [42]. The ethanol oxidation currents on the surface of Pd-PANI nanocomposite show saturation of electrocatalytic behavior at low (0.04M) ethanol concentrations. This behavior

demonstrates that the highly porous and hierarchical pore structure of electrodeposited Pd electrode causes an enhanced ethanol oxidation reaction. Remarkably, the reverse anodic peak currents are lower in the case of Pd-PANI GS electrode compared to Pd GS which suggests that concentration of impurities on Pd-PANI is very much less compared to just Pd on graphite sheet, even though the oxidation current is comparably more in the case of Pd-PANI. The significant increase in the ethanol oxidation currents on Pd-PANI surface and lesser surface impurities confirm the excellent electrocatalytic activity of Pd-PANI over Pd GS electrode substrate.

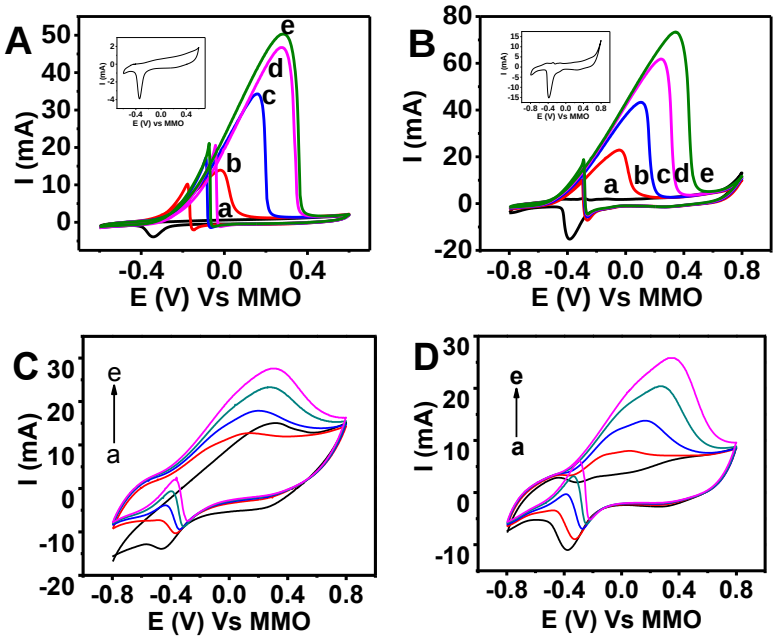

Figure 10. *Cyclic voltammograms of (A). Pd GS (0.1-0.4M ethanol), (B). Pd-PANI GS (0.05-0.2M ethanol), (C). Pd-PANI (+)IGS (0.01-0.04M ethanol), and (D). Pd-PANI (-)IGS (0.01-0.04M ethanol) electrode at various ethanol concentrations using 0.1M NaOH vs. Hg/HgO (MMO) reference electrode.* ***Inset:*** *Voltammograms of 0.1M NaOH solution.*

6.3.9.3. Reaction kinetics study of EOR:

The reaction kinetics of the EOR can be studied by measuring the effect of ethanol concentration on the reaction rate and calculating the reaction order by plotting the log I vs. log C (ethanol concentration) as shown in figure 11 [17]. The order of the reaction was calculated by using the following equation [46]:

$$I=nFkc^{m}$$

which can be expressed as

$$\log I=\log nFk + m \log c$$

where F-Faraday's constant, k-reaction constant, c-ethanol concentration, and m-reaction order with respect to ethanol.

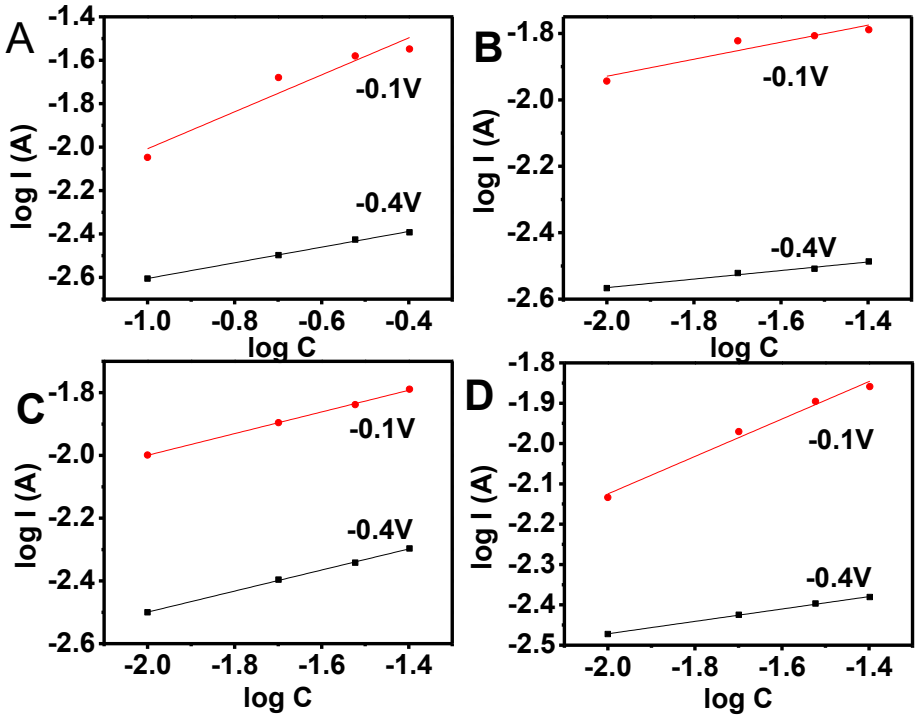

Figure 11. *Log I (A) vs. Log C (M) graph for (A). Pd GS, (B). Pd-PANI GS, (C). Pd-PANI (+)IGS, and (D). Pd-PANI (-)IGS in ethanol using 0.1M NaOH.*

The slope of the graph at a given potential gives the apparent reaction order (m) of ethanol electro-oxidation reaction with respect to the ethanol concentration. The reaction order was calculated at two different potentials namely, -0.4V and -0.1V vs. Hg/HgO reference electrode. The values of

the calculated reaction orders for Pd GS, Pd-PANI GS, Pd-PANI (+)IGS, and Pd-PANI (-)IGS electrodes are given below in Table 3 which shows that the reaction mechanism exhibits significant change in the reaction order with potentials in all the cases except on Pd-PANI (+)IGS. This leads to the inference that the reaction kinetics is influenced significantly by the applied potential in the case of the three systems. This can be explained by the availability of the active sites for adsorption of the molecules at more positive potential (-0.1V) which is not the case at potential of -0.4V.

Table 3. Reaction order measured for various electrodes using CV.

Substrate	Reaction order (m)	
	-0.4V	-0.1V
Pd GS	0.36	0.85
Pd-PANI GS	0.13	0.26
Pd-PANI (+)IGS	0.33	0.34
Pd-PANI (-)IGS	0.15	0.46

6.3.9.4. Tafel Analysis of EOR:

An analysis of Tafel plots (over potential (η) vs. log I) provides useful information which can help in understanding the nature and mechanism of the alcohol oxidation reactions. These plots do not often follow the relationship corresponding to the reaction and that as predicted by Butler-Volmer equation [42]. Therefore, the measured Tafel slopes deviate drastically from ideal values corresponding to usual electron transfer processes. This deviation arises due to adsorption of reactive intermediates formed during ethanol oxidation which decreases the available active sites for the fresh reactant molecules. The ethanol oxidation on Pd surface occurs through dissociative chemisorption of ethanol to form acetic acid and acetaldehyde, the active intermediate formed during the reaction adsorbs strongly on the electrode surface [42,47].

The steps involved in ethanol oxidation reaction have been earlier depicted in equations 1-4. The removal of CH_3CO_{ads} radical by adsorbed hydroxyl group (equation 3) is the rate determining step of the reaction. Recently, Ma *et al.* carried out a comparative study of the ethanol electrooxidation on Pt/C amd Pd/C surfaces in alkaline medium and observed that Pd/C shows higher catalytic

activity in alkaline medium [48]. Tripković *et al.* have suggested that the electrooxidation of ethanol at palladium surface follows a dual-path mechanism where acetic acid is the final product in one and carbon dioxide as the final product in the second pathway. They also observed that acetic acid is the major product when catalyzed by the adsorbed hydroxyl groups on the surface [47]. Wang *et al.* studied the electrooxidation of ethanol on Pt/C electrode at various concentrations of ethanol and observed that at low concentrations (1mM), acetic acid is the main product while at higher concentrations (0.5M) it is acetaldehyde [49]. Ethanol oxidation in alkaline media is being studied extensively in recent times by various groups due to its potential applications in low temperature alkaline fuel cells [38–40].

Figures 12 and 13 show the Tafel plots at Pd GS and Pd-PANI GS electrode in 0.2M ethanol in 0.1M NaOH supporting electrolyte at various temperatures and the corresponding Tafel slope values are presented in Table 4. These plots show abnormally high values of Tafel slopes which can be accounted for the adsorption of the carbonaceous intermediates resulting in the surface poisoning [42,50]. Therefore the Tafel slopes shown here are indicators that offer a wider perspective about the reaction process and the temperature dependence of the EOR. A change in the Tafel slope with temperature is indicative of the extent of adsorption of the reaction intermediates which inhibits the reactant molecules from adsorbing on the Pd GS and Pd-PANI GS electrode as the reaction advances. These adsorbed carbonaceous impurities block the active sites during the EOR.

Siddhardh *et al.* studied the ethanol oxidation on gold nanocomposites and observed two Tafel slopes for oxidation reaction in which the second Tafel slope shows higher values due to the surface poisoning of the catalyst material by the intermediates [50]. The data obtained in the present study exhibit two distinct slopes, with the value of second slope being higher than the first.

Since the change of current with the overpotential is also indicative of the availability of the free surface sites on the electrode, one can relate the change in the Tafel slope to the extent of surface poisoning during the course of the reaction. But in our study, there is a distinct decrease in the first Tafel slope values (Table 4), which is due to an increase in the EOR currents with increasing temperatures. This decline in the surface passivation with increasing temperature on the Pd-PANI GS nanocomposite electrode surface when compared to the Pd GS electrode points out an enhanced electrocatalytic activity of the nanocomposite system even at higher temperatures.

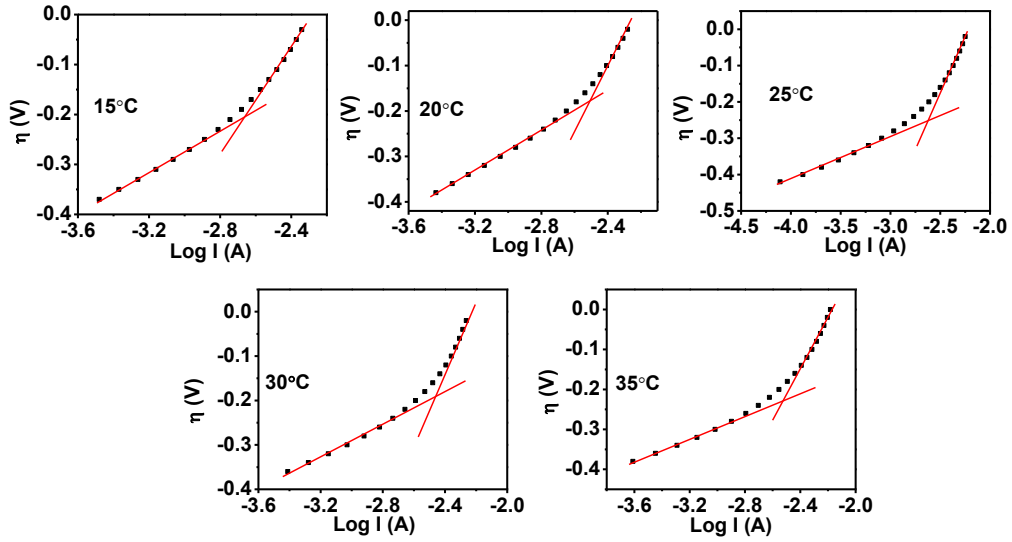

Figure 12. *Tafel plots over potential (η) vs. log I (A) for Pd GS electrode in 0.2M ethanol using 0.1M NaOH at different temperatures and the fitting for two slopes.*

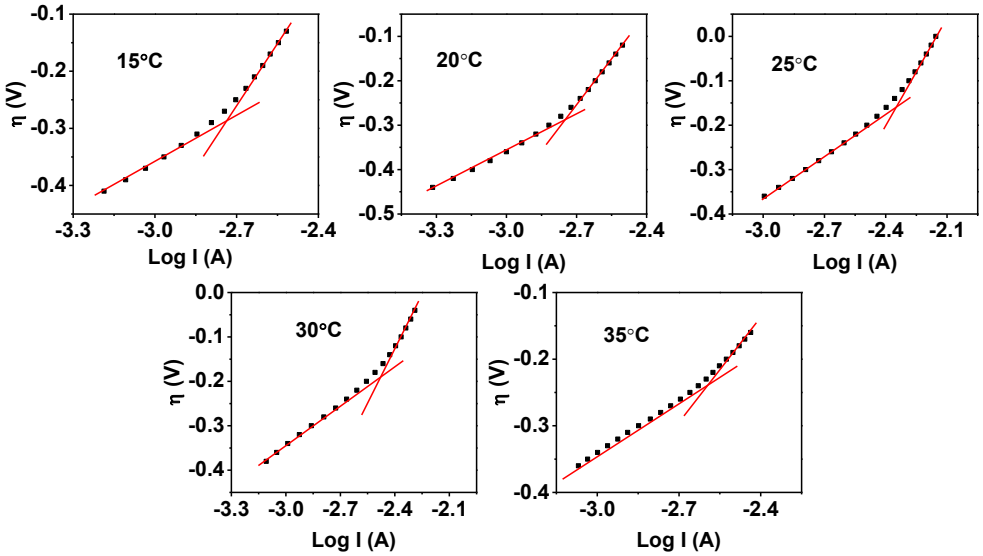

Figure 13. *Tafel plots over potential (η) vs. log I (A) for Pd-PANI GS electrode in 0.2M ethanol using 0.1M NaOH at different temperatures and the fitting for two slopes.*

Figures 14 and 15 show the Tafel plots of 0.04M ethanol at Pd-PANI (+)IGS, and Pd-PANI (-)IGS electrode using 0.1M NaOH. Tafel measurements were carried out at a temperature range of 15-35°C and in the potential range of -400mV to -50mV vs. MMO reference electrode. The concentration of ethanol used for catalytic studies was optimized from the saturation currents in cyclic voltammetry obtained for the Pd-PANI nanocomposite deposited on exfoliated graphite

substrates. The Tafel slopes obtained for the EOR is shown in Table 4. It can be seen that, there is a decrease of the Tafel slopes with increasing temperature. Lower Tafel slopes at higher temperatures indicate that enhanced catalytic activity contributed by decreased adsorption of reaction intermediates which results in higher oxidation current for a given overpotential.

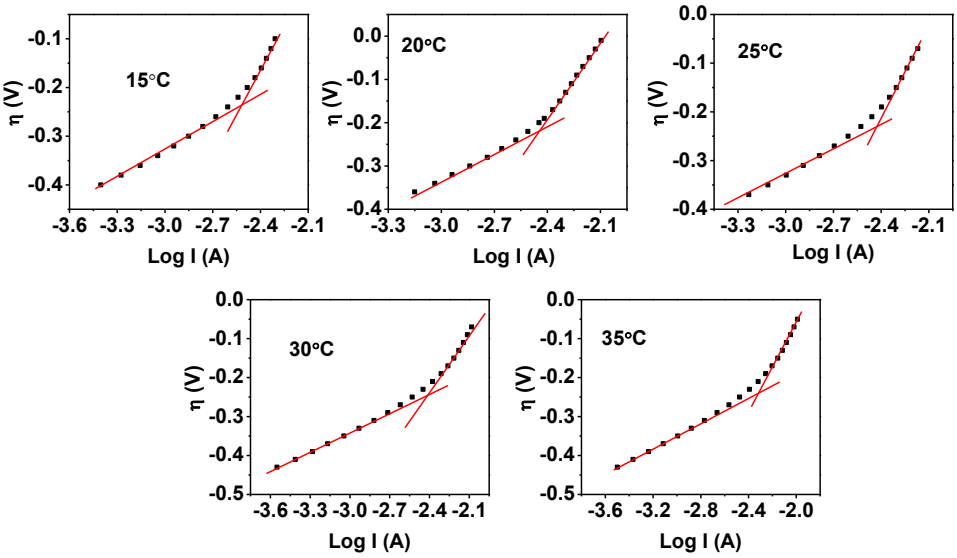

Figure 14. *Tafel slopes over potential (η) vs. log I (A) for Pd-PANI (+)IGS electrode in 0.04M ethanol at various temperatures and the fitting for two slopes.*

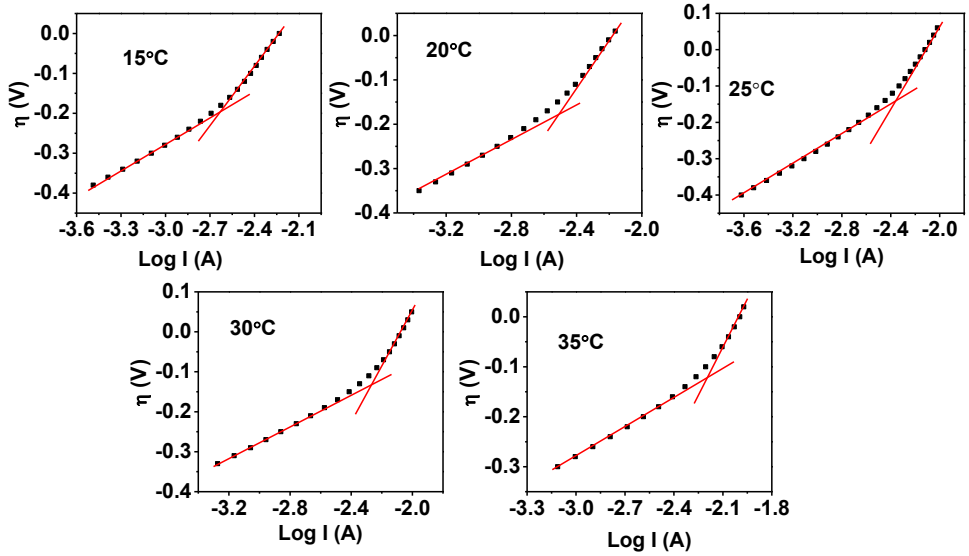

Figure 15. *Tafel slopes over potential (η) vs. log I (A) for Pd-PANI (-)IGS electrode in 0.04M ethanol at different temperatures and the fitting for two slopes.*

Table 4. Tafel slopes (mV/dec) for EOR process at Pd GS, Pd-PANI GS, Pd-PANI (+)IGS, and PdPANI (-)IGS electrodes respectively.

T (K)	Pd GS		Pd-PANI GS		Pd-PANI (+)IGS		Pd-PANI (-)IGS	
	Slope 1	Slope 2	Slope 1	Slope 2	Slope 1	Slope 2	Slope 1	Slope 2
288	270.7	674.6	211.7	386.9	193.1	512.7	219.4	490.3
293	222.6	590.8	164.7	341.5	216.5	592.4	221.7	481.7
298	174.7	582.1	136.1	375.5	184.8	572.7	208.6	478.8
303	163.8	635.5	125.4	447.2	171.6	275.2	194.3	594.2
308	178.8	635.5	114.7	405.2	184.9	636.7	187.1	445.4

6.3.9.5. Activation energy studies of EOR on PdGS, PdPANI GS, PdPANI (+)IGS, and PdPANI (-)IGS electrodes:

Electro organic reactions such as alcohol oxidation on electrode surfaces require high positive potentials under normal conditions due to their inherent poor reaction kinetics. In the presence of suitable electrocatalytic material, the surface interaction lowers the activation energy required for the reaction [51]. Ethanol oxidation reaction is one such reaction which takes place at higher oxidation potentials yielding relatively low current density. An inert electrode, like for example, graphite, noble metals like Pt, Au, Ag, and Pd are known to show varying extent of electrocatalytic behavior towards ethanol oxidation reaction. By immobilizing the noble metal atoms with conductive polymer material the electrocatalytic activity of the metal nanoparticles can be further enhanced. This is due to the network of conducting path provided by the polymer interconnectivity [16,17].

Figure 16 shows Arrhenius plots of (A) Pd GS and (B) Pd-PANI GS electrodes in 0.2M ethanol using 0.1M NaOH respectively. Activation energy (E_a) values measured from the slopes ($-E_a/2.303R$) obtained for the plots log I vs. 1/T are shown in Table 5, and the values obtained for EOR correlates with the Tafel slope values (Table 4). The linear relationship in these plots suggests that the mechanism essentially remains the same at temperature range of our study. The Table 5

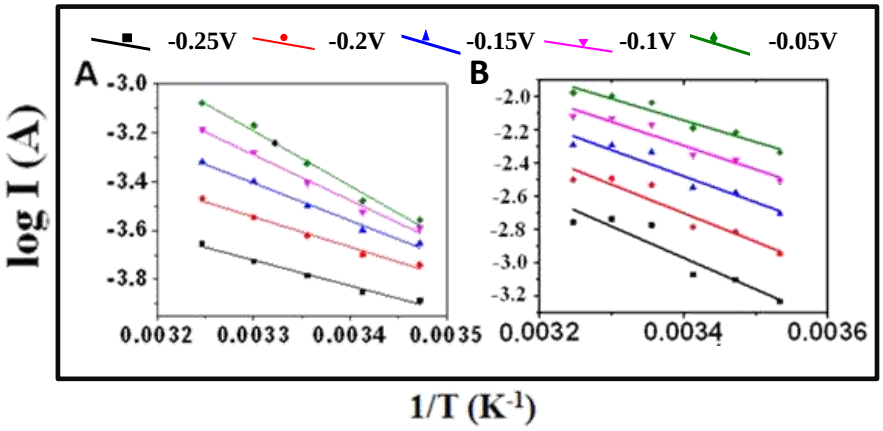

Figure 16. *Arrhenius plots at different over potentials for ethanol oxidation reaction (EOR) at (A) Pd GS and (B) Pd-PANI GS electrode in 0.2M ethanol using 0.1M NaOH respectively.*

also show that E_a value of Pd-PANI GS is significantly lower when compared to the Pd GS. The values of activation energies obtained in our study are relatively low when compared to the earlier reports [52]. This can be accounted for, by two explanations *i.e.* (i) the anti-fouling ability of Pd-PANI GS during the EOR, (ii) the enhanced EOR kinetics due to the large number of catalytically active sites present on a porous globular network of Pd-PANI as seen in the FESEM images figure 8. The Pd nanoparticles are well dispersed and optimally adhering on the network of PANI which provides multiple active sites for the ethanol molecules to adsorb on the surface initially. The activation energy (E_a) values (Table 5), increase with temperature in the case of Pd GS whereas it decreases for Pd-PANIGS which again confirms the anti-fouling activity of Pd-PANI GS at higher temperatures where even though the surface oxidation is enhanced, it does not lead to any significant blocking of active sites by the reaction intermediates. The continuous renewal of active sites by easy desorption of reaction intermediates can be the cause for enhanced electrocatalytic activity of Pd-PANI nanocomposite material.

Table 5. Activation energy (E_a) values at different temperatures obtained for ethanol oxidation reaction (EOR) on Pd GS and Pd-PANI GS electrode.

E (V)	E_a (kJ/mol)	
	Pd GS	**Pd-PANI GS**
-0.25	20.1	21.5
-0.2	23.5	19.3
-0.15	29.4	17.2
-0.1	35.7	15.4
-0.05	43.7	13.9

Figure 17 shows the Arrhenius plots obtained for (A) Pd-PANI (+)IGS and (B) Pd-PANI (-)IGS electrodes in 0.04M ethanol + 0.1M NaOH aqueous solution. The activation energy studies were carried out between the potential ranges -0.4V to -0.2V vs. MMO at varying the temperature from 15°C to 35°C. The low activation energies clearly suggest that the deposition of nanocomposite onto exfoliated substrates enhances the electrocatalytic property towards EOR. The increased surface area by the electrochemical exfoliation and the defects introduced during the process on the surface lead to a 3-dimensional surface structure. In addition, the formation of hydrophilic functional groups (-OH, -O-, -COOH) during the process of exfoliation enhances the interactions of ethanol molecules to the surface through hydrogen bonding interaction with –OH group. In addition, the hydrophobic groups facilitate alcohol diffusion into graphite layers, leading to larger three phase interface resulting in the reduction of liquid sealing effect [15,39].

From Table 6, it is seen that the activation energy (E_a) for ethanol oxidation is significantly lower for Pd-PANI exfoliated (+/-) IGS when compared to the E_a of 13.5kJ/mol for Pd-PANI supported graphite which is reported in literature [15]. This can be attributed to the microporous channels created on graphite surface after exfoliation behaving as individual nanoscale reactors.

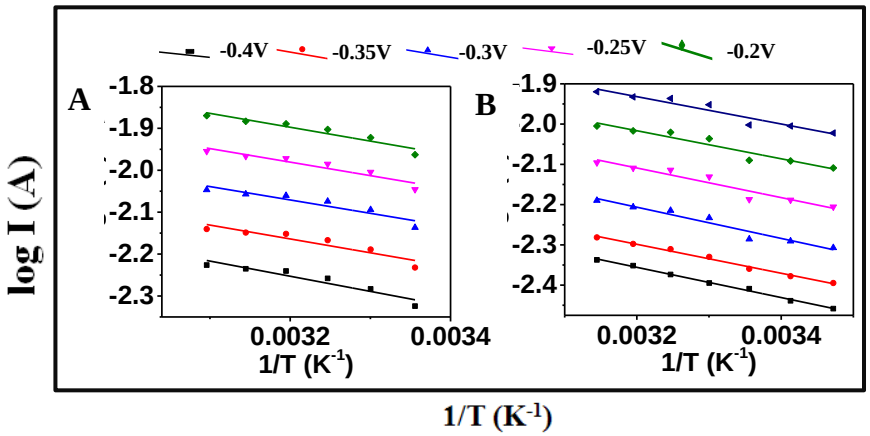

Figure 17. *Arrhenius plots at different over potential (η) values for (A). Pd-PANI (+)IGS and (B). Pd-PANI (-)IGS electrode in 0.04M ethanol using 0.1M NaOH.*

Table 6. Activation energy (E_a) values at different potentials for the ethanol oxidation on Pd-PANI (+)IGS and (-)IGS electrodes.

E (V)	E_a (kJ/mol)	
	Pd-PANI (+)IGS	**Pd-PANI (-)IGS**
-0.4	6.9	7.2
-0.35	6.3	6.9
-0.3	6.1	7.4
-0.25	6.2	7.0
-0.2	6.3	6.6

6.3.9.6. Methanol oxidation studies:

Methanol oxidation reactions on smooth electrode surfaces need high over potentials for the formation of final products. This is due to the strong adsorption of intermediates on the electrode substrates which inhibits the methanol electrooxidation and reduces the catalytic activity of the electrode. Bagotzki *et al*. [53] proposed that the methanol oxidation in acidic medium at Pt electrodes follows a reaction pathway, based on the sequential dehydrogenation of methanol molecules with formation of strongly bound intermediates occupying 1–3 Pt sites (x) as shown in the following scheme:

$$CH_3OH \longrightarrow CH_2OH_x \longrightarrow CHOH_{xx} \longrightarrow COH_{xxx} \longrightarrow CO_x$$

It was suggested that adsorbed CO_x can be oxidized to CO_2 at high overpotentials and adsorbed intermediate species like CH_2OH_x and $CHOH_{xx}$ would lead to the formation of formaldehyde and formic acid respectively.

At higher pH, the noble metal surfaces of Au and Pd undergo surface hydroxylation and get converted to metal hydroxides due to the adsorption of hydroxyl ions. These surface hydroxyl groups play a major role in methanol oxidation reaction on these surfaces. It was earlier reported that the reaction mechanism of methanol oxidation on polycrystalline gold in alkaline medium is catalyzed by the surface hydroxyl groups present on the surface [54]. Methanol molecule adsorbs onto metal electrode and the adjacent hydroxyl groups catalyze the oxidation of methanol.

$$CH_3OH + 5\ OH^- \longrightarrow HCOO^- + 4H_2O + 4e^- \qquad (5)$$

6.3.9.7. Cyclic voltammetry studies:

Figure 18 shows the cyclic voltammograms of methanol oxidation in 0.5M NaOH at various concentrations on (A). Pd GS, (B). Pd-PANI GS, (C). Pd-PANI (+)IGS, and (D). Pd-PANI (-)IGS respectively at a scan rate of 50mV/s. The CVs show a peak during anodic scan for the oxidation of methanol at the surface but interestingly, again an anodic peak appears during the reverse scan which corresponds to the oxidation of reaction intermediates formed during the forward cycle. The oxidation of intermediates take place on a freshly formed Pd surface lattice formed due to the reduction of PdO to Pd during the reverse scan. However, in the case of Pd-PANI on exfoliated substrates, only a reduction peak is observed and the reverse oxidation peak is absent. This can be attributed to the fact that the reaction intermediates do not remain on the surface of the catalyst thereby confirming the anti-fouling nature of nanocomposite deposited on exfoliated graphite sheets.

From the figure 18, it is observed that the peak potentials shift to positive values with increase in the concentration of methanol. The shifts in peak potentials for the methanol oxidation are due to the occupation of active sites of metal atoms by the methanol molecules and adsorbed intermediates. These molecules adsorb strongly to the electrode surface thereby inhibiting the MOR. This necessitates the application of higher positive potential to facilitate the oxidation process.

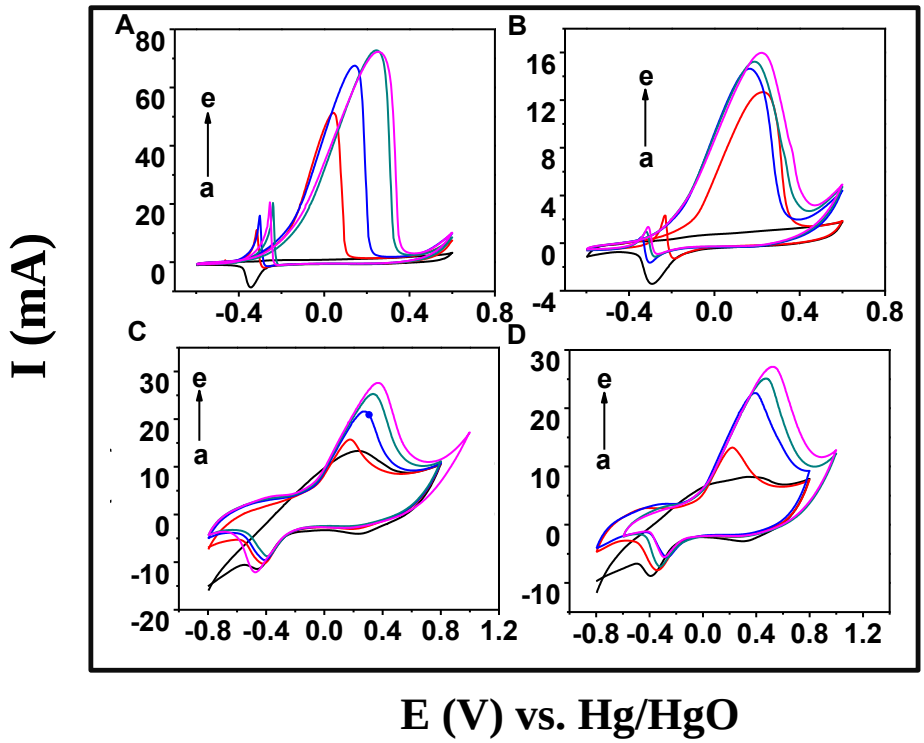

Figure 18. *Cyclic voltammograms of methanol in 0.5M NaOH on (A). Pd GS (0.1M-0.4M), (B). Pd-PANI GS (0.05M-0.2M), (C). Pd-PANI (+)IGS (0.01M-0.04M) and (D). Pd-PANI (-)IGS (0.01M-0.04M) electrodes.*

Figure 19 shows the cyclic voltammetric behavior of Pd GS, Pd-PANI GS, Pd-PANI (+)IGS, and Pd-PANI (-)IGS electrodes at different temperatures towards methanol oxidation in 0.5M NaOH at a scan rate of 100 V/s. It is observed that with increasing temperature, there is a trend towards increasing the peak current values for the oxidation of methanol. The trend in currents may be explained due to the fact that the increase in the temperature accelerates the adsorption of OH^- ions to form OH_{ads}. It has been reported that, presence of OH_{ads} improves the electrooxidation current of methanol by minimizing the formation of poisoning species on the electrode [42,44]. As a consequence, we find that the reverse anodic currents also increase with temperature.

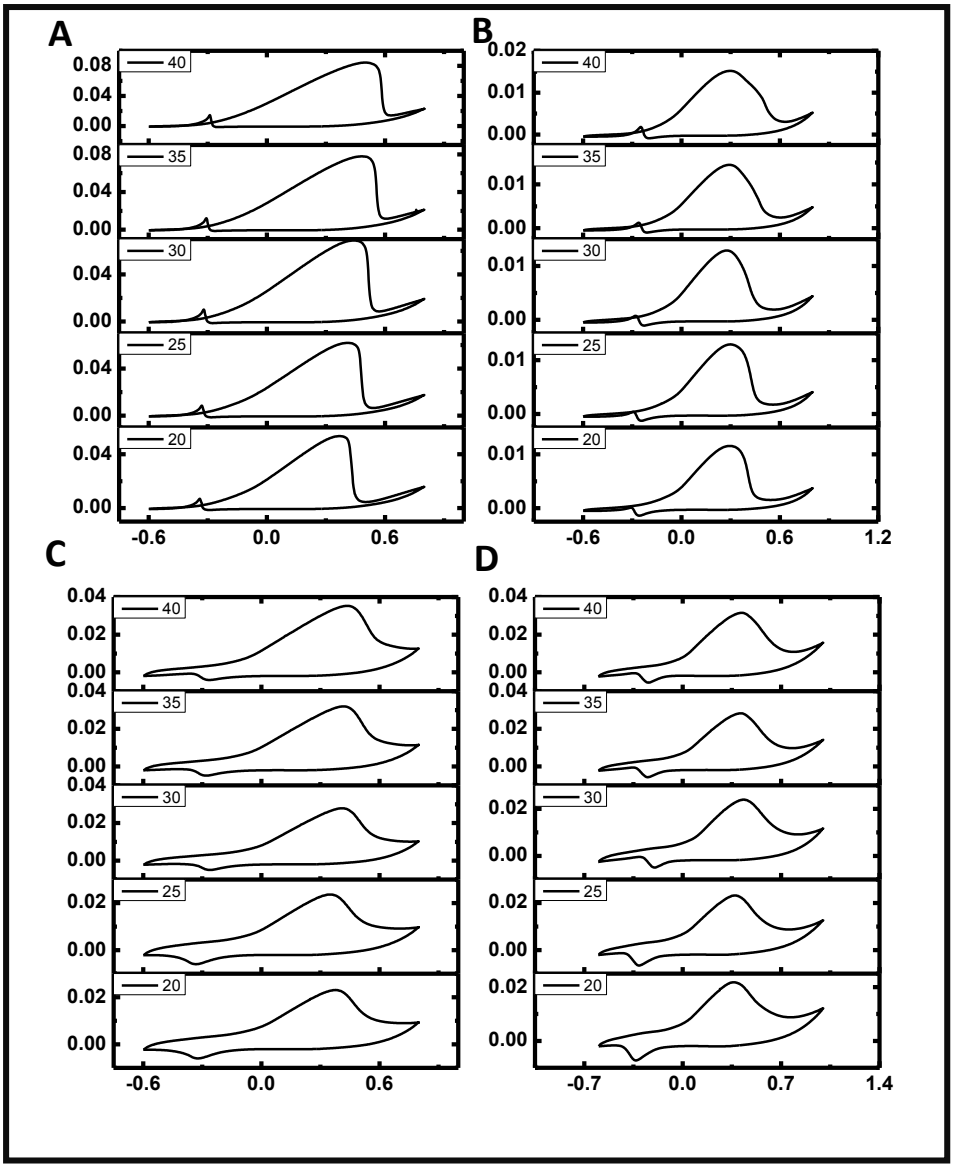

Figure 19. *Cyclic voltammograms of methanol in 0.5M NaOH at (A) Pd GS (2M MeOH), (B) Pd-PANI GS (0.4M MeOH), (B) Pd-PANI (+)IGS (0.1M MeOH), (C) Pd-PANI (-)IGS (0.1M MeOH) at various temperatures (Indicated in the inset of each CV).*

6.3.9.8 Tafel plot analysis of MOR:

Figures 20-23 show the Tafel plots for methanol oxidation reaction at temperature ranges of 20-40°C. These plots show two distinctive slopes suggesting two different electrochemical processes during the potential sweep. The values obtained for the MOR are given in Table 7 for respective electrodes. The Tafel slope values show large deviation from ideal values 120mV essentially due

to the electrode surface poisoning by reaction intermediates [55]. Whereas the nanocomposite modified electrodes show lower Tafel slopes compared to the Pd GS electrode, which can be attributed to the (i) improved electrocatalytic behavior of the electrode after functionalizing with the conducting polymer or (ii) anti-fouling ability of the Pd-PANI nanocomposite. Previous studies suggest that the second slope shows large deviation from the ideal values which is due to the formation of oxide layer on the Pd electrode [42].

The high values of second slope are due to the extensive high coverage of carbonaceous intermediates at active sites of the catalyst which in turn increases the potential to be applied for the oxidation of the alcohol.

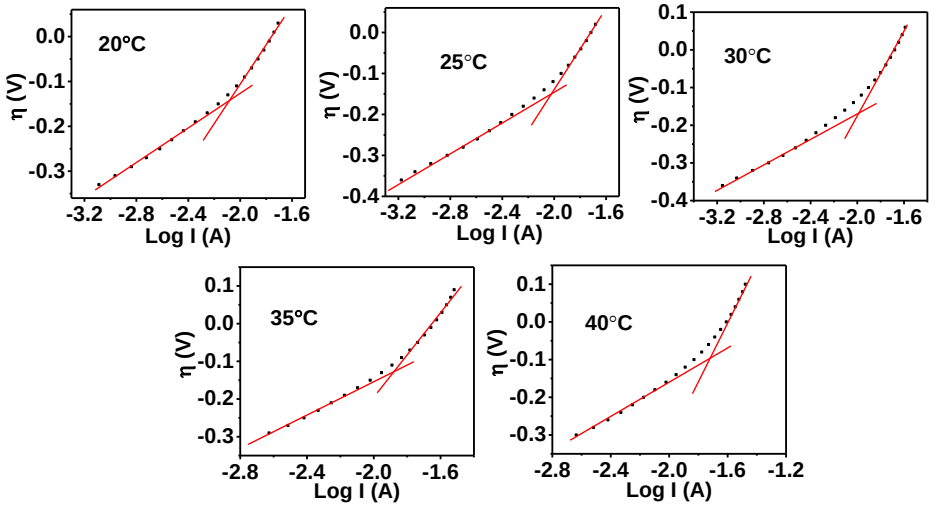

Figure 20. *Tafel plots (η vs. log I) graphs for Pd GS electrode in 2M methanol in 0.5M NaOH.*

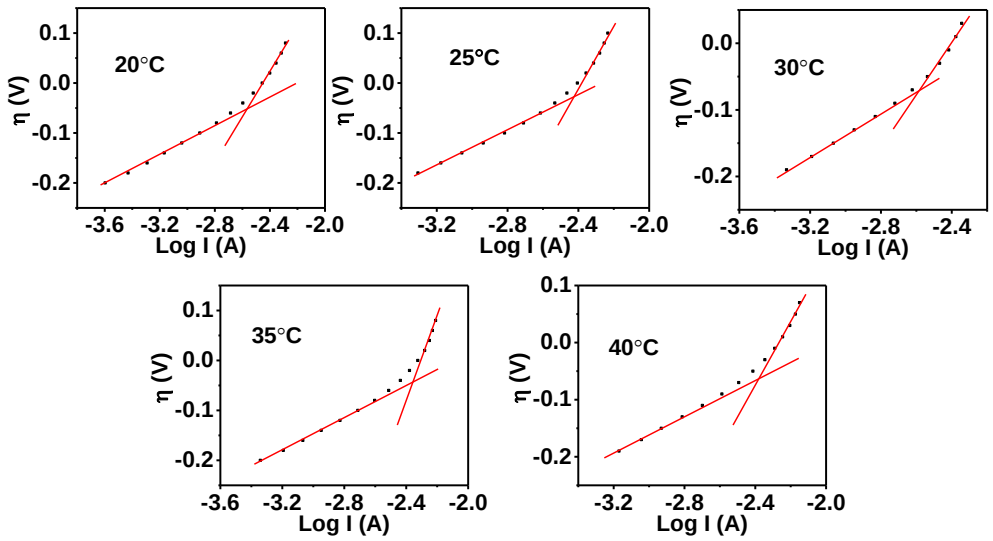

Figure 21. *Tafel plots (η vs. log I) graphs for Pd-PANI GS electrode in 0.4M methanol in 0.5M NaOH.*

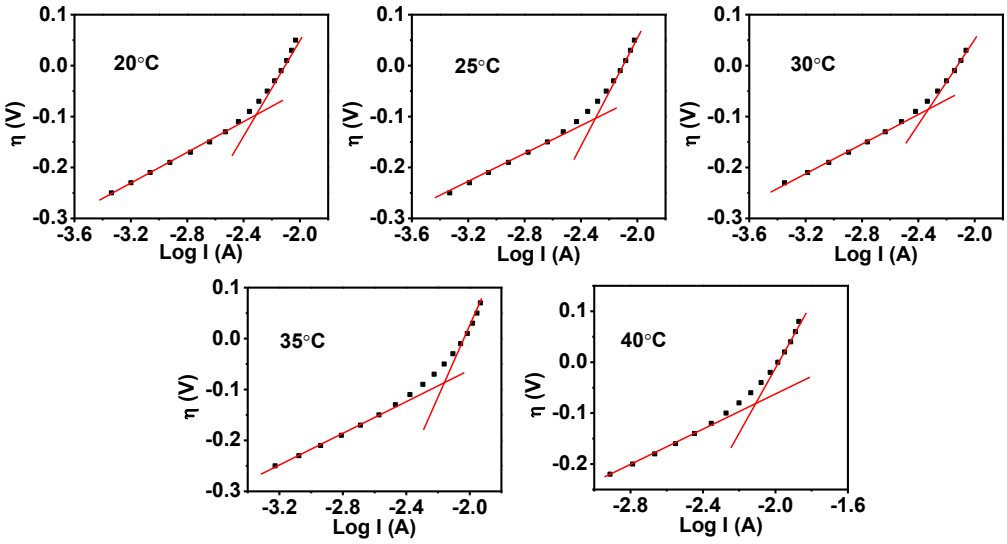

Figure 22. *Tafel plots (η vs. log I) graphs for Pd-PANI (+)IGS electrode in 0.1M methanol in 0.5M NaOH.*

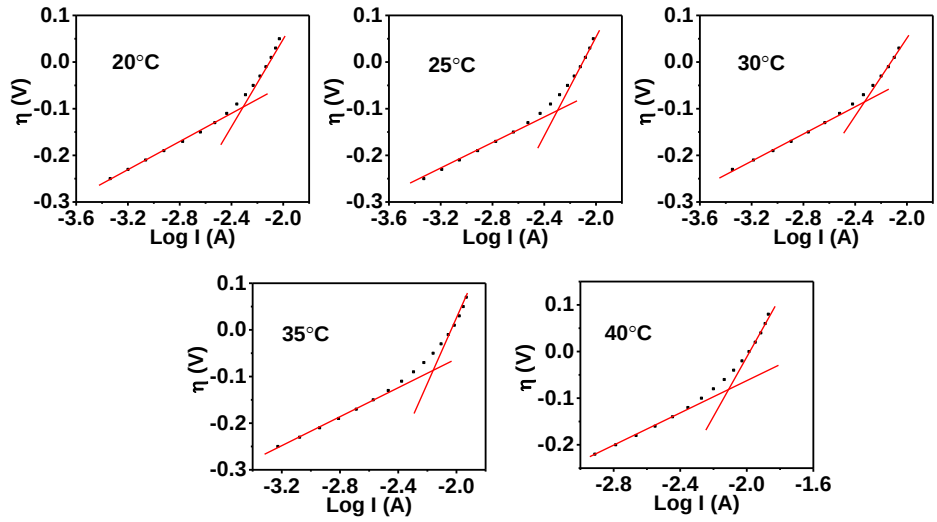

Figure 23. *Tafel plots (η vs. log I) graphs for 0.1M methanol in 0.5M NaOH at Pd-PANI (-)IGS electrode.*

Table 7. Tafel slope (mV/dec) values for MOR at Pd GS, Pd-PANI GS, Pd-PANI (+)IGS and Pd-PANI (-)IGS electrodes.

T (K)	Pd GS		Pd-PANI GS		Pd-PANI (+)IGS		Pd-PANI (-)IGS	
	Slope 1	Slope 2	Slope 1	Slope 2	Slope 1	Slope 2	Slope 1	Slope 2
293	193.0	410.5	144.3	386.2	145.4	397.0	139.3	392.0
298	188.0	402.3	139.0	326.2	148.8	489.0	160.9	445.7
303	195.7	476.8	146.5	490.6	132.4	331.1	159.3	377.9
308	240.3	563.2	168.4	691.4	149.1	436.3	164.8	333.2
313	244.0	592.4	159.6	405.2	148.5	395.0	161.0	420.0

6.3.9.9. Activation energy studies of MOR:

Figure 24 shows the Arrhenius plots (log I vs. 1/T) for methanol oxidation reaction at (A) Pd GS, (B) Pd-PANI GS in 0.5M NaOH solution respectively. Figure 25 shows the Arrhenius plots (log I

vs. 1/T) for methanol oxidation reaction at (A). Pd-PANI (+)IGS and (B). Pd-PANI (-)IGS, in 0.5M NaOH solution respectively. Activation energy values measured for the electrodes are shown in Tables 8 and 9. Average E_a values obtained for methanol oxidation reaction are 13.2, 15.3, 7.2, and 4.8kJ/mol for Pd GS, Pd-PANI GS, Pd-PANI (+)IGS and Pd-PANI (-)IGS respectively. From the Tables 8 and 9, it is inferred that Pd-PANI nanocomposite shows better electrocatalytic activity towards methanol oxidation compared to the just Pd nanoparticle. The electrocatalytic activity of the nanocomposite of Pd-PANI is very much enhanced by the deposition on electrochemically exfoliated graphite substrates. Marković *et al.* suggested the presence of hydroxyl functional group adjacent to the CO_{ads} enhances the conversion to CO_2 [56,57]. The lower activation energies for methanol oxidation reaction can be attributed to the availability of the hydroxyl sites adjacent to the methanol adsorption sites which facilitate the conversion of methanol to intermediates such as formaldehyde, formic acid, and finally CO_2. It can also be noted that the large number of hydrophilic functional groups in exfoliated graphite facilitates the conversion process.

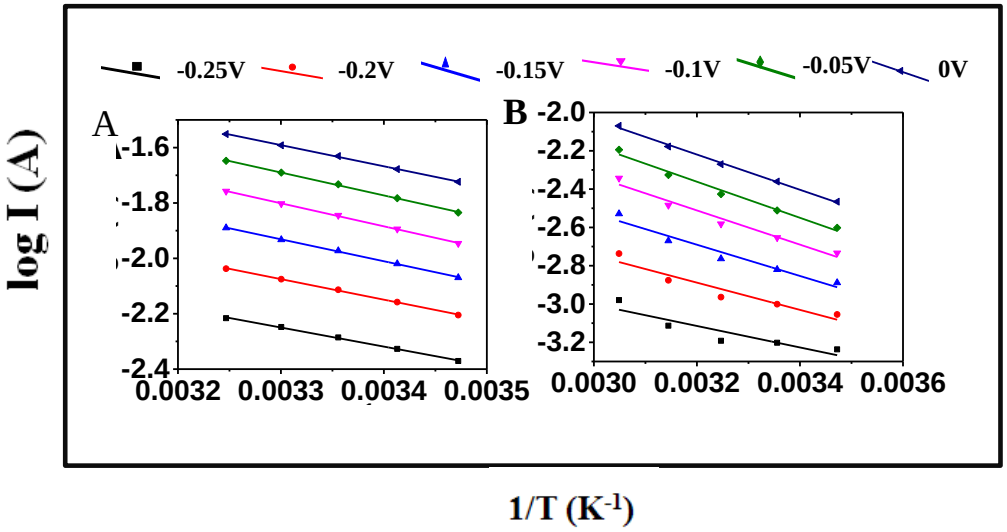

Figure 24. *Arrhenius plots for the methanol oxidation reaction at (A). Pd GS, (B). Pd-PANI GS, in 0.5M NaOH.*

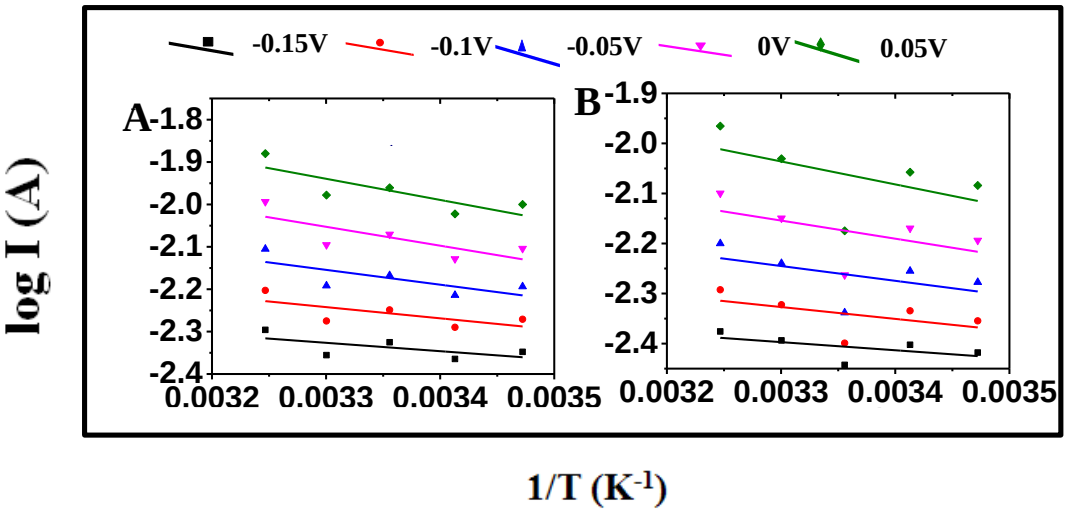

Figure 25. *Arrhenius plots for the methanol oxidation reaction at (A). Pd-PANI (+)IGS, (B). Pd-PANI (-)IGS, in 0.5M NaOH.*

Table 8. Activation energy values obtained for methanol oxidation reaction at Pd GS and Pd-PANI GS electrode.

E (V)	E_a (kJ/mol)	
	Pd GS	**Pd-PANI GS**
-0.25	13.2	10.7
-0.2	14.2	13.6
-0.15	15.2	15.6
-0.1	15.9	17.1
-0.05	15.9	18.0
0	14.6	17.6

Table 9. Activation energy (E_a) values obtained for methanol oxidation reaction at Pd-PANI (+)IGS and Pd-PANI (-)IGS electrode.

E (V)	E_a (kJ/mol)	
	Pd-PANI (+)IGS	**Pd-PANI (-)IGS**
-0.15	3.8	3.1
-0.1	5.0	4.5
-0.05	8.5	5.7
0	9.6	6.9
0.05	9.6	8.8

6.4. Conclusions:

Electrochemical exfoliation of flexible graphite sheets was carried out by the application of electrochemical potential in acetonitrile solvent with tetrabutylammonium tetrafluoroborate as supporting electrolyte. The exfoliation was carried out at positive and negative potential limits and were characterized by SEM, Raman, and XRD. They were used as integral electrode material for immobilizing Pd nanoparticles by electro deposition. The high Pd metal loading obtained for the substrates are due to the presence of edge planes and defects created over the surface. These defects act as heterogeneous sites for metal deposition. Similar method was adopted for depositing Pd-PANI nanocomposite on the electrodes. The large number of functional groups introduced on the graphite oxide during the exfoliation process aids in the methanol and ethanol oxidation reaction and significantly lowers the activation energy for the reaction. The Pd-PANI nanocomposite on graphite oxide showed very high electrocatalytic activity for methanol and ethanol oxidation. The excellent electrocatalytic activity has been attributed to substantial number of anchoring sites provided by the exfoliated graphite sheets due to the presence of large number of defects and inherent self-cleansing property of the Pd-PANI nanocomposite on the graphite oxide.

6.5. References:

[1] W.J. Zhou, B. Zhou, W.Z. Li, Z.H. Zhou, S.Q. Song, G.Q. Sun, Q. Xin, S. Douvartzides, M. Goula, P. Tsiakaras, Performance comparison of low-temperature direct alcohol fuel cells with different anode catalysts, J. Power Sources. 126 (2004) 16–22. doi:10.1016/j.jpowsour.2003.08.009.

[2] J.R. Varcoe, R.C.T. Slade, Prospects for alkaline anion-exchange membranes in low temperature fuel cells, Fuel Cells. 5 (2005) 187–200. doi:10.1002/fuce.200400045.

[3] G.R. Dieckmann, S.H. Langer, Comparisons of Ebonex® and graphite supports for platinum and nickel electrocatalysts, Electrochim. Acta. 44 (1998) 437–444. doi:10.1016/S0013-4686(98)00061-9.

[4] S. Bong, Y.R. Kim, I. Kim, S. Woo, S. Uhm, J. Lee, H. Kim, Graphene supported electrocatalysts for methanol oxidation, Electrochem. Commun. 12 (2010) 129–131. doi:10.1016/j.elecom.2009.11.005.

[5] B. Fang, N.K. Chaudhari, M.-S. Kim, J.H. Kim, J.-S. Yu, Homogeneous Deposition of Platinum Nanoparticles on Carbon Black for Proton Exchange Membrane Fuel Cell, J. Am. Chem. Soc. 131 (2009) 15330–15338. doi:10.1021/ja905749e.

[6] I.G. David, D.E. Popa, M. Buleandra, Pencil graphite electrodes: A versatile tool in electroanalysis, J. Anal. Methods Chem. 2017 (2017). doi:10.1155/2017/1905968.

[7] G. Lu, G. Zangari, Electrodeposition of platinum on highly oriented pyrolytic graphite. Part I: electrochemical characterization, J. Phys. Chem. B. 109 (2005) 7998–8007. doi:10.1021/jp0407324.

[8] B. Zhang, D.S. Su, Probing the Metal-Support Interaction in Carbon-Supported Catalysts by using Electron Microscopy, ChemCatChem. 7 (2015) 3639–3645. doi:10.1002/cctc.201500666.

[9] J.J. Liu, Advanced Electron Microscopy of Metal-Support Interactions in Supported Metal Catalysts, ChemCatChem. 3 (2011) 934–948. doi:10.1002/cctc.201100090.

[10] H.N. Pham, A.E. Anderson, R.L. Johnson, T.J. Schwartz, B.J. O'Neill, P. Duan, K.

Schmidt-Rohr, J.A. Dumesic, A.K. Datye, Carbon Overcoating of Supported Metal Catalysts for Improved Hydrothermal Stability, ACS Catal. 5 (2015) 4546–4555. doi:10.1021/acscatal.5b00329.

[11] P. EHRBURGER, O. MAHAJAN, P. WALKERJR, Carbon as a support for catalystsI. Effect of surface heterogeneity of carbon on dispersion of platinum, J. Catal. 43 (1976) 61–67. doi:10.1016/0021-9517(76)90293-1.

[12] C.A. Frysz, D.D.L. Chung, Electrochemical behavior of flexible graphite, Carbon N. Y. 35 (1997) 858–860. doi:10.1016/S0008-6223(97)80175-3.

[13] W. Yuan, Y. Zhou, Y. Li, C. Li, H. Peng, J. Zhang, Z. Liu, L. Dai, G. Shi, The edge- and basal-plane-specific electrochemistry of a single-layer graphene sheet, Sci. Rep. 3 (2013) 2248. doi:10.1038/srep02248.

[14] M. Nakahara, Y. Sanada, FT-IR ATR spectroscopy of the edge surface of pyrolytic graphite and its surface/PVC interface, J. Mater. Sci. 30 (1995) 4363–4368. doi:10.1007/BF00361518.

[15] C. Xu, L. Cheng, P. Shen, Y. Liu, Methanol and ethanol electrooxidation on Pt and Pd supported on carbon microspheres in alkaline media, Electrochem. Commun. 9 (2007) 997–1001. doi:10.1016/j.elecom.2006.12.003.

[16] S. Ghosh, A.-L. Teillout, D. Floresyona, P. de Oliveira, A. Hagège, H. Remita, Conducting polymer-supported palladium nanoplates for applications in direct alcohol oxidation, Int. J. Hydrogen Energy. 40 (2015) 4951–4959. doi:10.1016/j.ijhydene.2015.01.101.

[17] R.K. Pandey, V. Lakshminarayanan, Electro-oxidation of formic acid, methanol, and ethanol on electrodeposited Pd-polyaniline nanofiber films in acidic and alkaline medium, J. Phys. Chem. C. 113 (2009) 21596–21603. doi:10.1021/jp908239m.

[18] R. Santhanam, M. Noel, Effect of solvents on the intercalation/de-intercalation behaviour of monovalent ionic species from non-aqueous solvents on polypropylene-graphite composite electrode, J. Power Sources. 66 (1997) 47–54. doi:10.1016/S0378-7753(96)02472-X.

[19] B.H. Ka, S.M. Oh, Electrochemical Activation of Expanded Graphite Electrode for Electrochemical Capacitor, J. Electrochem. Soc. 155 (2008) A685. doi:10.1149/1.2953525.

[20] R. Santhanam, M. Noel, Electrochemical intercalation of ionic species of tetrabutylammonium perchlorate on graphite electrodes. A potential dual-intercalation battery system, J. Power Sources. 56 (1995) 101–105. doi:10.1016/0378-7753(95)80016-A.

[21] M. Noel, R. Santhanam, Electrochemistry of graphite intercalation compounds, J. Power Sources. 72 (1998) 53–65. doi:10.1016/S0378-7753(97)02675-X.

[22] A. Ambrosi, C.K. Chua, A. Bonanni, M. Pumera, Electrochemistry of graphene and related materials, Chem. Rev. 114 (2014) 7150–7188. doi:10.1021/cr500023c.

[23] P. Yu, S.E. Lowe, G.P. Simon, Y.L. Zhong, Electrochemical exfoliation of graphite and production of functional graphene, Curr. Opin. Colloid Interface Sci. 20 (2015) 329–338. doi:10.1016/j.cocis.2015.10.007.

[24] S. Hembacher, F.J. Giessibl, J. Mannhart, C.F. Quate, Revealing the hidden atom in graphite by low-temperature atomic force microscopy, Proc. Natl. Acad. Sci. 100 (2003) 12539–12542. doi:10.1073/pnas.2134173100.

[25] V. Lakshminarayanan, Design of a simple and compact scanning tunneling microscope, Curr. Sci. 74 (1998) 413–417.

[26] T. Sri Devi Kumari, A.J.J. Jebaraj, T.A. Raj, D. Jeyakumar, T.P. Kumar, A kish graphitic lithium-insertion anode material obtained from non-biodegradable plastic waste, Energy. 95 (2016) 483–493. doi:10.1016/j.energy.2015.11.069.

[27] P. Ramesh, S. Sampath, Selective determination of uric acid in presence of ascorbic acid and dopamine at neutral pH using exfoliated graphite electrodes, Electroanalysis. 16 (2004) 866–869. doi:10.1002/elan.200302890.

[28] M. Zhou, J. Tang, Q. Cheng, G. Xu, P. Cui, L.C. Qin, Few-layer graphene obtained by electrochemical exfoliation of graphite cathode, Chem. Phys. Lett. 572 (2013) 61–65. doi:10.1016/j.cplett.2013.04.013.

[29] A. Milev, M. Wilson, G.S.K. Kannangara, N. Tran, X-ray diffraction line profile analysis of nanocrystalline graphite, Mater. Chem. Phys. 111 (2008) 346–350. doi:10.1016/j.matchemphys.2008.04.024.

[30] F. Tuinstra, J.L. Koenig, Raman Spectrum of Graphite, J. Chem. Phys. 53 (1970) 1126–1130. doi:10.1063/1.1674108.

[31] L.J. Hardwick, P.W. Ruch, M. Hahn, W. Scheifele, R. Kötz, P. Novák, In situ Raman spectroscopy of insertion electrodes for lithium-ion batteries and supercapacitors: First cycle effects, J. Phys. Chem. Solids. 69 (2008) 1232–1237. doi:10.1016/j.jpcs.2007.10.017.

[32] M. Milica, Z. Branimir, S. Jasmina, L. Tomislav, N. Branimir, Electrochemical Polymerization of Aniline, in: Electropolymerization, InTech, 2011: pp. 77–96. doi:10.5772/28293.

[33] J. Yu, T. Fujita, A. Inoue, T. Sakurai, M. Chen, Electrochemical synthesis of palladium nanostructures with controllable morphology., Nanotechnology. 21 (2010) 85601. doi:10.1088/0957-4484/21/8/085601.

[34] Y. Li, G. Lu, X. Wu, G. Shi, Electrochemical fabrication of two-dimensional palladium nanostructures as substrates for surface enhanced raman scattering, J. Phys. Chem. B. 110 (2006) 24585–24592. doi:10.1021/jp0638787.

[35] L. Xiao, L. Zhuang, Y. Liu, J. Lu, Activating Pd by Morphology Tailoring for Oxygen Reduction, J. Am. Chem. Soc. 131 (2009) 602–608. doi:10.1021/ja8063765.

[36] W. Pan, X. Zhang, H. Ma, J. Zhang, Electrochemical synthesis, voltammetric behavior, and electrocatalytic activity of Pd nanoparticles, J. Phys. Chem. C. 112 (2008) 2456–2461. doi:10.1021/jp710092z.

[37] Z.P. Sun, X.G. Zhang, Y.Y. Liang, H.L. Li, A facile approach towards sulfonate functionalization of multi-walled carbon nanotubes as Pd catalyst support for ethylene glycol electro-oxidation, J. Power Sources. 191 (2009) 366–370. doi:10.1016/j.jpowsour.2009.01.093.

[38] M. Shibata, S. Motoo, Electrocatalysis by ad-atoms PART I. ENHANCEMENT OF THE

OXIDATION OF METHANOL ON PLATINUM AND PALLADIUM BY GOLD AD-ATOMS, J. Electroanal. Chem. Interfacial Electrochem. 209 (1986) 151–158. doi:10.1016/0022-0728(86)80193-0.

[39] E. Antolini, E.R. Gonzalez, Alkaline direct alcohol fuel cells, J. Power Sources. 195 (2010) 3431–3450. doi:10.1016/j.jpowsour.2009.11.145.

[40] E. Antolini, Catalysts for direct ethanol fuel cells, J. Power Sources. 170 (2007) 1–12. doi:10.1016/j.jpowsour.2007.04.009.

[41] C. Lamy, E.M. Belgsir, J.M. Léger, Electrocatalytic oxidation of aliphatic alcohols: Application to the direct alcohol fuel cell (DAFC), J. Appl. Electrochem. 31 (2001) 799–809. doi:10.1023/A:1017587310150.

[42] Z.X. Liang, T.S. Zhao, J.B. Xu, L.D. Zhu, Mechanism study of the ethanol oxidation reaction on palladium in alkaline media, Electrochim. Acta. 54 (2009) 2203–2208. doi:10.1016/j.electacta.2008.10.034.

[43] Y. Wang, S. Zou, W.-B. Cai, Recent Advances on Electro-Oxidation of Ethanol on Pt- and Pd-Based Catalysts: From Reaction Mechanisms to Catalytic Materials, Catalysts. 5 (2015) 1507–1534. doi:10.3390/catal5031507.

[44] Q. Kong, W. Feng, X. Zhu, J. Zhang, C. Sun, Fabrication, characterization and electrochemical properties of porous palladium bulk samples with high porosity and hierarchical pore structure, Chinese J. Catal. 38 (2017) 1038–1044. doi:10.1016/S1872-2067(17)62780-3.

[45] A.F.B. Barbosa, V.L. Oliveira, J. Van Drunen, G. Tremiliosi-Filho, Ethanol electro-oxidation reaction using a polycrystalline nickel electrode in alkaline media: Temperature influence and reaction mechanism, J. Electroanal. Chem. 746 (2015) 31–38. doi:10.1016/j.jelechem.2015.03.024.

[46] D. Chu, Methanol Electro-oxidation on Unsupported Pt-Ru Alloys at Different Temperatures, J. Electrochem. Soc. 143 (1996) 1685. doi:10.1149/1.1836700.

[47] A.V. Tripković, K.D. Popović, J.D. Lović, The influence of the oxygen-containing species on the electrooxidation of the C1–C4 alcohols at some platinum single crystal surfaces in

alkaline solution, Electrochim. Acta. 46 (2001) 3163–3173. doi:10.1016/S0013-4686(01)00608-9.

[48] L. Ma, D. Chu, R. Chen, Comparison of ethanol electro-oxidation on Pt/C and Pd/C catalysts in alkaline media, Int. J. Hydrogen Energy. 37 (2012) 11185–11194. doi:10.1016/j.ijhydene.2012.04.132.

[49] H. Wang, Z. Jusys, R.J. Behm, Ethanol Electrooxidation on a Carbon-Supported Pt Catalyst: Reaction Kinetics and Product Yields, J. Phys. Chem. B. 108 (2004) 19413–19424. doi:10.1021/jp046561k.

[50] R.S. Sai Siddhardha, M. Anupam Kumar, V. Lakshminarayanan, S.S. Ramamurthy, Anti-fouling response of gold-carbon nanotubes composite for enhanced ethanol electrooxidation, J. Power Sources. 271 (2014) 305–311. doi:10.1016/j.jpowsour.2014.08.023.

[51] D. Pletcher, R. Greff, R. Peat, L. M. Peter, J. Robinson, INSTRUMENTAL METHODS IN ELECTROCHEMISTRY, HORWOOD Publishers., 2011. https://www.sciencedirect.com/science/book/9781898563808.

[52] R.K. Pandey, V. Lakshminarayanan, Ethanol electrocatalysis on gold and conducting polymer nanocomposites: A study of the kinetic parameters, Appl. Catal. B Environ. 125 (2012) 271–281. doi:10.1016/j.apcatb.2012.06.002.

[53] V.S. Bagotzky, Y.B. Vassiliev, O.A. Khazova, Generalized scheme of chemisorption, electrooxidation and electroreduction of simple organic compounds on platinum group metals, J. Electroanal. Chem. 81 (1977) 229–238. doi:10.1016/S0022-0728(77)80019-3.

[54] Z. Borkowska, A. Tymosiak-Zielinska, G. Shul, Electrooxidation of methanol on polycrystalline and single crystal gold electrodes, in: Electrochim. Acta, 2004: pp. 1209–1220. doi:10.1016/j.electacta.2003.09.046.

[55] A. Renjith, V. Lakshminarayanan, One step preparation of “ready to use” Au@Pd nanoparticle modified surface using deep eutectic solvents and a study of its electrocatalytic properties in methanol oxidation reaction, J. Mater. Chem. A. 3 (2015) 3019–3028. doi:10.1039/C4TA05302H.

[56] N.M. Marković, T.J. Schmidt, B.N. Grgur, H.A. Gasteiger, R.J. Behm, P.N. Ross, Effect of Temperature on Surface Processes at the Pt(111)−Liquid Interface: Hydrogen Adsorption, Oxide Formation, and CO Oxidation, J. Phys. Chem. B. 103 (1999) 8568–8577. doi:10.1021/jp991826u.

[57] M.A.F. Akhairi, S.K. Kamarudin, Catalysts in direct ethanol fuel cell (DEFC): An overview, Int. J. Hydrogen Energy. 41 (2016) 4214–4228. doi:10.1016/j.ijhydene.2015.12.145.

Chapter 7

Summary and future scope of the work

Summary:

The thesis deals with the electrochemical studies of various SAMs on two oxide materials namely, Indium Tin Oxide (ITO) and graphite oxide (GrO). Surface functionalization of ITO opens up the potential for its use as a bio-sensing platform and provides an inert electrically conducting and optically transparent substrate which is cheaper and highly reliable for device development. The exfoliated graphite oxide can be used as a functional surface for depositing Pd nanoparticle which has been demonstrated to possess excellent electrocatalytic activity with very low activation energy for methanol and ethanol oxidation reactions in alkaline medium.

A more detailed summary of the work carried out is described as below:

1. Adsorption kinetics of phosphonic acids and proteins on functionalized Indium tin oxide (ITO) surfaces using electrochemical impedance spectroscopy

Adsorption kinetics of various phosphonic acids and proteins were studied using electrochemical impedance spectroscopy (EIS) by using small chain length PAs such as 3-phosphonopropionic acid (PPA), butylphosphonic acid (BuPA), benzylphosphonic acid (BPA), and 4-aminobenzylphosphonic acid (ABPA) which contain –COOH, $–CH_3$, phenyl, and $–NH_2$ groups as terminal groups. The adsorption rate constant of the PAs on ITO is dependent on their concentration and the terminal functional group of phosphonic acids. It is shown that, adsorption kinetics of phosphonic acids and proteins follow two time constants. During the first step, a rapid adsorption of phosphonic acid molecules takes place randomly over the surface followed by slow secondary adsorption which involves rearrangement of tail groups. The adsorption kinetics studies were carried out at an identified frequency for various phosphonic acid molecules by following the changes in imaginary component of the impedance with adsorption time (t) by keeping the frequency constant.

The PA modified surface was used as a platform for adsorption of a heme protein *cyt c* and an enzyme urease. The adsorption of these bio-molecules on the PA modified surface was confirmed

using atomic force microscopy (AFM) and their activity was studied using chronoamperometry (CA) technique.

2. Adsorption kinetics and electron transfer reactions on self-assembled monolayers (SAMs) of long chain alkylphosphonic acids, silanes, and carboxylic acids on Indium Tin Oxide (ITO) surface

A comparative study on the adsorption kinetics of long chain alkyl phosphonic acids, alkyl silanes, and alkanoic acids on ITO was carried out using electrochemical impedance spectroscopy (EIS). The electron transfer barrier properties of these monolayer substrates were studied by using cyclic voltammetry (CV) and electrochemical impedance spectroscopy (EIS). Phosphonic acids show effective blocking behavior towards $[Fe(CN)_6]^{3-/4-}$ redox species which increases with the chain length. A study of the adsorption kinetics of PAs, silanes, and CAs in ethanol shows that the kinetics of adsorption follows two distinct steps during the formation of a complete monolayer film. From these results, it is concluded that long chain phosphonic acid monolayers can form more impermeable films on ITO, than silanes and carboxylic acids. A quantitative study on the distribution of pinholes and defects in the monolayer film has been carried out using electrochemical impedance spectroscopy.

3. Electron transfer studies of ferrocene derivatives on short chain phosphonic acid (PA) modified Indium Tin Oxide (ITO) surfaces

Electron transfer behavior of different ferrocene derivatives were studied by benzylphosphonic acid (BPA), 3-phosphonopropionic acid (PPA), butylphosphonic acid (BuPA), and 4-aminobenzylphosphonic acid (ABPA) modified ITO electrodes. It is shown here that, the blocking behavior of modified ITO electrodes depends upon the terminal groups, nature of the redox moiety and solvent under study. For ionic redox species, electrostatic interaction stabilizes the species within the film that leads to a positive shift in formal potentials of redox moieties. However, in the case of hydrophobic redox species it is observed that the formal potential shifts towards negative side due to the favorable orientation of the ferrocene redox moiety. The behavior of phosphonate monolayers shows that the monolayer functionality influences the electron transfer behavior.

4. Electrochemical and morphological characterization 3-aminopropyltrimethoxy silane (APTMS) on indium tin oxide (ITO) surfaces

Electrochemical behavior of APTMS modified ITO substrate at different pH conditions were studied using two charged redox couples namely ferro/ferricyanide $[Fe(CN)_6]^{3-/4-}$, $[Ru(NH_3)_6]^{3+/2+}$, and a neutral molecule ferrocenemethanol (FcOH) as a redox probe. Electrochemical behavior of the substrates was examined using CV and EIS. It is observed that, the electrostatic interactions play a key role in determining the electron transfer behavior of $[Fe(CN)_6]^{3-/4-}$ and $[Ru(NH_3)_6]^{3+/2+}$ redox couple, whereas in the case of FcOH unfavorable hydrophobic interactions play a dominant role in determining the electron transfer behavior. It is shown here that, $[Fe(CN)_6]^{3-/4-}$ is trapped within the film of APTMS during the cycling process. The intercalation of redox couple has been explained by the electrostatic attraction between negatively charged redox couple and positively charged polymer film. Cytochrome *c* (*cyt c*) protein is immobilized onto APTMS/ITO and electrochemical studies were carried out to evaluate its electrocatalytic activity towards H_2O_2. It is also shown that, bare ITO is also quite sensitive to H_2O_2 and can be used for kinetics of enzyme reaction of glucose oxidase-glucose.

5. Electrochemically intercalated graphite substrates for immobilization of metal nanostructures

Flexible graphite sheets are electrochemically exfoliated by the application of two extremes, high positive and negative potentials. These exfoliated substrates used for the immobilization of Pd metal nanoparticles. These films have been prepared from a solution of 1mM $PdCl_2$ dissolved in 0.5M HCl solution. Metal deposition is carried out using chronopotentiometry (CP) technique. The Pd decorated substrates were used for oxidation of methanol and ethanol in alkaline medium. It is concluded from this work, that the metallic film deposited over exfoliated graphite shows excellent electrocatalytic activity with low activation energy towards alcohol oxidation reaction which has potential implications in the development of direct alcohol fuel cells (DAFCs).

Future scope of the work:

1. The highly hydrophobic monolayers formed by the surface modification of ITO, which is an optically transparent and conducting oxide, with phosphonic acid monolayer can be used for anchoring many bio-molecules like proteins and lipids. The process can lead to the development of either optically based or electrochemically based bio-sensors. The work

carried out here in electron transfer studies show encouraging results with potential for device development.

2. For homeotropic alignment of liquid crystals, silane monolayers hexadecyltrichlorosilane (HDTS) and octadecyltrichlorosilane (ODTS) are usually used. Surface modification with phosphonic acid monolayer provides an effective alternative to the silane film. Preliminary studies carried out in our laboratories demonstrate that phosphonate monolayer indeed help to align liquid crystals homeotropically.
3. The graphite oxide has the ability to encapsulate Pd nanoparticles. The rich functionalization of the graphite oxide with –OH and –COOH groups provide highly hydrophilic surface sites for the diffusion of methanol and ethanol molecules for eventful oxidation with relatively low activation energy. Therefore, the Pd-GrO nanocomposite material can be used as fuel cell electrode in alkaline direct alcohol fuel cells.